Technische Universität München
Fakultät für Maschinenwesen
Lehrstuhl für Aerodynamik und Strömungsmechanik

A low Mach number consistent compressible approach for simulation of cavitating flows

Steffen J. Schmidt

Vollständiger Abdruck der von der Fakultät für Maschinenwesen der Technischen Universität München zur Erlangung des akademischen Grades eines

Doktor-Ingenieurs

genehmigten Dissertation.

Vorsitzender:		Univ.-Prof. Dr.-Ing. Hans Kaltenbach
Prüfer der Dissertation:	1.	Univ.-Prof. Dr.-Ing. Nikolaus A. Adams
	2.	Prof. Dr. Ir. Tom J.C. van Terwisga, University of Technology, Delft/Niederlande

Die Dissertation wurde am 05.02.2015 bei der Technischen Universität München eingereicht und durch die Fakultät für Maschinenwesen am 06.07.2015 angenommen.

Steffen J. Schmidt
Carl-Orff-Bogen 114
80939 München
Germany

steffen.schmidt@tum.de

27. Januar 2015
Typesetting LaTeX

Danksagung

Die vorliegende Arbeit entstand während meiner Zeit am Lehrstuhl für Strömungsmechanik (Abteilung Gasdynamik) sowie am Lehrstuhl für Aerodynamik und Strömungsmechanik der Technischen Universität München.

An dieser Stelle möchte ich einigen Personen meinen Dank aussprechen, die in besonderer Weise zum Gelingen meiner Arbeit beigetragen haben.

Ich möchte mich ganz besonders bei meinem Doktorvater, Prof. Dr.-Ing. N.A. Adams, für seine Betreuung, Unterstützung, seine Geduld und sein Vertrauen in mich bedanken.

Weiterhin bedanke ich mich herzlich bei Prof. Dr. Ir. T.J.C. van Terwisga für die Übername des Zweitgutachtens und für zahlreiche Diskussionen auf Tagungen und bei Besuchen.

Für die Übernahme des Vorsitzes bedanke ich mich herzlich bei Prof. Dr.-Ing. H. Kaltenbach, bei Frau Grygier bedanke ich mich für die Organisation und die Durchführung des Umlaufs.

Ein sehr großes Dankeschön richte ich an zahlreiche ehemalige und aktuelle Mitarbeiterinnen und Mitarbeiter des Lehrstuhls für Strömungsmechanik sowie insbesondere des Lehrstuhls für Aerodynamik und Strömungsmechanik. Sie alle in einem angemessenen Rahmen zu nennen würde den Umfang einer Danksagung bei weitem sprengen, daher möge man mir nachsehen, dass ich von einer namentlichen Auflistung absehe. Ich bin absolut sicher, dass alle, denen ich mehr als nur ein einfaches "'Dankeschön"' schulde, dies früher oder später persönlich von mir hören werden.

Mein größter Dank geht an Andreas und Annemarie Schmidt. Arbeit ist wichtig und Familie ist heilig. Vielen Dank für die stetige Unterstützung, nahezu unendliche Geduld und das Ertragen gelegentlicher Launen, wenn's mal wieder unwetterlich war.

Ingolstadt, den 20.12.2015

Steffen J. Schmidt

Contents

Abstract

Liquid flows with partial evaporation (cavitation) play an important role in energy technology (pumps and turbines), in automotive technology (injection systems), in process technology (hydraulic presses), in naval architecture and in space engineering. While evaporation itself may limit the efficiency of a device or result in chocking of a nozzle, the collapse-like re-condensation often results in the formation of noise or erosion damage of a machine [13, 38]. The efficiency and the lifetime of a hydraulic device thus are strongly affected or even limited by cavitation phenomena. Experimental investigations of real-scale devices often are hardly possible. Furthermore, manufacturing of prototypes and performance of durability tests might be too costly and time consuming during early development stages.

Due to ongoing gain in computational resources, several computational fluid dynamics packages for simulation of cavitating flows have been developed. Aside of open source software (e.g. OpenFOAM), commercial software packages are mainly applied in industrial day-to-day 3-D simulations. Mean flow properties, such as discharge coefficients of nozzles or the efficiency of ship propellers, are often satisfactorily predictable by available software packages. However, the deduction of estimates to characterize potential risk for cavitation erosion was mostly impossible with available methods and approaches.

The major development in this thesis is a numerical approach which allows for the prediction of erosion risk. This is achieved by high temporal resolution of the dynamics of cavitating flows including collapse-induced loads. The key element of the approach is the developed flux-function. Unlike established techniques, the novel approach enables the computation of compressible cavitating flows including wave dynamic phenomena without the use of time-operator preconditioning even in case of low Mach number flows. Both efficiency and robustness of the method have been increased until industrial applicability was reached.

In combination with a thermodynamic equilibrium model several internal and external flows have been computed. Integral quantities, as well as computed cavitation phenomena, were validated against experiments. Due to high temporal resolution and inclusion of compressibility of the fluid, the computation of formation and propagation of shocks enabled the identification of peak loads at the walls of devices. Good agreement was found by comparing computed positions of intense loads with experimental findings. The ability of the inviscid approach to predict different shedding mechanisms [23, 24] as well as "crescent shaped re-

gions" [56] indicates that these phenomena are intrinsic instabilities that are mainly driven by inertia.

The behavior of the thermodynamic model with respect to spatial resolution was investigated by simulation of the collapse of a vapor bubble cloud. It was found that the duration of the collapse as well as the detected pressure at the wall of the test-configuration can be accurately predicted even in case of strongly insufficient spatial resolution. This motivates the application of the approach to predict collapse intensities even for typically under-resolved simulations of cavitating flows in real machines.

Kurzfassung

Strömungen mit lokaler Teilverdampfung (Kavitation) des flüssigen Arbeitsfluids treten beispielsweise in der Energietechnik (Pumpen, Turbinen), der Fahrzeugtechnik (Einspritzsysteme), der Prozess- und Automatisierungstechnik (hydraulische Systeme in Presswerken), der Schifffahrt und der Raumfahrt auf. Während die Verdampfung häufig den Wirkungsgrad einer Maschine oder den Massenstrom durch eine Drossel begrenzt, führt die kollapsartige Rekondensation des gebildeten Dampfes beispielsweise zur signifikanten Geräuschentwicklung, zur Schwingungsanregung und insbesondere zur erosiven Bauteilschädigung [13, 38]. Der Wirkungsgrad und die Lebensdauer einer hydraulischen Maschine sind somit wesentlich durch Kavitationsphänome beeinflusst und begrenzt. Experimentelle Untersuchungen sind einerseits häufig nicht in Realgröße durchführbar. Andererseits sind Prototypenbau und Dauerlauf gerade in den frühen Entwicklungsphasen meist zu zeit- und kostenintensiv.

Die stetige Zunahme der Rechenkapazität hat zur Entwicklung und industriellen Nutzung zahlreicher numerischer Programme zur Simulation kavitierender Strömungen geführt. Im industriellen Tagesgeschäft werden neben "'open source"' Programmen (z.B. OpenFOAM) hauptsächlich kommerzielle Programmpakete zur 3-D Simulation eingesetzt. Während zeitlich gemittelte Strömungseigenschaften wie etwa der Durchflusskoeffizient in Drosseln oder der Wirkungsgrad eines Schiffspropellers mit den verfügbaren numerischen Verfahren auch industriell meist sehr befriedigend ermittelt werden konnte, waren Aussagen zur Einschätzung der möglichen kavitationsbedingten Bauteilschädigung nur unzureichend durch die eingesetzten Modelle und Verfahren ableitbar.

Im Rahmen dieser Arbeit wurde ein Simulationsverfahren entwickelt, welches durch zeitliche Auflösung der Dynamik kavitierender Strömungen einschließlich der kollapsinduzierten Lastspitzen erstmals eine mindestens qualitative Vorhersage erosionsgefährdeter Bauteilbereiche ermöglicht. Das zentrale Element des entwickelten Verfahrens ist die zur Berechnung der Flüsse eingesetzte Flussfunktion. Im Gegensatz zu etablierten Methoden ermöglicht die im Rahmen dieser Arbeit entwickelte Methode die Berechnung kompressibler kavitierender Strömungen einschließlich wellendynamischer Phänomene auch im Bereich sehr kleiner Machzahlen ohne Vorkonditionierung des Zeitoperators. Die Methode wurde in ihrer Effizienz und Robustheit derart optimiert, dass sie industriell eingesetzt werden kann.

In Verbindung mit einem thermodynamischen Gleichgewichtsmodell wurden Durchströmungs-

und Umströmungsprobleme unter Vernachlässigung viskoser Effekte simuliert. Sowohl integrale Größen als auch die simulierten Kavitationsphänomene wurden mit Experimenten validiert. Die durch die hohe zeitliche Auflösung und die kompressible Modellierung ermöglichte Simulation der Bildung und Ausbreitung von Stoßwellen erlaubte eine Darstellung der Spitzenlasten auf Bauteilen. Ein Vergleich der Positionen der auftretenden Lasten mit experimentellen Befunden ergab eine sehr gute Übereinstimmung. Die erfolgreiche Darstellung verschiedener "'shedding"' Mechanismen [23, 24] sowie "'halbmondförmiger"' Strömungsstrukturen [56] deutet an, dass diese Kavitationsinstabilitäten intrinsisch und dominant trägheitskontrolliert sind.

Mit der Simulation des Kollapses einer diskreten Blasenwolke wurde das Verhalten des thermodynamischen Modells in Abhängigkeit der räumlichen Auflösung untersucht. Es zeigte sich, dass das Modell auch im Falle einer räumlichen Unterauflösung der hinreichend dichten Blasenwolke quantitativ korrekte Aussagen zur Kollapsdauer und dem auf der Wand wirkenden stoßinduzierten Spitzendruck liefert. Dies motiviert die Anwendung des Modells zur Vorhersage von Kollapsintensitäten auch für die typischerweise deutlich unteraufgelösten Simulationen kavitierender Strömungen in realen Maschinen.

1. Introduction

1.1. Fundamentals of cavitating flows

This work focuses on modeling and numerical simulation of liquid flows where flow-induced rarefaction enforces partial evaporation of the fluid [7, 25, 39]. The process of evaporation leads to a significant increase in compressibility of the fluid due to the formation of vapor cavities such as bubbles, sheets or vapor-filled vortex cores. The characteristic dimensionless quantity is the cavitation number σ, which is defined as

$$\sigma := \frac{p_{ref} - p_{sat}(T_{ref})}{1/2 \cdot \rho_{ref} \cdot u_{ref}^2}, \tag{1.1}$$

where p_{ref}, T_{ref}, ρ_{ref} and u_{ref} are case specific reference states (pressure, temperature, density and flow velocity) and $p_{sat}(T_{ref})$ is the saturation pressure or vapor pressure at reference temperature. Slightly different example the pressure loss $\Delta p = p_{in} - p_{out}$ within a test-section or a device. Operating conditions for which the onset of cavitation is observed correspond to the critical cavitation number σ_{crit}. Consequently, operating conditions with $\sigma > \sigma_{crit}$ usually lead to pure liquid flow (phase transition is avoided) while conditions for which $\sigma < \sigma_{crit}$ enhance the appearance of cavities with decreasing cavitation number.

It is well known that pure (ideal) liquids may sustain strong tension, i. e. pressures far below vapor pressure, before homogeneous nucleation takes place [81]. Realistic fluids, however, typically contain sufficient nucleation sites (micro bubbles within the liquid or attached to walls, as well as other impurities), such that heterogeneous phase transition is predominant [7]. Homogeneous nucleation can be an important mechanism if the thermodynamic conditions of the fluid are close to critical conditions (critical temperature), since surface tension and surface energy vanish in this special case. However, this case is not within the scope of this work as the considered temperature regime is far below the critical temperature. A major difference between homogeneous and heterogeneous cavitation is the absence or presence of phase boundaries. While homogeneous cavitation requires the formation of critical nuclei within the pure liquid, heterogeneous cavitation can already occur when the partial pressure of vapor within a micro bubble is lower than its saturation value. It should be pointed out that various definitions of "cavitation" and "cavitation onset" are found in

the literature. However, with respect to this work, the term "cavitation" is used when the following requirements are fulfilled: the formation and growth of a cavity is (mainly) controlled by a mass transfer from liquid to vapor without (significant) external heat supply. Neither degassing processes, nor the growth of (nearly pure) gas bubbles, nor the formation of a cavity due to heating (laser induced or spark induced phase transition) are discussed within this work.

Once vapor cavities are exposed to pressures higher than saturation pressure, they act as sinks. Thereby, the pressure gradient accelerates the surrounding liquid towards the cavity and the vapor condenses at the interfaces. Depending on the shape of the cavity, the structure of the underlying flow and on the vicinity of boundaries, re-condensation may take place in various ways. One famous and well known mechanism is the collapse of a single isolated and perfectly spherical bubble. In this case, detailed mathematical models show the formation of a strong shock wave, possibly guided by re-evaporation (rebounds) or even light emission (sonoluminescence). Asymmetric collapses of bubbles, vortex cores or sheet cavities often imply the formation of liquid jets that may impinge on material surfaces, where so-called "water hammers" are generated. Resulting shock waves with post shock pressures on the order of 10^9 Pa may arise [7, 25]. Often, these processes occur on time scales of nanoseconds.

The technical relevance of cavitating flows is significant and manifold. Pumps and turbines as well as ship propellers exhibit performance limitations due to cavitation. Noise generation and material fatigue due to violent collapses of cavities, i. e. cavitation erosion [26, 36, 40], may affect usability and life time of fluid machinery [46, 87]. On the other hand, cavitation and re-condensation may prevent coking processes in fuel injectors, improve spray quality and stabilize mass flows in chocked (super-cavitating) valves. Improvements of emulsion quality or of mixing processes might be further applications.

In the following, examples of cavitation types on hydrofoils are briefly discussed. A quasi two-dimensional NACA 16-012 hydrofoil is placed within a rectangular test-section. At zero angle of attack, a flat pressure minimum is reached at approximately 60% of the chord length, followed by a fast pressure recovery towards the trailing edge of the foil. The fluid is water at room temperature and the Reynolds number based on the characteristic velocity and on the chord length of the hydrofoil is $Re \approx 10^6$. Depending on the cavitation number and on the angle of attack, different cavitation patterns can occur - see Figure 1.1.

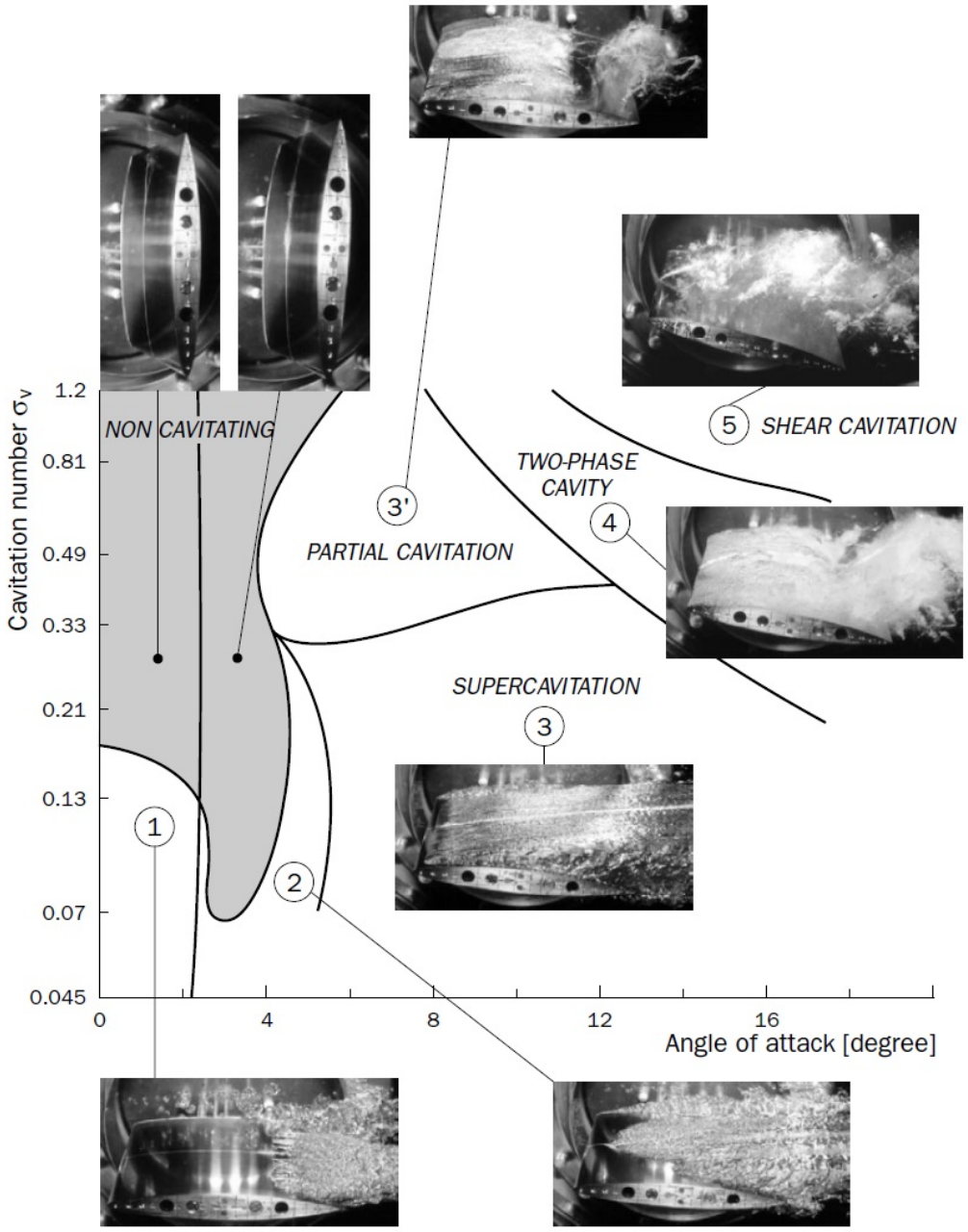

Figure 1.1.: Typical forms of cavitation on hydrofoils [25]. Reproduced with permission from Springer under License Number 3550741488027.

The following cavitation regimes can be distinguished:

- At small angle of attack the onset of cavitation is located slightly downstream of the pressure minimum (situation 1). The structure of the cavity appears to be very "clear", which means that large parts consist of pure vapor (coalescing big bubbles and partial cavities). This situation is very complex, as several physical processes interact. By comparison of the cavitating case with the non cavitating case at the same angle of attack, one observes that the positions of flow separation and cavitation onset coincide. Certainly this is not the case in general, but results from the shape of the investigated hydrofoil. A numerical prediction of this cavitation pattern requires a precise prediction of the separation position.
- In situation 2, the flow topology and the resulting cavitation pattern are even more complex. Due to the increased angle of attack, the suction peak (minimum pressure) is shifted towards the leading edge of the hydrofoil. Cavitation onset takes place at several positions in span-wise direction, probably depending on incoming nuclei, surface impurities as well as on highly dynamic separation zones. The overall impression is that the cavity is still somehow clear, although slightly less than in situation 1. Again, a numerical prediction of this cavitation pattern seems to be extremely challenging due to the amount of uncertainties.
- In contrast to operating points 1 and 2, the cavitating flow at condition 3 is well predictable. The angle of attack has pushed the onset of cavitation to a well defined and very narrow region close to the nose of the hydrofoil. The arising vapor pocket is very clear (nearly pure vapor) and ranges far beyond the trailing edge. This situation is often called "supercavitation" or "full cavitation" and it is known that this type of cavitation is very stable (stationary) and does not result in cavitation erosion on the surface of the hydrofoil. As this type of cavitation is strongly inertia driven, an inviscid modeling approach is often sufficient for numerical prediction of the flow.
- One of the most interesting and technically relevant operating points corresponds to situation 3'. This so called "partial cavitation" combines clear cavity regions, milky regions (highly dispersed bubbly flow) and periodic separation of bubbly clouds and vortex patterns. The periodic formation of a sheet-like structure, the onset of reverse flow (re-entrant jet) and the separation of bubbly clouds is often called "shedding", [23,24,37]. Strong noise, vibration and surface damage are correlated to this cavitation type [56]. The author has demonstrated in one of his publications [69] that these processes are dominated by inertia and do not require detailed representations of boundary layers.
- Situation 4 shows a typical two-phase (milky) cavity. As compared to 3', clear cavity regions do no longer occur. Although the dynamics of such two-phase cavities are quite similar to the dynamics of partial cavities, they might be less complicated with

respect to numerical modeling. It is reasonable to assume that most models based on mixture assumptions (bubbly dispersed mixtures or homogeneous mixtures) provide a reasonable representation of milky cavities.

- At high angles of attack (situation 5), flow separation close to the leading edge (or the nose) of the hydrofoil takes place. The cavity is no longer attached to the surface but is generated in the separated shear flow. Often, the observed cavities are milky clouds or bubbly vortex cores. A numerical prediction of this type of cavitation requires sufficient resolution of the turbulent flow. Inviscid approaches surely fail in this regime.

Considering water as operating fluid, the ratio between the saturation densities of liquid and vapor at room temperature ($T \approx 293\ K$) is $998.16/0.017 \approx 6 \cdot 10^4$. These quantities already provide a strong indication that cavitating water flows at approximately room temperature are dominated by the momentum (or the momentum density) of the liquid phase, as the momentum of the vapor phase is smaller by $4-5$ orders of magnitude. Density jumps (or gradients) of such a magnitude pose a considerable challenge to numerical models. Even small discretization errors may result in significant prediction deficiencies. As most of the high order approaches are neither monotonic nor positivity preserving, a suitable compromise between practical robustness and formal (asymptotic) order of accuracy is required.

The sound speeds are $c_l \approx 1482\ m/s$ in pure liquid and $c_v \approx 423\ m/s$ in pure vapor, both at saturation conditions at room temperature. Evaluating the isentropic compressibility $\beta_s = 1/(\rho c^2)$ as well as the acoustic impedance $Z = \rho c$ for both phases leads to $\beta_{s,l} = 4.56 \cdot 10^{-10}\ Pa^{-1}$, $\beta_{s,v} = 3.29 \cdot 10^{-4}\ Pa^{-1}$ and $Z_l = 1.48 \cdot 10^6\ Pa \cdot s/m$, $Z_v = 7.2\ Pa \cdot s/m$. Again, variations of several orders of magnitude have to be handled. Moreover, the quantities stated above characterize pure-phase behavior only. With respect to saturated mixtures of liquid and vapor, the effect on the speed of sound is even more critical. If phase transition is taken into account, the equilibrium speed of sound is discontinuous at the onset of phase change. Although the frozen speed of sound is mostly assumed to be a suitable choice for non equilibrium models of evaporation [84], the equilibrium speed of sound has to be used for equilibrium models. In this case one obtains for the values at the boundaries $\alpha \to 0^+$ and $\alpha \to 1^-$ of the vapor volume fraction α

$$\lim_{\alpha \to 0^+} c_{eq} = 0.0384\ m/s, \qquad \lim_{\alpha \to 1^-} c_{eq} = 419.7\ m/s. \tag{1.2}$$

Note that the jump in speed of sound from $c_{eq} \approx 1482\ m/s$ to $c_{eq} = 0.0384\ m/s$ once more demonstrates a dramatic change in material properties that has to be managed within the numerical framework.

1.2. Problem description and literature overview

The aim of this work is to develop a numerical simulation code for the prediction of the dynamics of low and high speed cavitating flows including wave dynamic processes. For this purpose, the compressibility of the fluid needs to be taken into account and time scales arising from collapse processes have to be resolved. The characteristic velocity of the underlying shear flow often leads to Mach numbers on the order of $M = O(10)^{-3} - O(10)^{-2}$ in classical hydraulic machinery, while maximum values of $M = O(10)^{-1} - O(1)$ are common in modern high pressure injection systems. Thus, numerical techniques have to be valid within this regime. An additional requirement is the applicability of the code for simulation of cavitating flows within realistic devices, wherefore efficient and flexible numerical approaches and physical models need to be chosen or developed. The numerical and physical requirements on this thesis can be summarized as follows:

- Handling of liquid-vapor phase transition
- Validity and accuracy for low and moderate Mach numbers $M = O(10)^{-3} - O(1)$
- Temporal resolution of wave dynamics, particularly of shock propagation within the liquid
- Three-dimensionality in space, realistic (non-trivial) flows
- Efficiency and robustness (in a practical sense)
- Validation for a wide range of academic and industrial problems.

In order to achieve these objectives, innovative developments were required, since available commercial codes or published academic achievements did not fulfill all of these requirements simultaneously. In the following, a short overview of available models and numerical techniques is given.

1.2.1. Numerical techniques for simulation of cavitating flows

The development of numerical techniques for simulation of cavitating flows follows two major paths. Path 1) starts from techniques that were introduced for the simulation of low speed, incompressible liquid flows, while path 2) originates in aerodynamics of high speed, compressible gas flows. Traditionally, the first path is mostly based on pressure-based solvers with implicit time discretization, whereas path 2) follows density-based shock capturing strategies combined with explicit time discretization. Although this differentiation is no longer sharp since both approaches have been extended towards wider application areas, they have sustained impact on cavitation modeling.

State of the art developments with respect to path 1) usually require an additional transport equation for the vapor volume (or vapor mass) fraction. A source term based on bubble dynamic considerations (Rayleigh equation) or based on empiric evaporation and condensation rates is used to model phase transition processes [8, 41]. Recent developments include more detailed information such as the bubble number density, radii distributions, gas content and surface tension. Although the inclusion of compressibility effects in the pure liquid (or in both phases) is possible in path 1), it is often neglected. One reason might be that the temporal resolution of wave dynamics requires time steps where implicit techniques are no longer efficient. However, if the computation of wave dynamics is not a main focus, and if the Mach number is sufficiently small, pressure based approaches using implicit time discretization and assuming constant liquid density can be a suitable choice for simulation of cavitating flows, particularly for fast steady state predictions in pumps, turbines and around ship propellers. Even though these approaches have been continuously improved over the last two decades, convergence and robustness as well as proper parametrization of empirical model coefficients are still partially unsolved issues.

Developments arising from path 2) lead to an increased interest since about one decade as well. One might differentiate between models and approaches that either focus on detailed simulations of discrete cavities (shock bubble interaction, collapses of single or few bubbles, interface dynamics) or models and approaches to simulate large scale dynamics of cavitation patterns (shedding processes, cloud fragmentation and cloud collapse, super-cavitation and large scale vortex cavitation). As the simulation of large scale dynamics is the dominant task in this work, special emphasis is put on those models and approaches. Provided that the Mach number is sufficiently high, classical Riemann solvers combined with nonlinear high resolution procedures are suitable building blocks. However, these schemes suffer from the low Mach number problem [2, 16, 49] due to an inconsistent asymptotic behavior of the non-central (i. e. dissipative) part in the flux computation [28, 29]. This issue is negligible if the characteristic Mach number is sufficiently high, as for example in modern injector components. In case of low Mach number flows, time operator preconditioning can be applied to restore an accurate asymptotic behavior of the fluxes [10, 12, 82]. The resulting technique is well suited to simulate cavity dynamics on the time scale of the flow velocity, but tends to filter out wave dynamics. Therefore, neither classical Riemann solvers (as used in case of high speed aerodynamics) nor time operator preconditioned methods fulfill the requested demands. A major contribution of this work is a novel flux function with correct asymptotic behavior in the low Mach number regime. The proposed scheme allows for an efficient computation of wave dynamics while being robust within the requested spectrum of applications.

1.2.2. Physical models for cavitating flows

Phase transition in a flow generally involves the transfer of mass, momentum and energy from one phase to the other. The most detailed continuum approaches consider two (or even multiple) sets of governing equations, i. e. balance laws for mass, momentum and energy for each component or phase [13, 32, 44, 45]. Transfer or interaction terms, as well as interface physics such as surface tension, can be defined [60]. The source terms are typically based on local differences in pressure and temperature across phase boundaries and may require calibration to optimize transfer rate coefficients. Models of this type are often combined with sharp interface techniques, for example level set approaches [43]. With respect to cavitating flows, models that are based on two sets of governing equations are mainly applied for investigations involving a very limited number of discrete cavities due to the relatively high numerical effort. Depending on the quality of transfer and interaction terms, predictions of very high quality are possible.

Substantial simplification is achieved if a common set of governing equations is used to describe the kinematics of the flow. In single-fluid models the phases are not treated separately, but they are characterized by their fractional contributions, i. e. by their mass and volume fractions. Thus, the governing equations describe the evolution of mixture quantities, such as the mixture density, the momentum and the total energy of the mixture.

Most of the models developed and used during the last two decades assumed constant densities of the liquid and the vapor [4, 31, 47, 58, 88]. Furthermore, thermal effects and the balance equation of the total energy of the mixture are often neglected. Phase transition is modeled by a single additional transport equation for the vapor mass (or volume) fraction of the form

$$\frac{\partial}{\partial t}(\alpha\rho_v) + div(\alpha \cdot \rho_v \cdot \vec{v}) = \rho_v \cdot S(\alpha, p, \vec{const}), \tag{1.3}$$

where ρ_v is the constant vapor density, p is the pressure in the liquid, α is the vapor volume fraction (sometimes called void fraction) and $\vec{const}$ contains parameters and calibration factors as part of the source term "S" [42, 58, 75, 89]. The source term usually contains the difference of the pressure in the liquid and the (constant) saturation pressure. Models of this type, as well as refined versions [15, 17, 54, 79], where additional transport equations for the bubble number density or for properties of the nuclei are incorporated, require case-dependent calibration.

Single-fluid models that enable the simulation of wave dynamics require compressible models of the phases [3, 5, 86]. Weakly compressible effects can be modeled assuming barotropic behavior. Either isentropic or isothermal equations of state could be used [9, 11, 48, 55]. Isentropic models can be suitable options if thermodynamic data are limited [22, 51, 76].

In general, the density ρ and the specific internal energy e of the mixture are convex combinations with convex parameters α and x (vapor mass fraction). Let the subscripts "l" and "v" denote liquid and vapor, then the mixture quantities are

$$\rho = \alpha \cdot \rho_v(p_v, T_v) + (1-\alpha) \cdot \rho_l(p_l, T_l), \tag{1.4}$$

$$e = x \cdot e_v(p_v, T_v) + (1-x) \cdot e_l(p_l, T_l), \tag{1.5}$$

$$\alpha \cdot \rho_v(p_v, T_v) = x \cdot \rho, \ (1-\alpha) \cdot \rho_l(p_l, T_l) = (1-x) \cdot \rho. \tag{1.6}$$

The previous set of three independent equations contains six unknowns: p_v, p_l, T_v, T_l, α and x. In case of $0 < \alpha < 1$, the assumptions of temperature equilibrium $(T = T_v = T_l)$ and pressure equilibrium $(p = p_v = p_l)$ reduce the number of unknowns to four: p, T, α, x. In order to close the the system, an additional assumption or an additional information is required. Let x be the local (non-equilibrium) vapor mass fraction and x_{eq} be the corresponding local equilibrium quantity under given conditions. Let τ be a (constant) relaxation time. Then one can derive a simple relaxation model in conservative form as follows:

$$\frac{\partial}{\partial t}((x - x_{eq}) \cdot \rho) + div((x - x_{eq}) \cdot \rho \cdot \vec{v}) = -\rho \cdot \frac{(x - x_{eq})}{\tau}. \tag{1.7}$$

In case of $\tau \to \infty$ the flow is called "frozen", while $\tau \to 0$ describes phase equilibrium. While frozen flows obviously do not allow phase transition, equilibrium flows do. In this special case, the degrees of freedom of the system are further reduced as pressure and temperature are no longer independent variables in a saturated mixture. Instead, pressure is exclusively dependent on temperature.

In this work, phase equilibrium is assumed, which can be interpreted as an infinitely fast relaxation process from a non-equilibrium state to the equilibrium value.

2. Physical model and numerical approaches

2.1. Governing equations and thermodynamic model

The governing equations are the three-dimensional and time dependent balance laws for mass, momentum and total energy. Since the major focus of this work is put on inertia driven effects, viscous effects as well as heat transfer are neglected. However, successful extension of the proposed methodology to more advanced approaches (Large Eddy Simulation) has been demonstrated in [22, 30]. Instead of solving governing equations for each phase separately, a common set of equations representing mixture properties is used. This implies that a common velocity field is assumed (no slip between phases). Surface tension, additional gas content and modeling of nuclei are neglected. The complexity is further reduced by assuming thermal equilibrium (equal temperatures in both phases), mechanical equilibrium (equal pressures) and phase equilibrium (equal Gibbs functions in case of two-phase flow). As a result, the governing equations are the compressible Euler equations equipped with suitable thermodynamic closure relations $p(\rho,e)$ and $T(\rho,e)$.

Let $\vec{q}$ be the vector of conserved quantities and $F(\vec{q},\vec{e}_i)$ be the corresponding flux associated with coordinate direction $\vec{e}_i$

$$\vec{q} := \begin{pmatrix} \rho \\ \rho\vec{v} \\ \rho E \end{pmatrix}, \qquad F(\vec{q},\vec{e}_i) := < \vec{v},\vec{e}_i > \cdot \vec{q} + p \cdot \begin{pmatrix} 0 \\ \vec{e}_i \\ < \vec{v},\vec{e}_i > \end{pmatrix}, \tag{2.1}$$

where the total energy ρE is the sum of internal energy ρe and kinetic energy $1/2 \cdot \rho |\vec{v}|^2$. The governing equations thus read

$$\frac{\partial}{\partial t}\vec{q} + \sum_{i=1}^{3} \frac{\partial}{\partial x_i} F(\vec{q},\vec{e}_i) = \vec{0}. \tag{2.2}$$

Any thermodynamic closure relation that implies a positive speed of sound results in (non-strict) hyperbolicity of the Euler equations. Since there are no source terms in this modeling

approach, the speed of sound is the equilibrium speed of sound [50].

Due to the assumption of local thermodynamic equilibrium, the vapor volume fraction and the vapor mass fraction correspond to equilibrium states as well, $\alpha = \alpha_{eq}$ and $x = x_{eq}$.

Thus, the density ρ and the specific internal energy e are convex combinations with convex parameters α_{eq} and x_{eq}:

$$\rho = \alpha_{eq} \cdot \rho_v(p,T) + (1-\alpha_{eq}) \cdot \rho_l(p,T), \tag{2.3}$$

$$e = x_{eq} \cdot e_v(p,T) + (1-x_{eq}) \cdot e_L(p,T), \tag{2.4}$$

$$\alpha_{eq} \cdot \rho_v(p,T) = x_{eq} \cdot \rho, \ (1-\alpha_{eq}) \cdot \rho_l(p,T) = (1-x_{eq}) \cdot \rho. \tag{2.5}$$

In case of $\alpha_{eq} = x_{eq} = 0$, the local properties of the fluid correspond to pure liquid. Consequently, $\alpha_{eq} = x_{eq} = 1$ refers to pure vapor.

In case of $0 < \alpha_{eq} < 1$ (implying $0 < x_{eq} < 1$) the local properties correspond to a saturated mixture of liquid and vapor where

$$p = p_{sat}(T). \tag{2.6}$$

Additionally, the densities of the liquid and the vapor are the temperature dependent saturation densities

$$\rho_l = \rho_{l,sat}(T), \ \rho_v = \rho_{v,sat}(T). \tag{2.7}$$

This allows for further simplification of equations 2.3, 2.4 and 2.5.

If the equilibrium state represents a pure state (pure liquid or pure vapor), then the system is closed provided that suitable state descriptions for liquid and vapor are known. Usually, these are of the form $\rho = \rho(p,T)$ and $e = e(p,T)$.

If the equilibrium state represents a saturated mixture $(0 < \alpha < 1)$, application of equations 2.3, 2.4 and 2.5 leads to

$$\rho = \alpha_{eq} \cdot \rho_{v,sat}(T) + (1-\alpha_{eq}) \cdot \rho_{l,sat}(T), \tag{2.8}$$

$$e = \alpha_{eq} \cdot \rho_{v,sat}(T) \cdot e_v(p_{sat}(T),T) + (1-\alpha_{eq}) \cdot \rho_{l,sat}(T) \cdot e_L(p_{sat}(T),T). \tag{2.9}$$

The remaining system (2.8 and 2.9) might require iterative solution procedures to obtain the

unknowns α and T. Once these are evaluated, all relevant thermodynamic quantities can be specified for a given set of (ρ, e).

Based on Saurel's recommendation [59], the following thermal approximation is used to model liquid water

$$p(\rho,T)+B = B\cdot\left(\frac{\rho}{\rho_{L,sat}(T)}\right)^N + p_{sat}(T), \tag{2.10}$$

with $B = 3.3\cdot 10^8\ Pa$ and $N = 7.15$ are assumed to be constants while the temperature dependent saturation conditions are given by polynomial fits [27], which are provided at the end of this subsection. Note that these polynomials are sometimes misleadingly referred to as "Oldenbourg-Polynomials". The functional form is based on the so called "Tait" equation [18].

The caloric model of (pure or saturated) liquid water reads

$$e_l(T) := c_{vl}(T_{ref})\cdot(T - T_{ref}) + e_l(T_{ref}), \tag{2.11}$$

with T_{ref} being a case dependent reference temperature and $c_{vl}(T_{ref})$ being the specific heat at constant volume. $e_l(T_{ref})$ is the internal energy of the liquid at T_{ref} and $p = p_{sat}(T_{ref})$. In this work, the reference temperature is $T_{ref} = 293.15\ K$ leading to $c_{vl}(T_{ref}) = 4157\ J/(kg\cdot K)$ and $e_l(T_{ref}) = 83.91\ kJ/kg$.

An efficient thermal model for water vapor is given by the ideal gas law

$$p = \rho\cdot R_v\cdot T, \tag{2.12}$$

where the specific gas constant $R_v = 462\ J/(kg\cdot K)$ is assumed.

The caloric model of (pure or saturated) water vapor shares a common structure to its counterpart applied for the liquid phase

$$e_v(T) := c_{vv}(T_{ref})\cdot(T - T_{ref}) + e_v(T_{ref}). \tag{2.13}$$

Based on a reference temperature of $T_{ref} = 293.15\ K$ and $p = p_{sat}(T_{ref})$ the constants are selected as $c_{vv}(T_{ref}) = 1427\ J/(kg\cdot K)$ and $e_v(T_{ref}) = 2402.3\ kJ/kg$. The reference internal energy contains the energy of vaporization.

The saturation conditions are modeled as proposed in [27]. Let $\theta := 1.0 - T/T_{krit}$ be the reduced temperature. Then one obtains

$$\rho_{l,sat}(T) = \rho_{krit}\cdot\mathscr{F}_l(\theta), \tag{2.14}$$

$a_1 = -7.85823$	$b_1 = 1.99206$	$c_1 = -2.02957$
$a_2 = 1.83991$	$b_2 = 1.10123$	$c_2 = -2.68781$
$a_3 = -11.7811$	$b_3 = -0.512506$	$c_3 = -5.38107$
$a_4 = 22.6705$	$b_4 = -1.75263$	$c_4 = -17.3151$
$a_5 = -15.9393$	$b_5 = -45.4485$	$c_5 = -44.6384$
$a_6 = 1.77516$	$b_6 = -6.75615 \cdot 10^5$	$c_6 = -64.3486$
$T_{krit} = 647.096\ K$	$p_{krit} = 22.064 \cdot 10^6\ Pa$	$\rho_{krit} = 322.0\ kg/m^3$

Table 2.1.: Polynomial coefficients and critical conditions for saturated states for water

with

$$\mathscr{F}_l(\theta) := 1.0 + b_1 \cdot \theta^{1/3} + b_2 \cdot \theta^{2/3} + b_3 \cdot \theta^{5/3} + b_4 \cdot \theta^{16/3} + b_5 \cdot \theta^{43/3} + b_6 \cdot \theta^{110/3}, \tag{2.15}$$

$$\rho_{v,sat}(T) = \rho_{krit} \cdot e^{\mathscr{F}_v(\theta)}, \tag{2.16}$$

with

$$\mathscr{F}_v(\theta) := c_1 \cdot \theta^{1/3} + c_2 \cdot \theta^{2/3} + c_3 \cdot \theta^{4/3} + c_4 \cdot \theta^3 + c_5 \cdot \theta^{37/6} + c_6 \cdot \theta^{71/6}, \tag{2.17}$$

and

$$p_{sat}(T) = p_{krit} \cdot e^{\mathscr{F}_p(\theta)}, \tag{2.18}$$

with

$$\mathscr{F}_p(\theta) := (T_{krit}/T) \cdot (a_1 \cdot \theta + a_2 \cdot \theta^{3/2} + a_3 \cdot \theta^3 + a_4 \cdot \theta^{7/2} + a_5 \cdot \theta^4 + a_6 \cdot \theta^{15/2}). \tag{2.19}$$

The critical conditions as well as the polynomial coefficients for water are summarized in table 2.1.

Remark on thermodynamic models using closed form equations

Although the author's work was almost exclusively based on the equations specified above, it should be pointed out that recent work performed by the author and especially by the colleagues at the Institute of Aerodynamics and Fluid Mechanics at Technische Universität München show that tabulated thermodynamic descriptions (either full energetic or barotropic) might be more suitable with respect to various fluids and, most importantly,

more efficient. It is thus recommended to apply tabulated data generated from reference equations of state whenever possible [1].

Analogy of filtering and finite volume methods

The physical model described above is based on a series of simplifications and assumptions. However, it is important to notice how the model interacts with numerical approaches. In order to highlight this interaction and to motivate the choice of the model, a preliminary thought experiment is conducted.

We consider a generic one-dimensional balance law in conservation form

$$\frac{\partial}{\partial t}\varphi + \frac{\partial}{\partial x}\big(f(\varphi)\big) = 0, \tag{2.20}$$

where $f(\varphi)$ represents a (nonlinear) flux and φ denotes the conserved quantity. A numerical approximation of φ requires that φ has compact support in wave-number space. If the maximum wave number is unbounded, the balance law needs to be regularized. Provided that the maximum wave number is bounded, but the available degrees of freedom (the number of cells or grid points) of a discretization are insufficient to represent the maximum wave number, then an additional (numerical) regularization is required. Note that solutions of Euler equations are unbounded in wave-number space, whereas those of the Navier Stokes equations might be but the maximum wave number is usually too large for direct numerical simulation. Therefore, regularization is usually applied.

In the following, a relation between filtered data and finite volume methods is discussed. As a result, it is demonstrated that the thermodynamic approach specified previously is well suited when combined with finite volume methods. We consider a one-dimensional periodic domain with length $n \cdot h$, where h is the constant size of a finite volume and n is the number of volumes. Writing equation 2.20 in integral (weak) form results in

$$\frac{\partial}{\partial t}\overline{\varphi}_i + \frac{f_{i+1/2} - f_{i-1/2}}{h} = 0, \tag{2.21}$$

where

$$\overline{\varphi}_i := \frac{1}{h}\int_{x_i-h/2}^{x_i+h/2} \varphi(x)\; dx \tag{2.22}$$

is the integral average (volume average) of φ for volume V_i with center point x_i and

$$f_{i\pm1/2} := f\big(\varphi(x_i \pm h/2)\big) \tag{2.23}$$

are the fluxes evaluated at the cell faces.

Note that equation 2.21 is identical to the result of the following approach: Let G_h be a box filter of width h and π_i be a Dirac comb (a sampling function at x_i, $i = 1...n$). Then, the above stated finite volume method can be written in equivalent form

$$\pi_i * G_h * \left\{ \frac{\partial}{\partial t}\varphi + \frac{\partial}{\partial x} f(\varphi) \right\} = 0, \tag{2.24}$$

or, when using equation 2.22

$$\pi_i * \left\{ \frac{\partial}{\partial t}\overline{\varphi} + \frac{\partial}{\partial x} f(\overline{\varphi}) \right\} = \pi_i * \left\{ \frac{\partial}{\partial x} f(\overline{\varphi}) - \frac{\partial}{\partial x}\overline{f(\varphi)} \right\}. \tag{2.25}$$

The resulting term on the right hand side may be of dissipative or of anti-dissipative nature. In order to ensure stability (in a practical sense, i. e. without proof), one can add additional regularization in an explicit or implicit fashion (i. e. provided by the discretization scheme). Let $Reg(h, \overline{\varphi}, \varphi)$ be a suitable regularization, then the equation reads

$$\pi_i * \left\{ \frac{\partial}{\partial t}\overline{\varphi} + \frac{\partial}{\partial x} f(\overline{\varphi}) \right\} = \pi_i * \left\{ \frac{\partial}{\partial x} f(\overline{\varphi}) - \frac{\partial}{\partial x}\overline{f(\varphi)} + Reg(h, \overline{\varphi}, \varphi) \right\}. \tag{2.26}$$

A combination of all contributions to find a modified flux f_{mod} yields

$$\pi_i * \left\{ \frac{\partial}{\partial t}\overline{\varphi} + \frac{\partial}{\partial x} f_{mod}(\overline{\varphi}) \right\} = 0. \tag{2.27}$$

This demonstrates that approximate solutions obtained by using finite volume methods can be interpreted as regularized approximate solutions of filtered quantities. Although physical (or mathematical) models are usually formulated in a point-wise fashion using partial differential equations of unfiltered quantities, one has to take into account the effects of the numerical approaches when analyzing or assessing a model. For example, the thermodynamic cavitation model specified above has an intrinsic scaling capability although it does not contain information about the inner structure of cavities, such as radii or number density of bubbles. Let h' be the characteristic length or diameter of a cavity and h the width of the numerical filter. Then one can distinguish three regimes:

- **Resolved cavities**: If $h'/h >> 1$, then filtering might have an effect on the sharpness of the boundary of the cavity, but it is still possible to recover or resolve the cavity in an accurate way. This, however, is only the case when clear sheet cavities are present, or, in case of bubble dynamic investigations, if the spatial resolution is sufficiently high. It should be noted that models and schemes that are especially designed to operate in this regime, such as sharp interface models, allow for higher solution quality, as they allow for incorporation of additional physical details such as surface tension or non-equilibrium processes.

- **Under-resolved cavities**: If $h'/h << 1$, then filtering removes all small scale structures. Bubbly mixtures are thus represented as homogenized mixtures. This is often the case in computations of cavitating flows around large scale devices where the characteristic length of the device (for example a ship propeller) is much larger than the typical diameter of a bubble. However, if it is ensured that $h'/h << 1$ holds within the entire flow field, and provided that cavities are (nearly) spherical, then bubbly mixture models might allow for additional conclusions or effects.
- **Marginally resolved cavities**: If $h'/h \approx 1$, then bubbly mixture models as well as sharp interface models can fail or at least may require additional techniques to handle this regime.

The advantage of the proposed model is its applicability to all regimes. Even transitions between regimes due to fragmentation of clear sheets or due to coalescence can be handled.

2.2. Numerical approach

A density based, conservative, three-dimensional volume method (FVM) operating on body-fitted hexahedral multi-block grids forms the basis of the spatial discretization scheme. The implementation of the finite volume scheme is carried out in an unsplit fashion, which enables the application of independent temporal discretization schemes (method of lines approach). Spatial discretization thus leads to a set of ordinary differential equations of dimension $5 \cdot n$, where n is the number of finite volumes and the factor 5 results from the balance laws of mass, momentum (three components) and total energy. In the author's work, only stationary (non-deforming and non-moving) grids are considered. The spatial discretization implies the following steps:

- Step 1: Selection of a two-dimensional quadrature rule for approximation of the surface flux integral.
- Step 2: Point-wise reconstruction of "left" and "right" states depending on the selected quadrature rule of step 1 and depending on the selected flux function (step 3).
- Step 3: Application of a suitable numerical flux function to evaluate point-wise fluxes from the states obtained within step 2.
- Step 4: Evaluation of the flux integral via application of the quadrature rule on the results of step 3.

In this work an efficient one-point quadrature rule is used. This limits the maximum achievable spatial order of accuracy to 2. If higher order is desired, a four point quadrature rule (max. order is four) has to be applied and "true multi-dimensional" reconstruction of left and right states is required. This, however, would increase numerical costs at least by a

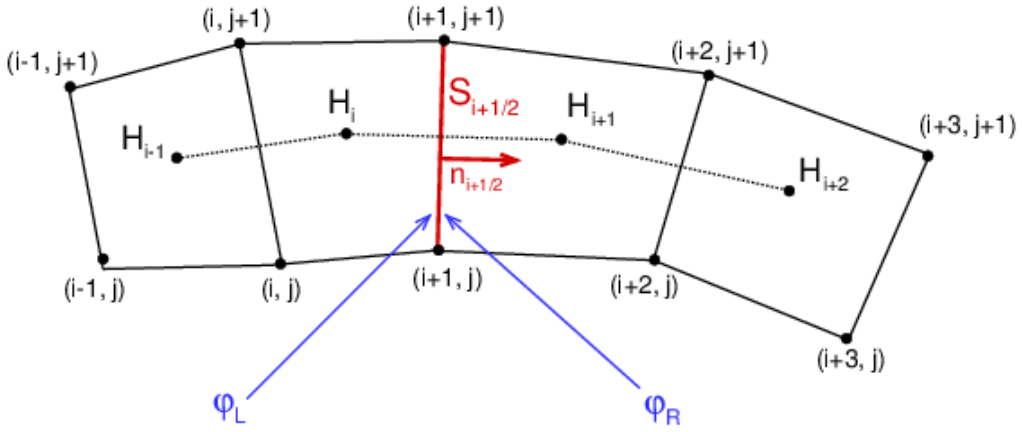

Figure 2.1.: Schematic showing cells as required for reconstruction of states to evaluate the flux across a cell face in coordinate direction "i" at constant "k".

factor of about 10, which seems to be not as beneficial as doubling the spatial resolution in all spatial directions.

2.2.1. Reconstruction of "left" and "right" states

The reconstruction of the required "left" and "right" states is performed along the index directions of the computational grids. Non-linear limiters (TVD limiters) and a WENO-3 procedure are available. As the computed flow fields involve large gradients in density while the velocity field might be smooth (phase boundaries), reconstruction of primitive variables (ρ, u, v, w, p, e) is favored. The procedure is demonstrated on the example of index direction "i".

We consider four adjacent hexahedra H_{i-1}, H_i, H_{i+1} and H_{i+2}, all of them defined by their point index sets $\{i-1, i+3\} \times \{j, j+1\} \times \{k, k+1\}$, see Figure 2.1. In order to compute the fluxes at the common surface $S_{i+1/2}$ adjacent to H_i and H_{i+1} the required states (left $=$ subscript L, right $=$ subscript R) need to be reconstructed. For each cell, primitive quantities (ρ, u, v, w, p, e) are computed from the known conserved quantities. More than twenty linear and nonlinear reconstruction procedures have been investigated. With respect to solution quality, robustness and efficiency, the following choices are recommended for simulation of cavitating flows: The "MinMod" limiter [80] is applied on pressure, density and on mass specific internal energy. The velocity field is reconstructed using either the WENO-3 scheme [74] or using the "Koren-limiter" [83], which is not as common as the well known limiters and will thus be briefly described in the following paragraph.

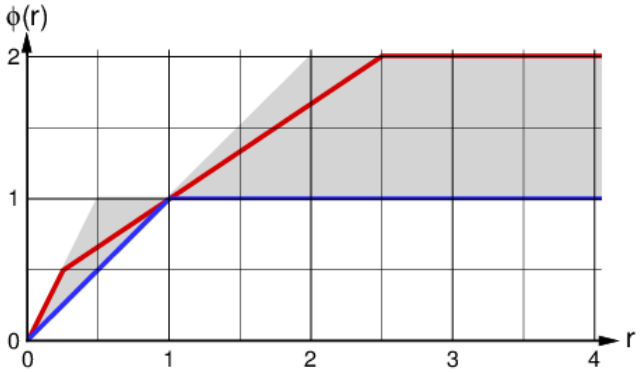

Figure 2.2.: TVD-diagram after Sweby [77]. The grey zone indicates TVD regime, the blue line is the switching function of the "MinMod" limiter and the red line depicts the limiter proposed by Koren [83].

Let $d_{i-1/2}$, $d_{i+1/2}$ and $d_{i+3/2}$ be the distances of the centroids of the hexahedra H_{i-1}, H_i, H_{i+1} and H_{i+2} and let φ be the quantity to be reconstructed at both sides of the interface. We define

$$r_L := \frac{d_{i+1/2}}{d_{i-1/2}} \cdot \frac{\varphi_i - \varphi_{i-1}}{\varphi_{i+1} - \varphi_i} \tag{2.28}$$

and

$$r_R := \frac{d_{i+1/2}}{d_{i+3/2}} \cdot \frac{\varphi_{i+1} - \varphi_{i+2}}{\varphi_i - \varphi_{i+1}}. \tag{2.29}$$

These ratios are bounded through the limiting function $\phi(r)$. In case of using the limiter proposed by Koren 2.2, this is achieved by

$$\phi(r) := \max[0, \min(2r,\ (1+2r)/3,\ 2)]. \tag{2.30}$$

Switching and limiting properties of this limiter are shown in Fig. 2.2 as TVD graph .

Finally, the reconstructed values on the left and right side are

$$\varphi_L = \varphi_i + 0.5 \cdot \phi(r_L) \cdot (\varphi_{i+1} - \varphi_i) \tag{2.31}$$

and

$$\varphi_R = \varphi_{i+1} + 0.5 \cdot \phi(r_R) \cdot (\varphi_i - \varphi_{i+1}). \tag{2.32}$$

Koren's limiter, when applied to one-dimensional problems with constant grid spacing, leads to parabolic reconstruction within the range $0.25 \leq r \leq 2.5$, i. e. linear and quadratic state functions are exactly recovered. The left hand state, for example, is obtained from

$$\varphi_L = \frac{2}{3} \cdot (\varphi_i + 0.5 \cdot (\varphi_{i+1} - \varphi_i)) + \frac{1}{3} \cdot (\varphi_i + 0.5 \cdot (\varphi_i - \varphi_{i-1})). \tag{2.33}$$

For the WENO-3 approach at the same ratio $r = 0.25$ we obtain

$$\varphi_L = \frac{1}{129} \cdot (\varphi_i + 0.5 \cdot (\varphi_{i+1} - \varphi_i)) + \frac{128}{129} \cdot (\varphi_i + 0.5 \cdot (\varphi_i - \varphi_{i-1})) \tag{2.34}$$

and for $r = 2.5$

$$\varphi_L = \frac{625}{657} \cdot (\varphi_i + 0.5 \cdot (\varphi_{i+1} - \varphi_i)) + \frac{32}{657} \cdot (\varphi_i + 0.5 \cdot (\varphi_i - \varphi_{i-1})). \tag{2.35}$$

Although the WENO-3 can be proven to be of (asymptotic) order of three, it can be shown that the optimal coefficients (in an asymptotic sense) of $2/3$ and $1/3$ are approximated with a deviation of less than $5\ \%$ when the ratio of gradients is in the range of $0.98 \leq r \leq 1.02$. This observation does not contradict the theoretical (asymptotic) order of accuracy, but it demonstrates that the asymptotic order of WENO schemes is reached only when the solution is extremely well resolved, which might not be the case for the majority of simulations of cavitating flows.

2.2.2. Numerical flux function

Once reconstructed left and right quantities are available, the point-wise flux computation can be performed.

First, the physical flux as specified in equation 2.1 is slightly rearranged to obtain an equivalent "enthalpy form". Using the definition of the volume specific total enthalpy $\rho H = \rho E + p$ allows for definition of $\vec{q}^H$ and $F(\vec{q}^H, \vec{e}_i)$ as

$$\vec{q}^H := \begin{pmatrix} \rho \\ \rho \vec{v} \\ \rho H \end{pmatrix}, \qquad F(\vec{q}^H, \vec{e}_i) := < \vec{v}, \vec{e}_i > \cdot \vec{q}^H + p \cdot \begin{pmatrix} 0 \\ \vec{e}_i \\ 0 \end{pmatrix}. \tag{2.36}$$

The new flux function is now based on three approximation steps:

1) Approximation of an "advection velocity" $< \vec{v}, \vec{e}_i >_*$
2) Approximation of an "advected vector" $\vec{q}^H_*$
3) Approximation of the "cell-face pressure" p_*.

In the following, we assume that the unit directional vector $\vec{e}_i$ is identical to the unit normal vector of the cell face of two adjacent cells (indicated by "L" and "R"). It is further assumed that $\vec{e}_i$ points towards cell "R".

Step 1: Approximation of an "advection velocity" $< \vec{v}, \vec{e}_i >_*$

For given (reconstructed) states $\vec{q}_L^H, p_L, c_L$ and $\vec{q}_R^H, p_R, c_R$ at the left (L) and at the right (R) side of the cell face, the approximation of the advection velocity is defined as follows.

We define the acoustic impedance at the cell face $(\rho c)_*$ as

$$(\rho c)_* := \max(\rho_L, \rho_R) \cdot \max(c_L, c_R, c_{min}). \tag{2.37}$$

Hereby, c_{min} is a numerical parameter which is used to prevent excessive pressure-velocity coupling in case of a very low speed of sound. Note that this parameter does not alter or affect the physical speed of sound.

In a next step, arithmetic averages of the normal velocities $\vec{v}_{vel}$ and of the density-weighted normal momentum densities $\vec{v}_{mom}$ are computed from

$$\vec{v}_{vel} := 0.5 \cdot \left(\frac{(\rho\vec{v})_L}{\rho_L} + \frac{(\rho\vec{v})_L}{\rho_r} \right) \tag{2.38}$$

and

$$\vec{v}_{mom} := \frac{(\rho\vec{v})_L + (\rho\vec{v})_L}{\rho_L + \rho_r}. \tag{2.39}$$

The resulting advection velocity $< \vec{v}, \vec{e}_i >_*$ is defined as

$$< \vec{v}, \vec{e}_i >_* := < (\chi \cdot \vec{v}_{vel} + (1-\chi) \cdot \vec{v}_{mom}), \vec{e}_i > - \frac{p_R - p_L}{2 \cdot (\rho c)_*}, \tag{2.40}$$

with parameter $0 \leq \chi \leq 1$.

Numerical experiments indicated that both, the velocity average and the momentum density average, can tend to improper approximations of the advection velocity. A robust compromise is $\chi = 0.5$, which gives

$$< \vec{v}, \vec{e}_i >_* := \frac{< \left(3(\rho_L + \rho_R)\vec{v}_L + 3(\rho_R + \rho_L)\vec{v}_R\right), \vec{e}_i >}{4 \cdot (\rho_L + \rho_R)} \cdot - \frac{p_R - p_L}{2 \cdot (\rho c)_*}, \tag{2.41}$$

where $\vec{v}_{L,R}$ is computed by $(\rho\vec{v})_{L,R} / \rho_{L,R}$.

Step 2: Approximation of an "advected vector" $\vec{q}_*^H$

The computation of the advected vector is based on upwinding with respect to the advection velocity. This can be written as

$$< \vec{v}, \vec{e}_i >_* \cdot \vec{q}_*^H := 0.5 \cdot < \vec{v}, \vec{e}_i >_* \cdot (\vec{q}_L^H + \vec{q}_R^H) - 0.5 \cdot | < \vec{v}, \vec{e}_i >_* | \cdot (\vec{q}_R^H - \vec{q}_L^H). \tag{2.42}$$

Step 3: Approximation of the cell-face pressure p_*

The pressure is computed by a simple arithmetic mean of reconstructed left and right sided quantities

$$p_* := \frac{p_L + p_R}{2}. \tag{2.43}$$

Combining all elements results in the proposed new flux function F_{mod}

$$F_{mod}(\vec{q}_L^H, \vec{q}_R^H, \vec{e}_i) := < \vec{v}, \vec{e}_i >_* \cdot \frac{\vec{q}_L^H + \vec{q}_R^H}{2} - | < \vec{v}, \vec{e}_i >_* | \cdot \frac{\vec{q}_R^H - \vec{q}_L^H}{2} + \frac{p_L + p_R}{2} \cdot \begin{pmatrix} 0 \\ \vec{e}_i \\ 0 \end{pmatrix}. \tag{2.44}$$

As face normals are pointing outward, the net-flux for cell $H_{i,j,k}$ is given by the following sum

$$\begin{aligned} \text{net-flux}(H_{i,j,k}) \;=\; & |S_{i+1/2}| \cdot F_{mod,i+1/2} - |S_{i-1/2}| \cdot F_{mod,i-1/2} \\ + \; & |S_{j+1/2}| \cdot F_{mod,j+1/2} - |S_{j-1/2}| \cdot F_{mod,j-1/2} \\ + \; & |S_{k+1/2}| \cdot F_{mod,k+1/2} - |S_{k-1/2}| \cdot F_{mod,k-1/2}. \end{aligned} \tag{2.45}$$

Therefore, the unsplit spatial discretization associated to hexahedron $H_{i,j,k}$ with volume $V_{i,j,k}$ is

$$\frac{\partial}{\partial t} \int_{V_{i,j,k}} \vec{q} \; dV = -\text{net-flux}(H_{i,j,k}). \tag{2.46}$$

2.2.3. Time integration

Several approaches have been considered for time integration of the semi-discrete method introduced in equation 2.46. As wave dynamic processes need to be resolved, explicit schemes are favored. Implicit techniques have recently been developed as well, but in the framework of this thesis, explicit methods are used exclusively.

In particular, low-storage multi-stage schemes have been investigated. Following [35], a reasonable option is given as:

$$\begin{aligned} q^{(i)} &= q^{(0)} + \triangle t \beta_i F\left(q^{(i-1)}\right), \quad i = 1,..,4 \\ q^{(0)} &= q^n, \quad q^{(4)} = q^{n+1} \end{aligned} \tag{2.47}$$

The specific choice of this scheme leads to discretizations of order ≤ 2 for non-linear problems [72]. Choosing coefficients $\beta_3 = 1/2$ and $\beta_4 = 1.0$ leads to schemes of 2nd order accuracy, which are related to classical Runge-Kutta schemes. The remaining coefficients can be used to optimize the stability region for the underlying problem, which may be simplified with the generic equation $q' = F(q)$.

Applied to Dahlquist's test equation [72]

$$\dot{q}(t) = \lambda q(t), \quad q(0) = 1, \quad \lambda \in \mathbb{Z} \text{ mit } Re(\lambda) < 0 \tag{2.48}$$

we obtain the stability polynomial with $z := \lambda \triangle t$

$$P(z) := 1 + \beta_4 z + \beta_4\beta_3 z^2 + \beta_4\beta_3\beta_2 z^3 + \beta_4\beta_3\beta_2\beta_1 z^4. \tag{2.49}$$

Determination of the region of absolute stability ($|P(z)| \leq 1$) as defined in [72] requires numerical experiments. Results for three sets of coefficients, which are summarized in table 2.2, are shown in Figure 2.3.

Scheme	β_1	β_2	β_3	β_4	Order of accuracy
LS 1 RK 4	11/100	5/18	1/2	1.0	2
LS 2 RK 4	9/112	2/9	1/2	1.0	2
LS 3 RK 4	1/3	4/15	5/9	1.0	1

Table 2.2.: Runge-Kutta coefficients

In order to demonstrate the effect of the coefficients β_1 and β_2 on the stability region, a comparison with stability regions of classical Runge-Kutta schemes of orders one to four

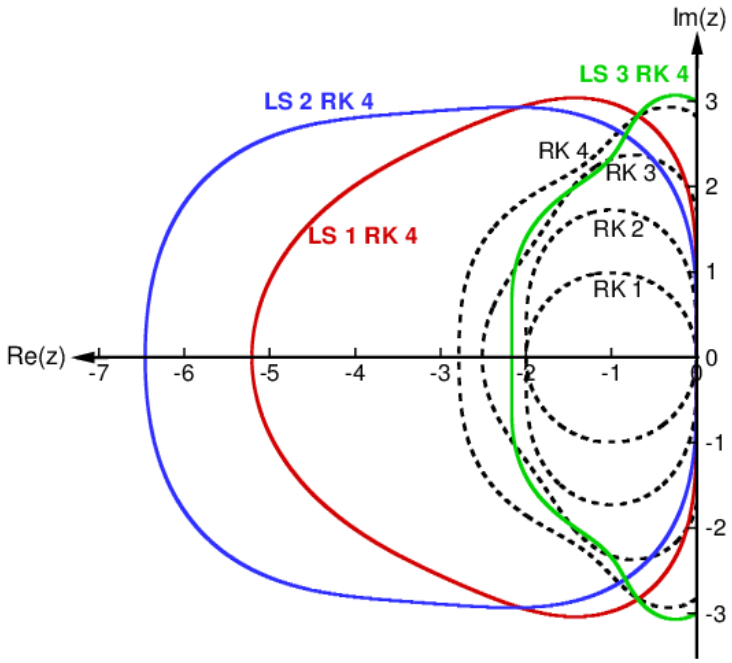

Figure 2.3.: Comparison of stability regions for different Runge-Kuttta schemes

is provided. "LS 3 RK 4" was not considered as the order of accuracy is insufficient but has the best imaginary axis stability properties. The scheme denoted as "LS 1 RK 4" is used in this work. In order to estimate the maximum allowable time step size, a linear one-dimensional advection equation in a periodic domain and two spatial discretizations were analyzed. Computing amplification factors $G := |(q^{n+1}/q^n)|$ for the eigenvalues of a first-order upwind discretization and a third-order upwind-biased discretization [34] indicates that upper bounds might be at $CFL = 2.49$ (first order upwind) and at $CFL = 2.09$ (third order upwind-biased). Although the scheme "LS 2 RK 4" showed an improvement of about 8 % for both test problems, it exhibits instabilities for CFL=2.0 when applied to the actual governing equations, while "LS 1 RK 4" remained stable. Note that both schemes, "LS 1 RK 4" and "LS 2 RK 4", do not contain parts of the imaginary axis except for the origin.

The computation of the time step size follows a simple procedure:

- Determine the maximum cell face area $S_{max,i,j,k}$ for a hexahedron $H_{i,j,k}$ with volume $V_{i,j,k}$.
- Estimate the maximum signal speed $\lambda_{max,i,j,k} := |\vec{v}| + c$.
- Compute the local time step $\Delta t_{i,j,k} := CFL \cdot \frac{V_{i,j,k}}{S_{max,i,j,k} \cdot \lambda_{max,i,j,k}} \cdot \frac{1}{dim}$, where "dim" is the number of non-trivial dimensions.
- Find the smallest local time step for each block of the multi-block grid.
- Find the smallest time step of all blocks.

In this work $CFL = 1.5$ was used for most of the computations. Although this might be a cautious choice, since computations with CFL=1.8 seem to run stable as well, it is recommended to use $CFL = 1.5$.

3. Summary of achievements

3.1. Contributions of the author

The author has developed a new flux function for the simulation of cavitating liquid flows including wave dynamics. In contrast to classical Riemann solvers, the developed scheme results in an asymptotically correct scaling of the numerical truncation errors with decreasing Mach number (low Mach number consistent). This is achieved by omitting the spectral radius $u \pm c$ as part of the regularization. Validation of the scheme is presented in the first publication in Appendix A.

The scheme was implemented in a finite volume method which was developed during the author's diploma thesis [62]. A thermodynamic model proposed by Saurel [59] was selected and implemented. The resulting simulation code was then applied to a series of high and low speed flows. Internal flows in fuel injector models and external flows around twisted and non-twisted hydrofoils as well as around a prismatic body and a sphere have been simulated and analyzed. The author has demonstrated that shedding processes are essentially inertia controlled (see publication number 5 in appendix E).

A major discovery was that the developed approach allows for the computation of collapsing vapor patterns together with the formation and propagation of strong shocks. The footprints of instantaneous loads can be used to determine regions of enhanced risk for cavitation erosion. Recent publications [52,53] indicate that the computed intensity and the frequency of events may allow for the derivation of load profiles. These profiles enable a quantitative evaluation of the aggressiveness of cavitating flows. The author of this thesis proposed the scaling law of the collapse intensity based on the decay law for spherical waves, as well as an empirical scaling law for the frequency of collapses.

By coarse-graining the computational resolution from resolved bubbles to an under-resolved vapor cloud an important property of the model was obtained. It was shown that the applied model can be used in case of fully resolved cavities, represented or marginally resolved cavities and under-resolved cavities. It is thus reasonable to interpret the model as a sub-grid model in case of insufficient spatial resolution. A mathematical motivation of the observed model behavior was proposed on basis of filtering which is implicitly contained in finite volume methods.

3.2. Awards

The author was a member of the winning team of ACM Gordon Bell Prize 2013, [57].

3.3. List of publications

The author's progress was continuously published. Contributions fulfilling the following requirements are listed below:

- At least 6 pages, no short papers or enlarged abstracts
- First authorship (9 publications) or co-authorship (18 publications)
- Available as printed version, online version or both
- Peer reviewed, either by a committee or by at least 2 referees.

1. "Compressible simulation of high-speed hydrodynamics with phase change" [61]

2. "Shock and wave dynamics of compressible liquid flows with special emphasis on unsteady load on hydrofoils and on cavitation in injection nozzles" [70]

3. "Shock waves as driving mechanism for cavitation erosion" [64]

4. "Compressible simulation of liquid/vapor two-phase flows with local phase transition" [67]

5. "Riemann technique for the simulation of compressible liquid flows with phase-transition at all Mach numbers – shock and wave dynamics in cavitating 3-D micro and macro systems" [66]

6. "Numerical investigation of 3-D cloud cavitation with special emphasis on collapse induced shock dynamics" [71]

7. "Numerical analysis of shock dynamics for detection of erosion sensitive areas in complex 3-D flows" [65]

8. "Density based CFD-techniques for simulation of cavitation induced shock emission" [68]

9. "Inertia controlled instability and small scale structures of sheet and cloud cavitation" [69]

10. "Unsteady bubbly cavitating nozzle flows" [15]

11. "Shock and wave dynamics in cavitating compressible liquid flows in injection nozzles" [73]

12. "Non-barotropic models of cavitation and their applications" [14]

13. "Collapse detection in compressible 3-D cavitating flows and assessment of erosion criteria" [51]

14. "Assessment of the prediction capability of a thermodynamic cavitation model for the collapse characteristics of a vapor-bubble cloud" [63]

15. "Numerical simulation of collapse induced shock dynamics for the prediction of the geometry, pressure and temperature impact on the cavitation erosion in micro channels" [76]

16. "Implicit large eddy simulation of cavitation in micro channel flows" [30]

17. "Numerical prediction of erosive collapse events in unsteady compressible cavitating flows" [53]

18. "Numerical simulation of sheet and cloud cavitation and detection of cavitation erosion" [78]

19. "Turbulence Modulation by Phase Change in a Cavitating Shear Layer" [20]

20. "Implicit large-eddy simulation of cavitation in a turbulent shear layer" [19]

21. "Quantitative Prediction of Erosion Aggressiveness through Numerical Simulation of 3-D Unsteady Cavitating Flows" [52]

22. "Bubble Dynamics and Shock Waves: Shocks in Cavitating Flows", Chapter 8, [13]

23. "LES of Turbulent Cavitating Shear Layers" [21]

24. "11 PFLOP/s simulation of cloud cavitation collapse" [57]

25. "Numerical Prediction of Erosive Collapse Events in Unsteady Compressible Cavitating Flows" [53]

26. "Recent progress in experimental and numerical cavitation erosion prediction", Chapter 14, [38]

27. "Large-eddy simulation of turbulent cavitating flow in a micro channel", [22]

Appendices

In the following, ten selected publications are presented. Prior to each original publication, a short summary of the achievements and/or developments is given and the contributions of the author of this thesis are clarified.

A. First publication

In the author's first publication [61] a low Mach number consistent flux scheme for simulation of cavitating liquid flows including wave-dynamics is proposed. In contrast to existing approaches, the novel technique does not require time-operator preconditioning to recover the correct low Mach number behavior in low speed flows. The flux scheme is implemented into an unsplit finite volume method using explicit time integration and block-structured body-fitted hexahedral grids. A thermodynamic cavitation model proposed by Saurel et al. [59] is applied and simplified equations of state for liquid water at approximately room temperature are presented.

The novel scheme is validated by computation of well-known 1-D test-cases and is applied to a low Mach number steady-state flow in a simplified 2-D nozzle. By computing the unsteady flow in two different 3-D injection nozzles, the applicability of the proposed methodology to simulate flows in technical devices is demonstrated. The effects of a swirl generator upstream of the nozzle inlet are analyzed and a favorable behavior of the intrinsic dynamics of the cavitating flow is observed. In particular, the cavity patterns are no longer in contact with the wall of the bore hole, but form a stable vapor core at the center of the emerging vortex. As a result, collapsing cavity patterns are kept away from the wall of the bore hole and shocks due to collapses of vapor patterns do not lead to high loads on the material.

Although the proposed methodology was refined with respect to robustness and efficiency during the author's ongoing work [66, 71], the developments presented in this publication served as basic concepts of all consecutive publications.

I developed the flux-function, implemented the thermodynamic approach, generated the grids, performed simulation and analysis of results and prepared the manuscript.

European Conference on Computational Fluid Dynamics
ECCOMAS CFD 2006
P. Wesseling, E. Oñate and J. Périaux (Eds)

COMPRESSIBLE SIMULATION OF HIGH-SPEED HYDRODYNAMICS WITH PHASE CHANGE

Steffen J. Schmidt*, Ismail H. Sezal and Günter H. Schnerr

*Technische Universität München, Faculty MW
Boltzmannstraße 15, D - 85748 Garching , Germany
e-mail: schmidt@flm.mw.tum.de
web page: http://www.lhm.mw.tu-muenchen.de/gd/

Key words: Cavitation, Riemann solvers, Hydrodynamics, Injection nozzles

Abstract. *The present paper focuses on a numerical approach based on the Riemann problem to simulate liquid flows with phase changes. Thereby, the flow properties include velocities from $\mathcal{O}(1)$ m/s to $\mathcal{O}(100)$ m/s and pressures from $p \approx 0$ bar to $\mathcal{O}(1000)$ bar. The thermal and caloric behavior of liquid and vapor is described by suitable equations of state that keep the considered governing equations hyperbolic in time. This enables us to study single-phase as well as two-phase wave propagation phenomena, which can have strong effects on the performance of dynamic systems, e.g. on high-speed hydrodynamics in injection nozzles or in high pressure valves. Our physical model is based on the assumption that the two-phase regime can be described as a homogeneous mixture that remains in thermodynamic and mechanical equilibrium. This model provides a macroscopic description of the phase change and is independent of empirical parameters. Subsequent to the description of the mathematical model and the numerical method, computations are carried out to demonstrate the accuracy and applicability of the numerical scheme to liquid flows for a large variety of industrial problems. Finally, the simulation results of the time-dependent cavitating flow through a 3-D injection nozzle will be presented.*

1 INTRODUCTION

Liquid flows at low or at least moderate Mach numbers are usually described as being incompressible. This simplification is justified by the observation that the density change along a particle path is almost zero as long as no phase change occurs. As a result, the continuity equation reduces to a kinematic constraint on the velocity field. Furthermore, the pressure is no longer a thermodynamic state variable and thus one has to calculate it from the known velocity field by a Poisson type equation. An important consequence of this formulation is the loss of hyperbolicity of the time-dependent convective flow equations, which means that the mathematical model does no longer describe wave motion with finite propagation speeds. In the case of subsonic steady-state solutions this treatment

gives satisfactory results. For unsteady flow patterns the elliptic pressure treatment can lead to completely wrong predictions, for example when calculating the pressure raise in a water hammer. Especially when dynamic systems such as high-speed valves or injection systems are considered, the wave propagation and thus the compressibility has to be taken into account. Most of the work done so far does consider only 1-D geometries[1]. Even if there is no external force present that introduces pressure waves to the flow field, strong compressibility effects can be observed when the liquid undergoes phase change. We will exclusively focus on phase change phenomena caused by a local pressure drop below the temperature-dependent saturation pressure - cavitation - , or if vapor is already present and the pressure rises above its saturation value - condensation. Both effects can be a consequence of acceleration or deceleration of the flow due to geometry properties as well as due to rarefaction or shock waves. The description of microscopic details of the phase change is beyond the scope of this investigation but there has been numerous research on this subject[2,3]. Instead we will follow the assumption that a given fluid volume can be represented by either a pure phase or by a homogeneous saturated mixture[4]. In the case of a mixture region we define macroscopic quantities. This can be achieved by the assumption that the flow particles undergo unconstrained thermodynamic equilibrium. Moreover, the equilibrium assumption enables us to define an equilibrium speed of sound c, which will be used to calculate the wave propagation in the two-phase mixture as well as in single phase regions.

2 GOVERNING EQUATIONS

As we are mainly interested in the wave dynamics of convective high-speed hydrodynamics, we base our mathematical model on the conservation laws of mass, momentum and energy and neglect viscous effects. The saturated mixture quantities are then defined as convex combinations of mass or volume fractions of the pure quantities. For liquid states we use the index l and for vapor states the index v is taken. Quantities without index represent either vapor-liquid equilibrium properties in the two-phase region or pure substance properties in single-phase regions. We further use the notations:

$$\begin{aligned} \alpha &:= \frac{V_v}{V_v + V_l} \qquad \text{volume fraction of vapor} \\ \mu &:= \frac{\rho_v V_v}{\rho_v V_v + \rho_l V_l} \qquad \text{mass fraction of vapor.} \end{aligned} \tag{1}$$

Mass and volume fractions fulfill the relations

$$0 \leq \alpha \leq 1 \quad \text{and} \quad 0 \leq \mu \leq 1. \tag{2}$$

The mixture density and the mixture internal energy can then be defined by

$$\begin{array}{rcccccl} \rho & = & \alpha\rho_v & + & (1-\alpha)\rho_l & & \\ \rho e & = & \alpha\rho_v e_v & + & (1-\alpha)\rho_l e_l & = & \rho\big\{\mu e_v + (1-\mu)e_l\big\}. \end{array} \tag{3}$$

By interpreting the mixture quantities $(\rho, \rho\vec{\mathbf{v}}, \rho E)$ as densities with respect to the Lebesgue measure we find formally the same set of equations as for single phase flows:

$$\begin{array}{rcccl} \partial_t\,\rho & + & \mathrm{div}(\rho\vec{\mathbf{v}}) & = & 0 \\ \partial_t(\rho\vec{\mathbf{v}}) & + & \mathrm{div}(\rho\vec{\mathbf{v}}\otimes\vec{\mathbf{v}} + p\underline{\mathbf{I}}) & = & \vec{0} \\ \partial_t(\rho E) & + & \mathrm{div}(\rho H\vec{\mathbf{v}}) & = & 0. \end{array} \tag{4}$$

Here, $\vec{\mathbf{v}} \in \mathbb{R}^3$ and $\underline{\mathbf{I}} = \delta_{ij}$. The total enthalpy H is given by:

$$H = E + \frac{p}{\rho} = e + \frac{|\vec{\mathbf{v}}|^2}{2} + \frac{p}{\rho}. \tag{5}$$

Furthermore, constitutive relations for the remaining quantities are needed. At this point we assume relations for pressure and internal energy to be given in the form

$$p = p(\rho, e) \quad \text{and} \quad T = T(\rho, e). \tag{6}$$

By writing the system (1) in quasi-linear form and calculating the eigenvalues in unit direction $\vec{\mathbf{n}}$ one obtains[5]:

$$\vec{\mathbf{v}}\cdot\vec{\mathbf{n}} - c,\ \vec{\mathbf{v}}\cdot\vec{\mathbf{n}},\ \vec{\mathbf{v}}\cdot\vec{\mathbf{n}},\ \vec{\mathbf{v}}\cdot\vec{\mathbf{n}},\ \vec{\mathbf{v}}\cdot\vec{\mathbf{n}} + c \tag{7}$$

where c^2 is defined by

$$c^2 = \left.\frac{\partial p}{\partial \rho}\right|_s = \left.\frac{\partial p}{\partial \rho}\right|_e + \frac{p}{\rho^2}\left.\frac{\partial p}{\partial e}\right|_\rho. \tag{8}$$

The Euler system (4) is hyperbolic if and only if $0 < c^2 < \infty$. Then the quantity c is called equilibrium speed of sound[6].

3 EQUATIONS OF STATE (EOS) FOR LIQUID, VAPOR AND SATURATED MIXTURE

In this section we give an example for the constitutive relations (6), which are suitable to describe the properties of water and water vapor for thermodynamic subcritical

conditions occurring in a large range of practical applications. Note that the general numerical method is not restricted to this special choice and hence, the use of problem-suited relations is possible.

3.1 EOS for liquid water

One often used relation for the properties of liquid water is the Tamman EOS or sometimes called Stiffened equation of state[7]. This EOS is well-designed for very high pressures and its evaluation is extremely fast. Unfortunately, for the considered pressure regime from nearly 0 bar up to 1000 bar the Tamman EOS is not suitable. Another well known relation is given by Tait's law:

$$\frac{p+B}{p_{ref}+B} = \left(\frac{\rho}{\rho_{ref}}\right)^N. \tag{9}$$

This equation is often used to describe isentropic variations and a thermally consistent description for the corresponding internal energy could be of the form:

$$e_l = C_{v_l}(T - T_{ref}) + e_{l_{ref}}. \tag{10}$$

In EOS (9) and (10) the reference values $(\cdot)_{ref}$, the "bulk coefficient" B, the "adiabatic exponent" N and the specific heat at constant specific volume C_{v_l} are assumed to be constants. The accuracy of the pressure law (9) can be increased by the use of temperature-dependent saturation values instead of constants[4]. We then obtain the modified Tait law:

$$\frac{p+B}{p_{sat}(T)+B} = \left(\frac{\rho}{\rho_{l,sat}(T)}\right)^N. \tag{11}$$

Equation (11) can be interpreted as a set of self similar curves starting from saturation values and then following Tait's law. Again, B and N are assumed to be constant. Unfortunately, the modified Tait equation together with formulation (10) does not fulfill Maxwell's relations. Nevertheless it gives an useful description not only for water but for a large range of materials[8,9]. It should be further pointed out that the resulting errors by checking the compatibility relations are relative small and hence, we suggest that the modified Tait law (11) together with (10) can be an appropriate set of constitutive relations for liquid flows. As the saturation properties are typically given by high-order non-linear functions (e.g. Oldenburg polynomials[10] for water and water vapor), the evaluation procedure is further simplified by approximating the saturation functions by problem specific lower order relations.
The speed of sound c_l for liquids is then found by applying (8) on (10) and (11). The obtained values do in general agree well with the measurement data[11], but relative errors up to three percent are possible.
All calculations in section 5 are performed with the same reference values, which can be found in the appendix.

3.2 EOS for water vapor

In comparison to liquids, the thermodynamics of ordinary gases at moderate conditions can be modeled in a more compact way. The simplest but still appropriate formulation is given by the ideal gas law:

$$\begin{aligned} p &= \rho_v RT \\ e_v &= C_{v_v}(T - T_{ref}) + e_{l_{ref}} + L_{v_{ref}}. \end{aligned} \tag{12}$$

For the sound speed c_v in pure vapor the well known relation $c = \sqrt{\kappa RT}$ is applied. Again, the used constants are given in the appendix.

3.3 EOS for saturated two phase mixture

The assumption of thermodynamic equilibrium enables us to define mixture states by the following conditions:

$$\begin{aligned} \rho &= \alpha\rho_{v_{sat}}(T) + (1-\alpha)\rho_{l_{sat}}(T) \\ \rho e &= \alpha\rho_{v_{sat}}(T)e_v(T) + (1-\alpha)\rho_{l_{sat}}(T)e_l(T) \\ p &= p_{sat}(T). \end{aligned} \tag{13}$$

The temperature-dependent saturation densities of water and vapor can again be approximated by exponential functions (appendix). Note that by solving the first equation for the volume fraction α and applying the result to the second equation we find:

$$\rho e = \frac{\rho - \rho_{l_{sat}}(T)}{\rho_{v_{sat}}(T) - \rho_{l_{sat}}(T)} \left\{ \rho_{v_{sat}}(T)e_v(T) - \rho_{l_{sat}}(T)e_l(T) \right\} + \rho_{l_{sat}}(T)e_l(T). \tag{14}$$

This is a single nonlinear equation for the unknown temperature T, which can be solved via appropriate numerical methods. In our case we have found a contradictive formulation, and by applying Banach's theorem we obtained a simple fixpoint scheme which has proven to be at least 3 to 4 times faster then our previously used Newton method. If the temperature is found, the first equation gives the volume fraction in a self-consistent way and the calculation of the saturation pressure is easily done.
The calculation of the mixture speed of sound c can be simplified by the commonly used formula[1,2] given by Wallis[12]. This leads to the relation:

$$\frac{1}{\rho \cdot c^2} = \frac{\alpha}{\rho_{v,sat} \cdot c_v^2} + \frac{1-\alpha}{\rho_{l,sat} \cdot c_l^2}. \tag{15}$$

Evaluating this expression for saturation values, a very strong dependence on the vapor

fraction α can be observed. The quantitative behavior for $T = 293\ K$ is demonstrated in Fig. 1 (left). Note that the sonic speed decreases from $\mathcal{O}(1000)\ m/s$ to $\mathcal{O}(1)\ m/s$. Even

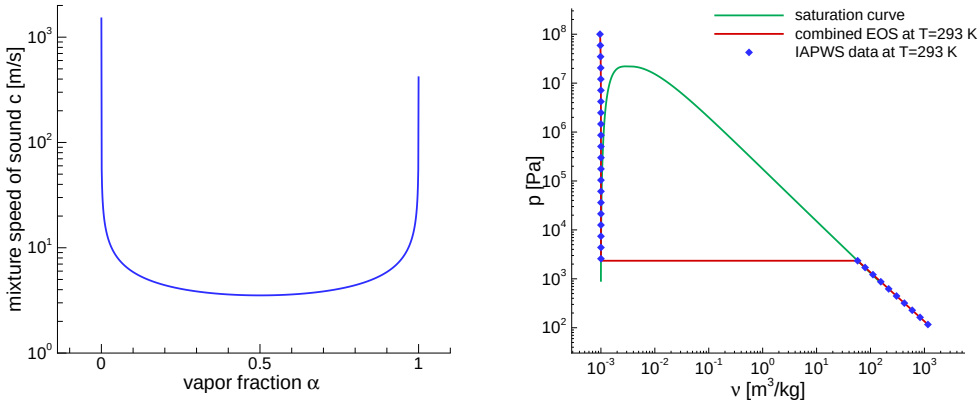

Figure 1: Speed of sound c for a two phase mixture in logarithmic scale (left) and combined EOS at T=293 K and IAPWS data[13] (right)

for very tiny mass and volume fractions an enormous reduction of the speed of sound is observable. This fact was experimentally used to generate hypersonic flow fields at relative low convective speeds[14].

3.4 Combined EOS for liquid flows with phase change

Connecting the above defined equations of state leads to a complete description of the properties of liquid and vapor. It should be pointed out that more accurate equations are known[15]. The advantages of the procedure given above are its applicability to fluids other then water and its high numerical efficiency. A comparison of the combined EOS with IAPWS measurement data[13] at a temperature $T = 293\ K$ is given in Fig. 1 (right).

4 NUMERICAL METHOD

The formulation of the governing equations as conservative hyperbolic system motivates the use of specially adapted solution strategies, such as the Godunov approach[16]. Although the Riemann problem is completely understood for 1-D ideal gas flows, the extension to multidimensions and arbitrary equations of state is still somehow empirical. Nevertheless, most of the results obtained by Godunov-type schemes are convincing and especially the sharp wave capturing ability is up to now not reached by other methods. A general Riemann problem description with special remark on ideal gases is given by

Toro[17]. The Riemann problem for water and the interesting case of Riemann problems for water/gas interfaces are solved for special equations of state[7,18]. General remarks on real material flows can be found in the literature[19]. In the last few years, the density-based solution procedures for the Cauchy problem of fluid dynamics have reached enormous interest and successful and sophisticated numerical codes have been developed[20]. While being well-designed for time-dependent wave propagation phenomena, it was found out[21] that the calculation of steady-state flows at sufficiently low Mach numbers cannot be done without modifying the density-based schemes. The introduction of asymptotic expansions in natural powers of the Mach number show that the numerical problems arising for M sufficiently small are due to wrong calculations in the pressure field[22]. To solve these drawbacks, a modification of the numerical dissipation was found to be successful[23]. The next subsections are therefore organized as follows: First, an approximate solution of the Riemann problem is given and the influences of the fluid properties on the accuracy of a numerical simulation are briefly discussed. As a main result, the calculation of the pressure flux may need some modifications to ensure accurate steady state solutions. Taking these modifications into account, a hybrid solution approach is given in subsection 4.2.

4.1 Accuracy of well-known Riemann solvers

Before we give a brief description of the numerical difficulties to solve compressible liquid flows we introduce further quantities and notations. Therefore a schematic sketch of the Riemann problem and the arising quantities is given in Fig. 2. The quantities on the

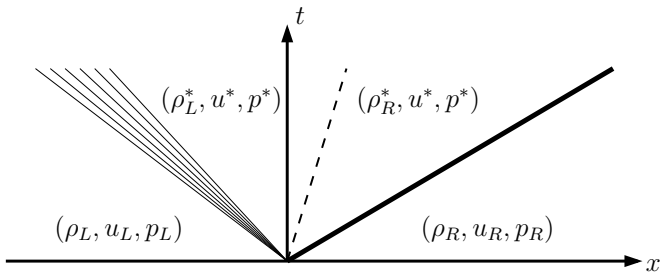

Figure 2: Schematic 1-D Riemann problem

very left ("L") and on the very right sides ("R") are the known integral averages from the last timestep. To calculate the fluxes over the cell faces, the star conditions $(\rho_L^*, \rho_R^*, u^*, p^*)$ are required. By assuming that the two outer states are close to some averages, a local linearisation around that averages could be performed and an approximate solution is

obtainable by applying Rankine-Hugoniot conditions across each wave:

$$\begin{aligned} u^* &= \frac{u_L + u_R}{2} + \frac{p_L - p_R}{2\bar{\rho}\bar{c}} \qquad & p^* &= \frac{p_L + p_R}{2} + \frac{\bar{\rho}\bar{c}(u_L - u_R)}{2} \\ \rho_L^* &= \rho_L + \frac{\bar{\rho}(u_L - u^*)}{\bar{c}} \qquad & \rho_R^* &= \rho_R + \frac{\bar{\rho}(u^* - u_R)}{\bar{c}} \end{aligned} \tag{16}$$

Note that the linearisation replaces the waves in the genuinely non-linear fields by jump discontinuities independently of the specific wave types. The barred variables $\bar{\rho}, \bar{c}$ could be specified as arithmetic means of left and right-sided values. Although more sophisticated approximations for the star conditions are known[17], the general properties of the resulting fluxes are quite similar to the one given above. Especially the behavior of the second equation should be briefly discussed: Therefore, we consider an inviscid steady water flow through a one-dimensional duct at a (nearly) constant temperature of 320 Kelvin and a constant total pressure of 1.125 bar. The velocity is assumed to accelerate from $5m/s$ at position x_1 to 15 m/s at position x_2. For these conditions, the steady density and sonic speed distributions will be to best approximation constants, say $\rho \cong 1000\ kg/m^3$ and $c \cong 1540\ m/s$. The static pressure drop can then be calculated from the Bernoulli equation and one obtains: $p(x_1) = 1\ bar$ and $p(x_2) = 0\ bar$. Note that the static pressure and the velocity both vary in the order of their "farfield values" at position x_1. Although the Mach number M of this problem is strictly smaller then 0.01, we are not allowed use the asymptotic techniques developed for low Mach number flows, because the leading-order variations do not permit the introduction of M-expansions[22]. In the context of a finite volume approach all quantities are given by integral averages. Assume the discretization leads to the following left- and right-sided values:

$$\begin{aligned} &u_L = 5\ m/s, && u_R = 5.13\ m/s, \\ &p_L = 1\ bar, && p_R = 0.993\ bar, \\ &\rho_L = 1000\ kg/m^3, && \rho_R = \rho_L - \varepsilon \quad (\varepsilon \ll 1). \end{aligned} \tag{17}$$

Evaluating the expressions in (16) does then give the conditions

$$u^* \approx 5.056\ m/s, \quad p^* \approx 0\ bar. \tag{18}$$

On the one hand both values can be verified to be quite accurate solutions of the Riemann problem for the given left and right sides. On the other hand the obtained pressure value indicates the difficulty to calculate the numerical flux for a smooth water flow. The calculated interface pressure p^* is extremely sensitive even to small "discrete jumps" in the velocity field. An explanation for this behavior could be obtained by the following observation: For nearly constant density and sonic speed the numerical approximation of the pressure $p_{L,R}$ at the cell interface is given by the p^* relation in (16):

$$p_{L,R} = \frac{p_L + p_R}{2} + \Delta x \rho c \frac{(u_L - u_R)}{2\Delta x} = \frac{p_L + p_R}{2} - \Delta x \rho c \frac{u'(\xi)}{2} \tag{19}$$

One can identify the product ρc as a scaling factor on the mesh dependent dissipation term $\Delta x u'(\xi)$. As a consequence, the use of the quantities arising from the Riemann problem to calculate the fluxes over the cell faces (as commonly done in the approximate Godunov approach) results in a scheme with a truncation error of $\mathcal{O}(\rho c \cdot \Delta x)$. A comparison of air and water at standard conditions leads to:

$$(\rho c)_{air} = \mathcal{O}(10^2) \quad \text{and} \quad (\rho c)_{water} = \mathcal{O}(10^6) \tag{20}$$

From equation (20) it can be concluded that the calculation of a steady water flow may require a much finer grid than a comparable air flow. Unfortunately, this is a consequence of the discretization and not part of flow physics, as the velocity jumps are - for the suggested smooth flow - not physically present. Keeping this in mind we can determine possible ways to obtain accurate solutions for steady and unsteady liquid flow problems: Fine grids, high-order reconstructions and/or a modification of the pressure flux calculation. The first two suggestions are in general limited in their efficiency and do not seem to be sufficient to obtain accurate steady-state results on typical 2-D and 3-D grids. This will be demonstrated in section 5.3 for a 2-D single-phase calculation.

4.2 Hybrid solver based on the Riemann problem and flux splitting

In order to study the behavior of well known flux functions we have applied the schemes of ROE, HLL and HLLC, as well as the Rusanov scheme and two simple linearized schemes on steady and unsteady water flow problems[17]. All schemes failed to give accurate steady-state solutions for typical 2-D and 3-D nozzle flows, but they performed excellent or at least satisfactory on shock tube problems. As supposed in the previous section, the steady-state solutions indicated a strongly dissipative behavior. Contrary to the mentioned flux functions, the AUSM+ scheme[24] performed quite well for $t \to \infty$. For shock tube calculations the scheme produced acceptable results but the mass flow was not as accurate as the one predicted by the ROE or HLLC fluxes. Comparing the pressure flux calculation in the AUSM type methods[24,25] with those methods that are directly related to the Riemann problem, one can figure out that the AUSM pressure splitting contains a significantly lower diffusion term. For the nozzle flow problem stated above the interface pressure calculated by the AUSM scheme is about 0.9 *bar*, which seems more reasonable than the result given in equation (18). We therefore tried to combine the AUSM flux with the HLLC flux to obtain a scheme[26] that is able to handle problems containing nearly steady regions as well as time dependent wave phenomena. Therefore, we follow the general philosophy of the AUSM type methods and divide the conservative Euler fluxes $F(Q)$ into a "convective component" and a "pressure part". This leads to the formula:

$$F(Q) = \begin{pmatrix} \rho u \\ \rho u u + p \\ \rho u v \\ \rho u w \\ \rho u H \end{pmatrix} = (\rho u) \cdot \begin{pmatrix} 1 \\ u \\ v \\ w \\ H \end{pmatrix} + \begin{pmatrix} 0 \\ p \\ 0 \\ 0 \\ 0 \end{pmatrix} = \dot{m} \cdot F_{conv} + F_{pres} \tag{21}$$

The mass flux $\dot{m} := (\rho u)$ is a common scalar for the convective flux. Instead of approximating $\dot{m}$ via polynomials (as done in the original AUSM methods) we use the HLLC mass flux[17]. For the schematic sketch given in Fig. 2 the mass flux reads then:

$$\dot{m} := (\rho_L^* u^*) \tag{22}$$

The convective vector F_{conv} is build up by pure left side states for positive mass flow and otherwise by right side values. This is again a common part of AUSM. To determine the pressure flux F_{pres} we apply the AUSM pressure splitting without additional modifications. The resulting interface pressure $p_{L,R}$ can be written as:

$$p_{L,R} := \mathcal{P}_5^+(u_L/c_L) \cdot p_L + \mathcal{P}_5^-(u_R/c_R) \cdot p_R \tag{23}$$

A very detailed description of the AUSM scheme including the full presentation of the polynomials $\mathcal{P}_5^{\pm}$ for the pressure splitting can be found in the literature[24].

4.3 Higher-order spatial reconstructions

The finite volume framework leads to a method of lines type approach where the spatial discretization can be selected independent of the time marching scheme. Although the straight forward extension of the TVD theory to multi-dimensions has proven to be not successful in a rigorous mathematical sense[27], the so called MUSCL-type reconstructions have been successfully used for many years. We apply the reconstruction procedures in a coordinate-wise manner on the variables ρ, u, v, w, e and select the type of limiting depending on the flow properties. For cavitating flows a positivity preserving reconstruction is needed for the density, such as the MinMod limiter[27]. The velocity field is recovered by a WENO-3 reconstruction[28] and for the internal energy we apply the VanLeer limiter[5].

4.4 Temporal integration

As the resolution of pressure waves requires a very small time step we use explicit time marching schemes only. We have tested a second order TVD-Runge-Kutta method[29] as well as a non-TVD four stage second order low storage RK scheme[5]. Both worked stable and accurate for all our numerical examples. It follows from the theory[29] that the CFL number for the TVD-RK has to be taken very small (< 0.3) to keep the scheme in the TVD region. The four stage RK allows a $CFL \approx 1.5$ and although it does not ensure TVD we did not observe overshoots for the simulations done jet.

5 NUMERICAL EXAMPLES

In the following section we validate the numerical scheme for 1-D and 2-D test cases and apply it then to a 3-D geometry. If possible, the obtained solutions will be compared with analytical results.

5.1 1-D single phase time-dependent test case

In order to verify the stability and the wave capturing ability of our method we start with a well-known Joukovski-Shock or water hammer problem, which is actually an ordinary moving normal shock. Thereby, a stationary water flow through a pipe with constant area and the constant conditions $\rho = \rho(p_\infty, T_\infty)$, $u = u_\infty > 0$, $p = p_\infty$ and $T = T_\infty$ is considered. At time $t = t_c$ the outflow boundary is entirely closed and a pressure rise at the wall instantaneously occurs. This (weak) shock wave then travels in opposite direction to the flow. Again, the pressure jump can be approximated by solving the generalized Riemann invariant across the wave

$$dp + \rho c du = 0 \quad \text{across} \quad \dot{x} = u - c. \tag{24}$$

By evaluating the product ρc at the foot of the characteristic one obtains:

$$p^* = p_\infty + \rho_\infty c_\infty u_\infty. \tag{25}$$

Using the experimental data from[11] we find for water at conditions $T_\infty = 319.0\ K$ and $p_\infty = 0.9\ bar$ the corresponding density $\rho_\infty = 989.86\ kg/m^3$ and the corresponding sonic speed $c_\infty = 1537.16\ m/s$. Taking $u_\infty = 1.0\ m/s$ and evaluating (25) for these conditions gives

$$p^* = 16.12\ bar. \tag{26}$$

We now perform a numerical simulation by using p_∞, T_∞ and u_∞ as stated above. The corresponding density and sonic speed follow thereby from the equation of state. First we find

$$\rho_{\infty,eos} = 989.84\ kg/m^3 \quad \text{and} \quad c_{\infty,eos} = 1544.14\ m/s. \tag{27}$$

The relative errors in density and sonic speed are $\Delta\rho/\rho_\infty = 2 \cdot 10^{-5}$ and $\Delta c/c_\infty = 4 \cdot 10^{-3}$. The calculated pressure after the shock gives $p^*_{num} = 16.20\ bar$. Taking the analytical estimate (26) as reference we find the relative error $\Delta p^*/p^* = 5 \cdot 10^{-3}$.

Remark 1: Calculating the Joukovski-Shock by integrating characteristic compatibility relations across the shock (equations 24, 25) results in an underestimation of the pressure jump. It is possible that the numerical result, which predicts a shock Mach number of $M_S \approx 1.0008$, is closer to the true solution then the analytical estimate.

Remark 2: Contrary to steady subsonic flow patterns, the water hammer can not be

calculated with an incompressible formulation. The divergence-free condition in incompressible formulations does not permit the formation of the necessary pressure wave and instead of the true time-dependent behavior the velocity in the whole pipe will be set to zero after the first time step. From a physical point of view, this could be interpreted as an infinitely fast signal speed, which is a general model error of incompressible formulations.

5.2 1-D two phase time-dependent test case

In this subsection we use the combined EOS and decrease the density below the saturation density of pure liquid by enforcing two symmetric expansion waves. The domain is given by a 1-D constant area tube with length 1 m. At time $t = 0$ s the whole tube is filled with water at a temperature $T = 303.15$ K and a pressure $p = 0.9$ bar. The velocity field is assumed to jump at $x = 0.5$ m from $u_L = -10$ m/s to $u_R = 10$ m/s. These conditions enforce the phase change to occur. In Fig. 3 the resulting flow features at time $t = 1.5 \cdot 10^{-4}$ s are shown. The domain was divided into 300 equally spaced cells and the time integration was performed with the LS-RK 4 at $CFL = 1.5$.

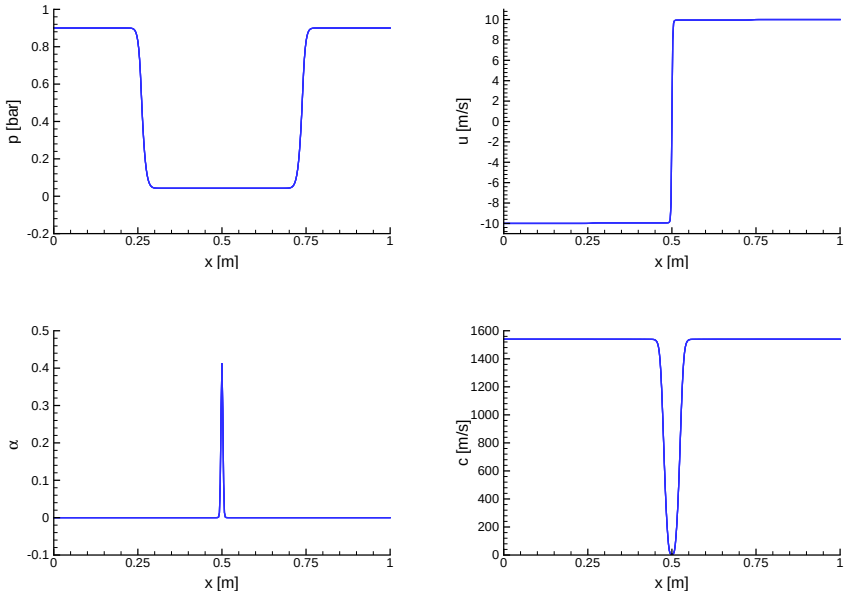

Figure 3: Flow quantities at time $t = 1.5 \cdot 10^{-4}$ s for the 1-D symmetric rarefaction problem.

5.3 2-D Single Phase Steady-states

We now compare our solution strategy with the well-known HLLC approach[7,17]. Therefore, we define a 2-D geometry typical for injection nozzles and search for the enforced single phase steady-state solution. This means that we do not allow the liquid to undergo a phase change by using the pure liquid EOS even if the density falls below its saturation value. The same simulation was performed with higher pressure fields, but the qualitative behavior was not affected. The geometry and the boundary conditions are given in Fig. 4. The spatial discretizations are the first order schemes (without any reconstruction)

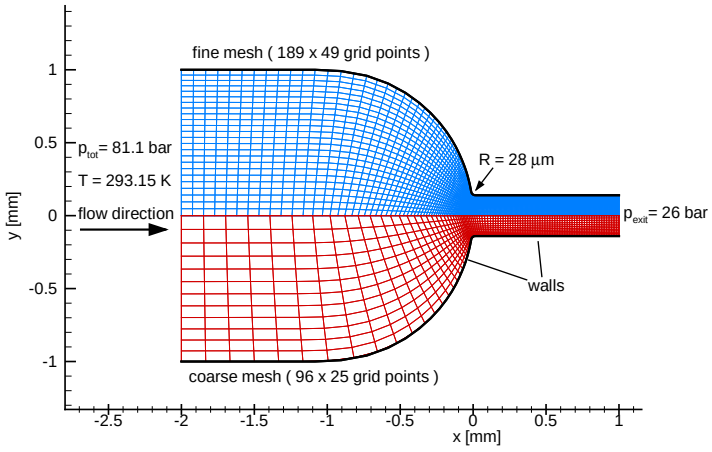

Figure 4: 2-D plane nozzle geometry, fine grid (top half), coarse grid (bottom half) and boundary definitions

and the quadratic interpolation of cell averages without limiters. The later one corresponds to a third order accurate formulation on equally spaced one dimensional grids[5]. For the time-marching the four stage RK scheme is applied and all solutions converged at least seven orders in magnitude measured in the common L_2-Norm of the conserved quantities. The boundary conditions are subsonic inlet, subsonic outlet and adiabatic inviscid walls. At the inlet we fix total pressure, static temperature and the direction of the velocity. At the outlet, the static pressure is specified and all remaining quantities are taken from inside. All boundaries are defined by ghost cells and hence, the treatment of a boundary cell is equivalent to the treatment of the interior domain. The grids for the full symmetric nozzle consist of 96 x 25 points (coarse grid) and 189 x 49 points (fine grid),

both with finer treatment of the region where the small corner like radius $R = 28\ \mu m$ will produce large gradients. For presentation purposes we show one half of the nozzle for each solver. The top half of each nozzle picture shows the result obtained with HLLC and the bottom shows the result of the Hybrid scheme. To verify the obtained solutions

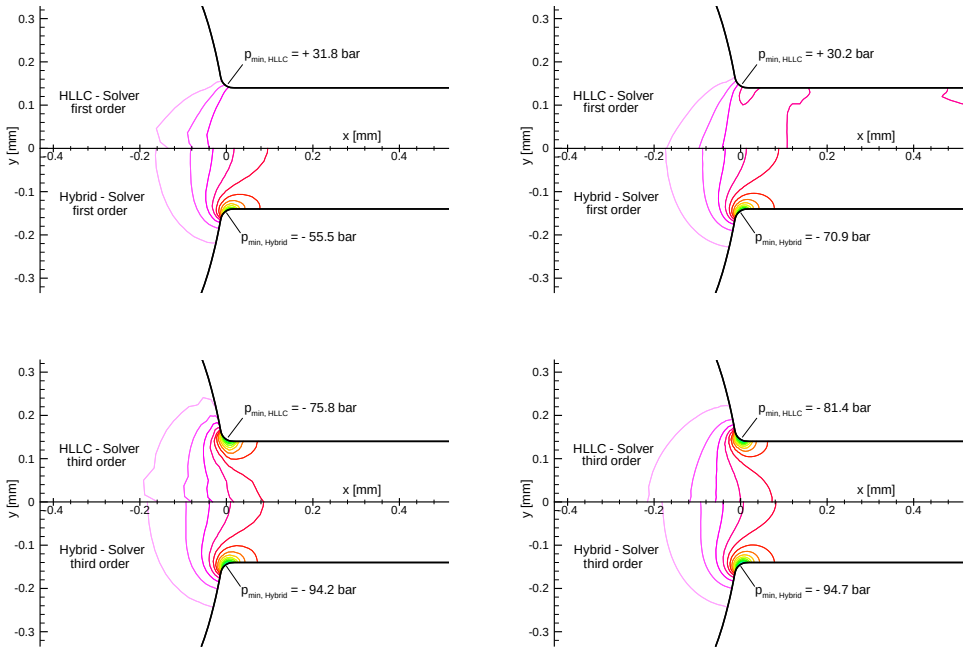

Figure 5: Comparison of HLLC (upper half) and Hybrid scheme (lower half) on the coarse grid (left) and on the fine grid (right) for the 2-D plane geometry.

we calculate the velocity at the outlet by using the given boundary conditions together with the area relation by evaluating the incompressible steady Bernoulli equation. For the given conditions we find an exit velocity of $u_{exit,Bernoulli} \approx 105\ m/s$. The first order HLLC scheme produces a steady-state result with an exit velocity of less then 50 m/s on the coarse grid and 64 m/s on the fine grid. This confirms the failure of the first order HLLC scheme on both grids. The pressure field as well as the velocity field (not shown) indicate a massively dissipating behavior of the HLLC solver for these flow conditions. For the third order simulations we find the same insufficiency, but the obtained solutions are more reasonable. The Hybrid scheme reproduced the analytical results very satisfactory

for all test cases. The gain in accuracy by using finer grids or higher order reconstructions is still noticeable, but a comparison of the isobars clearly shows that the main flow field is well predicted even for the first order solution on the coarse grid. We therefore conclude that our Hybrid formulation is a significant improvement.

5.4 3-D cavitating injection nozzles

To get more insight into the flow features in high-speed injection nozzles we have simulated a typical 3-D axisymmetric configuration with representative conditions (config 1). Additionally, we have modified the standard geometry by closing the axial inlet and adding four nearly tangential inlets in order to study swirl effects (config 2). This inlet configuration is then comparable to a mixing chamber. Both geometries are shown in Fig. 6. The nozzle dimensions are the same as for the previously presented 2-D single phase simulations (Fig. 4), but we added an outflow domain to study the wave dynamics outside the nozzle as well. Thereby, the whole domain is assumed to be initially filled with water at rest and pressure and temperature are assumed to be $p = 23\ bar$ and $T = 293.15\ K$. The conditions at the outflow boundaries are calculated by assuming that the farfield can

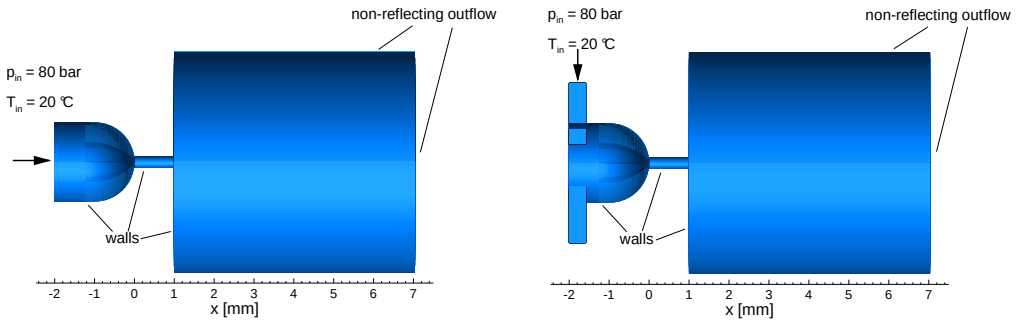

Figure 6: 3-D nozzle geometry with outflow and boundary definitions for nozzle configuration 1 (left) and configuration 2 (right)

be represented here by a liquid at rest (Fig. 6) with constant ambient pressure $p = 23\ bar$. According to these assumptions we derived characteristic boundary conditions that allow waves to pass through the boundary with minimum reflective behavior (non-reflecting boundary conditions). The walls are again defined as inviscid adiabatic and impermeable surfaces. The pressure for the ghost cells at the inlet plane was set to $p = 80\ bar$. The spatial reconstruction uses MinMod on density, WENO-3 on the velocities and VanLeer on internal energy. For the time integration the LS-RK 4 with $CFL = 1.3$ was used. To reduce calculation time, a 90 degree section of each full geometry was simulated. The

additionally resulting boundaries are treated with periodic conditions. Inside the nozzle we used a grid comparable to the coarse grid in Fig. 4. The total number of finite volumes for both geometries is $6 \cdot 10^4$ volumes per section and hence parameter studies are possible. For single-phase flows the grid was verified to be fine enough by comparing the numerical solutions with the Bernoulli theory. Nevertheless, we observed that a finer grid can lead to an increase in the resolved two-phase flow structures. The obtained flow fields for both configurations were found to be unconditionally time-dependent although the remaining variations are noticeably weaker then those during the buildup of the main flow fields. In Fig. 7 the iso-surfaces of constant vapor volume fraction α for configuration 1 are shown. The instantaneous picture gives an impression of the mean cavity length and the structure of the mixture region. Furthermore one can see two small cloudy structures that have been separated and convected into the outflow domain. The collapse of such structures can cause pressure waves of high amplitude with $\Delta p = \mathcal{O}(100)\ bar$. The second geometry

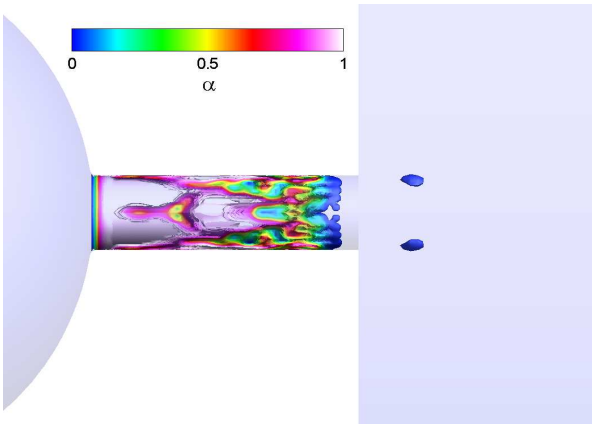

Figure 7: Iso-surfaces of the vapor volume fraction α at one instant in time for configuration 1

produces a more steady flow field because the inlet modification leads to the formation of a vortex structure. Only at the end of the cavitation core one can observe the separation of small cloudy structures. This breakup is periodic with a frequency $f = 60\ kHz$ and a series of planar cuts through the nozzle center is shown in Fig. 8. The flow inside the nozzle is nearly stationary and hence the use of a scheme that ensures accurate 3-D steady-state calculations is necessary for applications of this type[26]. To give an overall impression of the velocity field we generated stream traces starting from the inlets and ending at the outflow exit (Fig. 9). One can observe the acceleration in the convergent nozzle part and the rotational symmetric vapor core is visible (blue core).

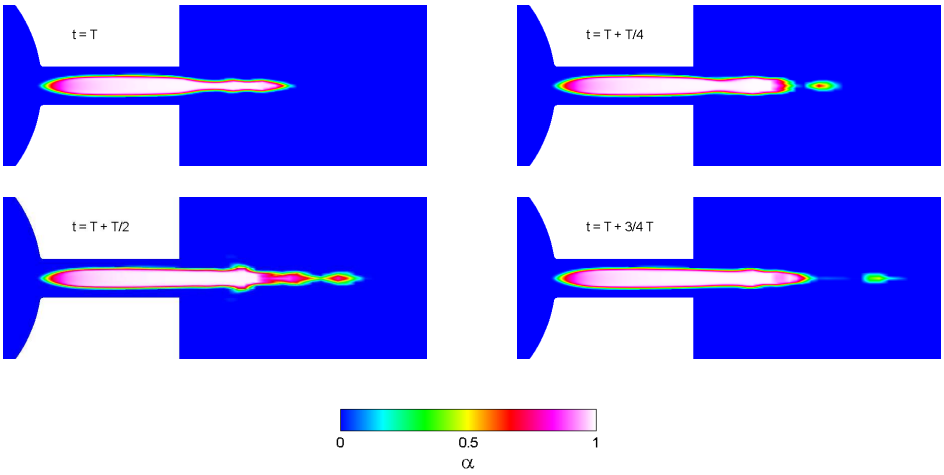

Figure 8: Vapor fraction α in configuration 2 for one period $T = 1/f = 1.7 \cdot 10^{-5}\ s$.

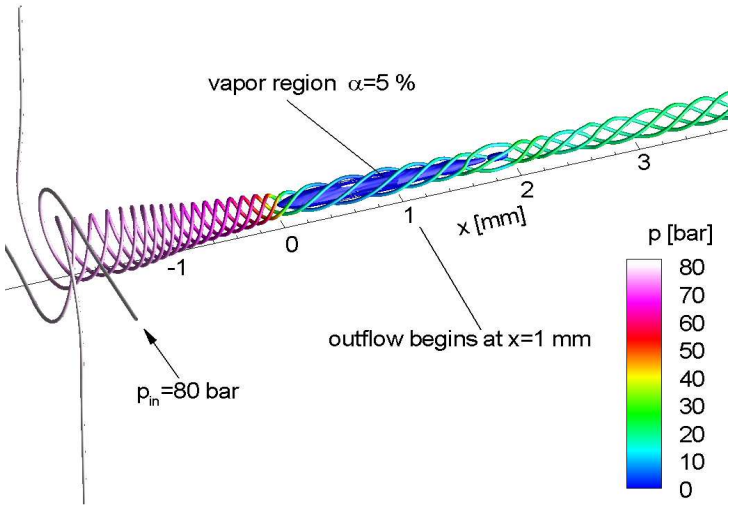

Figure 9: Stream traces at $t = T + T/2$ colored with the static pressure for configuration 2

6 CONCLUSIONS

- A general framework for solving the time dependent compressible Euler equations including the energy conservation law has been developed.
- An applicable set of constitutive relations for water and water vapor is given and their advantages as well as their disadvantages are described.
- It has been shown that accurate calculations of steady-state liquid flows require very fine grids and high-order reconstructions if common Riemann solvers are used.
- A Hybrid solver has been developed that overcomes the drawback of the previously stated approaches.
- The scheme was then shown to be able to handle two phase flow including the crucial phase change.
- Finally the cavitating flow fields through two different high-speed injection nozzles were presented.
- The present scheme should be extended to handle an additional gas component. This is especially important because it offers the possibility to simulate the outflow into a gaseous domain rather than a liquid one.

7 APPENDIX

For the simulations presented in section 6 the following set of constants and functions was used:

B	C_{v_l} $[kJ/(kgK)]$	T_{ref} $[K]$	$e_{l_{ref}}$ $[kJ/(kgK)]$	N
$3.3 \cdot 10^8$	4.18	273.15	0.617	7.15

Table 1: Constants for the liquid water EOS

R $[kJ/(kgK)]$	C_{v_v} $[kJ/(kgK)]$	T_{ref} $[K]$	$e_{l_{ref}}$ $[kJ/(kgK)]$	$L_{v_{ref}}$ $[kJ/(kgK)]$	κ
0.4615	1.4108	273.15	0.617	2375.3	1.327

Table 2: Constants for the water vapor EOS

The saturation conditions $p_{sat}(T)$, $\rho_{l,sat}(T)$ and $\rho_{v,sat}(T)$ are taken from[10]. If the temperature T is known to remain close to some reference value T_r, one can obtain approximations to the above cited functions which are more efficient to handle. The following example gives approximate conditions for a reference temperature $T_r = 293.15\ K$:

$$\theta := T - T_r \tag{28}$$

$$\begin{aligned} p_{sat}(T) &= exp(7.7585 + 0.0619166 \cdot \theta - 0.0002 \cdot \theta^2) \\ \rho_{l,sat}(T) &= exp(6.90591 - 0.00021 \cdot \theta - 0.000006 \cdot \theta^2 + 4.4 \cdot 10^{-8} \cdot \theta^3) \\ \rho_{v,sat}(T) &= exp(-4.05567 + 0.0585739 \cdot \theta - 0.000195 \cdot \theta^2) \end{aligned} \tag{29}$$

REFERENCES

[1] A. Berg, U. Iben, A. Meister, J. Schmidt. Modeling and simulation of cavitation in hydraulic pipelines based on the thermodynamic and caloric properties of liquid and steam. *Shock Waves*, (2005).

[2] C.E. Brennen. *Cavitation and Bubble Dynamics*, Oxford University Press, (1995).

[3] G.H. Schnerr. Modeling of unsteady cavitating flows - Status and future developments. *6th Int. Sym. on Experimental and Computational Aerothermodynamics of Internal Flows*, Shanghai, China, (2003).

[4] R. Saurel, J.P. Cocchi and P.B. Butler. Numerical study of cavitation in the wake of a hypervelocity underwater projectile. *Journal of Propulsion and Power*, **15**, 4, (1999).

[5] C. Hirsch. *Numerical Computation of Internal and External Flows*, John Wiley & Sons, Vol. 1-2, (1988).

[6] A. Harten, P.D. Lax, C.D. Levermore and W.J. Morokoff. Convex entropies and hyperbolicity for general Euler equations. *SIAM J. Numer. Anal.*, **35**, 6, 2117–2127, (1998).

[7] M.J. Ivings, D.M. Causon and E.F. Toro. On Riemann solvers for compressible liquids. *Int. J. Numer. Meth. Fluids*, **28**, 395–418, (1998).

[8] P.A. Thompson. *Compressible Fluid Dynamics*, McGraw Hill, (1972).

[9] J.O. Hirschfelder, C.F. Curtiss and R.B. Bird. *Molecular Theory of Gases and Liquids*, John Wiley & Sons, (1965).

[10] R. Oldenbourg. *Properties of Water and Steam in SI-Units*, Springer-Verlag, (1989).

[11] G. Benedetto, R.M. Gavioso, P.A.G. Albo, S. Lago, D.M. Ripa and R. Spagnolo. Speed of sound of pure water at temperatures between 274 and 394 K and pressures up to 90 MPa. *Fifteenth Symposium on Thermophysical Properties*, Boulder, Colorado, U.S.A., (2003).

[12] W. Wallis. *One Dimensional Two-Phase Flow*, McGraw Hill, (1975).

[13] The International Association for the Properties of Water and Steam, *http://www.iapws.org/*.

[14] R.B. Eddington. Investigation of supersonic phenomena in a two-phase (liquid-gas) tunnel. *AIAA Journal*, **8**, 1, (1970).

[15] W. Wagner, S. Span and T. Bonsen. *Wasser und Wasserdampf*, Electronic Media, Springer-Verlag, (1999).

[16] S.K. Godunov. A finite difference method for the numerical computation of discontinuous solutions of the equations of fluid dynamics. *Mat. Sb.*, **47**, (1959).

[17] E.F. Toro. *Riemann Solvers and Numerical Methods for Fluid Dynamics*, Springer-Verlag, (1999).

[18] T.J. Chen and H. Cooke. On the Riemann problem for liquid or gas-liquid media. *International Journal for Numerical Methods in Fluids*, **18**, 529–541, (1994).

[19] R. Menikoff, B.J. Plohr. The Riemann problem for fluid flow of real materials. *Reviews of Modern Physics*, **61**, 1, (1989).

[20] P. Colonna and S. Rebay, Numerical simulation of dense gas flows on unstructured grids with an implicit high resolution upwind Euler solver, *Int. J. Numer. Meth. Fluids*, **46**, 7, pp. 735-765, (2004).

[21] E. Turkel. Preconditioning techniques in fluid dynamics. *Annual Review of Fluid Mechanics*, **31**, (1999).

[22] A. Meister. Asymptotic single and multiple scale expansions in the low Mach number Limit. *SIAM J. Appl. Math.*, **60**, 1, 256–271 (1999).

[23] H. Guillard and C. Viozat. On the behaviour of upwind schemes in the low Mach number limit. *Computers & Fluids*, **28**, 66–86 (1999).

[24] M.S. Liou. A sequel to AUSM, part II: AUSM+ -up for all speeds. *Journal of Computational Physics*, **214**, 137–170, (2006).

[25] M.S. Liou and C.J. Steffen. A new flux splitting scheme. *Journal of Computational Physics*, **107**, 23–39, (1993).

[26] S.J. Schmidt, I.H. Sezal and G.H. Schnerr. On Godunov methods for liquid flows. to be published.

[27] R.J. Leveque. *Finite Volume Methods for Hyperbolic Problems*, Cambridge University Press, (2002).

[28] C.W. Shu. Essentially non-oscillatory and weighted essentially non-oscillatory schemes for hyperbolic conservation laws. *ICASE Report No. 97-65*

[29] S. Gottlieb and C.W. Shu. Total variation diminishing Runge-Kutta schemes. *Mathematics of Computation*, **67**, 221, (1998).

B. Second publication

In the second publication [67] the authors simulate the cavitating flow in the lower part of a realistic 6-hole fuel injector. Due to 6-fold symmetry of the injector geometry, a sixty degree section is selected as numerical domain. The position of the needle is assumed to be fixed at maximum lift throughout the simulation. In analogy to experimental investigations, the domain outside of the bore hole is filled with liquid (no injection into gas). In total, 11 operating conditions are investigated, where the pressure upstream of the nozzle covers a range from 100 bar to 1400 bar and the pressure in the outer domain ranges from 15 bar to 60 bar. The discharge coefficient is found to be approximately 0.76, which is in good agreement with experimental values.

The focus of this investigation is put on wave dynamics during the development of the cavity pocket inside the bore hole. Although the numerically enforced start-up process does not resemble the movement of the needle, the observed interaction of waves and cavitation demonstrates the effects of compressibility and strengthen the application of the proposed methodology. Instantaneous loads of more than 1000 bar are detected and the formation and collapse of vapor pockets during the transient phase are shown. The structure of the resulting cavity at steady state (where the mass flow remains constant) is presented and compared to typical experimental observations.

I defined the test-cases, supervised the students who generated the grid and performed the simulations, analyzed the results and prepared the manuscript. Note that the flux function applied in this investigation was published in [66] (Appendix G).

6th International Conference on Multiphase Flow,
ICMF 2007, Leipzig, Germany, July 9 – 13, 2007

Compressible Simulation of Liquid/Vapour Two-Phase Flows with Local Phase Transition

Schmidt S.J., Sezal I.H., Schnerr G.H., Thalhamer M., Förster M.

Technische Universität München, Fakultät für Maschinenwesen, Lehrstuhl für Fluidmechanik, FG Gasdynamik
Boltzmannstr. 15, Garching, D-85748, Germany
schmidt@flm.mw.tu-muenchen.de

Keywords: injection nozzle, two-phase flow, cavitation, wave dynamics, phase change, low Mach number problem

Abstract

A conservative 3-D high resolution Godunov-type method is modified and extended to handle high and low speed liquid flows. An equilibrium phase transition model is applied to include cavitation-recondensation processes. Thereby, the thermodynamic properties of liquid and vapour are described by thermal and caloric equations of state. Our fully compressible time-accurate treatment of the equations of motion enables the investigation of wave dynamic effects such as shock formation and diffraction. The highly time dependent flow field inside a 3-D multi-hole injector is simulated. Thereby, wave dynamics dominates the flow characteristics during the first hundred microseconds. Rarefaction waves lead to acoustic cavitation close to the spray hole exit. Subsequently, the development of hydrodynamic cavitation is presented and a collapse induced shock wave is detected. Finally, the 3-D structure of the arising cavitation pocket is studied in detail. For a series of realistic operating conditions the nozzle discharge is analyzed and compared to analytical estimates.

Introduction

The design and improvement of high-speed fuel injection systems of Diesel- and Otto-engines is a challenging field of research. The operating conditions contain exceptional high pressure differences p_{in}-p_{out}=$O(10^3)$ bar, which result in maximum flow velocities up to *500 m/s*. Furthermore, high frequency excitations due to the needle lift induce strong wave dynamic flow features. Thereby, the arising pressure drop typically leads to acoustic and hydrodynamic cavitation. The subsequent recondensation of the evaporated liquid enforces the formation of violent shock waves which often results in cavitation erosion.

Besides the reduction of the machine lifetime, cavitation significantly alters the flow field (Brennen, 1995, Franc & Michel, 2004). As a consequence, the nozzle discharge reduces and the occurrence of unsteadiness leads to a hardly controllable operating behaviour. However, cavitation often contains a self-cleaning effect inside the bore holes and might improve spray characteristics as well.

Due to typical bore hole diameters of the order of *0.1 mm*, experimental investigations are difficult and detailed studies of the flow field require numerical simulations (Alajbegovic et al., 2002). The simulation of phase transition requires a model to describe the arising mass transfer. Such models often rely on single bubble dynamics (Yuan & Schnerr 2001, 2003) or on thermodynamic considerations. The former ones are applicable to quasi incompressible formulations of the equations of motion where the pressure is no longer depending on the density (Delale et al., 2006). The later ones require a functional relation of pressure and density. Here, simplified formulas can be derived that lead to efficient barotropic cavitation models (Hoeijmakers et al., 1998). A less restrictive formulation is obtainable by the use of thermal and caloric equations of state for liquid and vapour (Schmidt et al., 2006). The coexistence of both phases is often modelled as homogeneous mixture where the thermodynamic properties are defined by temperature dependent saturation conditions (Berg et al., 2005).

Nomenclature

T	Static temperature (K)
p	Static pressure (N m^{-2})
u,v,w	Velocity components (m s^{-1})
V_{vap}	Integrated vapour volume (% of total volume)
c	Speed of sound (m s^{-1})
t	Time (s)
$\dot{m}$	Mass flow (g s^{-1})
$\Delta\dot{m}$	Mass flow defect
A	Area (m^2)
f	Frequency (s^{-1})
	Greek letters
α	Vapour volume fraction
ρ	Density (kg m^{-3})
	Subscripts
in	Inlet condition
out	Outlet condition
max	Maximum value
init	Initialization condition
ref	Reference value
num	Numerical value

Mathematical Model

The simulation of wave dynamics in single- and two-phase flows requires a fully compressible and time accurate treatment of the equations of motion (Iben et al., 2002). Therefore, the thermodynamic properties of liquid and vapour are expressed by thermal and caloric equations of state, which enable a well-posed definition of the speed of sound c. Contrary to barotropic formulations, our fully compressible formulation is not restricted to isothermal or homentropic processes. Hence, the simulation of strong shock waves, as well as the inclusion of heat transfer processes is possible.

The liquid phase is currently represented by a modified Tait equation while the vapour phase is treated as ideal gas. This combination agrees well with measurement data for various fluids and its numerical evaluation is significantly more efficient than the evaluation of more general thermodynamic formulations. However, the mathematical model is not limited to this special choice, e.g. other formulations, including tabulated values, are possible as well (Wrona, 2005).

The coexistence of both phases is modelled as local homogeneous mixture at temperature dependent saturation conditions. These conditions are obtained via curve fitting procedures from experimental data.

The application of saturation conditions implies the assumption of unconstraint thermodynamic equilibrium. Thus, the equilibrium speed of sound for two-phase domains is well defined, too. This aspect is of special importance as our numerical solution strategy directly relies on wave speeds.

Further consequences arising from our model are the local equalities of temperature and pressure in saturated domains, as well as the common local velocity of liquid and vapour. The last aspect is due to the homogeneous mixture assumption, which does not permit the differentiation between liquid and vapour in saturated regions.

An important advantage of the proposed model is its inexistence of a-priori unknown adjustable model parameters. Other formulations typically require the definition of the initial bubble number density or the initial void fraction, which may have to be adjusted by the user. Furthermore, no time calibration via a pre-defined reference velocity is required.

Numerical Scheme

Our recently developed CFD-tool CATUM (CAvitation TU Munich) is part of our multi-purpose solution package for compressible flow dynamics including phase transition, chemical reaction and heat addition (Schnerr et al., 2006). Its modular setup contains routines to solve the arising balance laws by splitting them into a hyperbolic part (convective fluxes), a parabolic part (viscous fluxes) and a source term part. As our recent work focuses on wave dynamics and phase transition in micro-scale systems, viscous effects are of minor importance and hence neglected. The balance laws are thus the conservation principles for mass, momentum and energy. Together with the thermodynamic equilibrium formulation of either pure liquid or saturated liquid/vapour mixture the remaining set of equations are the Euler equations for compressible flows. However, the density and the internal energy represent mixture quantities as soon as the thermodynamic states predict the coexistence of both phases. As the governing equations are hyperbolic in time, a Godunov-type method is suitable to describe the numerical fluxes through the cell faces of the finite volume scheme (Godunov, 1959). These methods rely on (approximate) solutions of the arising Riemann problem between adjacent cells. They are known to accurately reproduce even complicated wave structures, but their application to multidimensional low Mach number flow leads to wrong results (Guillard & Viozat, 1999) unless they are appropriately extended. We therefore introduce a modified pressure flux definition that enables accurate time dependent low Mach number calculations, including $M \rightarrow 0$, as well. Its basic idea is the reduction of the pressure-velocity coupling by assuming smoothness properties in the velocity field, although the finite volume averaging leads to discontinuous data. The mass flux is obtained without any additional assumptions and follows from an approximate solution of the Riemann problem (Schmidt et al., 2006).

Nonlinear reconstruction procedures based on the conserved quantities ensure high-resolution of discontinuities as well as 2nd order accurate discretization of smooth flows. The semi-discrete equations are advanced in time by an explicit 4-stage Runge-Kutta method with enlarged stability region. The simulation tool CATUM provides 2nd order accurate solutions in space and time and its results are validated for high and low speed flows including phase transition.

An explicit treatment of the time differentials enforces the compliance with the CFL condition. Therefore, the maximum time advancement per iteration is proportional to the ratio of the smallest spatial distance Δx to the maximum wave speed $|u|+c$. The dominating spatial scales in injection systems are of the order of 10^{-4} m (bore hole diameter). To ensure sufficient spatial resolution of the arising gradients close to the bore hole entry, the discretization leads to a cell width of $\Delta x \approx 10^{-6}$ m. Together with the maximum wave speed of $|u|+c \approx 1.5 \cdot 10^{3}$ m/s, the necessary numerical time step Δt_{CFD} is of the order of 10^{-10} s. Thus, the time accurate simulation of a typical injection time of 10^{-3} s requires the computation of 10^{7} time steps. To enable parameter studies of complex 3-D geometries, the maximum number of finite volumes is thus limited to the order of $O(10^{5})$. Furthermore, all simulations are performed on 32 processors on a SGI-Altix 3700Bx2 machine. The calculation time is approximately 2 weeks for a full simulation of an injection cycle and a spatial discretization of 10^{5} finite volumes.

Nozzle Geometry and Numerical Grids

Figure 1 depicts a 180 degree section of a multi-hole fuel injector. The actual needle placement corresponds to its maximum lift position and hence, the valve is fully open. Six cylindrical bore holes are located in the lower part of the sack volume. In order to suppress flow separation, the inlet tips of the bore holes are rounded with a radius of wall curvature of 0.028 mm. Such a micro-deburr is practically achieved by hydroerosive grinding and significantly improves the flow characteristics.

The inner diameter of the upstream part of the nozzle is 3.9 mm and the diameter of the needle is 3.26 mm. The diameters of the spray holes are 0.22 mm and their length to diameter ratio is 4.54.

Figure 2 depicts the discretization of the flow domain. Due to *6*-fold radial periodicity of the injector we solve the flow equations for a *60* degree section. At the outlets of the bore holes enlarged domains are added in order to simulate the arising flow outside of the nozzle as well. This enables the physically consistent treatment of the flow dynamics close to the bore hole exits, which cannot be ensured if the domain outside the nozzle is replaced by numerical boundary conditions. To study the mesh dependence of the numerical results, calculations are carried out for three different grids containing 10^5, $2.6 \cdot 10^5$ and $4 \cdot 10^5$ cells (shown in **Fig. 2**). For all cases a high grid quality is achieved by the use of *85* matching O- and H-grids, which consist of low aspect ratio hexahedrons only.

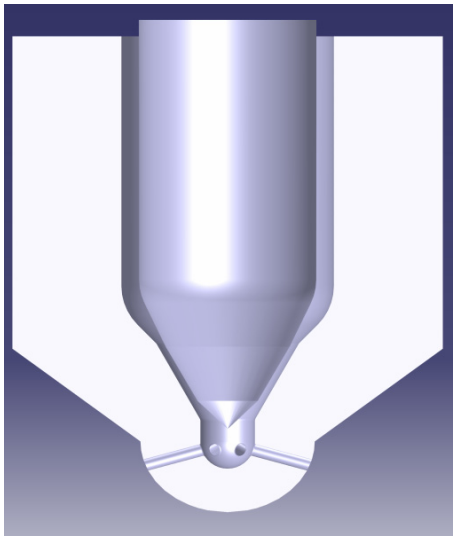

Figure 1: 180 degree section of the 3-D 6-hole injector geometry; needle position at maximum lift.

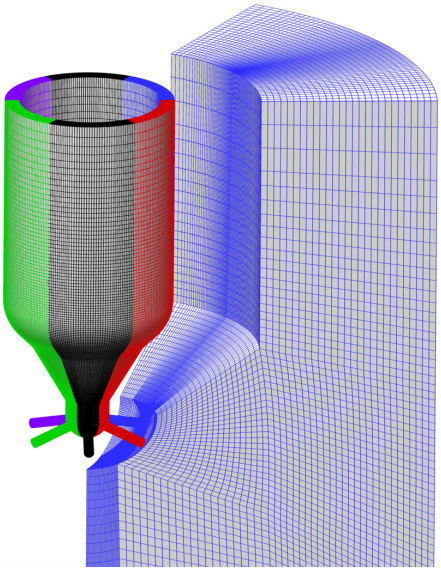

Figure 2: Discretization of the injection nozzle including one sixth of the surrounding domain. Each 60 degree section contains $4 \cdot 10^5$ cells (fine grid).

Flow properties and Numerical Boundary Conditions

We assume the nozzle and the surrounding domain to be initially filled with pure liquid at rest. The pressure and the temperature are initially set constant to $p_{init}=p_{out}$ and $T_{init}=333$ K throughout the numerical domain. In spite of being a common experimental setup, this assumption may lead to different results than the more practical condition where the nozzle sack and the domain outside of the nozzle are initially filled with gas. However, this will require the implementation of non-condensable gas as a third compressible component into the numerical scheme, which is part of our current research.

All solid walls are treated as adiabatic, inviscid, impermeable and stationary. Hence, the needle movement is not modelled. Instead we focus on the maximum lift position of the needle as shown in **Fig.1**.

The numerical boundary treatment along the outer surface of the surrounding domain allows waves passing through (characteristic boundary conditions), but ensures constant prescribed pressure p_{out} asymptotically (Rudy & Strickwerda, 1980). Due to the large distances between the bore holes and the boundary surface, the oncoming disturbances are already very weak, which additionally improves the quality of this boundary treatment.

At the inlet area we apply similar boundary conditions, but the prescribed pressure p_{in} now resembles the rail pressure. Although the disturbances at the inlet boundary are partially of the same order as the pre-defined asymptotic conditions, our numerical boundary treatment is able to reproduce the experimentally observed time dependent pressure behaviour.

Due to the six-fold symmetry of the injector geometry we apply symmetry boundary conditions at the lateral section planes. The enforced boundary conditions are thereby identical to those applied to inviscid walls.

For this investigation all simulations are performed with water as the test-fluid at an initial temperature $T_{init}=333\ K$.

Results and Discussion

Figure 3 contains the time history of the mass flow $\dot{m}$ (top) and the corresponding integrated vapour volume V_{vap} (bottom) for the pressure conditions $p_{in}=600\ bar$ and $p_{out}=26\ bar$. Both graphs are plotted against a logarithmic time axis (large pictures) as well as against a linear time axis (small pictures). The mass flows as well as the integrated vapour volume show a strong transient behaviour and reduce to constant values at time $t \approx 10^{-4}\ s$. As it will be presented in the following subsections, the solution turns out to reach a stable steady state at that time. However, comparison of the final values with their maximum amplitude during the transient flow development demonstrates the necessity of time accurate simulations of injection processes, especially if pilot or multipoint injections are considered. Moreover, comparison of the mass flow $\dot{m}_{in}$ at the nozzle inlet to the mass flow $\dot{m}_{out}$ at the exit of the spray holes highlights the compressible behaviour of the liquid fluid and the wave dynamics as dominating features. Any incompressible formulation would enforce the velocity field to be strictly divergence free, which implies the equality of $\dot{m}_{in}$ and $\dot{m}_{out}$ throughout the simulation.

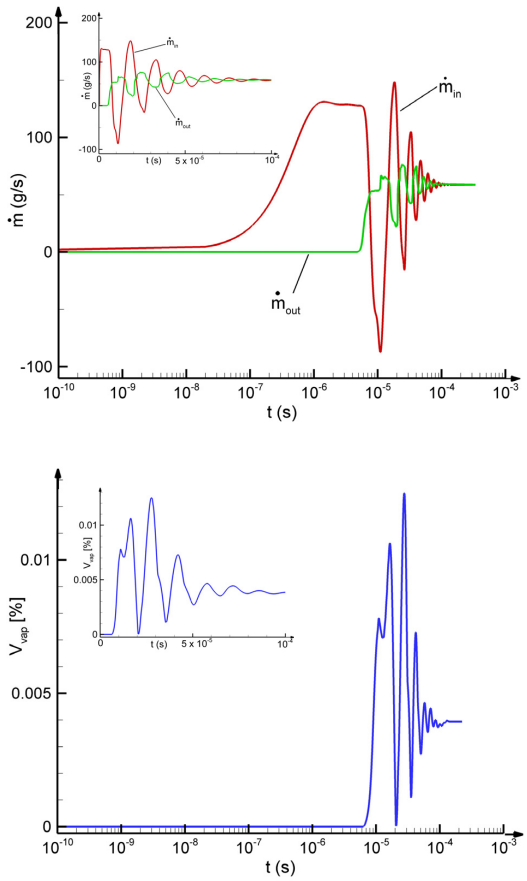

Figure 3: Time history of the mass flow rate at the nozzle inlet and at the exit of the spray holes (top). Time history of the integrated vapour volume V_{vap} [% total volume] (bottom). p_{in}=*600 bar*, p_{out}=*26 bar*, T_{init}=*333 K*, Δt_{CFD}=10^{-10} *s*.

As shown in **Fig. 3**, the mass flows do not fulfil this assumption. Instead we observe oscillations with a mean frequency of $\bar{f}$ =*70.5 kHz* and a constant phase shift of π between $\dot{m}_{in}$ and $\dot{m}_{out}$. The amplitudes show exponential decay in time, which motivates a comparison of the transient flow dynamics with an under-damped harmonic oscillator.
The following analysis is divided into three time intervals. The first time segment contains the initiated wave motion as a consequence of the enforced initial conditions. The second time segment includes the development of the mass flow at the bore hole exits which is accompanied with acoustic and hydrodynamic cavitation. The third time interval covers the main period of the transient development of the flow field. Finally, the properties of the steady state solution are analysed and special emphasis is placed on the arising cavitation pocket inside the bore holes.
Picture 1-4 of **Fig. 4** depict the pressure development during the first time interval $0\ s \le t \le 5.36 \cdot 10^{-6}\ s$. Due to the initially enforced pressure jump $\Delta p = p_{in} - p_{out} = 574\ bar$ across the inlet boundary a shock wave instantaneously forms and propagates through the nozzle. The arising post-shock velocity $\hat{u}$ can be estimated by characteristic compatibility conditions (Zierep, 1991)

$$\hat{u} = \frac{p_{in} - p_{out}}{\rho \cdot c}.$$

Together with the properties of water at T_{init}=*333 K* and p_{out}=*26 bar*, the density ρ and the speed of sound c are of the order of $10^3\ kg\ m^{-3}$ and $1.5 \cdot 10\ m\ s^{-1}$, respectively. Hence, the post-shock velocity $\hat{u}$ turns out to be $38.2\ m\ s^{-1}$. The applied single-wave approximation is thereby motivated with the pressure boundary condition at the inlet. The shock strength as well as the post-shock velocity remains unaltered as long as the wave propagates through to the constant area gap between the inner nozzle wall and the needle. This is due to the 1-D flow character through the annular gap. As soon as the shock wave reaches the conical part of the needle, the flow direction alters according to the wall geometry. Furthermore, the effective nozzle area reaches a local minimum at the uppermost part of the needle seat (**Pic. 1**). The combination of both geometrical features lead to shock deflection and shock focussing, respectively. Thereby, velocity and pressure increase, which results in a compression being effective backwards to the inlet. The shock propagates further and reaches the needle tip **(Pic. 2)**. As the geometry is now divergent an opposite effect is observed. Due to the decreasing shock strength the post-shock pressure $\hat{p}$ reduces as well. However, as the pressure slightly upstream is larger than the post-shock value, pressure equalization once more occurs. Inside the sack the shock front is no longer planar (**Pic. 3**) and strong diffraction is observable when the front reaches the bore hole. The diffraction result in a wave propagating towards the bottom of the sack and a nearly planar wave travelling through the throat (**Pic. 4**).
Picture 1-12 of **Fig. 5** focus on the flow development close to the bore holes. The time interval covers the period $5.48 \cdot 10^{-6}\ s \le t \le 8.88 \cdot 10^{-6}\ s$. **Picture 1** depicts the multidimensional shock focusing at the lower wall of the sack. The maximum pressure p_{max}=*2163 bar* is thereby reached at t=$5.55 \cdot 10^{-6}$ *s* (**Pic. 2**). In **Pic. 3** the shock wave reaches the exit of the bore hole. There it diffracts to a spherical front and propagates into the outside domain. At this time, the mass flow $\dot{m}_{out}$ at the bore hole exit starts to develop. The shock-strength decreases proportional to the radius of the front and a rarefaction wave propagates inside the throat. This expansion is strong enough to partially reduce the static pressure to vapour pressure and thus to enforce cavitation. Two-phase domains are thereby indicated by isolines of the void fraction α=*0.001*. In **Pic. 4** and **5** we observe two types of cavitation. Strong expansions around the edges of the spray holes result in vortex cavitation in the surrounding domain of the nozzle. The 3-D toroidal structures of the arising saturation regions outside the bore holes are indicated by closed isolines. Inside the bore holes acoustic cavitation is visible. Thereby, the whole cross section close to the bore hole exit is affected. However, as typical for wave induced phase transition, the maximum void fraction α is of the order of 10^{-3}. Due to the remaining velocity field the vapour content is compressed and recondenses within $5 \cdot 10^{-7}$ *s* (**Pic. 6**). In **Pic. 8** we observe another acoustic cavitation. Furthermore, continuous reduction of the pressure inside the sack volume is visible. At the curved bore hole entry we observe the onset

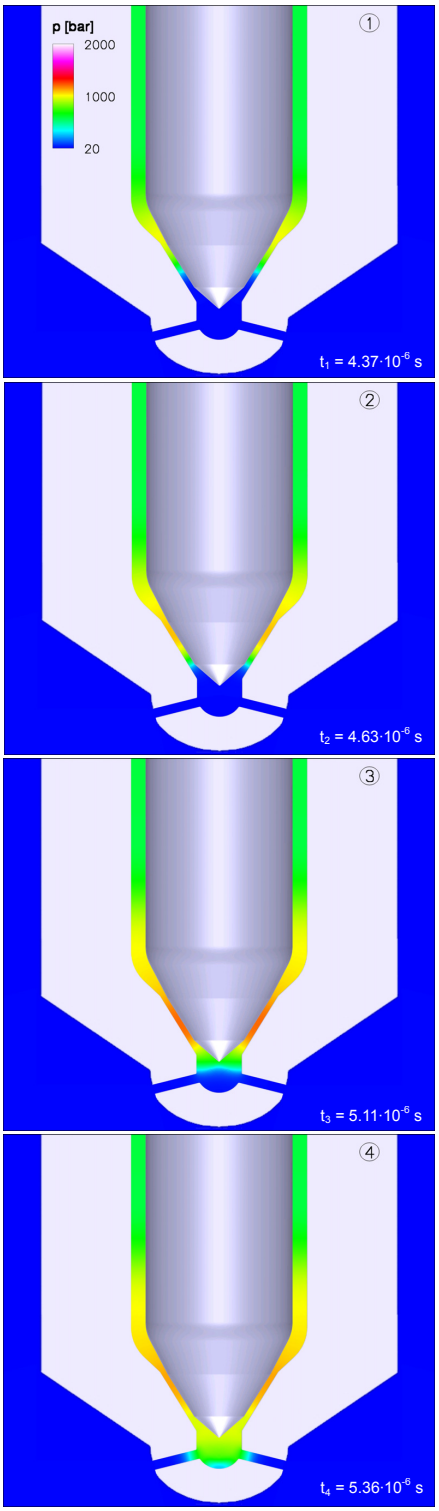

Figure 4: Pure liquid wave dynamics inside the nozzle as consequence of the initiated shock wave, p_{in}=*600 bar*, p_{out}=*26 bar*, T_{init}=*333 K*, Δt_{CFD}=10^{-10} *s*.

of hydrodynamic cavitation (**Pic. 9**). The hydrodynamic cavitation pocket forms a torus-shaped structure as well. Only the upper part of the saturated two-phase domain grows along the flow direction, while the lower cavitation region disappears (**Pic. 10-12**). At this instant in time the integrated vapour volume fraction V_{vap} starts to grow significantly. However, this is due to the growth of the cavity inside the bore holes as well as in the outside domain, where the vortical structures lead to further evaporation.

The subsequent quasi periodic behaviour will be termed as time interval three. **Figure 6** depicts the formation and collapse of the hydrodynamic cavity. In **Pic. 1** the cavitation pocket inside the bore hole already covers two thirds of the bore hole length. Further growth of the pocket takes place until the cavity reaches its maximum dimension at t=$1.67\cdot10^{-5}$ *s* (**Pic. 2**). This instance in time corresponds to the first local maximum of the integrated vapour volume (**Fig. 3, bottom**). Both cavities start to recondense, which results in the shrinking of the vapour domains **(Pic. 3**). At t=$1.95\cdot10^{-5}$ *s* the cavitation pocket inside the bore hole breaks slightly behind the bore hole inlet (**Pic. 4**). Thereby, an increase of the pressure due to inertia forces is visible. The vapour pocket is rapidly compressed along the flow direction until the complete saturated domain disappears. Subsequently, a violent collapse occurs. As this process is accompanied with a significant increase of the velocity behind the collapsing cavity, as well as with a requisite decrease of the velocity ahead the cavitation pocket, the resulting velocity field directly after the collapse necessarily causes a discontinuity. The resulting "water-hammer" enforces the formation of a shock wave where the pressure raise is proportional to the velocity difference. **Picture 5** depicts the arising shock which leads to a maximum pressure of p_{max}=*1029 bar*, which is about twice the inlet pressure p_{in}=*600 bar*. As it is known from 3-D spherical symmetric explosion theory, the formation of a rarefaction wave is inevitable. Together with the afresh forming vortex cavitation (**Pic. 6**) a cavity pocket inside the bore hole starts to grow. At t=$2.77\cdot10^{-5}$ *s* the integrated vapour volume again reaches its local maximum value and the period recommences. However, with each repetition of the process the break of the cavity occurs slightly closer to the bore hole outlet. Thus, the collapsing part of the cavity reduces its size and the collapse as well as the combination of shock and rarefaction weakens. Consequently, the vapour volume of the recreated vortex cavitation reduces as well. As a conclusion, the integrated vapour volume reduces its amplitude because the stable part of the cavity increases while the unstable cavitation pockets decrease. This explains the asymptotic behaviour of V_{vap} in **Fig. 3** (bottom).

At time t=$1.1\cdot10^{-4}$ *s* the repetition is no longer possible, vortex cavitation is no longer present and the complete hydrodynamic cavity is stable. The flow field reaches a steady state and thus vapour volume and mass flows remain constant. In **Fig. 7** the resulting void fraction distribution at the centre cut of the injector is presented. For the same instant in time we isolate the cavity structure to study their shape in detail (**Fig. 8**). At the bore hole inlet the vapour pocket is nearly circular shaped. Slightly downstream of the inlet the structure is confined to the upper part of the spray hole. Although the shape of the cavity varies along the flow direction, the covered area is almost constant for each cross section of the bore hole (Hiroyasu et al., 1991).

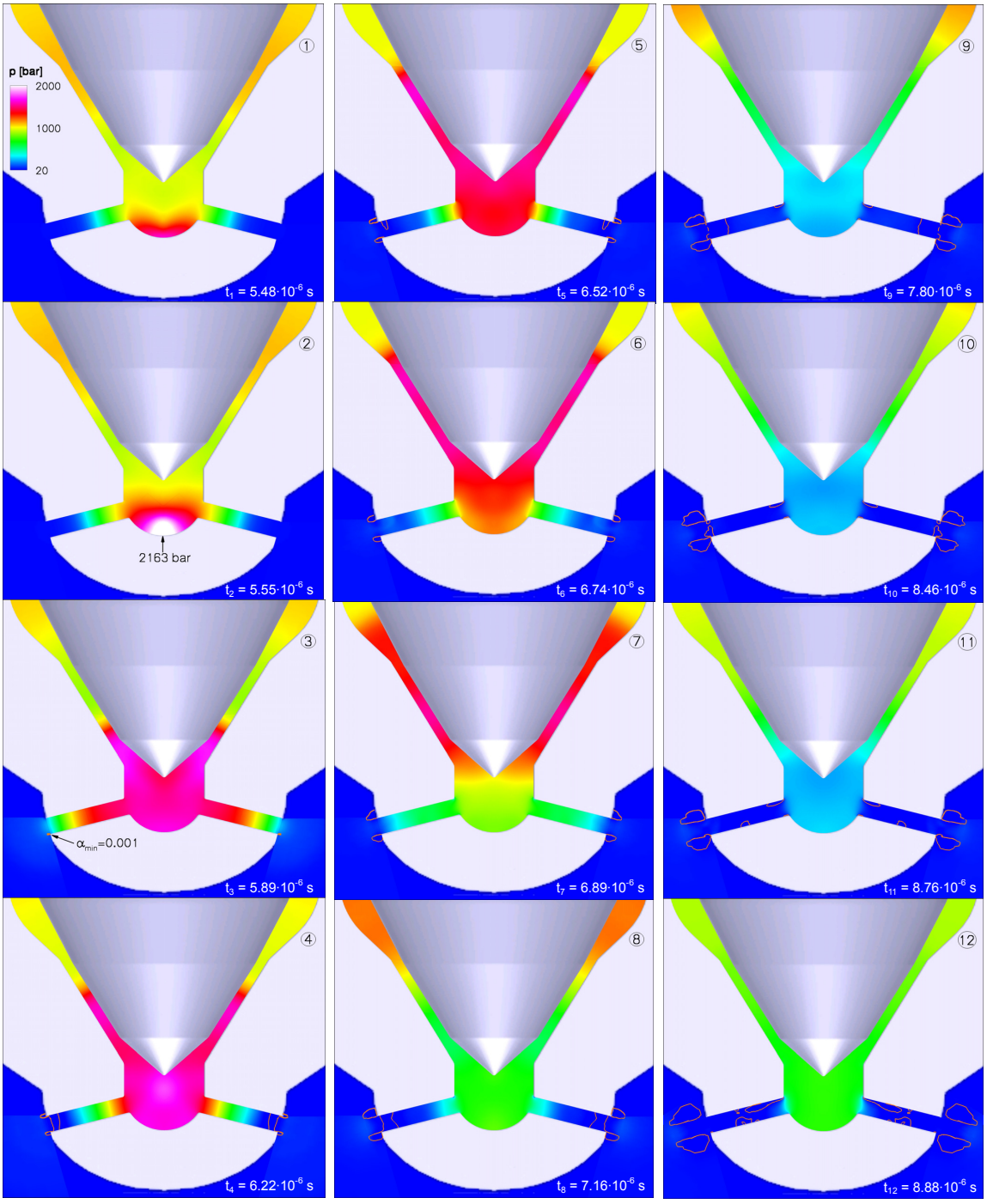

Figure 5: Pressure field in the vicinity of the bore holes for the time interval $\Delta t_{1\text{-}12} = 4.41 \cdot 10^{-6}$ *s*. Orange lines indicate iso-values of constant void fraction of $\alpha_{min} = 0.001$. $p_{in} = 600$ *bar*, $p_{out} = 26$ *bar*, $T_{init} = 333$ *K*, $\Delta t_{CFD} = 10^{-10}$ *s*.

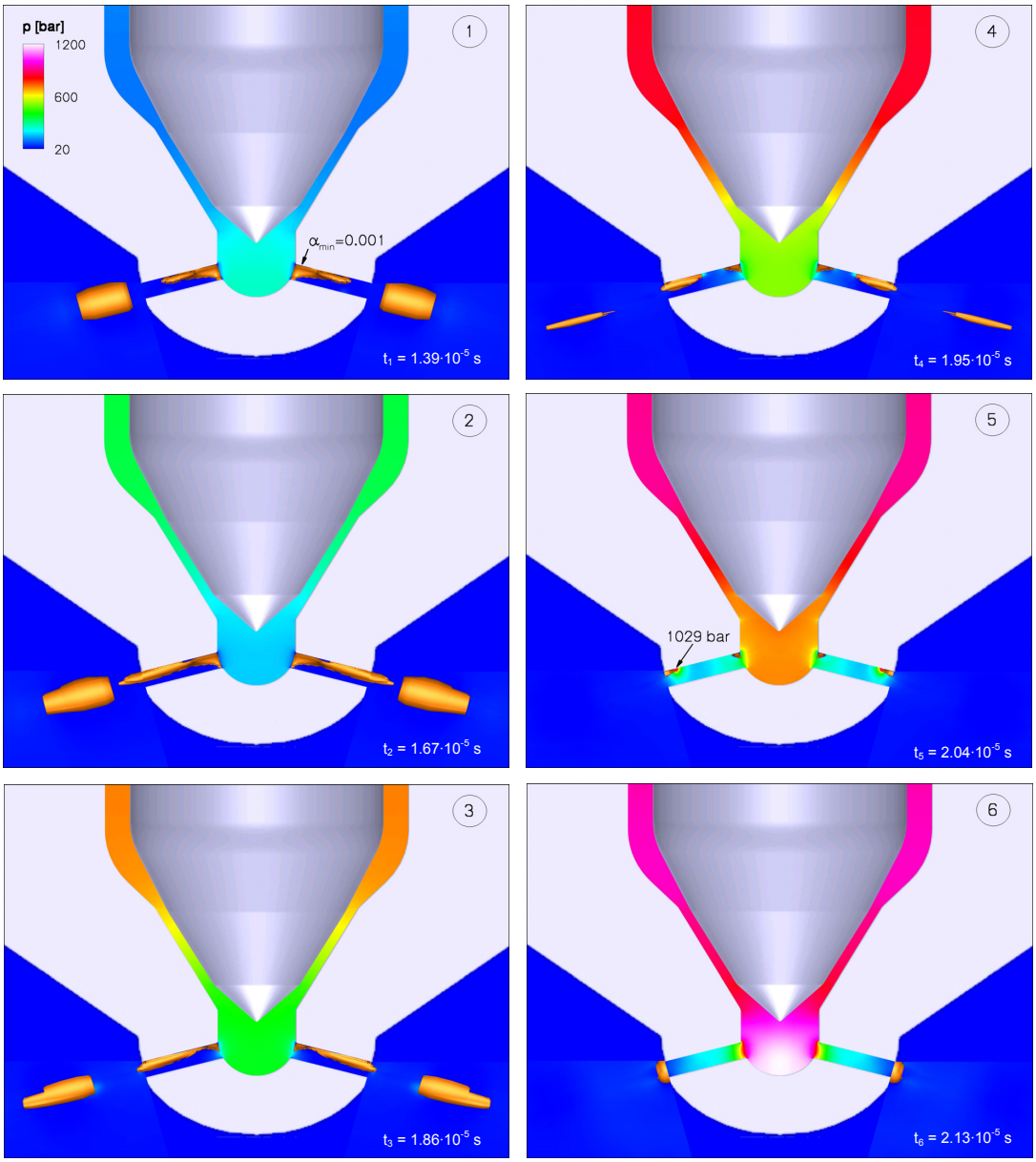

Figure 6: Growth and collapse of hydrodynamic cavity during the time interval $\Delta t_{1\text{-}6}$= 7.40·10^{-6} *s*. Orange surfaces indicate iso-surfaces of the cavity with a minimum void fraction of α_{min}=0.001. Picture 5 shows the maximum instantaneous pressure p_{max}=1029 *bar*.
p_{in}=600 *bar*, p_{out}=26 *bar*, T_{init}=333 *K*, Δt_{CFD}=10^{-10} *s*.

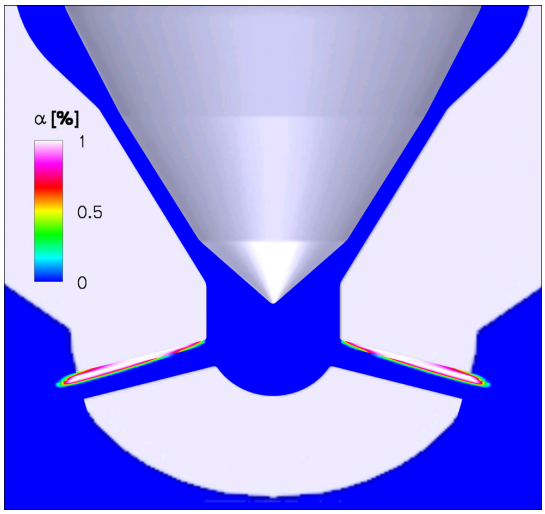

Figure 7: Steady-state cavitation pattern inside the bore holes at $t \geq 10^{-4}$ *s*. p_{in}=*600 bar*, p_{out}=*26 bar*, T_{init}=*333 K*, $\Delta t_{CFD}=10^{-10}$ *s*.

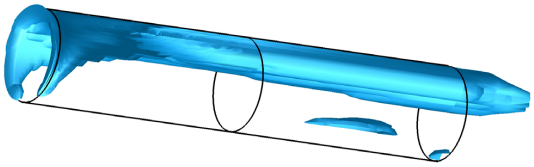

Figure 8: Isolated 3-D view of the cavitation pattern inside the bore holes at $t \geq 10^{-4}$ *s*. Flow from left to right. p_{in}=*600 bar*, p_{out}=*26 bar*, T_{init}=*333 K*, $\Delta t_{CFD}=10^{-10}$ *s*.

In the following subsection, the influence of the prescribed inlet pressure p_{in} on the steady state mass flow is discussed. Therefore, a reference mass flow $\dot{m}_{ref}$ is calculated by the Bernoulli equation. Assuming that the fluid is pure water with constant density ρ we find for the reference mass flow

$$\dot{m}_{ref} = A_{in} \cdot A_{out} \cdot \sqrt{\frac{2 \cdot \rho \cdot (p_{in} - p_{out})}{A_{in}^2 - A_{out}^2}}.$$

In combination with the numerically obtained mass flow a relative mass flow defect due to cavitation is defined as

$$\Delta\dot{m} := \frac{\dot{m}_{ref} - \dot{m}_{num}}{\dot{m}_{ref}} \cdot 100\%.$$

Table 1 presents the relative mass flow defect for different inlet pressures, while the outlet pressure is kept constant at p_{out}=*26 bar*. For the simulated conditions the relative defect is approximately *24%*. This defect can be interpreted as a *24%* reduction of the outlet area (Numachi et al., 1960). Our simulation results confirm this interpretation as they show for all cases a virtually identical vapour domain that covers an area of about *24%* as shown in **Fig. 9**. It should be pointed out that the reference mass flow is based on 1-D inviscid theory.

Our 3-D simulations neglect viscous effects as well, and hence, the mass flow defect is exclusively caused by the contracting effect of cavitation. The inclusion of viscous effects might lead to an even further reduction of the discharge of the nozzle.
Subsequently to the inlet pressure variation we vary p_{out} while keeping p_{in}=*600 bar* constant. It is known that for sufficiently large pressure differences $\Delta p = p_{in} - p_{out}$ no further increase of the mass flow is achievable, even if the outlet pressure is significantly decreased (Randall, 1952). We simulate a series of outlet pressures of *60*, *40*, *26* and *15 bar*. In all cases the numerically obtained mass flows are equal while the integrated vapour volume V_{vap} accordingly increases. However, as the outlet velocity scales with the square root of the pressure difference, the observed increase of the vapour volume is of the order of less than *1%* for each reduction step of the outlet pressure.

p_{in} (bar)	$\dot{m}_{ref}$ (g s^{-1})	$\dot{m}_{num}$ (g s^{-1})	$\Delta\dot{m}$ (%)
100	27.7	21.3	23.1
200	42.5	32.1	24.5
400	62.3	47.4	24.0
600	77.4	58.8	24.0
1000	100.8	75.9	24.7
1200	110.7	84.8	23.4
1400	120.1	90.3	24.8

Table 1: Comparison of estimated mass flow for pure water and numerically observed mass flow in the presence of cavitation for a series of inlet pressures. The outlet pressure p_{out}=26 bar is kept constant.

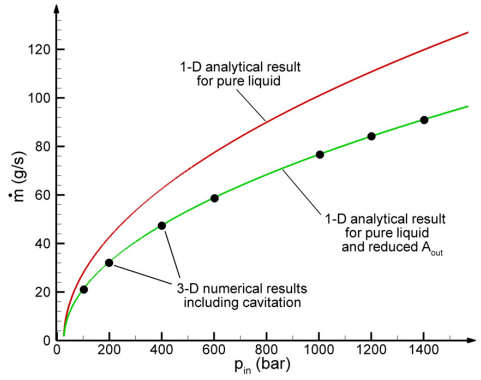

Figure 9: Influence of the outlet area reduction of 24% with respect to the analytically obtained mass flow. Points represent numerically obtained mass flow rates including the contractive effects of cavitation.

Conclusions

A 3-D time accurate numerical method which enables highly resolved simulations of liquid flows with phase transition is proposed. The scheme is applied to simulate the flow field inside a realistic 3-D fuel injector for a series of operating conditions. All numerical results match the experimental observations (Roosen et al., 1994, Busch, 2001). The importance of the compressible treatment of the governing equations is manifested by the detection of wave dynamics as essential feature of the temporal flow development. Special emphasis is put on the time history of the mass flow and of the vapour volume. During the first 10^{-4} s both quantities undergo massive variations. Especially for pilot or multi-point injections the observed highly unsteady flow characteristics dominate. Acoustic, hydrodynamic and vortex cavitation patterns are presented. A violent collapse inside the bore hole is resolved and the occurring shock wave is analysed in its strength. Although the outlet pressure is p_{out}=*26 bar*, a maximum instantaneous pressure of more than *1000 bar* is observed. Finally, the arising cavitation pocket inside the spray hole is presented and the resulting nozzle discharge is analysed.

Acknowledgements

This work was partially supported by Deutsche Forschungsgemeinschaft (DFG) under SCHN 352/16-3.

References

Alajbegovic A., Meister G., Greif D. & Basara B., 'Three phase cavitating flows in high-pressure swirl injectors', Experimental Thermal and Fluid Science Vol. 26, pp 677-681, 2002.

Berg A., Iben U., Meister A. & Schmidt J., 'Modeling and simulation of cavitation in hydraulic pipelines based on the thermodynamic properties of liquid and steam', Shock Waves Vol. 14, pp. 111-121, 2005.

Brennen C.E., 'Cavitation and bubble dynamics', Oxford University Press, 1995

Busch R., 'Untersuchung von Kavitationsphänomenen in Dieseleinspritzdüsen', Ph.D. thesis, Fachbereich Maschinenbau, Universität Hannover, 2001.

Delale C.F., Schnerr G.H. & Pasinlioglu S., 'Model evolution equations for unsteady cavitating nozzle flows and their applications', Proceedings of the 6th Inter. Symp. on Cavitation, Wageningen, The Netherlands, 2006.

Franc J.P. & Michel J.M., 'Fundamentals of cavitation', Fluid mechanics and its applications, Kluwer Academic Publishers, 2004.

Godunov S.K., 'A difference scheme for numerical computation of discontinuous solution of hydrodynamic equations', Math. Sbornik Vol. 47, pp. 271-306, 1959.

Guillard H. & Viozat C., 'On the behaviour of upwind schemes in the low Mach number limit', Computers & Fluids Vol. 28, pp. 63-86, 1999.

Hiroyasu H., Arai M. & Shimizu M., 'Break-up length of a liquid jet and internal flow in a nozzle', ICLASS-91 Gaithersburg, MD, July, 1991.

Hoeijmakers H.W.M., Janssens M.E. & Kwan W., 'Numerical simulation of sheet cavitation', 3rd International Symposium on Cavitation, Grenoble, France 1998.

Iben U., Wrona F., Munz C.-D. & Beck M., 'Cavitation in hydraulic tools based on thermodynamic properties of liquid and gas', J. Fluids Engineering Vol. 124, pp. 1011-1017, 2002.

Numachi F., Yamabe M. & Oba R., 'Cavitation effect on the discharge coefficient of the sharp-edged orifice plate', Journal of Basic Engineering, March, 1960.

Randall L.N:, 'Rocket applications of the cavitating venturi', ARS Journal, Jan-Feb, 1952.

Roosen P., Kluitmann S. & Knoche K.-F., 'Untersuchung und Modellierung des transienten Verhaltens von Kavitationserscheinungen bei ein- und mehrkomponentigen Kraftstoffen in schnell durchströmten Düsen', Abschlußbericht zur ersten Antragsperiode des DFG-Schwerpunktprogramms "Transiente Vorgänge in mehrphasigen Systemen mit einer oder mehreren Komponenten, Aachen, 1994.

Rudy D.H. & Strickwerda J.C., 'A non-reflecting outflow boundary condition for subsonic Navier-Stokes calculations', J. Computational Physics Vol. 36, pp. 55-70, 1980.

Schmidt S., Sezal I. & Schnerr G.H., 'Compressible simulation of high-speed hydrodynamics with phase change', ECCOMAS CFD, European Conference on Computational Fluid Dynamics, The Netherlands, 2006.

Schnerr G.H., Schmidt S.J., Sezal I.H. & Thalhamer M., 'Shock and Wave Dynamics of Compressible Liquid Flows with Special Emphasis on Unsteady Load on Hydrofoils and on Cavitation in Injection Nozzles', Invited Lecture. In: Proceedings CAV2006 - Sixth International Symposium on Cavitation, Wageningen, The Netherlands, CD-ROM publication, 2006.

Yuan W. & Schnerr G.H., 'Cavitation in injection nozzles - effect of injection pressure fluctuations', Proceedings of the 4th Inter. Symp. on Cavitation, CALTECH, Pasadena, USA, 2001.

Yuan W. & Schnerr G.H., 'Numerical simulation of two-phase flow in injection nozzles: Interaction of cavitation and external jet formation', J. Fluids Engineering Vol. 125, pp.963-969, 2003.

Wrona F., 'Simulation von kavitierenden Strömungen in Hochdrucksystemen', Ph.D. thesis, Institut für Aerodynamik und Gasdynamik, Universität Stuttgart, 2005.

Zierep J., 'Theoretische Gasdynamik', G. Braun, Karlsruhe, reprint of 3rd ed., 1991.

C. Third publication

The third publication [64] contains numerical analysis of the cavitating flow around a twisted NACA0015 hydrofoil in a rectangular test-section. Due to twisting, the sheet cavity does not reach the sidewalls of the test-section, wherefore typical interactions of boundary layers with the cavity are omitted [23]. First, a cyclic shedding process and experimentally detected "side entrant jets" are discussed. Time histories of lift and drag as well as instantaneous surface pressures are analyzed. The results confirm that high impulse loads are generated by collapse induced shock waves. Furthermore, the necessity to use a fully compressible numerical method and a sufficiently high time resolution of 10^{-7} seconds for this characteristic length scale is shown. Even though the characteristic velocity is just $12\ m/s$, the resolution of wave propagation requires time steps based on the speed of sound of the liquid.

Discrepancies in maximum pressures, which are also found in the experiments, are related to the transducer sampling frequencies. This correlation is demonstrated by gradually down-sampling of high resolution numerical data.

Load-intensive domains can be detected from the pressure foot prints on the surface of the hydrofoil obtained numerically. This information enables the prediction of erosion endangered areas already during the design process.

I generated the grid, performed the simulations, analyzed the results and prepared the manuscript.

Proceedings of the 8th International Symposium
on Experimental and Computational
Aerothermodynamics of Internal Flows
Lyon, July 2007
Paper reference: ISAIF8-0044

Shock Waves as Driving Mechanism for Cavitation Erosion

S.J. Schmidt, I.H. Sezal, G.H. Schnerr and M. Thalhamer

Technische Universität München, Faculty MW, Boltzmannstraße 15, D-85748 Garching, Germany
e-mail: schmidt@flm.mw.tu-muenchen.de
homepage: http://www.lhm.mw.tu-muenchen.de/gd/

The purpose of this study is the detailed numerical analysis of shock waves arising in cavitating liquid flows. Therefore, our recently developed CFD code CATUM is used to simulate the highly unsteady two-phase flow around a three dimensional twisted hydrofoil. The selected geometry is representative for pump and turbine blades as well as for ship propellers and allows the detailed study of sheet and cloud cavitation patterns. Special emphasis is put on the correlation of the time dependent void fraction distribution and the pressure field frequency spectrum. Thereby, recondensation induced shock waves are identified and analysed in their strength and their development. In order to relate our numerical results to measurement data, gradually downsampling to typical experimental sampling frequencies is performed. The resulting maximum static pressures for each sampling frequency are in excellent agreement with several comparable experimental setups and prove the necessity of using high frequency sensors to record the correct orders of magnitude. Finally, a detailed analysis of complete cycles of the pressure dynamics on the surface of the hydrofoil is presented and regions of instantaneous peak loads, which result in cavitation erosion, are obtained.

Keywords: Cavitation, Shock wave, Erosion, Phase transition, Riemann-solver

Introduction

The break up of a sheet cavity often leads to the separation of a liquid embedded cluster of vapour bubbles. This flow type, commonly known as cloud cavitation, typically arises around pump or turbine blades as well as around ship propellers and results in strong noise production and erosion. The main mechanism of both effects is the collapse-like recondensation of the vapour content which includes the formation of complex shock wave configurations.

The collapse mechanism for a single isolated bubble has been extensively studied both theoretically and experimentally by several research groups [1-4]. One main result is the possibility of collapse induced shock formations. Experimental observations indicate a comparable behaviour for bubble clouds as well, in spite of being much more complicated due to various bubble-bubble interaction processes. However, the reported maximum intensity of those shock waves not only varies according to the operating conditions for a given setup but it seems to be strongly dependent on the properties of the selected measurement equipment, especially on the sampling frequency and the transducer location. The range of maximum instantaneous pressure variations reported in the literature covers the huge

S.J. Schmidt: Research scientist

interval of *O(1) bar* to *O(100) bar*. In order to improve the understanding of cavitation erosion it seems inevitably necessary to separate deviations caused by different measurement techniques from those related to different flow patterns arising during the shedding cycle. Reisman et al. [5] therefore introduced a classification into local and global shock events according to their flow dynamic origin. The local ones are associated with the less coherent collapse of vapour clouds and are termed 'crescent-shaped regions' and 'leading-edge structures'. Contrary to the previously mentioned local events, the collapse of a well-defined and separate cloud leads to a global one when the vapour structure is convected into a region of higher pressure.

This investigation contains numerical studies of the cavitating flow field around a 3-D twisted hydrofoil. Therefore, we present the time-dependent vapour structure and correlate lift and drag variations. Special emphasis is put on a high resolution pressure analysis on the surface of the hydrofoil in order to get insight into collapse induced shock formations and their specific properties such as shock strength and impact time. Finally, the pressure signal close to the exit plane of the numerical domain is analysed and its frequency spectrum is given.

Mathematical Model and Numerical Approach

Mathematical model

In order to predict and explain wave dynamic effects in two-phase flows a fully coupled compressible mathematical formulation of the 3-D time-dependent governing equations of inviscid fluid motion is applied [6]. Instead of resolving the coupled physics for thousands of individual bubbles we describe an integral average behaviour of a bubbly liquid in small finite domains, commonly referred as homogeneous mixture approach. The thermodynamic properties are expressed by thermal and caloric equations of state for water and water vapour, together with temperature dependent saturation conditions in arising two-phase domains. The speed of sound is derived from the fluid specific equation of state and describes equilibrium properties in domains of saturated liquid/vapour flow. The model is hence independent of any additional parameters and can be applied to various fluids as well.

Numerical approach

The hyperbolic character of the arising governing equations motivates the choice of a Godunov method [7] as basic solution strategy. Approximate solutions to the non-linear reconstructed Riemann problem over each cell face are used to describe the fluxes for the unsplit finite volume method. A modified pressure flux definition is introduced into the Riemann-solver to maintain accurate solutions for smooth flow, especially for regions of low speed pure liquid flow [8]. To advance the conserved quantities in time, an explicit 4-stage Runge Kutta method is applied. The resulting numerical approach CATUM (CAvitation TU Munich) is second order accurate in space and time.

As our major research interest contains strong wave dynamic aspects we apply numerical time-steps in the order of 10^{-8}-10^{-7} seconds. Significantly larger step sizes would act like a filter on the propagation of the high frequency genuinely non-linear waves. A grid refinement study was performed in order to exclude strong mesh dependence of the solutions. On the finest grid we use three different time-step sizes according to *CFL* numbers of *1.5*, *1.0* and *0.5*. All configurations of time and space discretizations give highly comparable results. Relative deviations in lift and drag, measured in l^2-*norm*, are smaller than *1 ‰* for the selected time steps. The relative deviation of the mean shedding frequency is of the same order for both grids. This indicates that further grid refinement will not lead to qualitatively different structures. Nevertheless, a higher spatial resolution is expected to give more detailed fine-structures for the separated clouds and a sharper phase boundary of the sheet cavity.

Geometry definition and grid properties

It is known form experiments [9] that the interaction of cavitation with the sidewalls of the test-section often leads to rather stochastic cavitation patterns without well-defined and repeatable structures. To avoid strong sidewall effects a twisted geometry was designed which leads to well defined cavitation patterns for a certain range of operating conditions [10, 11]. Therefore a NACA 0015 profile with cord length *c=0.15 m* is turned around its middle point to obtain a varying angle of attack from *-3°* at the side walls to *+6°* at midspan. The resulting foil is placed in the middle of a rectangular test-section with length *0.6 m* and quadratic cross section of *0.3 x 0.3* meters as sketched in **Fig. 1**.

As the geometry is symmetric to the midspan-plane the simulation is performed in one half of the domain. The implied assumption of flow symmetry is verified in the experiments of Foeth et al [12].

The grid for the simulated half-foil is an O-grid with sufficient high resolution close to the foil, consisting of *75000* hexahedrons for the finest case. For parallelization purposes the grid is divided in *8* equally large blocks and calculated on *8* processors. The calculation time could thereby be reduced to *24* hours per shedding cycle.

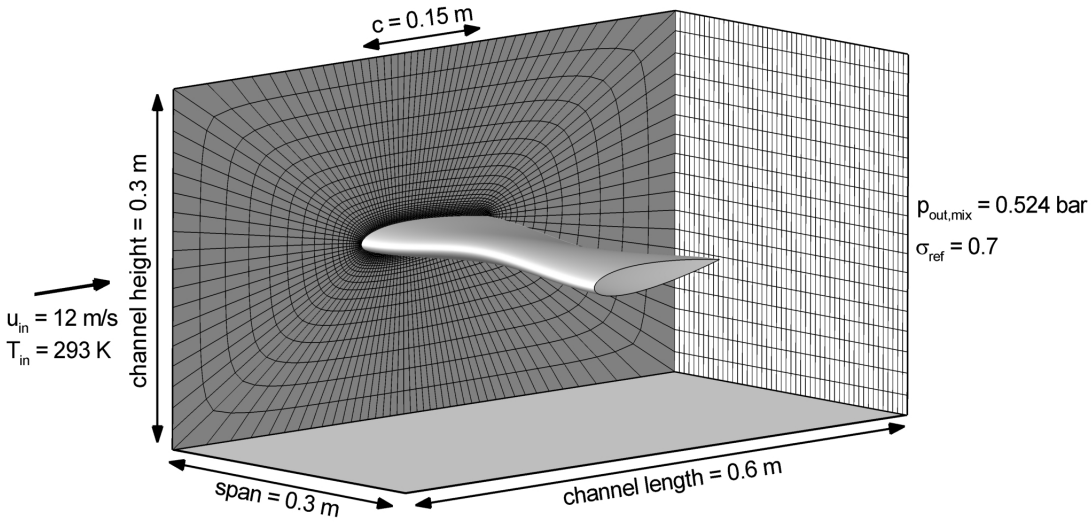

Fig. 1 Computational domain and boundary conditions;
Fluid: water, coming from left;
Hydrofoil: NACA 0015, angle of attack is *-3°* (walls) and *+6°* (midspan).

Initial and boundary conditions

The selected geometry requires the definition of inflow, outflow and wall boundary conditions. We use two ghost-cells to maintain 2^{nd} order accuracy on the boundaries as well. All walls and the foil surface are treated as adiabatic, inviscid and impermeable. The inflow conditions define pure water with fixed inlet velocity $u_{in}=12\ m/s$ parallel to the test-section and fixed static temperature $T_{in}=293\ K$. The outflow conditions consist of asymptotically matching non-reflecting conditions [6]. The static pressure at the outflow cross section is not fixed but will asymptotically reach an average value of $p_{out,mix}=0.524\ bar$. Together with these quantities we define the reference cavitation parameter $\sigma_{ref}=0.7$ as a time average property but not as a constant state.

The initialization of the domain is achieved by a steady state solution of the single-phase pure water simulation by applying the same boundary conditions as for the two-phase simulation. As the time-dependent character is a major part of the cavitating flow we compared the long-time behaviour of the resulting solutions for different initial conditions. In all cases the obtained shedding frequency and the qualitative flow character matched very well, so we suggest that the selected geometry together with the boundary formulation provides a unique and repeatable global flow character.

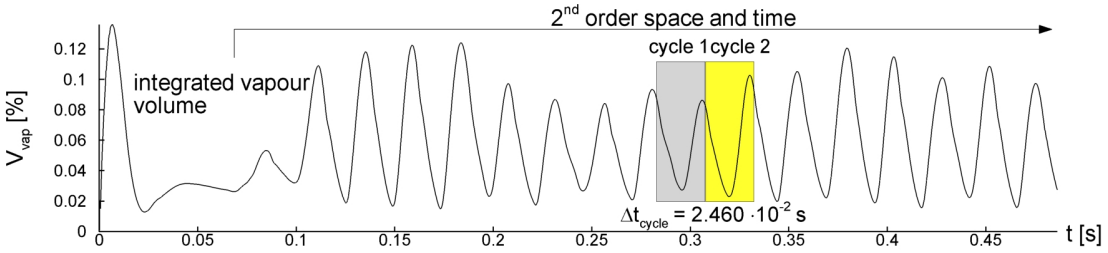

Fig. 2 Total vapor volume V_{vap} integrated over the computational domain for the complete time-accurate simulation. Investigated cycles 1 and 2 are highlighted.

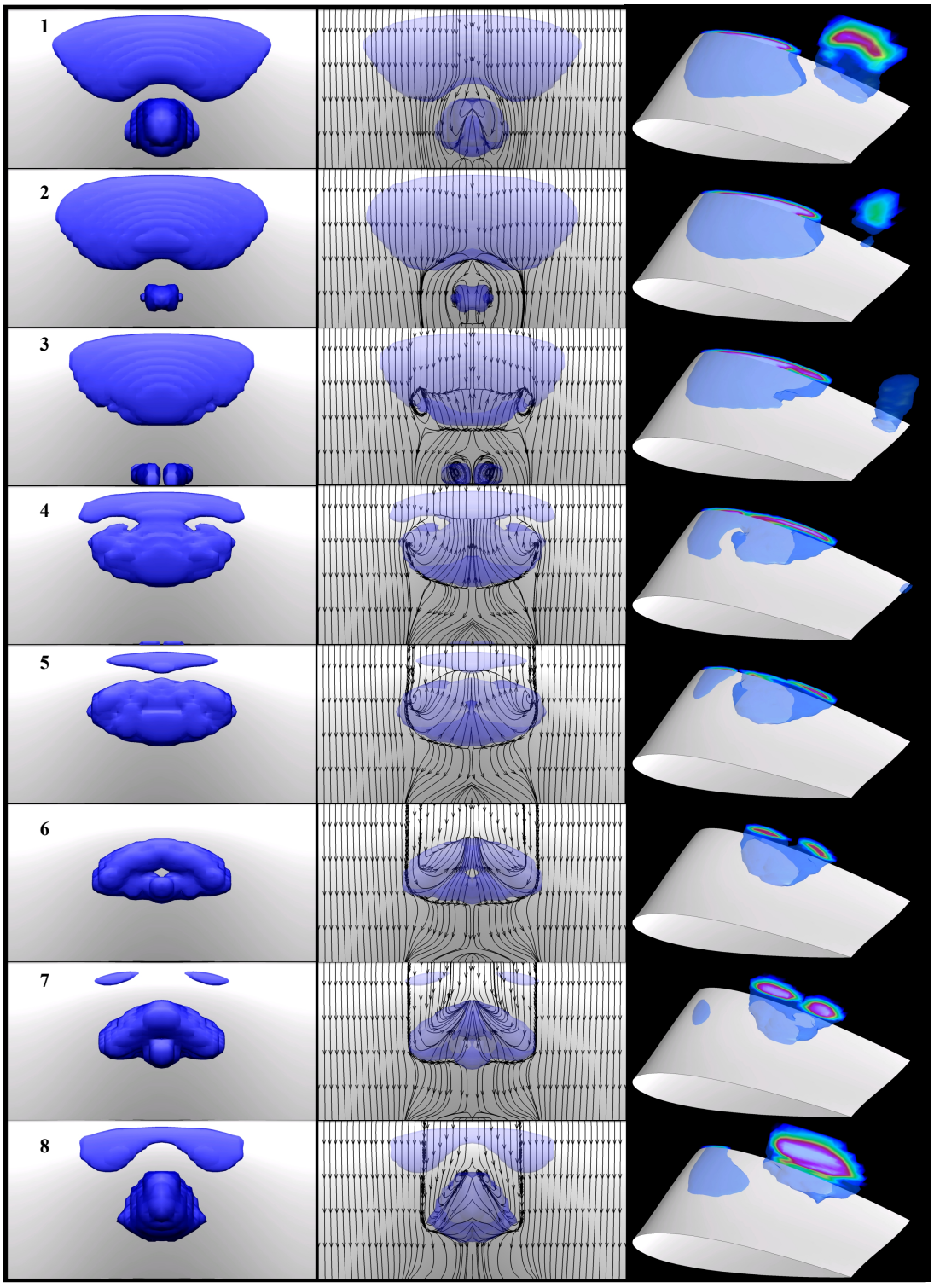

Fig. 3 Cavitation cycle 1 - visualized by iso-surfaces of a void fraction α=5 % together with instantaneous stream traces.

Computational Results

Vapour structure and shedding cycle

Figure 2 depicts the development of the integrated vapour volume V_{vap}. After a short transitional time a regular structure with mean frequency $f=40.65\ Hz$ is established. Although the frequency is only slightly varying within the range of $\pm 1.5\ Hz$, the amplitude of the curve shows larger variations. In order to highlight possible variations as well as common aspects the following analysis will focus on cycle 1 and cycle 2.

To give an impression of the cavitation development eight representative instants in time for cycle 1 are plotted. **Figure 3** contains a top-view of the hydrofoil showing iso-surfaces of the void fraction $\alpha=5\ \%$ (left column) as well as plots of instantaneous stream traces (middle column) and a perspective view from the left side to the midspan plane (right column).

The first instant in time resembles a triangular shaped attached sheet cavity and a nearly spherical cloud. The stream traces indicate that the re-entry jet has not yet reached the sheet, but in the perspective view a slight detachment of the cavity closure region is already visible. The maximum length for the fully attached sheet is $0.07\ m$ (roughly half cord length). The second and third time instants show the downstream convection of the cloud and the formation of reverse flow below the sheet cavity. In time instants (4) and (5) the re-entry jet is no longer formed by pure reverse flow but includes a significant spanwise velocity component. Spiral singularities indicate the formation of vortices. Time instance (6) contains a fully wetted leading edge and a horseshoe-like cavitation cloud. At instance (7) and (8) the upstream part of the cloud overtakes the downstream part, leading to a reunification of the vapour structures to a single spherical cloud. The sheet on the leading edge develops and the cycle starts from the beginning.

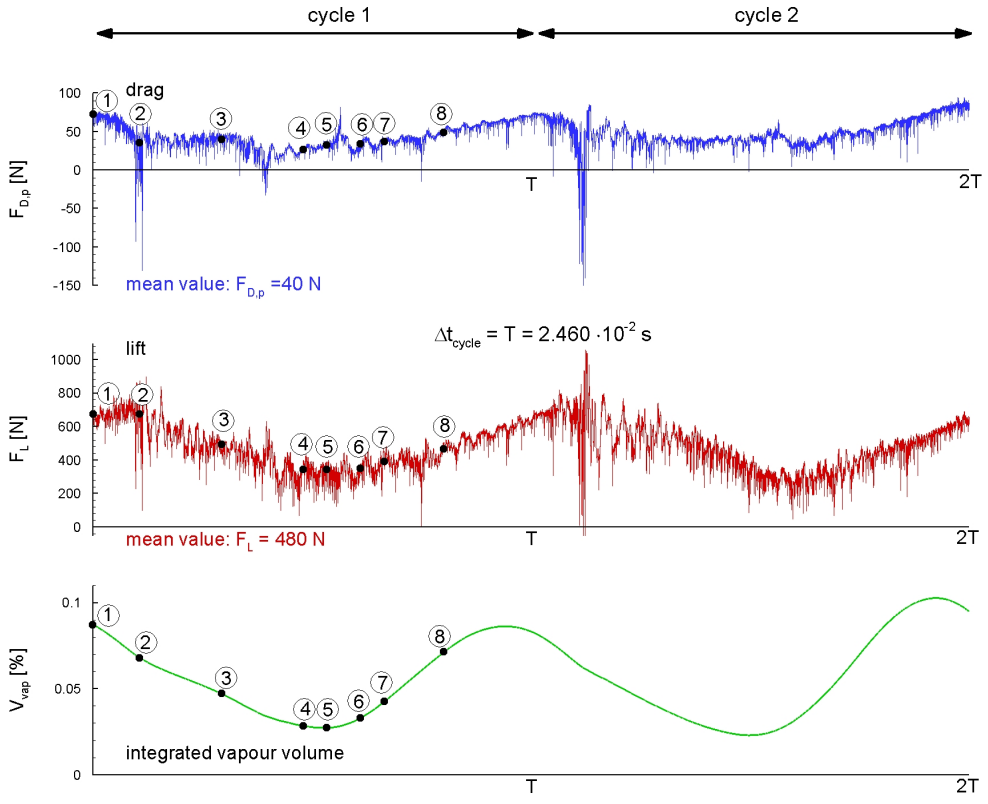

Fig. 4 Time history of drag force $F_{D,p}$ *[N]*, lift force F_L *[N]* and integrated vapour volume V_{vap} of cycles 1 and 2; The emphasized numbers correspond to the *8* instants in time presented in **Fig. 3**.

Lift and drag forces

The dynamic behaviour of the shedding process results in strongly time-dependent lift and drag forces (**Fig. 4**). Both curves contain significant decreases of lift and drag including negative values corresponding to time instant (2) in **Figure 3**. A detailed analysis of the flow field at this stage of the shedding cycle is given by Schnerr et al [6]. Thereby, the collapse of the small vapour cloud located between the foil surface and the main cloud was found to result in a shock wave that increases the surface pressure on the suction side close to the trailing edge of the foil. The shock wave leads to maximum instantaneous surface pressures of *84 bar* in cycle 1 and *133 bar* in cycle 2. This difference is related to slightly varying void fraction distributions. To show the influence of the shedded structures on the shock wave strength and thus on the surface pressure of the foil, we record the maximum surface pressure for each computational cell during cycle 1 (**Fig. 5**, top) and cycle 2 (**Fig. 5**, bottom). The plots demonstrate that the most violating collapse in cycle 1 is close to midspan position (**Fig. 5** top, location B) while the maximum shock wave impact is noticeably dislocated in cycle 2 (**Fig. 5** bottom, location C). In order to understand this cycle-dependent behaviour we analyse the vapour structure of 7 cycles. The already obtained results indicate an almost alternating collapse behaviour comparable either to cycle 1 or to cycle 2.

Surface pressure analysis

A more detailed analysis of the time dependent static pressure requires the definition of "numerical pressure transducers". We therefore record the static pressure during cycle 1 of all computational cells located on the hydrofoil and of one finite volume located close to the outflow plane. The size of our numerical transducers is thus the computational cell size, which covers a surface area of about *12 mm*^{2} *(2 x 6 mm*) on the hydrofoil. In comparison with real sensors this area is relatively large, resulting in a spatial averaging of local events. The main advantage of numerical sensors is their high time resolution. As our numerical time-step is given by Δt_{CFD}*=5.5 x 10*$^{-8}$ *s*, the numerical sampling frequency turns out to be *18 MHz*. This numerical sampling frequency is based on the requirement that even the fastest signals (shock waves) are not allowed to travel further than half of the distance defined by the shortest edge length of any finite volume. Hence, all time-scales of the physical model are fully resolved without aliasing effects. Moreover, numerics are not limited within a certain range of static pressures that can be accurately recorded by the transducers. In order to model the temporal averaging of sensors with lower sampling rate we define top-hat filtered time average values according to the following mapping

$$p_\delta(t) := \frac{1}{\delta}\int_{t-\delta/2}^{t+\delta/2} p(\tau)\, d\tau$$

Here, δ is the reciprocal value of the desired reduced sampling frequency f_{sample} and represents the width of the top-hat window. The purpose is to study the dependence of the maximum recorded pressure and its impact time with respect to sampling frequencies of real transducers. Therefore, we start with the numerical pressure data obtained with f_{sample}*=18 MHz* recorded at point B of cycle 1 (**Fig. 6** top). As stated before, a significant peak occurs at *t=T/10*, corresponding to time instance (2) in **Fig. 3**. Besides the occurrence of small peaks with p_{max}*<5 bar* around *t=T/4* no further deviation from the expected pressure is visible. It should be noted that the scaling of the ordinate of **Fig. 6** does not permit the visualization of weak pressure variations although they are present throughout the cycle. A strong magnification of the maximum peak is given in **Fig. 6** (bottom), where the squares represent discrete samples obtained by the numerical transducer. Here, the impulsive pressure rise is fully resolved and a sudden increase from *p=0.02 bar* to *p=84 bar* within *10*$^{-6}$ *s* is observed. The decay time is -for this event- defined as the time interval which is needed to relax the pressure from p_{max} to *p<2 bar*. This definition leads to a duration of *8 x 10*$^{-6}$ *s* and an impulse strength of *23.7 Pa s*. The effects of reducing the sampling frequency can be seen in the two pictures in the middle of **Fig. 6**, where the upper one resembles the pressure signal obtained with f_{sample}*=100 kHz* and the lower one the corresponding signal for f_{sample}*=20 kHz*. The following table gives an overview of the resulting p_{max} together with duration and impulse strength for various sampling frequencies.

f_{sample}	p_{max}	duration	impulse strength
18 MHz	84 bar	8.0 x 10^{-6} s	23.7 Pa s
100 kHz	22 bar	1.4 x 10^{-5} s	22.3 Pa s
20 kHz	5 bar	5.0 x 10^{-5} s	22.5 Pa s
2 kHz	1 bar	5.0 x 10^{-4} s	25.3 Pa s

Table 1 Influence of sampling frequency f_{sample} on p_{max} as well as on duration and resulting impulse strength.

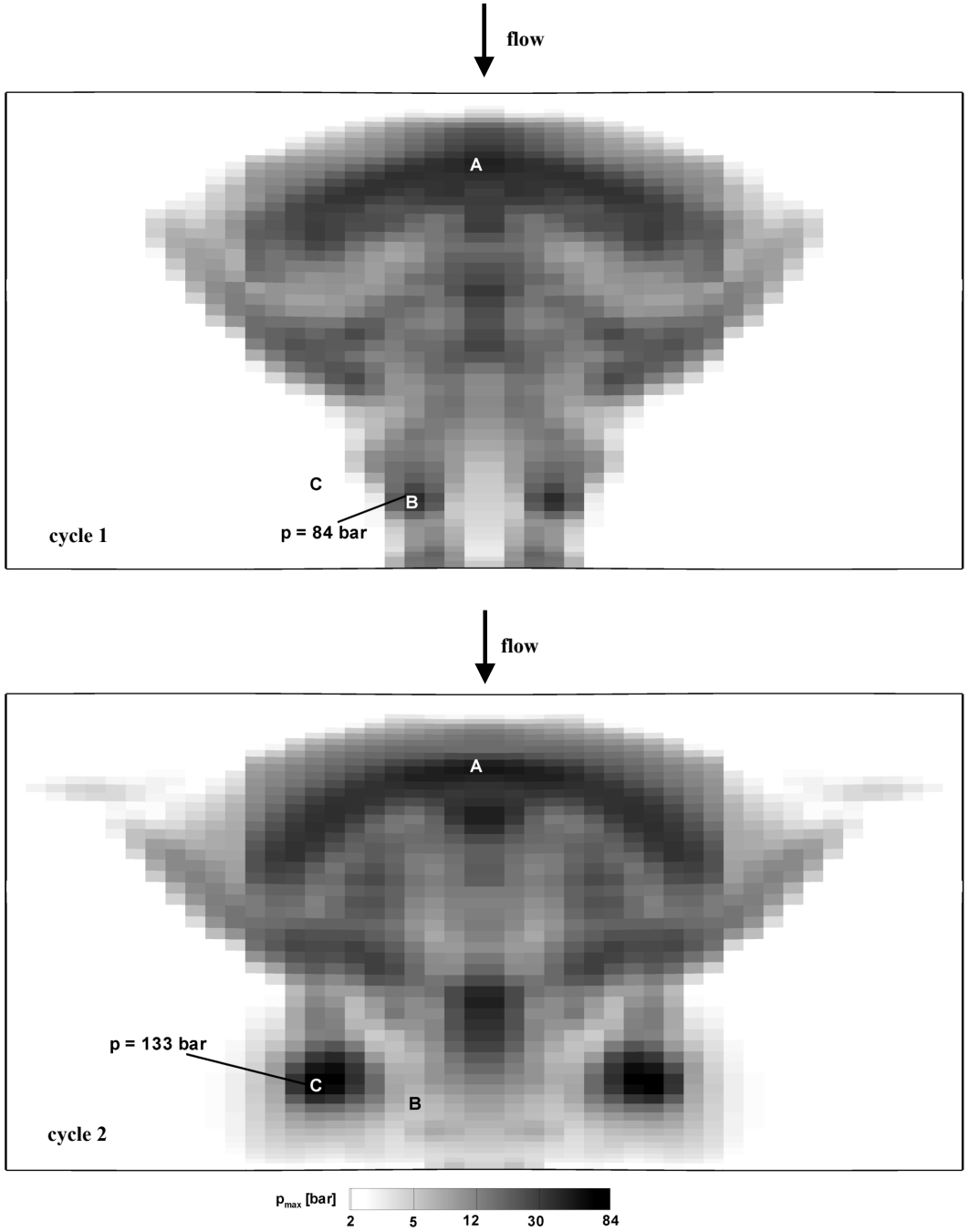

Fig. 5 Cell wise recorded maximum static pressure during **cycle 1 (top)** and during **cycle 2 (bottom)**. In both pictures the maximum instantaneous static pressure occurs on the upper surface (suction side) of the hydrofoil, close to the trailing edge. The spanwise position varies from cycle to cycle in an alternating manner. The collapse of the leading edge cavity produces in both cases maximum static pressures of the order of *40 bar* (point A).

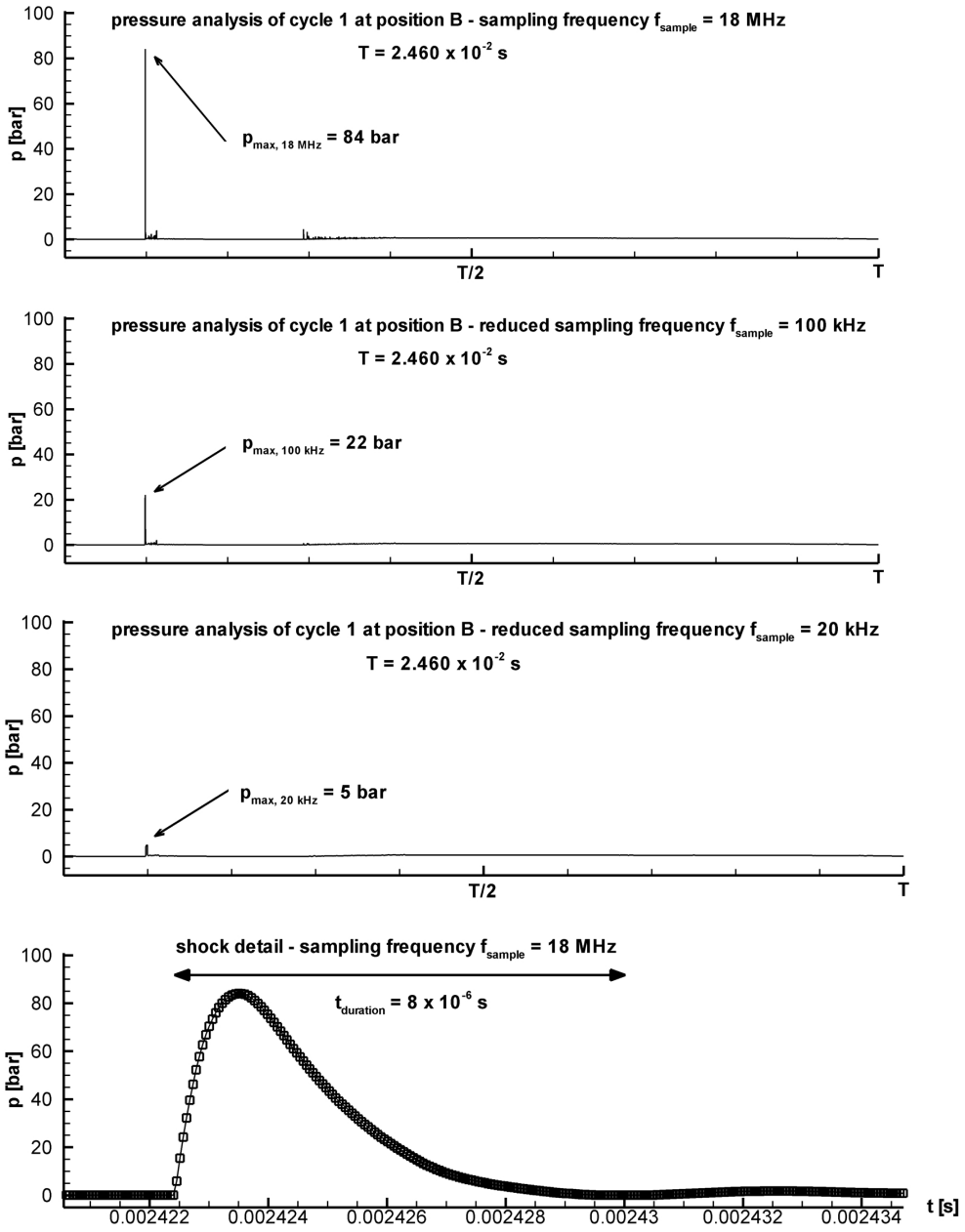

Fig. 6 Pressure signal at point B of cycle 1 for three sampling frequencies and magnified shock detail. From top to bottom: Signal obtained by sampling frequencies f_{sample}=*18 MHz*, f_{sample}=*100 kHz*, f_{sample}=*20 kHz*. Lowermost picture shows magnified rise and decay of the p_{max} impulse as recorded in the *18 MHz* sample.

The results presented in **Table 1** indicate that the impulse strength behaves nearly invariant under the defined low pass filter. While the observed maximum static pressure is successively reduced due to insufficient time resolution, the duration time grows according to the smoothing effect of the filter. Although we present this analysis only for cycle 1 at point B, our numerical studies for different locations confirm this behaviour without exception.

A quantitative comparison of our numerical results with experimental data obtained from various cloud cavitation patterns fully supports our study. Le et al [13] give pulse magnitudes in the order of *70 bar* (natural transducer frequency *1.7 MHz*) while Shen and Peterson [14] reported pulses only in the order of *1 bar* (sampling frequency *2 kHz*). Another detailed experimental study was performed by Reisman et al [5] where different transducers where applied. They found maximum values in the order of *40 bar* (transducer frequencies around *100 kHz*) as well as maximum pressures in the order of *5 bar* for transducers with sampling frequencies in the order of *20 kHz*. Moreover, they report impulse strengths of the order of *20-40 Pa s*, which convincingly agree with our simulation results.

Because none of the experiments named above was performed for the geometry defined in this study, we conclude that the qualitative and quantitative agreement indicate general properties of cloud cavitation patterns occurring at free stream velocities of about *10 m/s* and mean static pressures in the order of *1 bar*.

Besides the maximum static pressures we analyse radiated pulses at a certain distance away from the hydrofoil. We therefore record the static pressure in a computational cell located close to the exit plane in the centre of the cross-section of our numerical domain. Here, the maximum pulses are of the order of *1 bar* and correspond to the collapse of the downstream convected cloud. As this vapour structure is embedded by vortical flow, the collapse turns out to be less intense. In **Fig. 7** (top) the arising pressure signal for 7 cycles is presented. Thereby, the time instant t_1 corresponds to the beginning of cycle 1 in **Fig. 2**. In **Fig. 7** (bottom) the spectral characteristics of this signal is presented. Besides the fundamental frequency of *40.65 Hz* and the first 3 harmonics we observe additional maxima at frequencies around *1 kHz*, *2 kHz* and *2.5 kHz*, as well as at *5.5 kHz*. The cause of this high frequency content in our inviscid simulation is not yet fully understood but might stem from multiple reflections of shock waves

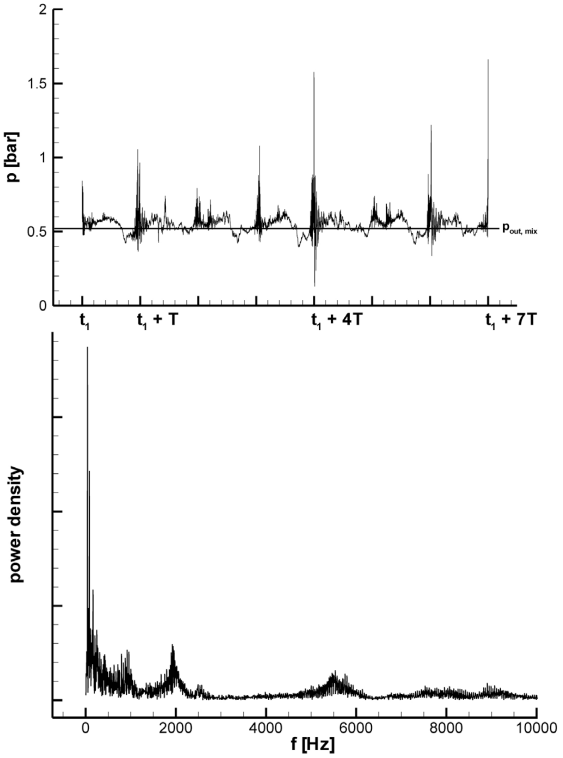

Fig. 7 Time history of static pressure close to the exit plane of the computational domain (top) and corresponding spectral analysis (bottom).
The starting time t_1 corresponds to the beginning of cycle 1, subsequently 7 cycles are presented.

inside the test-section, i.e. inside the computational domain. Additional simulations with enlarged computational domains are therefore planned.

Scaling of pulse strength with velocity

Le at al [13] analysed the scaling of the shock strength with respect to the inlet velocity while keeping the cavitation parameter σ constant. They state that the pulse height is then directly proportional to the characteristic velocity. Our numerical studies of the same hydrofoil at an inlet velocity of *17 m/s* confirm this behaviour very well. For high speed flows with characteristic velocities above *100 m/s* we obtained a correlation of inlet velocity and shock strength as well, but our prediction states that the dependency is then much weaker.

C. Third publication

Conclusions

This investigation provides a quantitative analysis of surface loads of a 3-D unsteady cavitating hydrofoil. The results confirm that high impulse loads are generated by collapse induced shock waves. Furthermore, the necessity to use a fully compressible numerical method and a sufficiently high time resolution of 10^{-7} seconds for this characteristic length scale is shown. Comparisons with available measurement data demonstrate the capability of the method to accurately predict complex 3-D shedding cycles as well as the resulting forces. The experimental discrepancies in maximum pressures are related to the transducer sampling frequencies. This correlation is demonstrated by gradually downsampling of high resolution numerical data. Load intensive domains can be detected from the numerically obtainable pressure foot-prints on the hydrofoil surface. This quantitative information enables the prediction and reduction of cavitation erosion already during the design process.

Although the physical model is able to reproduce most of the experimental observations, further extensions are planned. Therefore, we will include the presence of non-condensable gas (air) in order to study possible wave damping effects.

In order to archive long time statistical data, additional simulations with different operating conditions are currently investigated.

Acknowledgments

This research project is supported by the KSB-Stiftung, Stuttgart, Germany.

References

[1] Brennen, C.E., ‘Cavitation and bubble dynamics’, Oxford University Press, 1995.

[2] Rayleigh, Lord, ‘On the pressure developed in a liquid during the collapse of a spherical cavity’, Phil. Mag. Vol. 34, 1917.

[3] Johnsen, E. & Colonius, T., ‘Computations of shock-bubble interaction and aspherical bubble collapse’, Proceedings CAV2006 - Sixth International Symposium on Cavitation, Wageningen, The Netherlands, CD-ROM publication, 2006.

[4] Popinet, S. & Zaleski, S., ‘Bubble collapse near a solid boundary: A numerical study of the influence of viscosity’, JFM, Vol. 464, pp 137-163, 2002.

[5] Reissmann, G.E., Wang, Y.-C. & Brennen, C.E., ‘Observations of shock waves in cloud cavitation’, J. Fluid Mech. Vol. 355, pp. 255-283, 1998.

[6] Schnerr, G.H., Schmidt, S.J., Sezal, I.H. & Thalhamer M., ‘Shock and wave dynamics of compressible liquid flows with special emphasis on unsteady load on hydrofoils and on cavitation in injection nozzles’, Invited lecture, Proceedings CAV2006 - Sixth International Symposium on Cavitation, Wageningen, The Netherlands, CD-ROM publication, 2006.

[7] Godunov, S.K., ‘A finite difference method for the numerical computation of discontinuous solutions of the equations of fluid dynamics’, Mat. Sb., 47, 1959.

[8] Schmidt, S., Sezal, I. & Schnerr, G.H., ‘Compressible simulation of high-speed hydrodynamics with phase change’, ECCOMAS CFD, European Conference on Computational Fluid Dynamics, The Netherlands, 2006.

[9] Keller, A. & Arndt, R.A., ‘Hochgeschwindigkeits-Videoaufzeichnungen von Kavitation an einem NACA 0015 Profil’, Versuchsanstalt für Wasserbau und Wasserwirtschaft, TU München, private communication, 1999.

[10] Dang, J., 'Numerical simulation of unsteady partial cavity flows', Ph.D. Thesis, Delft University of Technology, Delft, 2001.

[11] Koop, A.H., Hoeijmakers, H.W.M., Schnerr, G.H. & Foeth, E.J., ‘Design of twisted cavitating hydrofoil using a barotropic flow method’, Proceedings CAV2006 - Sixth International Symposium on Cavitation, Wageningen, The Netherlands, CD-ROM publication, 2006.

[12] Foeth, E.J. & van Terwisga, T., ‘Observations of an attached cavity on a three-dimensional hydrofoil’, Proceedings CAV2006 - Sixth International Symposium on Cavitation, Wageningen, The Netherlands, CD-ROM publication, 2006.

[13] Le, Q., Franc, J.P. & Michel, J.M., ‘Partial cavities: Pressure pulse distribution around cavity closure’, J. Fluids Eng., Vol. 115, pp. 249-254, 1993.

[14] Shen, Y. & Peterson, F.B., ‘Unsteady cavitation on an oscillating hydrofoil’, In Proc. 12th ONR Symp. On Naval Hydrodynamics, pp. 362-384, 1978.

D. Fourth publication

In the fourth publication [65] simulations of two cavitating low speed flows are analyzed. The first one is the flow around a prismatic body, where shear cavitation and vortex cavitation are predominant. In this case, experimental information about cavitation erosion is compared to positions of intense peak loads found in the simulation. Good overall agreement of cavitation patterns and erosion endangered areas is achieved [33]. Due to numerical viscosity, the inviscid formulation of the governing equations is sufficient to correctly predict global flow features.

In the second part, the cavitating flow around a sphere is computed and compared to experimental findings [6]. Although most characteristic flow phenomena are well predicted by the simulation, it is concluded that viscous effects (and maybe dissolved gas) may play an important role for accurate prediction of the onset position of the sheet cavity. Numerical viscosity is certainly not sufficient for proper boundary layer representation and thus, the precise prediction of the pressure field around the sphere requires more sophisticated, but also more costly numerical models and computations.

Both flows investigated here contain regions of pure vapor (sheets, vapor vortex cores) as well as highly dispersed bubbly regions (clouds). As the proposed numerical model does not rely on single bubble considerations, it is readily applicable to simulate both regimes.

I defined the test-cases, supervised the student who generated the grids and conducted the computations, analyzed the results and prepared the manuscript. Note that the flux function applied in this investigation was published in [66] (Appendix G).

D. Fourth publication

Cavitation: Turbo-machinery & Medical Applications
WIMRC FORUM 2008
Warwick University, UK, 7th-9th July 2008

Numerical Analysis of Shock Dynamics for Detection of Erosion Sensitive Areas in Complex 3-D Flows

Steffen J. Schmidt*, Ismail H. Sezal, Günter H. Schnerr and Matthias Thalhamer

Technische Universität München, Fachgebiet Gasdynamik, Boltzmannstr. 15, D-85748 Garching

*schmidt@flm.mw.tu-muenchen.de

ABSTRACT

The aim of the present investigation is modelling and simulation of the dynamic phase transition of complex *3-D* unsteady liquid flows including the formation and propagation of collapse-induced shocks. We therefore developed the CFD-Tool **CATUM - Ca**vitation **T**echnische **U**niversität **M**ünchen, which is a conservative finite volume method based on the weak form of the balance laws for mass, momentum and energy [1-2]. For this investigation, the employed thermodynamic model is based on an equation of state for liquid water (modified Tait equation), on one for water vapor (ideal gas law), and on one for saturated water/vapor states (Oldenbourg polynomials). Meta-stable or supercritical thermodynamic conditions are not modelled and the effects of viscosity are neglected.

First we apply **CATUM** to simulate the *3-D* cavitating flow field around a prismatic body. Here, we demonstrate the ability to predict the complex unsteady flow field including violent shocks that arise from collapsing vapor clouds. The impingements of these shocks on a solid wall are recorded in order to compare the predicted erosion sensitive areas with experimental observations. Finally, we investigate the ability to predict the shedding of cloud cavitation around a sphere. Again, comparison with experimental data is given.

NOMENCLATURE

u, u_i	=	velocity, velocity components	[m·s^{-1}]
c	=	speed of sound	[m·s^{-1}]
M	=	Mach number	
$\vec{q}$	=	conserved quantities	[kg·m^{-3}, kg·m^{-2}·s^{-1} , J·m^{-3}]
$F_i(\vec{q})$	=	flux in direction x_i	[kg·m^{-2}·s^{-1} , kg·m^{-1}·s^{-2} , J·m^{-2}·s^{-1}]
ρ	=	density, local average density	[kg·m^{-3}]
E	=	mass specific total energy	[J·kg^{-1}]
e	=	mass specific internal energy	[J·kg^{-1}]
p	=	static pressure	[Pa]
T	=	static temperature	[K]
α	=	vapor volume fraction	
ε	=	vapor mass fraction	
σ	=	cavitation parameter	
x_i	=	coordinate direction/length	[m]
Δt_{CFD}	=	numerical time step	[s]
V_{vap}	=	integrated vapor volume [% total volume of the computational domain]	
f	=	frequency	[Hz]

1. INTRODUCTION

The numerical simulation of wave dynamics such as shock formation and propagation in compressible multiphase flows offers the possibility to predict the formation and collapse of cavitation structures as well as to predict collapse induced shocks of cavitating flows. Serious numerical difficulties arise due to the different time scales defined by the flow velocity $u=O(10)$ *m/s* and the speed of sound $c=O(1000)$ *m/s* of the liquid. As long as no phase transition occurs the Mach number remains very low, typically $0<M<0.1$. However, the thermodynamic properties of two-phase mixtures imply a strong reduction of the speed of sound [3] and hence, the Mach number reaches even supersonic values if the vapor volume content is sufficiently large. The collapse-like condensation of the vapor content results in the formation of shock structures that propagate through the flow [4]. These shocks result in instantaneous loads and are supposed to be a driving mechanism of cavitation erosion. The present investigation focuses on the simulation of *3-D* time-dependent cavitating liquid flows including wave dynamics. The resolution of the latter one requires numerical time steps based on the fastest signal speeds of the system, which are of the order of the speed of sound of the liquid. Besides this physical constraint the numerical flux function must resemble the asymptotic behaviour [5] of the continuous equations for $M \rightarrow 0$. It is known that classical Riemann approaches suffer from the low Mach number problem and hence, their application as flux function typically leads to large errors in the calculated flow field [6-8]. Several numerical techniques have been developed to overcome the low Mach number problem. Time derivative preconditioning removes the stiffness of the governing equations and permits accurate steady state solutions in the low Mach number limit [9]. In combination with dual time-stepping approaches these techniques are applicable to simulate unsteady flows as well, but the resolution of wave dynamics is no longer possible [10-11]. Pressure correction methods enable the simulation of low Mach number flow [12], but their application to solve wave propagation problems suffers from the lack of efficiency of these techniques if the physically required time step is very small. If the Mach number is small throughout the flow domain, the discretization of the compressible low Mach number equations [13] is suitable. However, with respect to cavitating flow this condition is not fulfilled. In addition to the numerical difficulties of low Mach

number flows the simulation of cavitating flows require modeling of evaporation/condensation as well as of the resulting two-phase mixtures. The modeling of the phase-change is either achieved by finite rate models [14-16] or by thermodynamic closure relations [17-18, 1-2]. These models can be applied to single-fluid formulations as well as to two-fluid formulations. The latter ones enforce the solution of two sets of governing equations, together with the modeling of mass, momentum and energy transfer between both fluids [19]. A recently developed hybrid model is based on the assumption of locally stratified flow [20]. The advantages of single-fluid formulations together with suitable thermodynamic closure relations are their hyperbolic structure and the existing conservation form of the governing equations [21].

The present investigation is organized as follows: In chapters **2** and **3** we briefly summarize the mathematical model and the solution algorithm implemented in our CFD-Tool **CATUM** for time-dependent compressible liquid flows including the effects of evaporation and condensation. Chapter **4** contains a detailed analysis of numerically predicted pressure loads of collapsing two-phase regions. Here, we compare our numerical observations of the cavitating flow around a prismatic body with experimental results of Huber [22]. Special emphasis is put on the correlation of experimentally observed regions of cavitation erosion with the numerical prediction. Finally, the cavitating flow around a sphere is investigated in chapter **5**. We present pictures of the void fraction distribution as obtained by our currently performed simulation and compare these to the experimental results obtained by Brandner et al. [23].

2. PHYSICAL MODEL

As our major interests contain wave and inertia driven flows we neglect viscous effects. From several experimental investigations it is known that cavitating flow is only weakly dependent on the Reynolds number and thus this approximation is suitable. However, the inclusion of viscous effects within the model is possible.

Let $\vec{q}$ be the vector of conserved quantities defined by the density ρ, the components u_i of the velocities in coordinate direction x_i and the specific total energy E as the sum of the specific internal energy e per unit mass and the specific kinetic energy $0.5 \cdot \sum (u_i)^2$. Let $F_i(\vec{q})$ be the physical flux in coordinate direction x_i, while δ_{ij} and p denote the Kronecker symbol and the pressure respectively

$$\vec{q} = \begin{pmatrix} \rho \\ \rho u_1 \\ \rho u_2 \\ \rho u_3 \\ \rho E \end{pmatrix} \qquad F_i(\vec{q}) = \rho u_i \cdot \begin{pmatrix} 1 \\ u_1 \\ u_2 \\ u_3 \\ E \end{pmatrix} + p \cdot \begin{pmatrix} 0 \\ \delta_{1i} \\ \delta_{2i} \\ \delta_{3i} \\ u_i \end{pmatrix} \quad . \tag{1}$$

The differential or pointwise form of the Euler equations can be written as

$$\frac{\partial}{\partial t}\vec{q} = -\sum_{i=1}^{3} \frac{\partial}{\partial x_i} F_i(\vec{q}) \, . \tag{2}$$

Instead of enforcing the conservation principles in a pointwise fashion we use the weak form of the Euler equations. Therefore, we partition the flow domain into disjoint fixed control volumes C_k of a corresponding volume V_k, a surface S_k and an outer unit normal vector $\vec{n}_k = (n_{k,1} \quad n_{k,2} \quad n_{k,3})^t$. The weak form of the Euler equations for each control volume C_k follows as

$$\frac{d}{dt} \int_{C_k} \vec{q} \, \mathrm{dV_k} = -\int_{S_k} \sum_{i=1}^{3} n_{k,i} F_i(\vec{q}) \, \mathrm{dS_k} \, . \tag{3}$$

By defining the cell average operator A_k

$$A_k(\vec{q}) := \frac{1}{V_k} \int_{C_k} \vec{q} \, \mathrm{dV_k} \, , \tag{4}$$

we assign to all weak solutions within the cell C_k their common integral average value $\vec{q}_k = A_k(\vec{q})$. It turns out that the weak form of the Euler equations resembles a system of evolution equations of the cell averages of weak solutions

$$\frac{d}{dt}\vec{q}_k = -\int_{S_k} \sum_{i=1}^{3} n_{k,i} F_i(\vec{q}) \, \mathrm{dS_k} \, . \tag{5}$$

Up to now we have not made any additional assumption on the flow field itself, which means that equation (5) is valid for any type of inviscid multicomponent and multiphase flow, even if the species do not share a common pressure, temperature or velocity. Nonetheless, the closure of the defined initial-boundary value problem (5) necessitates constitutive relations for the thermodynamic quantities ρ_k, e_k, p_k as well as consistent initial and boundary conditions. In this section we assume that consistent initial and boundary data are available. Thus, the physical fluxes along the boundary surfaces are known and hence, equation (5) reduces to an initial value problem. At each instant in time the corresponding initial values $\vec{q}_k$ already determine the average density ρ_k, velocity $\vec{u}_k$ and total energy E_k within the control volume C_k. Therefore, the average specific internal energy e_k is known as well. However, the definition of the average pressure p_k requires additional model assumptions. In this investigation we neglect surface tension and restrict the fluid to consist of two species: water and water vapor. It is known that highly purified water allows for the occurrence of meta-stable states far beyond saturation conditions [24], whereas tap water does not show this behaviour. In the latter case, the large number of impurities immediately results in heterogeneous nucleation [25] and thus in the formation of vapor bubbles. As the specific volume of water vapor is by several orders of magnitude larger than the one of liquid water,

the phase transition results in rapid pressure equalization close to the stable saturation state. Although impurities like solid particles or solute gas are currently not explicitly modelled in our CFD-Tool, we assume that infinitely fast pressure equalization takes place. This allows us to neglect meta-stable states and to consider stable thermodynamic conditions. Consequently, the coexistence of both phases implies that the pressure p_k is determined by the Clausius-Clapeyron relation and the average density ρ_k within cell C_k is a convex combination of the saturation densities $\rho_{l,sat}$, $\rho_{v,sat}$ of liquid and vapor. Furthermore, we define at each instant in time and for each control volume an average temperature T_k in order to relate the saturation density to the internal energy. By defining the vapor volume fraction α_k and the vapor mass fraction ε_k we obtain the unknown quantities T_k, α_k, ε_k and p_k as solutions of the system

$$\rho_k = \alpha_k \cdot \rho_{v,sat}(T_k) + (1-\alpha_k)\cdot \rho_{l,sat}(T_k) \tag{6}$$

$$e_k = \varepsilon_k \cdot e_{v,sat}(T_k) + (1-\varepsilon_k)\cdot e_{l,sat}(T_k) \tag{7}$$

$$\varepsilon_k \cdot \rho_k = \alpha_k \cdot \rho_{v,sat}(T_k) \tag{8}$$

$$p_k = p_{sat}(T_k) \tag{9}$$

$$0 < \alpha, \varepsilon < 1. \tag{10}$$

Thereby, the incorporated temperature dependent functions have to be specified. In the case of water and water vapor we model these by Oldenbourg polynomials [26]. The required closure relation in the presence of two-phase flow is thus completely defined.

If the average density ρ_k is larger then the saturation density of liquid water, we replace the closure relation by the modified Tait model ($\alpha_k, \varepsilon_k = 0$)

$$\frac{p_k + B}{p_{sat}(T_k) + B} = \left(\frac{\rho_k}{\rho_{l,sat}(T_k)} \right)^N , \tag{11}$$

together with an equation for the internal energy [27]. Even though the temperature variation of the liquid is typically small, the modification of the Tait equation remains necessary in order to ensure a continuous connection of the Tait model to the temperature dependent saturation conditions. For water we use *B=3300 bar* and *N=7.15,* independent of the temperature.

If the average density ρ_k is smaller then the saturation density of vapor, the applied constitutive relation models pure vapor *($\alpha_k, \varepsilon_k = 1$)*, treated as calorically perfect gas, where the ratio of the specific heats is given by *κ=1.327* and the specific gas constant is *461.5 J/kg K*.

The comparison of the described thermodynamic closure relations with respect to the IAPWS data [28] demonstrates that the relations accurately model the behaviour of water and water vapor for a large range of thermodynamic subcritical conditions. Moreover, the presented model is neither restricted to the described set of thermodynamic closure relations nor to the assumption of instantaneous pressure equalization.

3. NUMERICAL METHOD – CFD-TOOL CATUM

Our CFD-Tool CATUM relies on an approximate solution of the evolution equation (5) for each control volume C_k. The hyperbolic character of the compressible formulation of the governing equations motivates a Godunov type approximation of these fluxes. Thereby, the average values $\bar{q}_k$ and $\bar{q}_i$ of two adjacent control volumes C_k, C_i are used to define the Riemann problem *RP* across the shared surface $S_{k,i} = C_k \cap C_i$. The solution $RP(\bar{q}_k, \bar{q}_i)$ of the Riemann problem at the surface $S_{k,i}$ is constant in time within a time interval $\Delta t_{RP} \approx l/(|\vec{u}| + c)$, where l is the length scale of the volume and $|\vec{u}| + c$ represents the fastest signal speed. By replacing the physical fluxes $F(\bar{q}_k)$ in Eq. (5) with the numerical fluxes $F(RP(\bar{q}_k, \bar{q}_i))$, we obtain a set of ordinary differential equations, which represent a semi-discrete unsplit finite volume method for hexahedral volumes

$$\frac{d}{dt}\bar{q}_k = -\sum_{i=1}^{6} S_{k,i} \cdot F(RP(\bar{q}_k, \bar{q}_i)). \tag{12}$$

This framework is well developed for the simulation of steady and unsteady compressible aerodynamics of moderate and high Mach number flows as well as for the investigation of wave propagation phenomena including sharp and accurate shock capturing in unsteady flow. Furthermore, methods based on Eq. (12) are conservative by construction and enable efficient time dependent simulations. Contrary to pressure based approaches, all fluxes are calculated without the need for sub-iterations. However, the application of Godunov type methods to low speed flows requires substantial modification to overcome the low Mach number problem. Otherwise, the accuracy of the Godunov approximation significantly decreases if the Mach number is in the weakly compressible regime, $M \lesssim 0.1$. With respect to the high acoustic impedance $\rho \cdot c$ of liquids, the decrease of accuracy is further intensified.

We obtain a consistent flux function with respect to the asymptotic behavior for $M \to 0$ by modifying the pressure flux of the classical approaches. This is achieved by using the arithmetic average of the pressure of adjacent cells to define the pressure flux. The velocity and the density at the common interface of adjacent cells are calculated according to the classical solution of the Riemann problem.

By applying high resolution reconstruction procedures (WENO-3, TVD) in space together with an explicit 4-stage Runge-Kutta method in time we obtain an efficient CFD-Tool that enables us to investigate wave dynamics arising in complex *3-D* cavitating flows in an accurate manner.

4. CAVITATING FLOW AROUND A PRISMATIC BODY

The occurrence of cavitation typically leads to a decrease of the efficiency of hydraulic machinery. For pumps the NPSH (net positive suction head) significantly reduces as soon as evaporation of the fluid takes place. Furthermore, cavitating flow tends to be inherently time dependent due to the periodic or chaotic fragmentation of vapor sheets and the subsequent formation of vortical cavitation clouds [29-30]. These clouds are convected into areas of increased static pressure, where a collapse-like recondensation is initiated. Thereby, shock structures form and propagate through the fluid. If the collapse of a vapor cloud occurs close to a solid surface, e.g. close to a pump or turbine blade, then the shock induced dynamic loads are supposed to be a major part of the mechanism of cavitation erosion [31]. It is further supposed that the interaction of a shock with a simultaneously collapsing single vapor bubble intensifies the erosive behavior. Within a previous investigation [1] we applied the CFD-Tool **CATUM** to simulate the collapse of a single vapor bubble and found excellent agreement with the theoretical prediction given by the Rayleigh-Plesset equation. However, the resolution of single bubble dynamics is not possible for *3-D* cavitating flow as this would require unaffordable high mesh resolution. Here, we investigate the dynamics of large scale structures that can be interpreted as clouds of liquid embedded vapor bubbles. Therefore, we model and discretize an experimental setup consisting of a rectangular test-section of length *0.85 m*, depth *0.3 m* and height *0.3 m,* where a prismatic body of height *0.1 m* is located at the bottom wall. The lateral section of the prismatic body forms an equilateral triangle with side length *0.075 m*. The mesh consists of $3.1 \cdot 10^6$ finite volumes and it is partitioned into *64* bocks (**Fig. 1**). Liquid water at *T=300 K* enters the inlet plane with an average velocity $u_{in}=11\ m/s$. At the outlet plane of the numerical domain asymptotic non-reflective boundary conditions are applied, which ensure an average pressure $p_{out,mix}=1.12\ bar$. Based on the inlet velocity, the inlet temperature and the outlet pressure we obtain a cavitation parameter $\sigma_{ref}=1.8$. The numerical analysis is performed within *240* hours on a *SGI Altix 3700Bx2* using *64* processors.

We perform 10^6 time steps with a step size of $\Delta t_{CFD}=2.9 \cdot 10^{-7}\ s$, which leads to a physical simulation time of *0.29 s*. The first *0.116 s* of the simulation are not analyzed in detail as during this time the flow dynamics are supposed to be affected by the initialization of the simulation. In **Fig. 2** the time history of the integrated vapor volume fraction V_{vap} within the complete numerical domain is shown. Starting from $t=0.116\ s$ we define three time intervals *1-3* with length $\Delta t_{analysis\ cycle}=0.058\ s$. Within all three time intervals the graph of the integrated vapor volume fraction V_{vap} depicts oscillations of the frequencies $f_1=22.8\ Hz$, $f_2=62.7\ Hz$ and $f_3=136.8\ Hz$.

Figure 3 depicts a series of top views of the prismatic body (red) for *10* equidistant instants in time t_1-t_{10} with $\Delta t_{pic}=0.019\ s$. The flow is from left to right and the arising two-phase structures are visualized by blue iso-surfaces of the void fraction $\alpha=0.1\%$. We observe weakly time dependent cavitating tip vortices at the top of the prismatic body as well as highly unsteady cavitating vortices in the shear layers downstream of the body. Furthermore, we detect a transition of the shape of the cavitation structures from compact clouds in the near wake of the body to elongated structures (tubes) in the far wake (**Pic. 9** of **Fig. 3**). This transition is related to the interaction of the shear layer vortices arising at the vertical edges of the body with the shear layer at the trailing edge at the top of the body.

Figure 4 provides a one-to-one comparison of the visualization of the experimentally observed cavitation pattern [22] with our numerically obtained result for one instant in time. The cavitating vortices at the tip of the body, the dispersed bubbly clouds in the near wake and the tubular cavitation structures in the far wake are well predicted by the simulation. The agreement of both visualizations confirms our view that the underlying dynamics of the investigated cavitating flow are mainly inertia controlled.

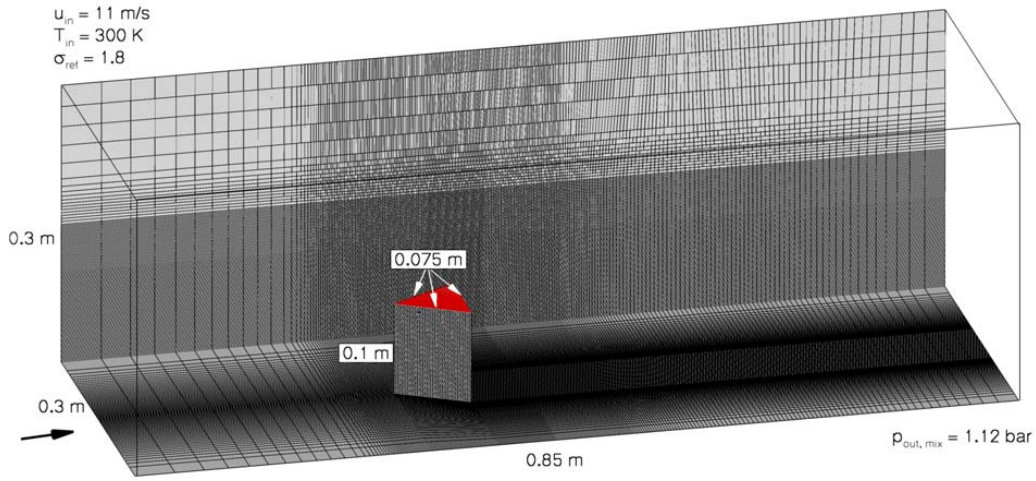

Fig. 1: **Numerical test-section including the prismatic body and computational discretization of the domain.** Fluid: water from left to right, ***$T_{in}=300\ K$, $u_{in}=11\ m/s$, $p_{out}=1.12\ bar$, $\Delta t_{CFD}=2.9 \cdot 10^{-7}\ s$, $3.1 \cdot 10^6$*** finite volumes.

Figure 5 depicts three perspective views of the prismatic body as well as of the bottom wall and of one side wall of the numerical test-section. Both walls are colored according to the corresponding static pressure and two-phase structures are visualized by blue iso-surfaces of the void fraction $\alpha=0.1\%$. At $t_1=0.234\ s$ (**Pic. 1** of **Fig. 5**) we observe a vortical two-phase structure that slightly touches the bottom wall. In **Pic. 2** at $t_2=t_1+1.17\cdot10^{-4}\ s$ the tubular structure is fragmented into two parts. The smaller one is located at the bottom wall where it collapses violently. Thereby, the surrounding liquid accelerates towards the center of the cloud and impacts onto the wall at the bottom of the test-section. This impact results in the formation of a spherical shock (**Pic. 3** of **Fig. 15**, $t_3=t_2+5.85\cdot10^{-5}\ s$), which propagates through the numerical domain and enforces a strong increase Δp of the static pressure. For the presented collapse the maximum pressure increase reaches $\Delta p=65\ bar$ directly after the impact of the liquid. The pressure increase behind the shock is approximately inverse proportional to the radius of the spherical shock front. Hence, the shock induced load on the walls of the numerical test-section strongly depends on the position of the collapsing cloud. If the distance between the cloud and the wall of the test-section is sufficiently small, then the instantaneous force on the wall might be strong enough to damage the material of the wall. Additionally, it is supposed that the erosive effect of the collapse induced shock is intensified by the interaction of a cloud collapse with a single vapor bubble that is in contact with the wall. Although the mechanism of cavitation erosion is not yet clarified in detail, it is reasonable to consider shock induced loads as a driving mechanism within the complex process of cavitation erosion. Therefore, we investigate the forces acting on the bottom wall of the numerical test-section for the previously defined "analysis cycles" 1-3 as shown in **Fig. 2**. For each of these time intervals we record the maximum static pressure within those computational cells that are directly located at the bottom wall. The resulting "foot-print" of the maximum pressure is depicted in **Fig. 6** for each analysis cycle. Within the experimental investigation [22] the areas of intense erosion at the bottom walls were detected. The centers of these areas are marked by red crosses in **Fig. 6** in order to relate the numerical prediction of the maximum forces to the experimentally observed damage at the surface of the bottom wall. Although the numerically predicted maximum loads of *60-100 bar* occur slightly upstream of the experimentally determined areas of most intense erosion, the results demonstrate that the physical model together with the numerical approach is suitable to predict the position of erosion critical areas. Furthermore, it should be pointed out that the experiment runs for about *5400 s* while the numerical simulation covers a small time interval of *0.058 s* for each analysis cycle. Nevertheless, even for the performed short time analysis a statistical behavior is present. We observe 2-5 strong impacts ($\Delta p > 50\ bar$) per cycle, which leads to an estimated number of impacts of $3\cdot10^5$ for an experimental analysis of *5400 s*. However, as previously stated, the number of erosive events could be 1 or 2 orders of magnitude smaller if it turns out that the coexistence of a cloud collapse together with a single bubble collapse should be the necessary constellation of cavitation erosion. Therefore, further experimental and numerical investigations are required to determine a correlation of erosion rates with the number of cloud collapse events.

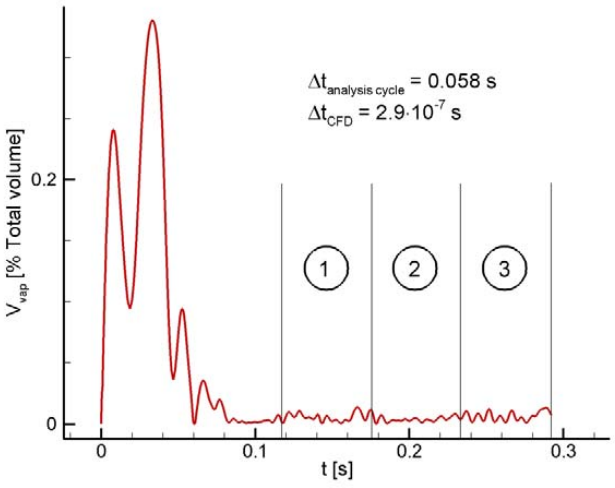

Fig. 2: **Time history of the integrated vapor volume V_{vap} [% total volume of the computational domain].** Fluid: water, $T_{in}=300\ K$, $u_{in}=11\ m/s$, $p_{out}=1.12\ bar$, $\Delta t_{CFD}=2.9\cdot10^{-7}\ s$.

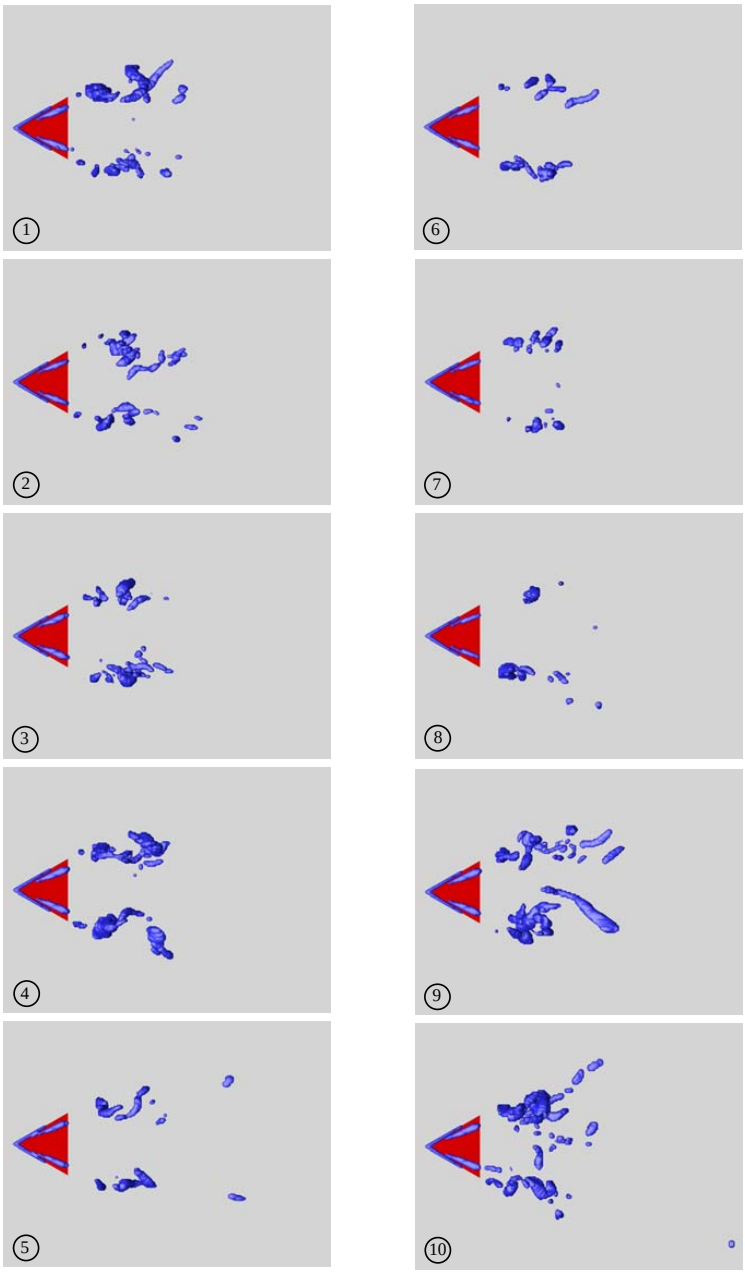

Fig. 3: **Top view of the prismatic body and arising cavitation structures at 10 equidistant instants in time within the analysis cycles 1-3 of Fig. 2. Blue surfaces indicate two-phase regions with $\alpha \geq 0.1\%$.**
Fluid: water from left to right, $T_{in}=300\ K$, $u_{in}=11\ m/s$, $p_{out}=1.12\ bar$, $\Delta t_{CFD}=2.9 \cdot 10^{-7}\ s$, $\Delta t_{pic}=0.019\ s$.

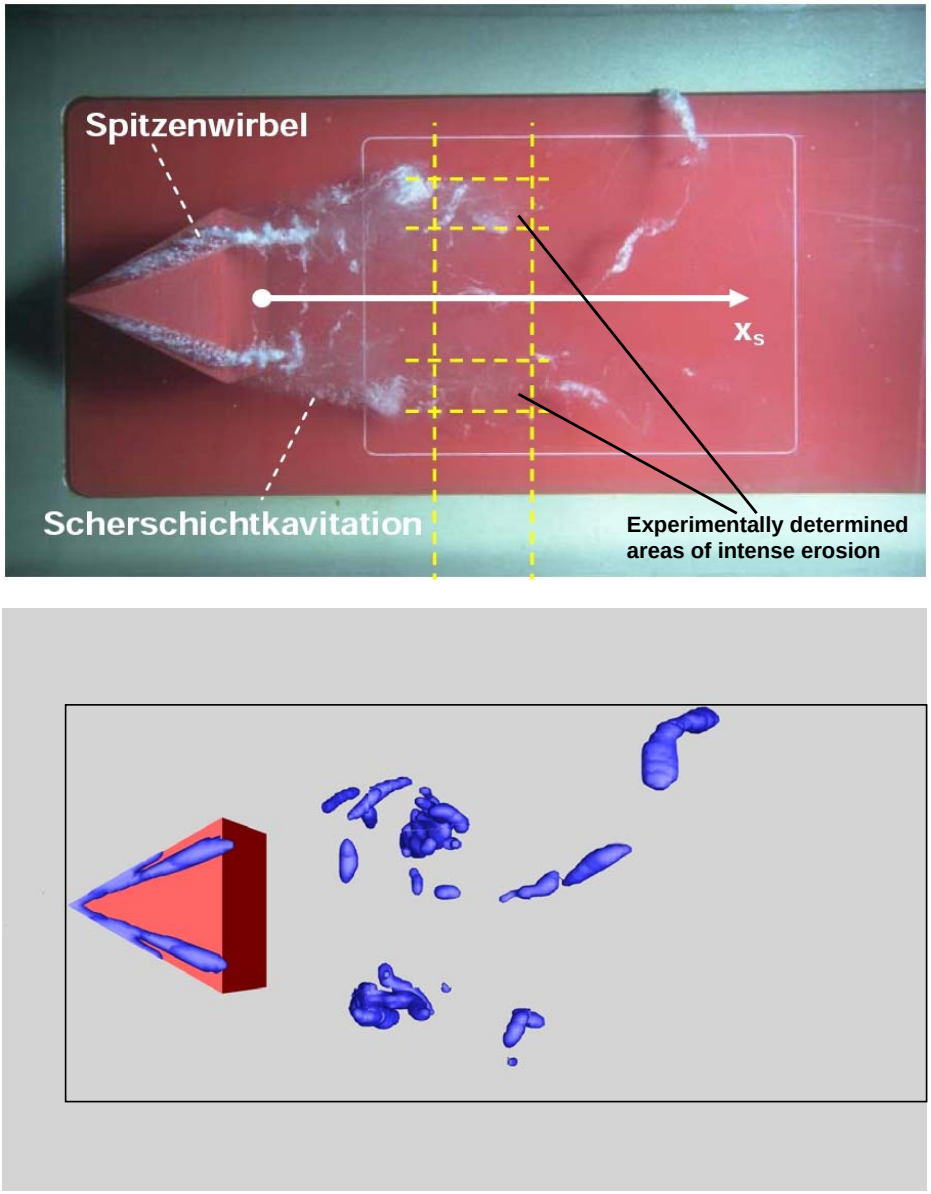

Fig. 4: Top view of the prismatic body and arising cavitation structures at one instant in time. Visualization of the experiment [22] (top) and of the numerical result (bottom). Blue surfaces indicate two-phase regions with α≥0.1%.
Fluid: water from left to right, T_{in}=300 K, u_{in}=11 m/s, p_{out}=1.12 bar, $\Delta t_{CFD}=2.9\cdot10^{-7}$ s.

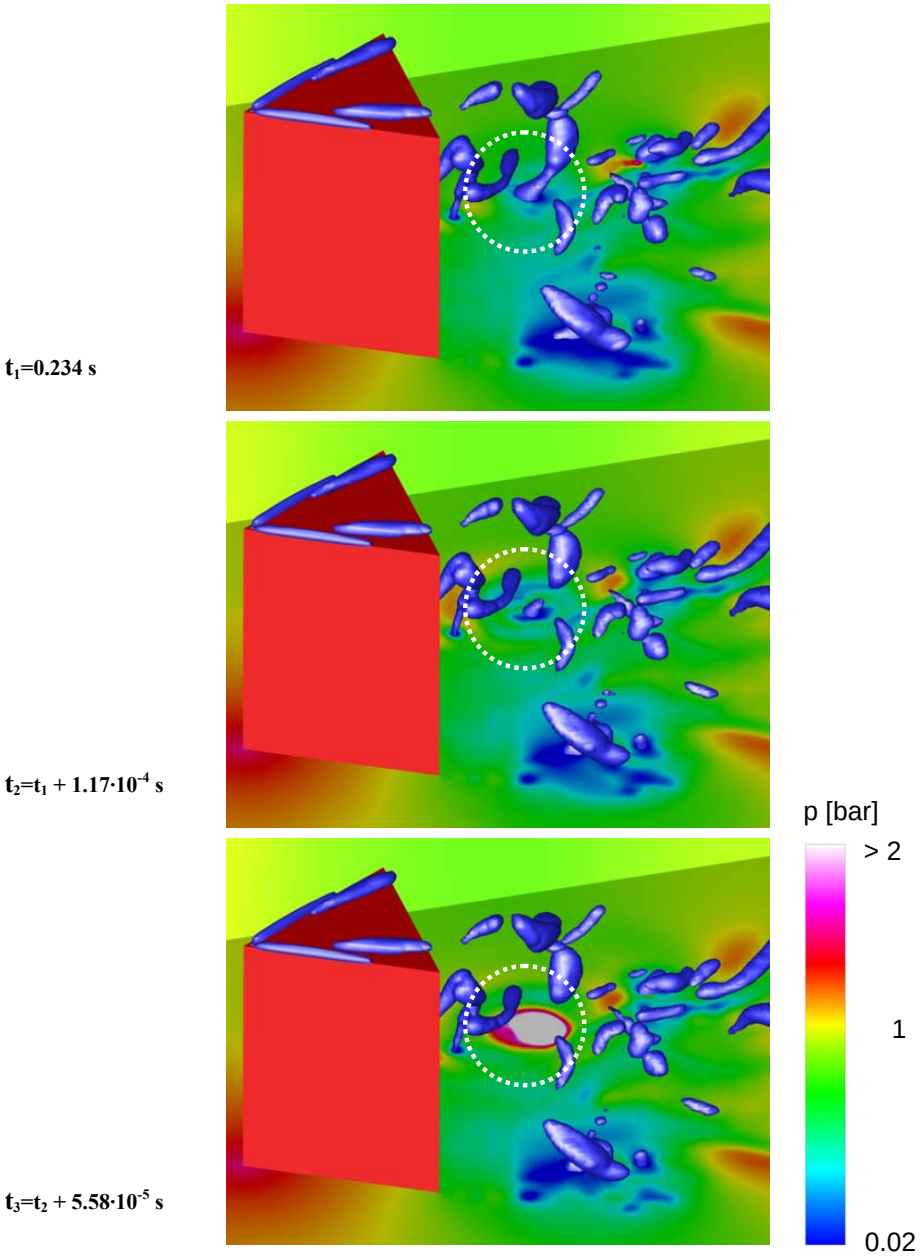

Fig. 5: Perspective view of the prismatic body and shock formation due to collapsing cavitation structure at 3 instants in time. The bottom wall and the side wall are colored according to the static pressure. The maximum pressure at the bottom wall reaches 65 bar. Blue surfaces indicate two-phase regions with α≥0.1%. Fluid: water from left to right, ***T_{in}=300 K, u_{in}=11 m/s, p_{out}=1.12 bar, $\Delta t_{CFD}=2.9\cdot10^{-7}$ s.***

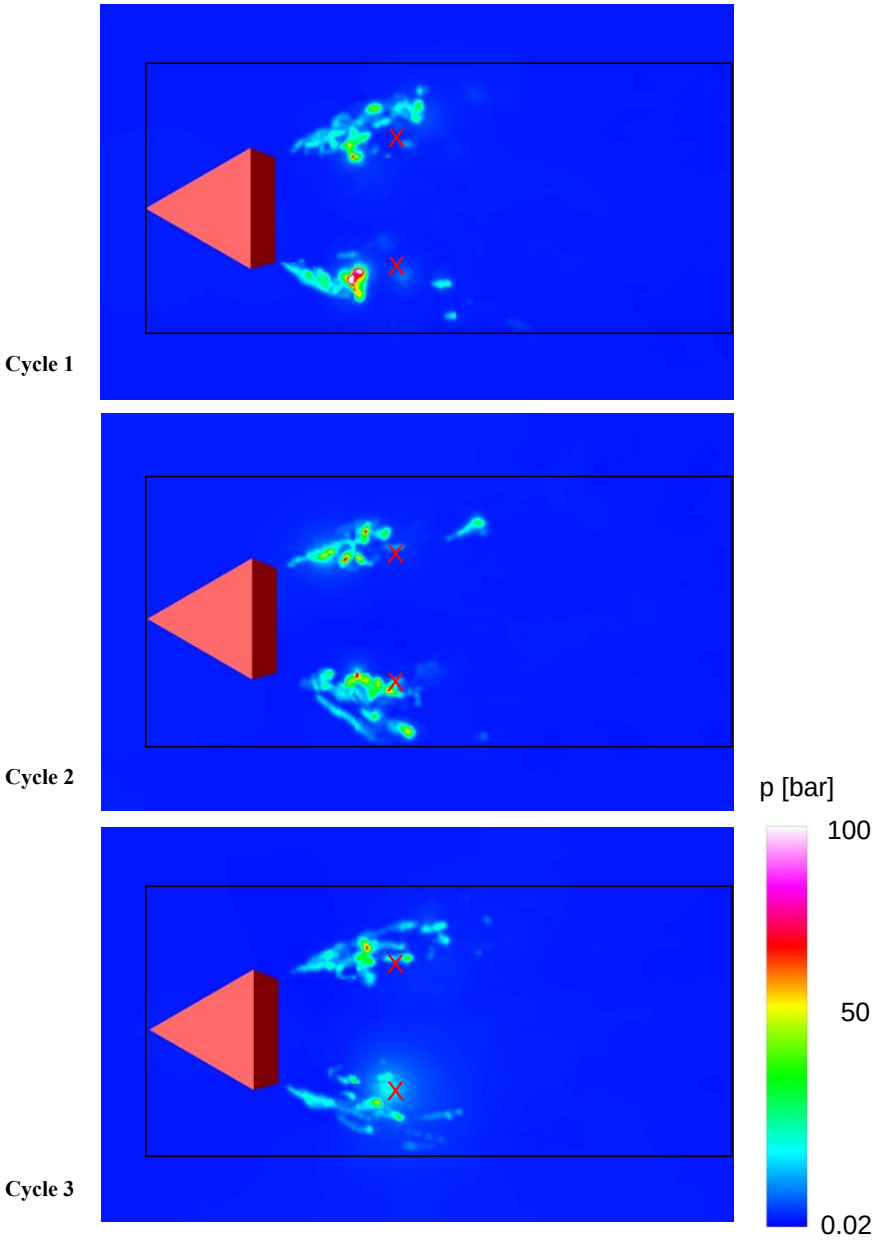

Fig. 6: Top view of the prismatic body and the numerically obtained pressure "foot-prints" for the analysis cycles 1-3 as defined in Fig. 2. Red crosses mark the experimentally [22] obtained centers of most intense erosion. In picture 3 the small orange spot to the top left of the red cross corresponds to the collapse depicted in Fig. 5.
Fluid: water from left to right, T_{in}=300 K, u_{in}=11 m/s, p_{out}=1.12 bar, $\Delta t_{CFD}=2.9\cdot10^{-7}$ s.

5. CAVITATING FLOW AROUND A SPHERE

In order to investigate the shedding of cloud cavitation we model and discretize an experimental setup as applied by Brandner et al. [23]. The setup consists of a rectangular test-section of length *2.75 m*, depth *0.6 m* and height *0.6 m,* where a sphere of diameter *0.15 m* is located at the center of the cross section. The mesh consists of $1.3 \cdot 10^6$ finite volumes and it is partitioned into *84* bocks (**Fig. 7**). Liquid water at *T=293 K* enters the inlet plane with an average velocity $u_{in}=10\ m/s$. At the outlet plane of the numerical domain asymptotic non-reflective boundary conditions are applied, which ensure an average pressure $p_{out,mix}=0.42\ bar$. Based on the inlet velocity, the inlet temperature and the outlet pressure we obtain a cavitation parameter $\sigma_{ref}=0.8$. The numerical analysis is performed within *120* hours on an AMD Opteron cluster using *84* processors.

We perform $1.2 \cdot 10^6$ time steps with a step size of $\Delta t_{CFD}=3.3 \cdot 10^{-7}\ s$, which leads to a physical simulation time of *0.39 s*. The first *0.08 s* of the simulation are not analyzed in detail as during this time the flow dynamics are supposed to be affected by the initialization of the simulation. In **Fig. 8** we depict *6* equidistant instants in time t_1-t_6 with $\Delta t_{pic}=3.3 \cdot 10^{-3}\ s$. The flow is from left to right and the arising two-phase structures are visualized by blue iso-surfaces of the void fraction $\alpha=5\ \%$. In **Pic. 1** of **Fig. 8** we observe an attached sheet cavity around the meridian of the sphere. Slightly downstream detached clouds are visible. In the wake of the sphere tubular cavitation structures are predicted. **Picture 2** depicts a subsequent instant in time, where the previously attached sheet cavity is partially separated from the surface of the sphere. In **Pic. 3** a new attached sheet starts to develop from the bottom of the sphere. As the sheet grows it forms an almost regular band around the meridian of the sphere (**Pic. 4**). Before the elongation of the sheet reaches its maximum (**Pic. 5**) we observe the onset of re-entry jets that lead to the breakup of the sheet (**Pic. 6**) and to the subsequent detachment of fragmented clouds. Thereby, the formation of large scale vortices is predicted by our simulation.

As presented by Brandner et al. [23], the dynamic behavior of the shedding contains two dominant frequencies that depend on the value of the cavitation parameter $\sigma_{experiment}$. For $\sigma_{experiment}=0.8$ they report Strouhal numbers based on the diameter of the sphere of $Str_1=0.24$ and $Str_2=0.4$. From our simulation at $\sigma_{ref}=0.8$ we obtain values of $Str_1=0.21$ and $Str_2=0.52$, but we want to point out that our currently simulated time interval might not be long enough to obtain representative statistics. Additional investigations of the shedding behavior and its dependence on the cavitation parameter are part of current research.

Figure 9 (top) depicts a photograph of the experimental investigation of Brandner et al. [23] together with the first instant in time (bottom) of the series presented in **Fig. 8**. As both pictures present snap-shots of highly unsteady flow fields, only qualitative comparison is reasonable. We observe good agreement of the predicted large scale structures, although there is a slight discrepancy of the position of the attached sheet cavity. The numerically predicted position is upstream to the meridian of the sphere, close to the position observed in the experiment for the slightly lower value of $\sigma_{experiment}=0.7$. This might have several reasons: Our current investigation does neither take the effects of dissolved gas into account, nor do we model viscous effects such as pressure losses and the thickness of the boundary layers. These issues will be addressed in further investigations and are part of the ongoing development of our CFD-Tool **CATUM**.

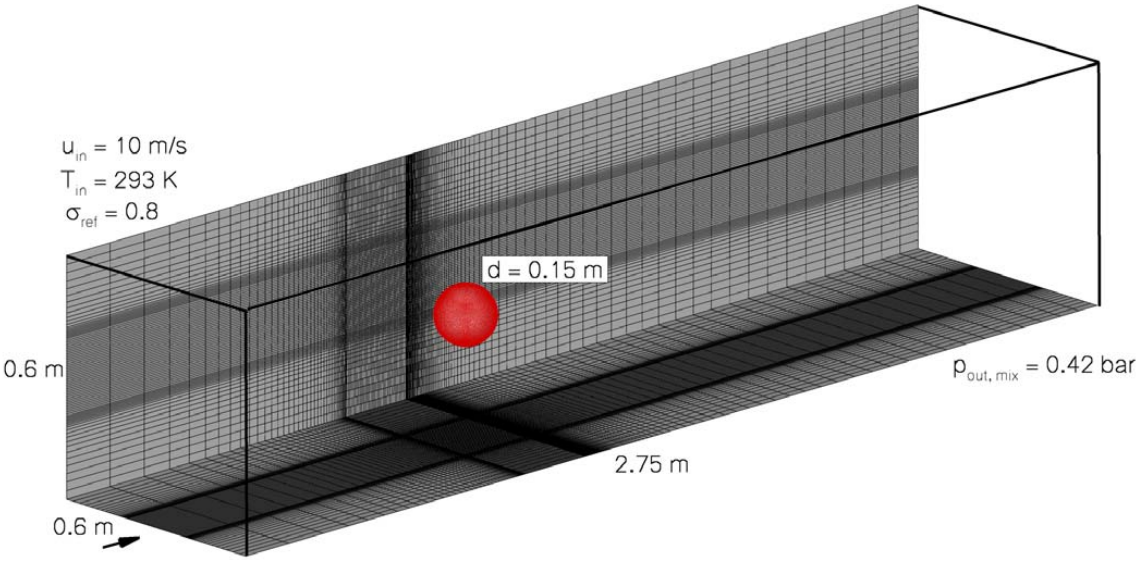

Fig. 7: **Numerical test-section including the sphere (red) and computational discretization of the domain.**
Fluid: water from left to right, $T_{in}=293\ K$, $u_{in}=10\ m/s$, $p_{out}=0.42\ bar$, $\Delta t_{CFD}=3.3 \cdot 10^{-7}\ s$, $1.3 \cdot 10^6$ finite volumes.

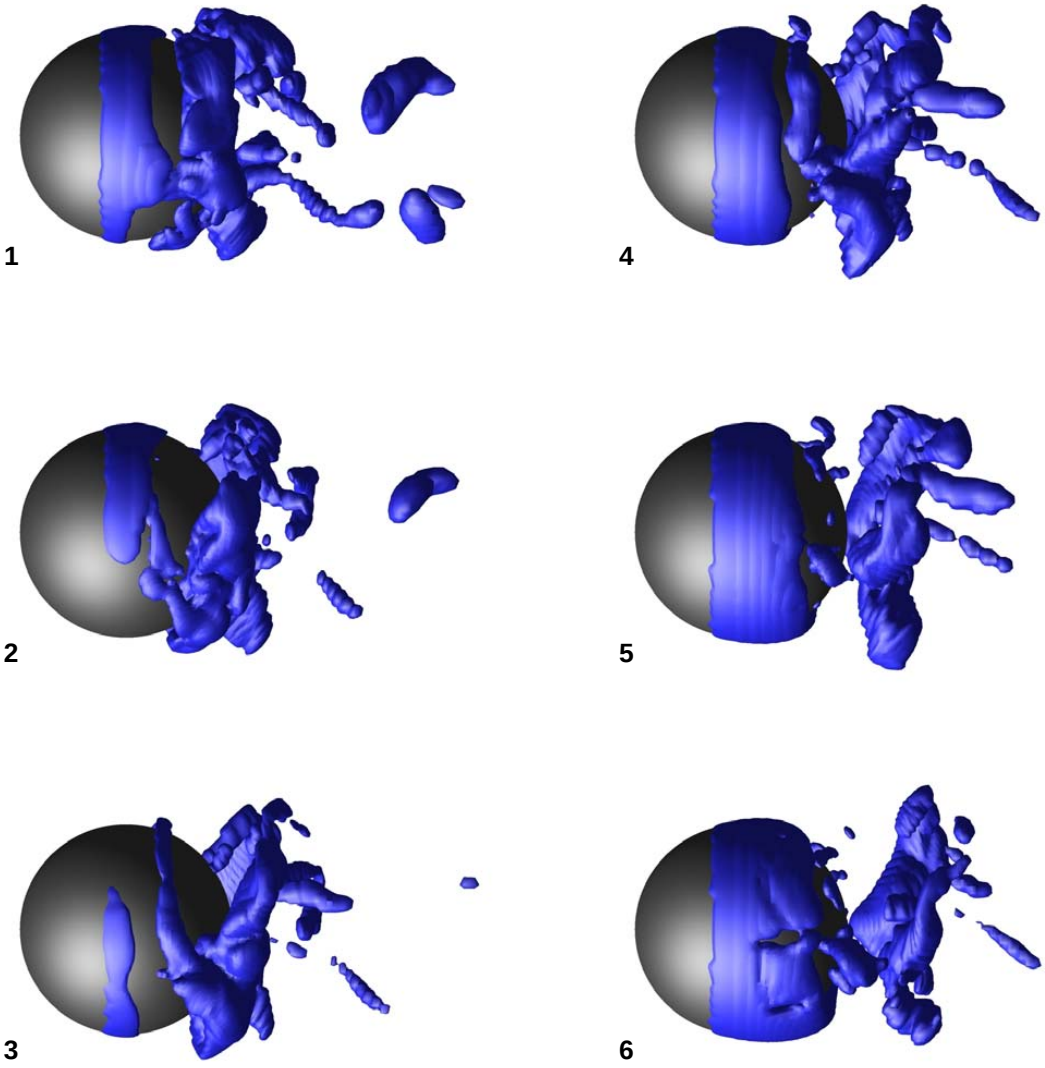

Fig. 8: **Side view of the sphere and arising cavitation structures at 6 equidistant instants in time. Blue surfaces indicate two-phase regions with α≥5%.**
Fluid: water from left to right, T_{in}=293 K, u_{in}=10 m/s, p_{out}=0.42 bar, $\Delta t_{pic}=3.3\cdot10^{-3}$ s, $\Delta t_{CFD}=3.3\cdot10^{-7}$ s.

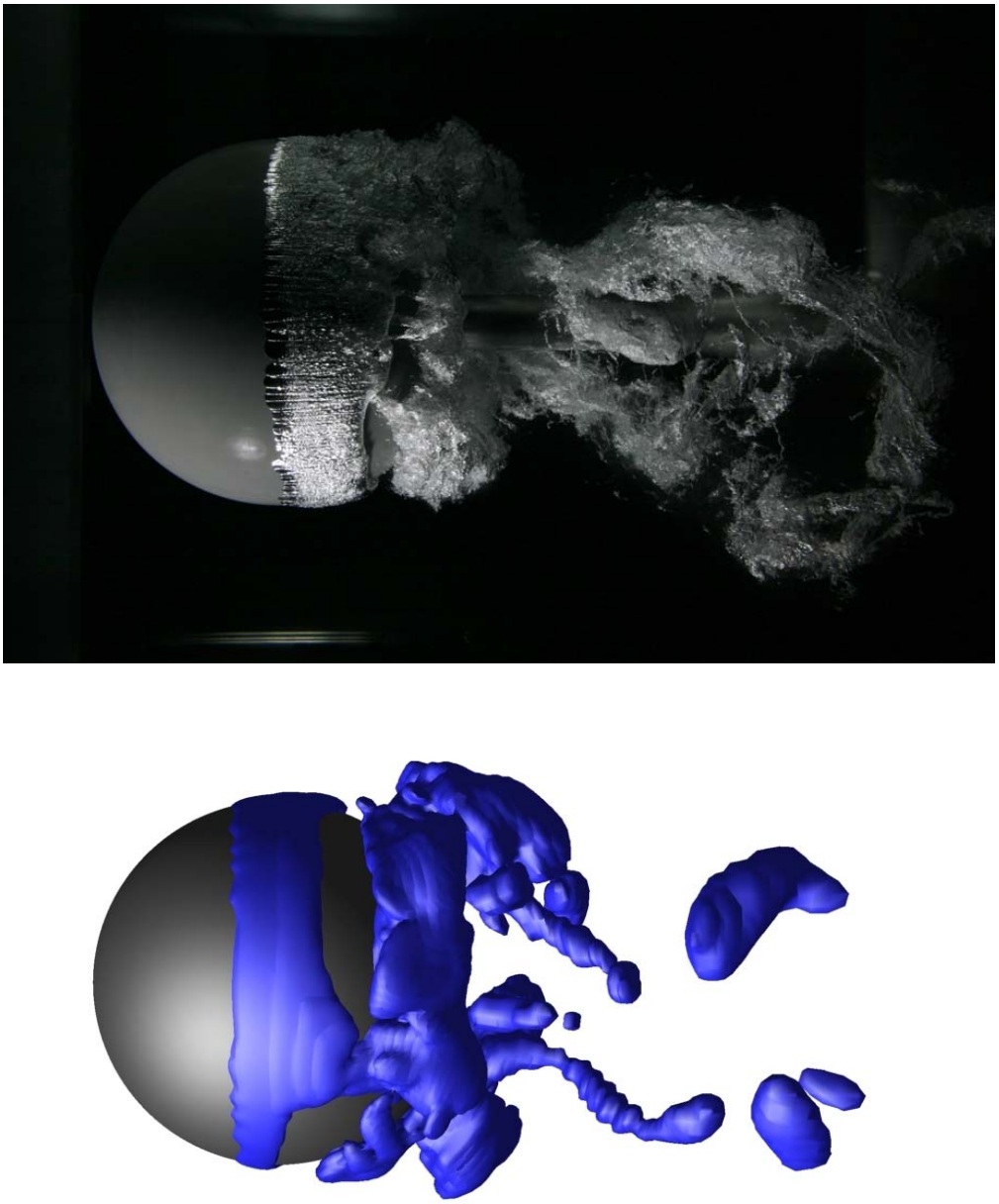

Fig. 9: Side view of the sphere and arising cavitation structures at one instant in time.
Visualization of the experiment [23] (top) and of the numerical result (bottom).
Blue surfaces indicate two-phase regions with α≥5%.
Simulation: Fluid: water from left to right, T_{in}=293 K, u_{in}=10 m/s, p_{out}=0.42 bar, $\Delta t_{CFD}=3.3\cdot10^{-7}$ s.
Experiment [23]: Fluid: water from left to right, $Re_D = 1.5\cdot10^6$.

CONCLUSIONS

By investigating the flow around a prismatic body we demonstrate the ability of our recently developed CFD-Tool **CATUM** to predict erosion sensitive areas. This is achieved by a physically enforced time resolution of the order of 10^{-7} *seconds* and the necessarily compressible treatment of the governing equations. By comparison of our numerical results with experimental observations we further show that even complex features of cavitating flows are reasonable predicted without explicit modeling of viscous effects. This justifies the numerical approach and motivates our view, that the underlying dynamics of the investigated cavitating flows is strongly inertia controlled. Both investigated flows contain regions of pure vapor (sheets) as well as highly dispersed bubbly regions (clouds). As the proposed numerical model does not rely on single bubble considerations, it is readily applicable to simulate both regimes. However, the effects of dissolved gas within the flow field are thought to be an important aspect in order to further improve the quality of the numerical predictions. This issue is currently under development and will be prospectively presented in another investigation.

ACKNOWLEDGMENTS

We like to thank P.A. Brandner et al. [23] for kindly providing high quality visualizations of their experimental investigation of cloud cavitation about a sphere, as well as for fruitful discussions.

REFERENCES

[1] Schnerr, G. H., Sezal, I. H. and Schmidt, S. J.,"Numerical Investigation of Three-dimensional Cloud Cavitation with Special Emphasis on Collapse Induced Shock Dynamics." *Phys. Fluids*, Vol. 20, issue 4, 2008, 040703.

[2] Schmidt, S. J., Sezal, I. H., Schnerr, G. H., and Thalhamer, M., "Riemann Techniques for the Simulation of Compressible Liquid Flows with Phase-transition at all Mach numbers - Shock and Wave Dynamics in Cavitating 3-D Micro and Macro Systems." In: *46th AIAA Aerospace Sciences Meeting and Exhibit, 7 - 10 January 2008, Reno, Nevada, USA*, AIAA paper 2008-1238, 2008.

[3] Brennen, C. E., *Cavitation and Bubble Dynamics*, Oxford Engineering Science Series, Oxford University Press, New York, 1995.

[4] Reisman, G. E., Wang, Y. -C., and Brennen, C. E., "Observations of Shock Waves in Cloud Cavitation," *J. Fluid Mech.*, Vol. 355, 1998, pp. 255-283.

[5] Meister, A., "Asymptotic Single and Multiple Scale Expansions in the Low Mach Number Limit," *SIAM J. Appl. Math.*, Vol. 60, No. , 1999, pp. 256-271.

[6] Guillard, H., and Murrone, A., "On the Behavior of Upwind Schemes in the Low Mach Number Limit: II. Godunov Type Schemes," *Computers & Fluids*, Vol. 33, No. 4, 2004, pp. 655-675.

[7] Guillard, H., and Viozat, C., "On the Behavior of Upwind Schemes in the Low Mach Number Limit," *Computers & Fluids*, Vol. 28, No. 1, 1999, pp. 63-86.

[8] Schmidt, S. J., Sezal, I. H., Schnerr, "Compressible Simulation of High Speed Hydrodynamics with Phase Change," In: *ECCOMAS CFD 2006 - European Conference on Computational Fluid Dynamics*, edited by P. Wesseling, E. Onate, J. Périaux, 2006.

[9] Turkel, E., "Preconditioning Techniques in Fluid Dynamics," *Annual Review of Fluid Mechanics*, Vol. 31, 1999, pp. 385 - 416.

[10] Kunz, R. F, Boger, D. A., Stinebirg, D. R., Chyczewski, T. S., Lindau, J. W., Gibeling, H. J., Venkateswaran, S., and Govindan, T. R., "A Preconditioned Navier-Stokes Method for Two-Phase Flows with Application to Cavitation Prediction," *Computers & Fluids*, Vol. 29, No. 8, 2000, pp. 849-875.

[11] Huang, D. G., "Preconditioned Dual-Time Procedures and its Application to Simulating the Flow with Cavitations," *J. Comput. Phys.*, Vol. 223, No. 2, 2007, pp. 685-689.

[12] Senocak, I., and Shyy, W., "A Pressure Based Method for Turbulent Cavitating Flow Computations," *J. Comput. Phys.*, Vol. 176, No. 2, 2002, pp. 363-383.

[13] Müller, B., "Low Mach Number Asymptotics of the Navier-Stokes Equations and Numerical Implications," von Karman Institute for Fluid Dynamics, Lecture Series 1999-03, 1999.

[14] Sauer, J., "Instationär kavitierende Strömungen - Ein neues Modell, basierend auf Front Capturing (VoF) und Blasendynamik," Ph.D. Dissertation, Universität Karlsruhe, Karlsruhe, Germany, 2000.

[15] Venkateswaran, S., Lindau, J. W., Kunz, R. F., and Merkle, C. L., "Computation of Multiphase Mixture Flows with Compressibility Effects," *J. Comput. Phys.*, Vol. 180, No. 1, 2002, pp. 54-77.

[16] Delale, C. F., Schnerr, G. H., and Sauer, J, "Quasi-One-Dimensional Steady-State Cavitating Nozzle Flows," *J. Fluid Mech.*, Vol. 427, 2001, pp. 167-204.

[17] Berg, A., Iben, U., Meister, A., and Schmidt, J., "Cavitation in Hydraulic Tools Based on Thermodynamic Properties of Liquid and Gas," *Shock Waves*, Vol. 14, 2005, pp. 111-121.

[18] Schnerr, G. H., Schmidt, S. J., Sezal, I. H., and Thalhamer, M., "Shock and Wave Dynamics of Compressible Liquid Flows with Special Emphasis on Unsteady Load on Hydrofoils and on Cavitation in Injection Nozzles," Invited Lecture. In: *Proceedings CAV2006 - Sixth International Symposium on Cavitation*, CD- ROM publication, 2006.

[19] Paillère, H, Corre, C., and García Cascales, J. R., "On the Extension of the AUSM+ Scheme to Compressible Two-Fluid Models," *Computers & Fluids*, Vol. 32, No. 6, 2003, pp. 891-916.

[20] Chang, C. -H., and Liou, M. -S., "A robust and accurate approach to computing compressible multiphase flow: Stratified flow model and AUSM+-up scheme," *J. Comput. Phys.*, Vol. 225, No. 1, 2007, pp. 840-873.

[21] Harten, A., Lax, P. D., Lavermore, D., and Morokoff, W. J., "Convex Entropies and Hyperbolicity for General Euler Equations," *SIAM J. Numer. Anal.*, Vol. 35, No. 6, 1998, pp. 2117-2127.

[22] Huber, R., "Geschwindigkeitsmaßstabseffekte bei der Kavitationserosion in der Scherschicht nach prismatischen Kavitatoren," Report Nr. 102, Lehrstuhl und Versuchsanstalt für Wasserbau und Wasserwirtschaft, TU München, Munich, Germany, 2004.

[23] Brandner, P. A., Walker, G. J., Niekamp, P. N. and Anderson, B., "An Investigation of Cloud Cavitation about a Sphere." In: 16th Australasian Fluid Mechanics Conference, 2 – 7 December 2007, Crown Placa, Gold Coast, Australia, 2007.

[24] Trevena, D. H., "Cavitation and the Generation of Tension in Liquids," *J. Phys. D: Appl. Phys.*, Vol. 17, 1984, pp. 2139-2164.

[25] Delale, C. F., Okita, K., and Matsumoto, Y., "Steady-State Cavitating Nozzle Flows with Nucleation," *J. Fluids Eng.*, Vol. 127, 2005, pp. 770-777.

[26] Oldenbourg, R., *Properties of Water and Steam in SI-units*, Springer-Verlag, Berlin, 1989.
[27] Saurel, R., Cocchi, J. P., and Butler, P. B., "Numerical Study of Cavitation in the Wake of a Hypervelocity Projectile", *J. Propulsion and Power*, Vol. 15, No. 4, 1999, pp. 513-522.
[28] IAPWS, International Association for the Properties of Water and Steam.
[29] Kjeldsen, M., Arndt, R .E. A., and Effertz, M., "Spectral Characteristics of Sheet/Cloud Cavitation," *J. Fluids Eng.*, Vol. 122, 2000, pp. 481-487.
[30] Foeth, E.J., van Doorne, C.W.H., van Terwisga, T., and Wienke, B., "Time Resolved PIV and Flow Visualization of 3D Sheet Cavitation," *Exp. in Fluids*, Vol. 40, 2006, pp. 503-513.
[31] Schmidt, S. J., Sezal, I. H., Schnerr, G. H., and Thalhamer, M., "Shock Waves as Driving Mechanism for Cavitation Erosion," In: *ISAIF - International Symposium on Experimental and Computational Aerothermodynamics of Internal Flows*, edited by I. Trebinjak, CD-ROM publication, 2007.

E. Fifth publication

The fifth publication [69] places a focus on the numerical simulation of inertia driven dynamics of 3-D sheet and cloud cavitation on a NACA 0015 hydrofoil. Special emphasis is on the numerical analysis of the re-entrant flow, the break-up of the sheet cavity and the formation of clouds, as well as on self-excited instabilities in span-wise direction. It is demonstrated that these instabilities may be predicted by the assumption of inviscid flow and equilibrium thermodynamics. The importance of sufficient resolution in space and time is analyzed by a grid dependence study. Large scale characteristics are only weakly dependent on the resolution, while small scale structures are strongly grid dependent. The simulation predicts various irregular break-up patterns, hairpin and horseshoe vortices. These delicate flow features vary from cycle to cycle, strong periodicity is not observed for the investigated set-up. The development of the re-entry jet as part of the shedding mechanism is analyzed. Here, we observe significant vorticity production during the growth and the collapse of the sheet cavity. It is demonstrated that the vorticity production is caused by a discontinuity at the end of the attached part of the cavity where condensation takes place. The discontinuity is part of the re-entry flow and fulfills Rankine-Hugoniot conditions as known from gasdynamic shocks. Additionally, shocks due to collapsing fragments of clouds are computed. These shocks produce significant maximum loads of $2400\ bar$, particularly close to the trailing edge of the investigated hydrofoil. We conclude that the dynamics of sheet and cloud cavitation are essentially inertia controlled. Hence, the application of an inviscid flow model to simulate cavitating flows is justified as long as the boundary layers of the corresponding single-phase flow remain attached. The numerically predicted flow features agree well with the experimental observations of Kawanami et al [37].

I defined the test-cases, supervised the student who generated the grids and performed the computations, analyzed the results and prepared the manuscript.

Proceedings of the 7th International Symposium on Cavitation
CAV2009 – Paper No. 17
August 17-22, 2009, Ann Arbor, Michigan, USA

INERTIA CONTROLLED INSTABILITY AND SMALL SCALE STRUCTURES OF SHEET AND CLOUD CAVITATION

Steffen J. Schmidt, Matthias Thalhamer, Günter H. Schnerr
Technische Universität München - Fachgebiet Gasdynamik
Boltzmannstr. 15, D-85748 Garching, Germany
schmidt@flm.mw.tu-muenchen.de, http://www.lhm.mw.tu-muenchen.de/gd/

ABSTRACT
The present investigation focuses on the numerical simulation of inertia driven dynamics of 3-D sheet and cloud cavitation on a 2-D NACA 0015 hydrofoil. Special emphasis is put on the numerical analysis of the re-entrant flow, the break-up of the sheet cavity and the formation of clouds. We demonstrate that our CFD-Tool **CATUM** (**CA**vitation **T**echnische **U**niversität **M**ünchen) is able to predict even delicate 3-D flow features such as irregular break-up patterns, cavitating hairpin and horseshoe vortices, 3-D instabilities in spanwise direction and the formation and propagation of shocks due to collapsing clouds close to the trailing edge of the hydrofoil. The numerically predicted flow features agree well with the experimental observations of Kawanami et al [1].

INTRODUCTION
Kawanami et al [1] investigate the 3-D structure of the cavitating flow around a NACA 0015 hydrofoil with cord length l_{cord}=0.08 m and span l_{span}=0.15 m. The hydrofoil is placed within a rectangular test section, the angle of attack is 8.36°. They observe that the dimensionless spanwise length $l_{cav,s}/l_{cord}$ of the clouds is roughly proportional to the dimensionless length $l_{cav,c}/l_{cord}$ of the sheet cavity along the cord of the hydrofoil. Furthermore, they show the formation and shedding of multiple clouds if $l_{cav,c}<<l_{span}$ (**Fig. 1**). An interesting situation arises at the region of $l_{cav,c}/l_{cord}>0.5$, where Kawanami et al observe irregular break-up patterns. If $l_{cav,c}/l_{cord}\approx1$, then the irregular pattern is replaced by the shedding of one single cloud that covers the full width of the test section. Franc [2] refers the previously stated 3-D aspects of cloud shedding as being intrinsic instabilities - often referred as self-excited instabilities. Although the width of the test section might influence the characteristics of multiple shedding and irregular break-up, the physical origin of these instabilities seems to be determined by the cavity itself. It is known that the basic shedding mechanisms - the formation of re-entrant flow, the resulting separation of the sheet cavity, the formation of a downstream traveling spanwise vortex and the subsequent break-up into numerous cloudy structures - are mainly inertia controlled [3]. **The aim of this investigation is to demonstrate that the occurrence of irregular break-up patterns and of 3-D spanwise instabilities is essentially inertia controlled as well**. The key idea is to focus exclusively on the inviscid dynamics of cavitating flows by means of numerical simulation. This allows distinguishing inertia driven instabilities from instabilities due to viscosity/turbulence.

PHYSICAL MODEL
It is known that highly purified water can reach significant metastable thermodynamic states including tension [4]. The classical nucleation theory predicts that homogeneous nucleation is negligible for the typically arising flow conditions within hydraulic machinery. It is widely accepted that flow induced evaporation - cavitation - is dominated by heterogeneous processes such as the growth of liquid embedded gas bubbles [5]. Provided that the number density and the average size of heterogeneous nuclei are sufficiently large, the onset of evaporation occurs close to the saturation conditions defined by the Clausius-Clapeyron relation. Concerning natural (unpurified) water as working fluid within large scale hydraulic machinery, it is reasonable to neglect metastable thermodynamic conditions and to assume stable thermodynamic conditions exclusively. This assumption is questionable for operating conditions close to cavitation inception, yet it is sophisticated for sufficiently developed cavitating flow such as the investigated sheet and cloud cavitation. If we consider an open thermodynamic system at one instant in time $t=t_1$ with given total mass $m(t_1)$, total internal energy $U(t_1)$ and fixed volume V, then the fundamental laws of thermodynamics imply that the only stable thermodynamic state is the equilibrium state, denoted by the subscript "eq". It follows that the pressure $p_{eq}(t_1)$, the temperature $T_{eq}(t_1)$ and the mass specific Gibbs energy $g_{eq}(t_1)$ are spatially and temporally constant within the specified thermodynamic system. Moreover, the system has minimal total Gibbs energy $G_{eq}(t_1)$ and maximal total entropy $S_{eq}(t_1)$. This information provides a unique and complete specification of the thermodynamic state including the phase properties (e.g. the mass fractions of liquid and vapor) of the system at time instant $t=t_1$. The previous consideration is the thermodynamic basis for modeling and simulation of cavitating flows due to the following aspects.

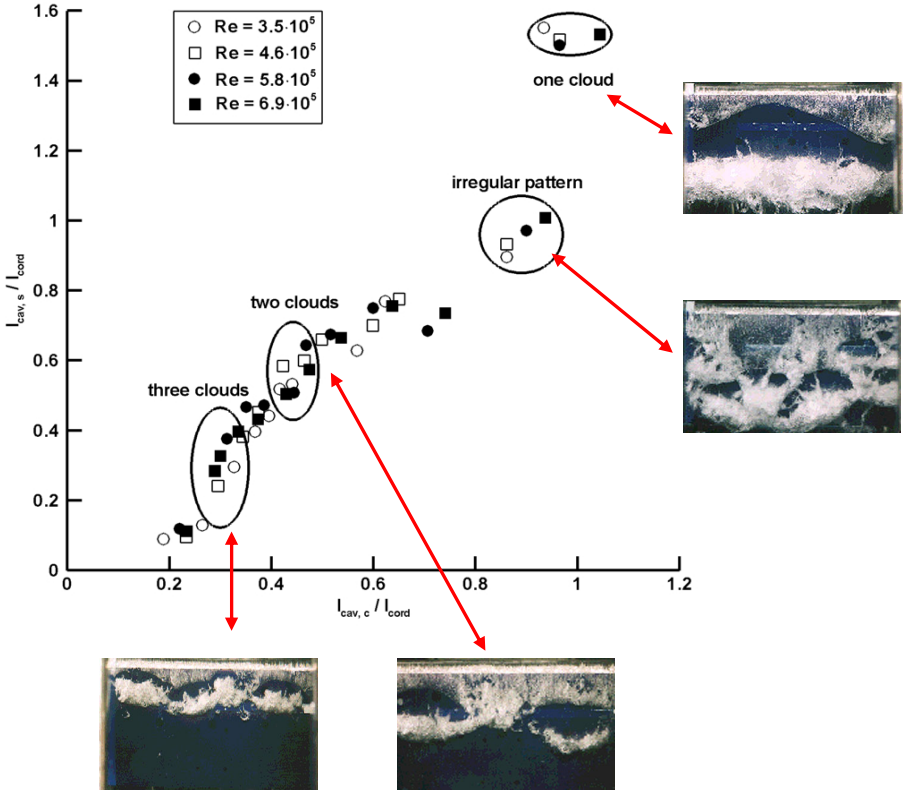

Fig. 1 **Multiple shedding of clouds on a 2-D NACA 0015 hydrofoil**
The arising cloud patterns show a correlation of the length $l_{cav,c}$ of the cavity along the cord with the spanwise length $l_{cav,s}$ of the shedded clouds. For $l_{cav,c}/l_{cord}\approx 0.8$ irregular break-up is observed, for $l_{cav,c}/l_{cord}\approx 1.0$ a single cloud is shedded.
NACA 0015, l_{cord}=0.08 m, l_{span}=0.15 m, 8.36° angle of attack, u_{in}=6.0 m/s -12 m/s, $T_{in}\approx$299 K, $Re_c=3.5\cdot10^5$ - $6.9\cdot10^5$, σ_{ref}=1.05 - 2.13, fluid water/water vapor.
The experiments indicate that the arising structures are independent of the Reynolds number.
Experiments and data from [1], reproduced with permission from Hajime Yamaguchi.

1) If the numerical method is a finite volume method, then the derivation of the stable thermodynamic state within each finite volume follows exactly the previously described consideration for each instant in time. The spatial resolution of the model is then consistent with the spatial resolution of the numerical approach, which is defined by the size of the finite volumes.
2) The phase properties are directly obtainable from the total mass and the total internal energy U within each finite volume. Contrary to other models, the thermodynamic model does neither require the specification of (unknown) parameters nor does it require the formulation and solution of additional transport equations.
3) The model takes compressibility effects into account. This is necessary for simulation of shock formation and propagation.
4) The model is applicable to simulate saturated mixtures as well as pure vapor sheets and pure liquid flow.
5) If the model is combined with a conservative numerical algorithm (conservative Euler solver), then the combination of both provides a mathematically well posed hyperbolic problem where the speed of sound is implicitly defined by the equilibrium speed of sound c_{eq}.
6) The model includes the effects of the latent heat due to phase transition.
As our major interests are intrinsic instabilities of wave and inertia driven flows the governing equations are the 3-D compressible time dependent Euler equations. Several experimental and numerical investigations show that the dynamics of developed cavitating flow is only weakly dependent on the Reynolds number (see **Fig. 1**). Presuming that

the boundary layers of the investigated flow remain attached as long as phase transition does not occur, the inviscid treatment of the fluid leads to suitable physical models that can be simulated significantly more efficient and more accurate than viscous fluids. However, the inclusion of viscous effects within the model is possible.

Let $\vec{q}$ be the vector of conserved quantities composed by the density ρ, the components u_i of the velocities in coordinate direction x_i and the specific total energy E as the sum of the specific internal energy e per unit mass and the specific kinetic energy $0.5 \cdot \sum (u_i)^2$. Let $F_i(\vec{q})$ be the physical flux in coordinate direction x_i, while δ_{ij} and p denote the Kronecker symbol and the pressure respectively

$$\vec{q} = \begin{pmatrix} \rho \\ \rho u_1 \\ \rho u_2 \\ \rho u_3 \\ \rho E \end{pmatrix}, \quad F_i(\vec{q}) = \rho u_i \cdot \begin{pmatrix} 1 \\ u_1 \\ u_2 \\ u_3 \\ E \end{pmatrix} + p \cdot \begin{pmatrix} 0 \\ \delta_{1i} \\ \delta_{2i} \\ \delta_{3i} \\ u_i \end{pmatrix}. \tag{1}$$

The differential or pointwise form of the Euler equations can be written as

$$\frac{\partial}{\partial t}\vec{q} = -\sum_{i=1}^{3} \frac{\partial}{\partial x_i} F_i(\vec{q}) . \tag{2}$$

Instead of enforcing the conservation principles in a pointwise fashion we use the weak form of the Euler equations. Therefore, we partition the flow domain into disjoint fixed control volumes C_k of a corresponding volume V_k, a surface S_k and an outer unit normal vector $\vec{n}_k = (n_{k,1}\ n_{k,2}\ n_{k,3})^t$. The weak form of the Euler equations for each control volume C_k follows as

$$\frac{d}{dt} \int_{C_k} \vec{q}\, dV_k = -\int_{S_k} \sum_{i=1}^{3} n_{k,i} F_i(\vec{q}) dS_k . \tag{3}$$

By defining the cell average operator A_k

$$A_k(\vec{q}) := \frac{1}{V_k} \int_{C_k} \vec{q}\, dV_k , \tag{4}$$

we assign to all weak solutions within the cell C_k their common integral average value $\vec{q}_k = A_k(\vec{q})$. It turns out that the weak form of the Euler equations resembles a system of evolution equations of the cell averages of weak solutions

$$\frac{d}{dt}\vec{q}_k = -\int_{S_k} \sum_{i=1}^{3} n_{k,i} F_i(\vec{q}) dS_k . \tag{5}$$

The closure of the defined initial-boundary value problem (5) necessitates constitutive relations for the thermodynamic quantities ρ_k, e_k, p_k as well as consistent initial and boundary conditions. In this section we assume that consistent initial and boundary data are available. Thus, the physical fluxes along the boundary surfaces are known and hence, equation (5) reduces to an initial value problem. At each instant in time and for each control volume C_k the known values $\vec{q}_k$ determine the average density ρ_k, velocity $\vec{u}_k$ and total energy E_k within the control volume C_k. Therefore, the average specific internal energy e_k is known as well. We now follow the thermodynamic considerations stated at the beginning of this section by interpreting each control volume C_k at each instant in time as an open thermodynamic system with known total mass m_k, total internal energy U_k and fixed volume V_k. In order to obtain the stable thermodynamic states p_{eq} and T_{eq} from the known conditions we relate them by suitable equations of state. The most accurate database for the thermodynamic properties of water, water vapor and saturated mixtures of water and water vapor is the IAPWS - International Association for the Properties of Water and Steam - database. They provide "state of the art" equations of state, so called reference equations of state [6]. Although it is possible to apply these equations to determine the unknown thermodynamic properties, we prefer to use suitable approximate equations. The reason therefore is given by the fact that the evaluation of the IAPWS equations is enormously time consuming. Although our approximate equations are significantly more efficient then the IAPWS equations, they are still highly accurate within the relevant thermodynamic regime of the considered flow. Following an idea of Saurel et al. [7], we distinguish the following three cases.

Case 1) The stable thermodynamic state corresponds to a **pure liquid state**. Here, we apply a modified Tait model

$$\frac{p_k + B}{p_{sat}(T_k) + B} = \left(\frac{\rho_k}{\rho_{l,sat}(T_k)} \right)^N \tag{6}$$

to relate the pressure p_k to the density ρ_k and the temperature T_k of the liquid. The temperature T_k is obtained by a caloric equation that relates the known specific internal energy e_k to the unknown temperature T_k. Even though the temperature variation of the liquid is typically small, the modification of the Tait equation remains necessary in order to ensure a continuous connection of the Tait model to the temperature dependent saturation conditions - see case 2). For water we use the constants B=3300 bar and N=7.15.

Case 2) The stable thermodynamic state corresponds to a **saturated mixture of water and water vapor**. The stable coexistence of both phases implies that the pressure p_k is determined by the Clausius-Clapeyron relation and the average density ρ_k within each cell C_k is a convex combination of the saturation densities $\rho_{l,sat}$, $\rho_{v,sat}$ of liquid and vapor. The temperature T_k is a function of the mass specific internal

energy e_k. By defining the vapor volume fraction α_k and the vapor mass fraction ε_k we obtain the unknown quantities T_k, α_k, ε_k and p_k as unique solutions of the system

$$\rho_k = \alpha_k \cdot \rho_{v,sat}(T_k) + (1-\alpha_k) \cdot \rho_{l,sat}(T_k) \tag{7}$$

$$e_k = \varepsilon_k \cdot e_{v,sat}(T_k) + (1-\varepsilon_k) \cdot e_{l,sat}(T_k) \tag{8}$$

$$\varepsilon_k \cdot \rho_k = \alpha_k \cdot \rho_{v,sat}(T_k) \tag{9}$$

$$p_k = p_{sat}(T_k) \tag{10}$$

$$0 < \alpha, \varepsilon < 1 . \tag{11}$$

Thereby, the incorporated temperature dependent saturation conditions are modeled by the Oldenbourg polynomials [8].

Case 3) The stable thermodynamic state corresponds to a **pure vapor state**. Here, the applied constitutive relation models pure vapor as calorically perfect gas, where the ratio of the specific heats is given by κ=1.327 and the specific gas constant is 461.5 J/kg K.

The comparison of the described thermodynamic closure relations with respect to the IAPWS data [6] demonstrates that the relations accurately model the behavior of water and water vapor for a large range of thermodynamic subcritical conditions, especially for the temperature range of 283 K ≤ T ≤ 350 K.

NUMERICAL METHOD

The CFD-Tool **CATUM** (**CA**vitation **T**echnische **U**niversität **M**ünchen) is based on a semi-discrete unsplit finite volume method that operates on block structured meshes. The spatial discretization is obtained by a modified flux function that enables time accurate simulations of compressible high and low Mach number flows including wave dynamics and shock propagation [9]. We apply non-linear reconstruction procedures (TVB, TVD) to the primitive variables and obtain 2nd order accurate approximations of smooth quantities as well as sharp representations of discontinuous flow features. The temporal discretization is obtained by a 2nd order accurate explicit 4-stage Runge-Kutta method with enlarged stability region. Our CFD-Tool **CATUM** relies on an approximate solution of the evolution equation (5) for each control volume C_k. The thermodynamic model is given by the constitutive relations (6)-(11). By replacing the physical fluxes $F(\bar{q})$ in Eq. (5) with the numerical fluxes $F(\bar{q}^*)$, we obtain a set of ordinary differential equations, which represent a semi-discrete unsplit finite volume method for hexahedral volumes

$$\frac{d}{dt}\bar{q}_k = -\sum_{i=1}^{6} S_{k,i} \cdot F(\bar{q}^*) . \tag{12}$$

For presentation purposes we assume that $\bar{q}_k$ and $\bar{q}_i$ are the average conserved quantities within two adjacent control volumes C_k, C_i and let $S_{k,i}$ be the shared surface $S_{k,i} = C_k \cap C_i$ which is supposed to be perpendicular to the x_1 spatial direction. We further assume that the x_1 spatial direction increases from C_k to C_i. Hence, the required flux is the approximate flux $F_1(\bar{q})$ in x_1 spatial direction. Provided that the flow is subsonic, the approximate states $\bar{q}^*$ at the shared surface are obtained by the following procedure. The approximate velocity u_1^* is given by

$$u_1^* := \frac{u_{1,k} + u_{1,i}}{2} + \frac{2 \cdot (p_k - p_i)}{\rho_k \cdot c_k + \rho_i \cdot c_i} . \tag{13}$$

The pressure p_k, the density ρ_k, the speed of sound c_k and the $u_{1,k}$ velocity component correspond to the cell average values within cell C_k, otherwise the values correspond to cell C_i. Equation (13) can be interpreted as an approximate solution for the resulting velocity of the associated Riemann problem between cells C_k and C_i. A detailed derivation of Eq. (13) based on the theory of characteristics was recently published (Schmidt et al [10]). The pressure p^* at the shared surface is defined by

$$p^* := \frac{p_k + p_i}{2} . \tag{14}$$

Assuming that the value of u_1^* as defined by Eq. (13) is positive, the upwind character of the discretization is obtained by defining the remaining quantities at the shared surface as

$$\rho^* := \rho_k, \quad u_2^* := u_{2,k}, \quad u_3^* := u_{3,k}, \quad E^* := E_k . \tag{15}$$

Otherwise, if u_1^* as defined by Eq. (13) is negative, the subscripts k in Eq. (15) are replaced by i. With these definitions the numerical fluxes are completely defined. In contrast to classical numerical flux functions the proposed numerical flux is consistent with respect to the asymptotic behavior of the governing equations for $M \to 0$. Therefore, the novel method enables the simulation of low Mach number flows including wave dynamics without the well known draw backs of classical schemes as stated in the introduction part of this investigation. The consistency with respect to $M \to 0$ is achieved by Eq. (14) which defines the pressure p^* at the shared surface as the arithmetic mean of the pressure within the adjacent cells. The proposed flux function is replaced by pure upwinding of all quantities if the flow is locally supersonic. In order to ensure high resolution of discontinuities such as shocks and contact waves we apply the minmod TVD-limiter to reconstruct the density field and the WENO-3 procedure to reconstruct the velocity field. This choice is based on the observation that the density field requires a monotone

reconstruction procedure in order to avoid oscillations in regions of large gradients, especially in regions where evaporation/condensation takes place.
The temporal discretization is obtained by a 4-stage Runge-Kutta method. The 2nd order accurate low-storage time discretization for cell C_k is given by

$$\bar{q}_k^0 := \bar{q}_k(t_0), \quad \bar{q}_k^i := \bar{q}_k^0 - \alpha_i \cdot \frac{\Delta t_{CFD}}{V_k} \cdot D_s(\bar{q}^i), \qquad (16)$$

$$\bar{q}_k\,(t_0 + \Delta t_{CFD}) := \bar{q}_k^4 \qquad (17)$$

Here, the expression $D_s(\bar{q}^i)$ corresponds to the spatial discretization as given by Eq. (12). In order to optimize the stability region of the method, numerical stability tests have been performed. The resulting coefficients $\alpha_{i=1...4}$ are $\alpha_1 = 0.11$, $\alpha_2 = 0.2766$, $\alpha_3 = 0.5$ and $\alpha_4 = 1.0$ which enable stable time integration for CFL-numbers up to 2.0. A detailed description of the CFD-Tool **CATUM** including validation examples is given by Schmidt et al. [10]. The derivation of weakly reflective boundary conditions for simulation of wave dynamics within cavitating flows is given by Schnerr et al. [11]. The numerical analysis of cavitating flows within fuel injection nozzles and around profiles of propeller blades are published by Schmidt et al.[12,13] and Sezal et al.[14].

NUMERICAL RESULTS

We simulate the cavitating flow around a 2-D NACA 0015 hydrofoil (angle of attack 6°, cord length l_{cord}=0.13 m, span width l_{span}=0.3 m) that is placed in the middle of a rectangular test section (height 0.3 m, depth 0.3 m, length 0.9 m). The walls of the test section and the surface of the hydrofoil are modelled as inviscid adiabatic walls. At the inlet of the numerical domain the velocity u_{in}=30 m/s and the static temperature T_{in}=293 K of the pure liquid inflow are prescribed.

At the outlet we apply an asymptotic boundary condition for the static pressure p_{exit}=4.5 bar. The resulting cavitation number is σ_{ref}=1.0. The numerical domain is discretized by $2 \cdot 10^5$ cells (coarse grid G1), $4 \cdot 10^5$ cells (medium grid G2), $3 \cdot 10^6$ cells (fine grid G3) and $2.4 \cdot 10^7$ cells (finest/target grid G4). All computational grids are structured multi-block hexahedral grids. Let Δx be the characteristic length of the smallest computational cell, then the numerical time step is necessarily of the order of $\Delta t_{CFD} \sim \Delta x / c_l$, where c_l is the speed of sound of pure liquid. Hence, the numerical time step Δt_{CFD} and the characteristic length Δx are directly related. The finest grid (target grid) used for this investigation leads to the characteristic length $\Delta x \approx 0.4$ mm of the smallest cells, which is at least one order of magnitude larger than the radius of a typical micro-bubble and definitely one order of magnitude larger than the Taylor microscale, which provides an indication of the minimum length scale on which inertia effects are still dominant over viscous effects. The resulting numerical time step for the finest grid is $\Delta t_{CFD,fine} = 8.5 \cdot 10^{-8}$s. These small numerical time steps are necessary to resolve wave dynamics such as shock formation and propagation. In order to accelerate the numerical simulation we apply a grid sequencing technique. At first, a simulation on the coarse gird is performed until the typical periodic shedding of the cavitating flow is observed. To determine the shedding frequency we analyse the integrated vapor volume content V_{vap} [%] within the computational domain. **Figure 2** depicts the temporal evolution of V_{vap} during the simulated time interval of $\Delta t_{sim} \approx 0.25$ s. The simulated time interval Δt_{coarse}=0.15 s on the coarse grid corresponds to approximately 17 shedding cycles. This time interval is sufficient to ensure that the disturbances due to the initialization of the flow field are no longer present. As the minimum cell size of the coarse grid is significantly larger than the one of the target grid, the numerical time step is larger as well. Additionally, the number of evolution equations (5) is by 2 orders of magnitude smaller. Thus, the numerical effort to simulate 17 shedding cycles on the coarse grid is about 500 times smaller than on the finest grid. The grid sequencing technique takes advantage of this fact by using the established

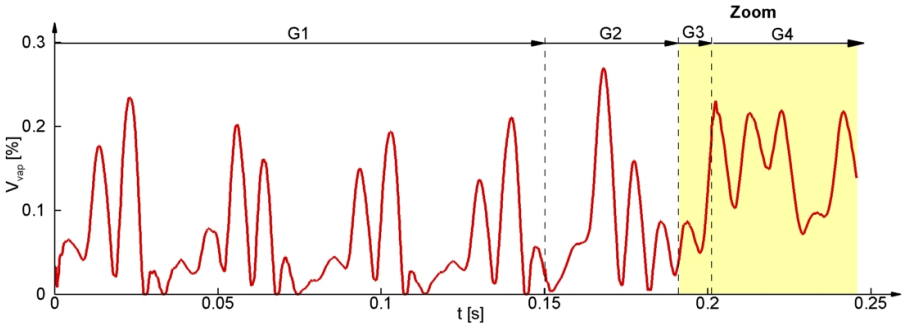

Fig. 2 **Temporal evolution of the total vapor volume content V_{vap} [%] within the computational domain**
Grid sequencing procedure applied to 4 successively refined grids: G1 - $2 \cdot 10^5$ cells (coarse grid), G2 - $4 \cdot 10^5$ cells (medium grid), G3 - $3 \cdot 10^6$ cells (fine grid), G4 - $2.4 \cdot 10^7$ cells (finest/target grid). The coarse grids G1/G2 contain low frequency disturbances that vanish on the finest grid. See **Fig. 3** for detailed information of the simulation on the finest grid G4. Shedding frequency f≈100 Hz, $\Delta t_{CFD,fine} = 8.5 \cdot 10^{-8}$ s.

solution obtained for the coarse grid as an improved initial solution for the following finer grids. Thereby, all necessary quantities are interpolated to the next finer grid in a conservative manner and the simulation is continued. Due to the significantly improved initial solution, the simulation of 1 to 5 consecutive shedding cycles is sufficient to obtain an established solution on the finer grid. The process is continued until the finest grid (target grid) is reached. **Figure 3** depicts the zoomed temporal evolution of V_{vap} during the simulated time interval of $\Delta t_{sim} \approx 0.05$ s on the grids G3 (fine) and G4 (finest). The marked time instants correspond to the subsequently analysed flow features. On the finest grid with $2.4 \cdot 10^7$ cells the simulation is performed on 192 processors. The required simulation time to simulate 5 shedding cycles is 4 weeks.

Single-phase reference solution

In order to relate the flow properties of the cavitating flow we calculate a single-phase reference solution of the same numerical set-up, including the same solution algorithm, computational grid (medium grid G2), initial and boundary conditions. We disable the phase transition routines of our numerical method and, hence, the thermodynamic model is given by Eq. (6). We observe a maximum velocity $u_{max}=53.1$ m/s and a minimum pressure coefficient $c_p=-2.37$ (corresponding to a minimum "pressure" of $p_{min}=-6.0$ bar). The numerically predicted drag coefficient is $c_{d,\,num} \approx 10^{-4}$, which is two orders of magnitude smaller than experimentally observed drag coefficients for comparable Reynolds numbers. **As expected, the single-phase flow field is perfectly two dimensional, e.g. the variation of the thermodynamic quantities and of the velocities in spanwise direction is of the order of the numerical round-off error (approx. 10^{-15} for normalized quantities)**.

The steady single-phase solution only depends on the boundary conditions but not on the initial conditions. Moreover, the inviscid single-phase solution is stable - any enforced disturbance damps out and the unique steady solution recovers.

Grid dependence of cavitating flows

Neither the assumed inviscid flow nor the thermodynamic model defines a physical limit of the spatial resolution. However, in practice the resolution is limited by the available hardware resources. The key questions are as follows.

1) Is the model suitable to predict the fragmentation of coherent structures such as clouds and sheets into smaller unities?

2) Are large scale properties such as shedding frequencies and characteristic void fraction distributions (basic shapes of sheet and cloud cavities) grid independent?

3) Provided that 1) and 2) are fulfilled, then how fine has the spatial resolution to be chosen in order to ensure that the desired flow information is resolved?

In order to investigate **1)** and **2)** we analyse the structure of the cavitating flow as obtained during the grid sequencing process. **Figure 4** depicts a comparison of the predicted vapor volume fraction of all four grids. The glossy surfaces are iso-surfaces of the vapor volume fraction $\alpha=0.05$. It is important to note that the depicted flow patterns do not correspond to the same instant in time. The reason therefore is that the applied grid sequencing technique operates consecutively from the coarsest to the finest grid. However, the depicted comparison of the resolved cavitation structures is still representative as it shows corresponding time instants with respect to the shedding process. Our observations are as follows. The simulation predicts the periodic shedding of at least one cloud - independent of the applied computational grid. The shedding frequencies are within a range of $f_{min}=90$ Hz to $f_{max}=107$ Hz. During the first 10 cycles the flow field on the **coarse** grid G1 is essentially two dimensional.

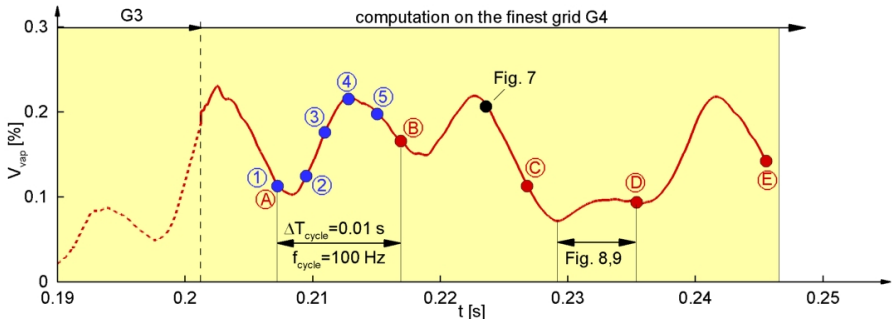

Fig. 3 **Zoom of Fig. 2 - total vapor volume [%] versus time - computation on the finest grid G4**
Dots **1** to **5** denote equidistant time instants $\Delta t=2 \cdot 10^{-3}$ s of one shedding cycle with $\Delta T_{cycle}=0.01$ s - see **Fig. 5**.
Dots **A** to **E** denote the break-up of the sheet cavity for 5 consecutive cycles - see **Fig. 6**.
The black dot denotes the time instant analysed in **Fig. 7**, the re-entrant flow analysis is performed within the marked time interval between dots **C** and **D** - see **Fig. 8,9**.
Shedding frequency $f \approx 100$ Hz, $\Delta t_{CFD,fine}=8.5 \cdot 10^{-8}$ s, grid resolution G4 - $2.4 \cdot 10^7$ cells.

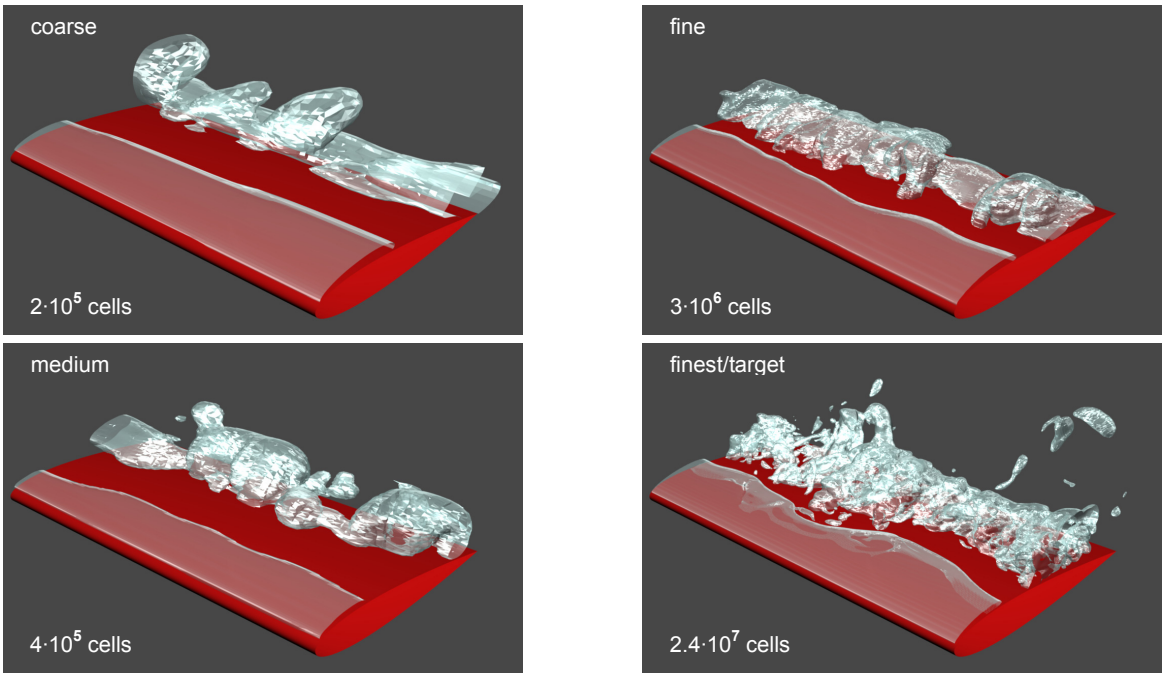

Fig. 4 **Increase of resolved cavitation structures on 4 different computational grids as obtained during grid sequencing**
Perspective view of the hydrofoil and iso-surfaces of the vapor volume fraction α=0.05.
Large scale structures are essentially grid independent, resolved small scale structures (richness of the flow) increases with grid refinement - grid dependence of unsteady cavitating flow. Observed 3-D instabilities are inertia driven (**inviscid** flow model) and develop naturally - self-excited instabilities. Shedding frequency f≈100 Hz, grid resolution G1 (coarse) - $2\cdot10^5$ cells, G2 (medium) - $4\cdot10^5$ cells, G3 (fine) - $3\cdot10^6$ cells, G4 (finest/target) - $2.4\cdot10^7$ cells.
NACA 0015, 6° angle of attack, l_{cord}=0.13 m, l_{span}=0.3 m, u_{in}=30 m/s, T_{in}=293 K, p_{exit}=4.5 bar, σ_{ref}=1.0, f_{cycle}≈100 Hz, T_{cycle}≈0.01 s.

After about 10 cycles the first spanwise variation of the shape of the cloud is visible. During a few subsequent cycles the spanwise variation intensifies and reaches a constant order of magnitude (**pic 1** of **Fig. 4**) - a return to a 2-D pattern is not observed. A possible explanation could be that the re-entry flow leads to the onset of the (**inviscid**) Rayleigh-Taylor instability. Thereby, the re-entry flow is lastingly altered in spanwise direction, which results in a non-uniform deformation of the sheet cavity. The first grid sequencing step to the medium grid does not significantly alter the characteristics of the flow field (**pic 2** of **Fig. 4**). The structure of the sheet cavity is still approximately 2-D close to the leading edge, but the richness of the structures within the cloud is slightly increased. The same observation is obtained at the second grid sequencing step to the fine grid. Here, we have to note that the simulation time on the fine grid is supposed to be too short to observe significant differences with respect to the medium grid. However, the last grid sequencing step to the target grid provides new insight into the arising dynamics. Both, the sheet and the cloud contain small scale structures that cannot be resolved on the coarser grids and the 3-D character of the predicted flow is well represented (**pic 4** of **Fig. 4**). The observed rise of small scale structures with increasing spatial resolution motivates the following conclusion. **Unsteady solutions of cavitating flows are typically grid dependent with respect to small scale properties.** However, large scale properties such as shedding frequencies and characteristic void fraction distributions (basic shape of sheet and cloud cavities) seem to be less dependent on the chosen spatial resolution.

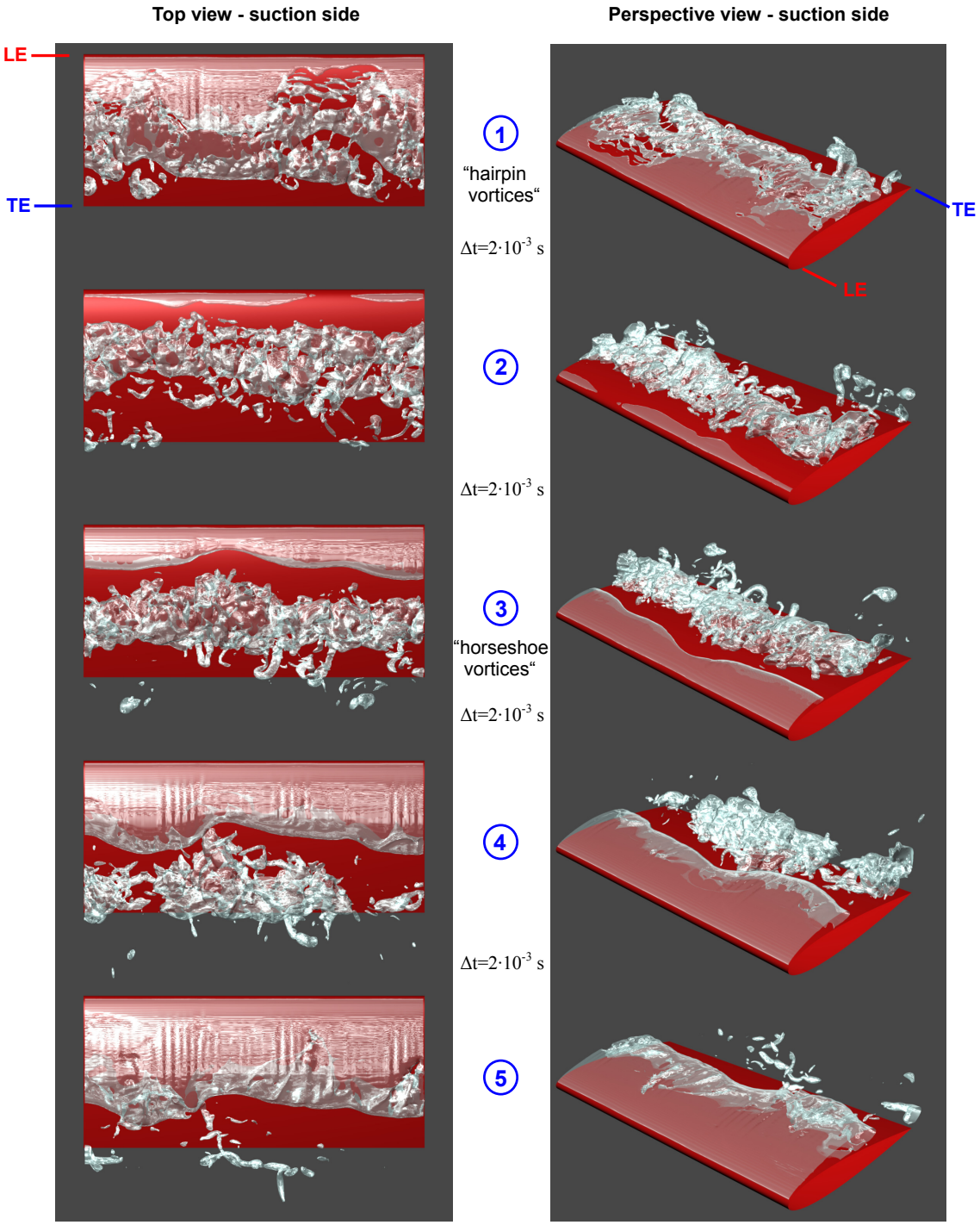

Fig. 5 **Numerically predicted cavitation structures at time instants 1-5 during the shedding cycle A-B as defined in Fig. 3**
Iso-surfaces of the vapor volume fraction α=0.05, top view - left, perspective view - right
Flow: water/water vapor, u_{in}=30 m/s, T_{in}=293 K, p_{exit}=4.5 bar, σ_{ref}=1.0, $f_{cycle}\approx$100 Hz, $T_{cycle}\approx$0.01 s
Hydrofoil: NACA 0015, 6° angle of attack, l_{cord}=0.13 m, l_{span}=0.3 m
Simulation: **CATUM**, finest grid G4 $2.4\cdot10^{7}$ cells, 2nd order in space and time, $\Delta t_{CFD}=8.5\cdot10^{-8}$ s.

Shedding pattern on the target grid

Figure 5 depicts a series of 5 equidistant instants in time of the arising cavitation structures during the shedding cycle **A**-**B** (**Fig. 3**) with $f_{cycle}\approx100$ Hz as observed on the **finest** grid with $2.4\cdot10^7$ cells. The 5 time instants are denoted by blue dots **1**-**5** along the temporal evolution of the vapor volume content V_{vap} in **Fig. 3.** The left column presents the top view of the suction side (**LE**-leading edge, **TE**-trailing edge) and the right column depicts the corresponding perspective view. The glossy surfaces are iso-surfaces of the vapor volume fraction α=0.05. Due to different illumination of the iso-surfaces the small scale disturbances of the sheet cavity are clearly visible within the top view but they are less pronounced within the perspective view. At time instant **1** we observe an irregular break-up of the cavity and the formation of cavitating hairpin vortices in streamwise direction. The hairpins connect the larger structures in spanwise direction, both together form crescent shaped regions [15]. At the right hand side, the re-entry flow nearly reaches the leading edge of the foil. The streamwise length of the cavity is $l_{cav}/l_{cord}\approx0.8$ at this instant in time. In accordance with Kawanami at al. [1] we observe a complete separation of the sheet cavity up to its onset close to the leading edge. At time instant **2** the formation of a new sheet cavity is partially visible. The irregular break-up pattern is integrated into a single coherent cloud. At time instant **3** the redeveloped sheet cavity covers roughly one third of the suction side of the hydrofoil. Close to the trailing edge we observe cavitating horseshoe vortices at the end of the downstream travelling cloud. At time instant **4** the downstream part of the sheet cavity is no longer fully attached to the surface of the hydrofoil and the downstream travelling cloud reaches the trailing edge where it fragments and collapses. At time instant **5** the sheet cavity nearly reaches its maximum length and the re-entrant flow is already present.

Comparison of arising break-up patterns

Although the previously described shedding process is periodic with respect to large scale dynamics it varies from cycle to cycle with respect to small scale phenomena. In order to indicate the bandwidth of small scale structures we discuss the break-up patterns for 5 consecutive shedding cycles **A**-**E** as defined within **Fig. 3**. The selected time instants correspond to the same relative position within the shedding process - the instant where the re-entrant flow reaches the onset of the sheet cavity close to the leading edge. **Figure 6** depicts a series of top views of the suction side of the hydrofoil. Glossy surfaces correspond to iso-surfaces of the vapor volume fraction α=0.05 and the flow is from top to bottom. The time interval between two successive pictures is $\Delta t=T_{cycle}=0.01$ s. The uppermost picture **A** of **Fig. 6** depicts the break-up pattern of the previously discussed shedding cycle **A**-**B**. The break-up patterns of the following two cycles (**Pics 2** and **3** of **Fig. 6**) contain 5 to 6 crescent shaped regions that occur at approximately the same positions. In cycle 4 we observe a break-up pattern that is biased to the left side of the sheet cavity. This pattern **D** distinguishes from all others as the length of the cavity along the cord is noticeably reduced. The lowermost picture of **Fig. 6** depicts the break-up pattern of cycle 5. **We conclude that the numerically predicted small scale structures undergo significant variations from cycle to cycle and the overall flow field is highly 3-D.**

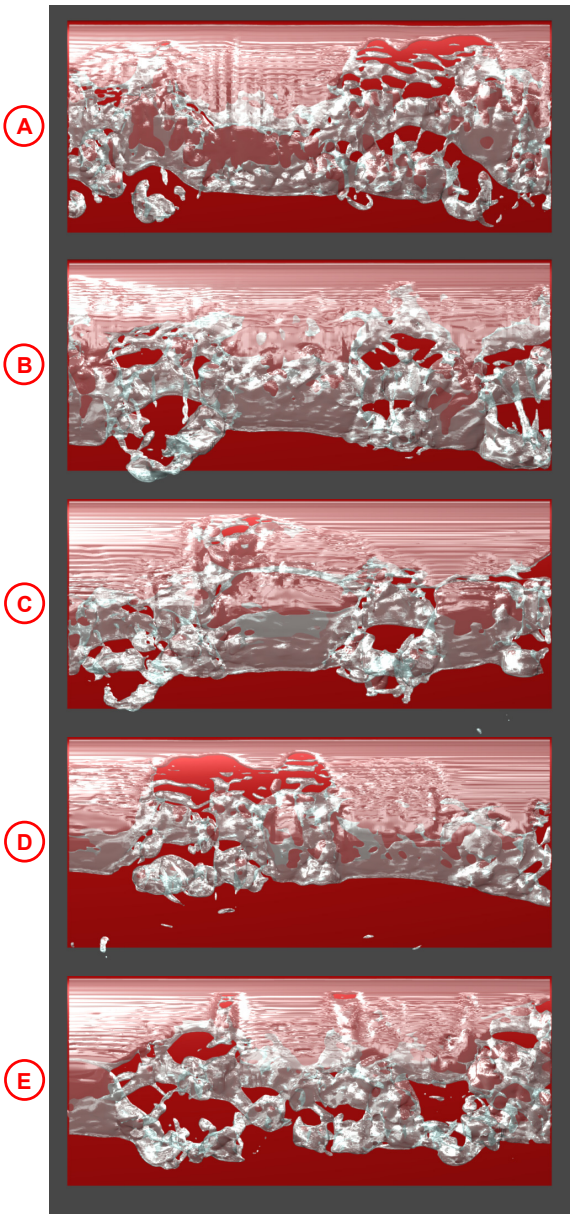

Fig. 6 **Break-up patterns A to E of 5 consecutive shedding cycles**
Top view of the suction side of the hydrofoil at time instants **A** to **E** with $\Delta t_{pic}=T_{cycle}=0.01$ s as denoted with red dots in **Fig. 3**. The selected time instants correspond to the same relative position within consecutive shedding cycles. Iso-surfaces of the void fraction α=0.05 demonstrate the occurrence of irregular break-up patterns including hairpin vortices and crescent shaped regions.
Finest grid G4 - $2.4\cdot10^7$ cells, $\Delta t_{CFD}=8.5\cdot10^{-8}$ s.

The predicted inner structure of a cloud

Figure 7 provides further insight into the arising small scale structures within a typical sheet and cloud cavitation pattern at one instant in time - see **Fig. 3**. We define the analysis plane A-A, which is indicated within the top view of the suction side of the hydrofoil (**Fig. 7** - top). The corresponding vapor volume fraction α within this plane is depicted at the bottom of **Fig. 7**. As expected, the void fraction α is approximately uniform within the sheet cavity. However, the downstream travelling cloud contains a significantly non-uniform distribution of the void fraction. The results of our simulations indicate that this non-uniformity is mainly due to superposition of cavitating vortices during the formation of the cloud. The inhomogeneity of the void fraction distribution and of the velocity field plays an important role at the stage of the cloud collapse. We observe that regions with low values of the void fraction partially condense during the advection of the cloud downstream to the trailing edge. The resulting fragmentation into smaller cloud structures lead to a series of violent cloud collapses including the formation and propagation of shocks with instantaneous pressure rises of up to 2400 bar. These shocks are known to be a driving mechanism of cavitation erosion. Moreover, they enforce total pressure losses, vorticity production and further alternation of the flow field.

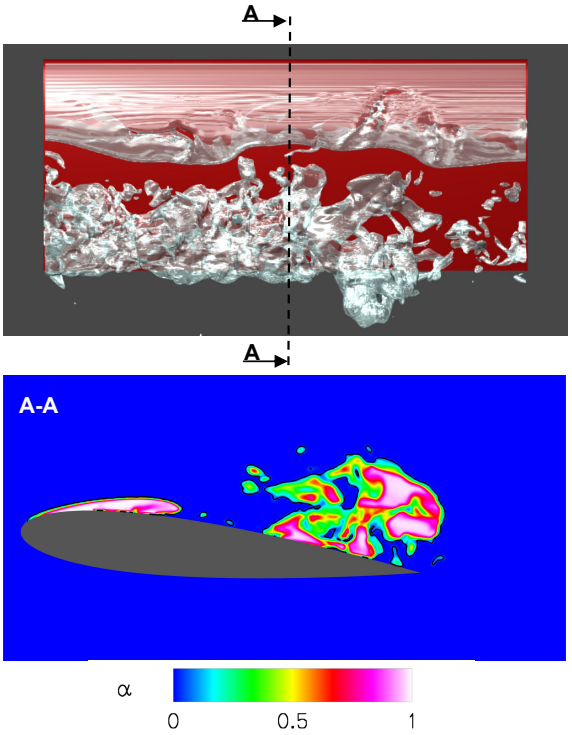

Fig. 7 **Inner structure of the cavity**
Top - typical sheet and cloud cavitation on the suction side of the hydrofoil, iso-surfaces of the void fraction α=0.05.
Bottom - void fraction α at plane A-A indicating the complex inner structure of the flow within the cloud.
Time instant is marked within **Fig. 3**.
Finest grid G4 - $2.4 \cdot 10^7$ cells, $\Delta t_{CFD} = 8.5 \cdot 10^{-8}$ s.

Analysis of re-entry flow

In this section we analyse the shedding process as it is predicted by the applied model. It is important to review that the model is based on the assumptions of inviscid and adiabatic flow and equilibrium thermodynamics within each computational cell. It can be shown that these assumptions imply that the total entropy remains constant along each particle path **as long as the flow is continuous (shock free)**. **However, the model predicts a discontinuous recondensation at the closure region of the sheet cavity. The states on both sides of the discontinuity fulfill the Rankine-Hugoniot conditions as known from gasdynamic shocks. We observe a maximum total pressure loss of up to 70% close to the surface of the hydrofoil and significant formation of vorticity. Figure 8** depicts a series of 5 instants in time with time intervals $\Delta t_{1\text{-}2} = 2.5 \cdot 10^{-3}$ s, $\Delta t_{2\text{-}3} = 1.5 \cdot 10^{-3}$ s, $\Delta t_{3\text{-}4} = 1.0 \cdot 10^{-3}$ s and $\Delta t_{4\text{-}5} = 1.0 \cdot 10^{-3}$ s. The complete time interval $\Delta t_{1\text{-}5}$ is marked in **Fig. 3**. The left column contains the vapor volume fraction α within the plane A-A as defined in **Fig. 7**. The right column shows the corresponding x component of the velocity. At the first time instant a recently developed sheet cavity nearly reaches the position of the thickness maximum of the hydrofoil. The sheet undergoes further growth along the cord of the hydrofoil and its closure region steepens up. The x component of the velocity within the sheet is $u_l \approx 44$ m/s and the static pressure is the vapor pressure. At time instant **2** the sheet cavity consists of two portions, an attached upstream part and a detached downstream part. The upstream part of the sheet is no longer growing - its position on the surface of the hydrofoil is frozen for a short time. At the end of the upstream part, particularly close to the surface of the hydrofoil, we observe a discontinuous variation of the void fraction and of the x component of the velocity u_l (black arrow in **pic 2** of **Fig. 8**). This is the position where significant vorticity production is observed - see subsequent section and **Fig. 9**. The velocity directly downstream of the discontinuity is nearly zero but further downstream a re-entry jet is already present and reaches a value of $u_l \approx -5$ m/s of the x component of the velocity. The downstream part of the sheet is still growing along the spanwise direction. At time instant **3** the reverse flow covers roughly one third of the thickness of the downstream part of the sheet ($\delta_{re\text{-}entrant} \approx 3$ mm). The x component of the velocity of the re-entrant jet is $u_l \approx -20$ m/s close to the end of the downstream part. Additionally, the two parts of the sheet are no longer directly linked together - the downstream part is from now on termed as cloud. The discontinuous transition at the end of the upstream part moves towards the leading edge with $u_l \approx -7$ m/s (position of black arrow in **pics 3,4** of **Fig. 8**). At time instant **4** the maximum thickness of the re-entry flow is $\delta_{re\text{-}entrant} \approx 7$ mm and the x component of the velocity is $u_l \approx -30$ m/s. The remaining attached sheet terminates slightly upstream to the thickness maximum of the hydrofoil and the cloud starts to grow in height. At time instant **5** the previously attached sheet forms another cloud as the re-entry flow reaches the onset position of the cavity close to the leading edge. The maximum value of the x component of the velocity of the re-entry flow at this instant in time is $u_l \approx -52$ m/s.

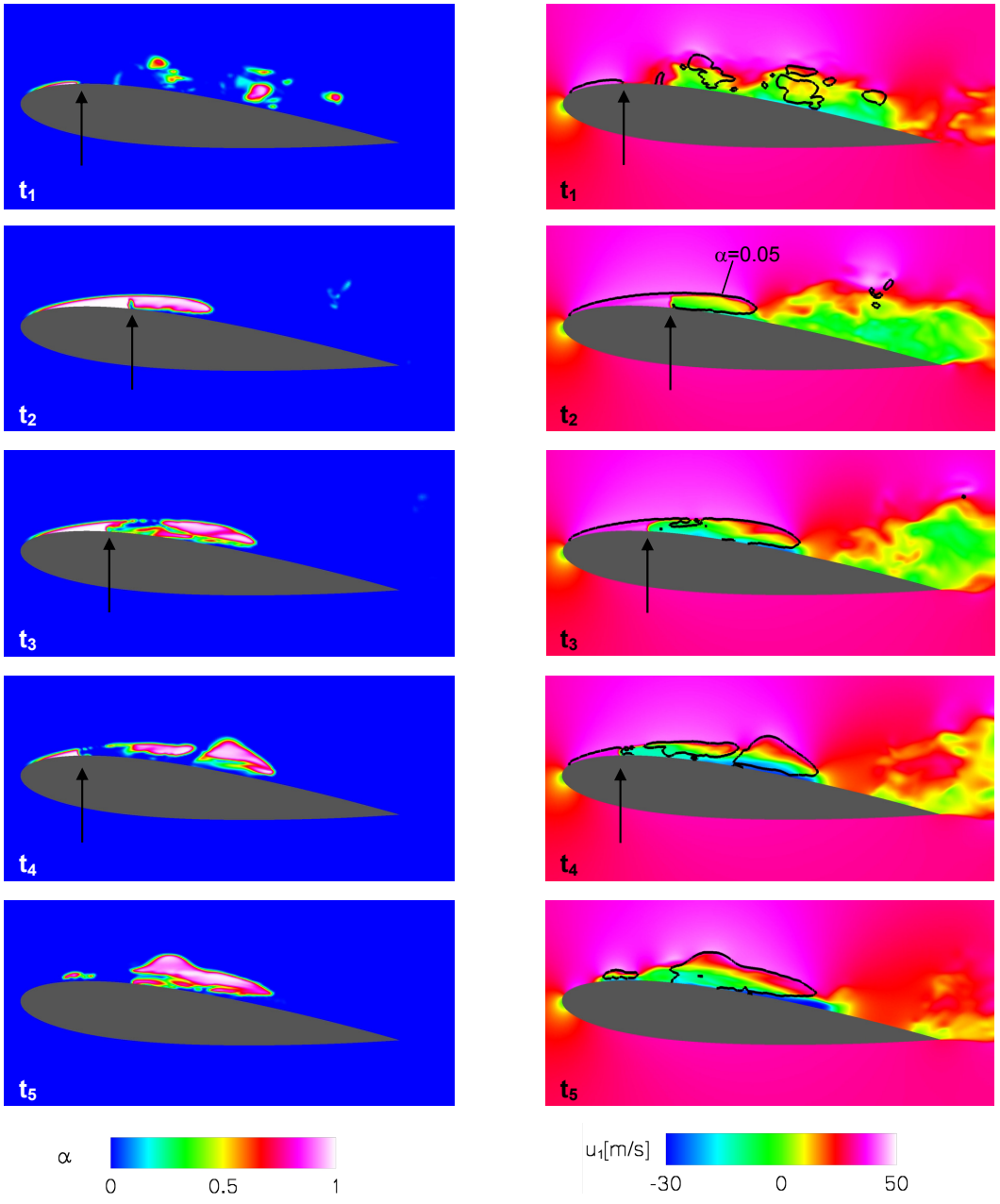

Fig. 8 **Development and subsequent separation of a sheet cavity - analysis of the re-entrant jet**
left void fraction α at 5 instants in time with intervals $\Delta t_{1\text{-}2}=2.5\cdot10^{-3}$ s, $\Delta t_{2\text{-}3}=1.5\cdot10^{-3}$ s, $\Delta t_{3\text{-}4}=1.0\cdot10^{-3}$ s, $\Delta t_{4\text{-}5}=1.0\cdot10^{-3}$ s.
right x component of the velocity u_1 corresponding to t_1 - t_5, black isolines correspond to the void fraction α=0.05.
The time interval t_1 - t_5 is indicated within **Fig. 3**. Arrows point to the attached part of the sheet where the discontinuity appears.
Finest grid G4 - $2.4\cdot10^7$ cells, $\Delta t_{CFD}=8.5\cdot10^{-8}$ s.

Vorticity production due flow discontinuities

As stated in the previous section, the predicted formation of vorticity is due to the discontinuous condensation at the closure region of the sheet during the growth process and during the collapse of the cavity. Hence, the flow is strongly rotational even before the re-entrant jet and the shedding mechanism become relevant. **Figure 9** corresponds to the same instant in time as **pic 2** of **Fig. 8**. The upper picture shows iso-surfaces of the vapor volume fraction α=0.05 on the suction side of the hydrofoil. The lower one depicts iso-surfaces of the magnitude $|\omega|=10^4$ 1/s of the vorticity vector. It is observed that the onset of strong vorticity is located within the sheet cavity, precisely at that location where the attached part of the cavity recondenses. The growth of the detached part of the sheet results in the advection of the vorticity along the hydrofoil (smooth iso-surface of **Fig. 9**). The fragmentation of the sheet and the subsequent cloud shedding alters the flow field and leads to a rich vortical flow pattern. It is obvious that such pronounced 3-D characteristics result in highly 3-D cavitation structures as observed and discussed within this investigation.

Shock induced maximum loads

The collapse of a cloud or of a small structure within a cloud enforces the acceleration of the surrounding liquid towards the center of the cloud, comparable to the flow field of an isolated sink. At the instance of the final collapse, a significant part of the kinetic energy of the surrounding liquid is transferred to the formation of a shock, which leads to the discontinuous deceleration of the velocity towards the center of the cloud. The approximately spherical shock front propagates with a velocity $u_S \approx 1500$ m/s through the liquid. Due to the rise of the pressure behind the shock, the collapse of surrounding clouds/bubbles is initiated or intensified. With respect to cavitation erosion this process is especially important if it takes place close to the surface of the hydrofoil. The CFD-Tool **CATUM** enables the simulation of shock formation and propagation [9-14] and provides a prediction of shock induced maximum loads on the surface of the hydrofoil. The key idea is to record the static pressure within all computational cells that are located at the surface of the hydrofoil for the time interval $\Delta t_{A\text{-}E}$=0.04 s as denoted within **Fig. 3**. The computational cells at the surface of the hydrofoil are thus interpreted as pressure transducers. The corresponding sampling frequency of the numerical transducers is $f_{sample} \approx 10^7$ Hz, the average area of each of the numerical transducers is 0.5 mm x 1.2 mm = 0.6 mm². Those positions where the highest pressure peaks are recognized provide an indication of erosion sensitive areas. **Figure 10** depicts an output of the numerical transducers. For each computational cell at the surface of the hydrofoil the maximum pressure during the time interval $\Delta t_{A\text{-}E}$=0.04 s is determined and visualized. We observe instantaneous maximum loads of 2400 bar close to the trailing edge of the hydrofoil. It should be noted that the analysed time interval $\Delta t_{A\text{-}E}$=0.04 s is extremely short compared to experimental investigations [16] on cavitation erosion. However, our previous investigations [13,14] indicate that 5 to 10 shedding cycles provide sufficient data to determine the locations where erosion is most likely to occur.

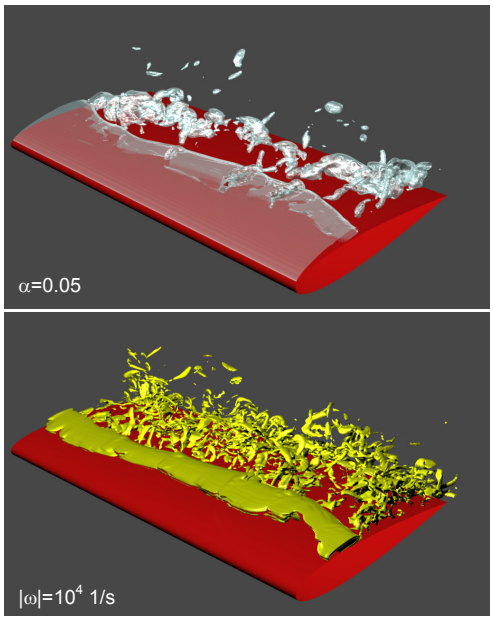

Fig. 9 **Correlation of void fraction α and vorticity |ω|**
Iso-surfaces of the vapor volume fraction α=0.05 (top) and iso-surfaces of the magnitude $|\omega|=10^4$ 1/s of the vorticity vector (bottom) on the suction side of the hydrofoil. The corresponding time instant $\mathbf{t_2}$ is defined in **Fig. 8**.
Finest grid G4 - $2.4 \cdot 10^7$ cells, $\Delta t_{CFD}=8.5 \cdot 10^{-8}$ s.

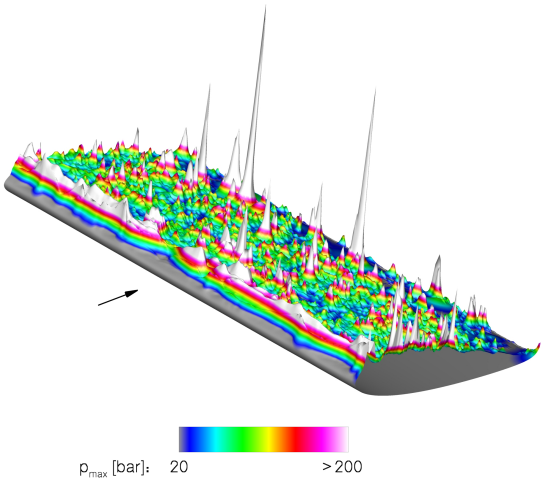

Fig. 10 **Instantaneous maximum loads**
Analysis of occurring maximum pressure within each computational cell at the suction side of the hydrofoil during the analysis interval **A** to **E** with $\Delta t_{A\text{-}E}$=0.04 s as defined in **Fig. 3**. The maximum pressure at the trailing edge is p_{max}=2400 bar.
Finest grid G4 - $2.4 \cdot 10^7$ cells, $\Delta t_{CFD}=8.5 \cdot 10^{-8}$ s.

CONCLUSION

The investigation focuses on wave and inertia driven mechanisms of cavitating flows. We apply the CFD-Tool **CATUM** (**CA**vitation **T**echnische **U**niversität **M**ünchen) to simulate the 3-D flow around a 2-D hydrofoil with special emphasis on self-excited instabilities in spanwise direction. It is demonstrated that these instabilities are predictable by the assumption of inviscid flow and equilibrium thermodynamics. The importance of sufficient resolution in space and time is analyzed by a grid dependence study. Large scale characteristics are only weakly dependent on the resolution while small scale structures are strongly grid dependent. The simulation predicts various irregular break-up patterns, hairpin and horseshoe vortices. These delicate features of the flow vary from cycle to cycle, strong periodicity is not observed for the investigated set-up. The development of the re-entry jet as part of the shedding mechanism is analyzed. Here, we observe significant vorticity production during the growth and the collapse of the sheet cavity. It is demonstrated that the vorticity production is caused by a discontinuity at the end of the attached part of the cavity where condensation takes place. The discontinuity fulfills Rankine-Hugoniot conditions as known from gasdynamic shocks. Contrary to the discontinuity related with the formation and break-up of the sheet cavity, we observe shocks due to collapsing fragments of clouds. These shocks produce significant maximum loads of $p_{max} \approx 2400$ bar, particularly close to the trailing edge of the investigated hydrofoil. We conclude that the dynamics of sheet and cloud cavitation are essentially inertia controlled. Hence, the application of an inviscid flow model to simulate cavitating flows is justified - provided that it is ensured that the boundary layers of the corresponding single-phase flow remain attached.

ACKNOWLEDGMENTS

We like to thank the KSB Stiftung Frankenthal, and the Deutsche Forschungsgemeinschaft DFG, Germany, for supporting our research on numerical simulation of cavitating flows including the prediction of erosion sensitive areas.

NOMENCLATURE

u, u_i	velocity, velocity components
c	speed of sound
M	Mach number
$\vec{q}$	vector of conserved quantities
$F_i(\vec{q})$	flux-vector in direction x_i
ρ	density
$\rho_{v,sat}$	saturation vapor density
$\rho_{l,sat}$	saturation liquid density
E	mass specific total energy
e	mass specific internal energy
U	total internal energy
p	static pressure
T	static temperature
α	vapor volume fraction
ε	vapor mass fraction
σ_{ref}	cavitation number
x_i	coordinate direction
Δt_{CFD}	numerical time step
V_{vap}	integrated vapor volume [%]
f	frequency
l_{cord}	cord length
l_{span}	span width
$l_{cav,c}$	length of the cavity along the cord
$l_{cav,s}$	spanwise length of a shedded cloud
$\delta_{re\text{-}entrant}$	thickness of re-entrant jet

REFERENCES

[1] Kawanami, Y., Kato, H., Yamaguchi, H. 1998, "*Three-Dimensional Characteristics of the Cavities Formed on a Two-Dimensional Hydrofoil*", Proceedings CAV1998 - Third International Symposium on Cavitation, Grenoble, France, pp. 191-196, 1998.

[2] Franc, J. P., 2001, "*Partial Cavity Instabilities and Re-Entrant Jet*", Invited Lecture, Proceedings CAV2001 - Fourth International Symposium on Cavitation, Pasadena, USA, CD- ROM publication, 2001.

[3] Franc, J. P., Michel, J. M. 2004, "*Fundamentals of Cavitation*", Kluwer Academic Publishers, Fluid Mechanics and its Applications, Volume 76, ISBN 1-4020-2233-6, p. 134, 2004.

[4] Trevena, D. H. 1984, "*Cavitation and the Generation of Tension in Liquids*", J. Phys. D: Appl. Phys., Vol. 17, pp. 2139-2164, 1984.

[5] Delale, C. F., Okita, K., and Matsumoto, Y. 2005, "*Steady-State Cavitating Nozzle Flows with Nucleation*", J. Fluids Eng., Vol. 127, pp. 770-777, 2005.

[6] IAPWS, International Association for the Properties of Water and Steam, www.iapws.org, "*The IAPWS Industrial Formulation 1997 for the Thermodynamic Properties of Water and Steam*", ASME J. Eng. Gas Turbines and Power, **122**, 150-182, 2000.

[7] Saurel, R., Cocchi, J. P., and Butler, P. B. 1999, "*Numerical Study of Cavitation in the Wake of a Hypervelocity Projectile*", J. Propulsion and Power, Vol. 15, No. 4, pp. 513-522, 1999.

[8] Oldenbourg, R. 1989, "*Properties of Water and Steam in SI-units"*, Springer-Verlag, Berlin, 1989.

[9] Schnerr, G. H., Schmidt, S. J., Sezal, I. H., and Thalhamer, M. 2006, "*Shock and Wave Dynamics of Compressible Liquid Flows with Special Emphasis on Unsteady Load on Hydrofoils and on Cavitation in Injection Nozzles*", Invited Lecture, Proceedings CAV2006 - Sixth International Symposium on Cavitation, CD- ROM publication, 2006.

[10] Schmidt, S. J., Sezal, I. H., Schnerr, G. H., and Thalhamer, M. 2008, "*Riemann Techniques for the Simulation of Compressible Liquid Flows with Phase-transition at all Mach numbers - Shock and Wave Dynamics in Cavitating 3-D Micro and Macro Systems*", Proceedings 46th AIAA Aerospace Sciences Meeting and Exhibit, Nevada, USA, AIAA paper 2008-1238, 2008.

[11] Schnerr, G. H., Sezal, I. H., Schmidt, S. J. 2008, "*Numerical Investigation of Three-dimensional Cloud Cavitation with Special Emphasis on Collapse Induced Shock Dynamics*", Physics of Fluids, Vol. 20, Issue 4, 2008.

[12] Schmidt, S. J., Sezal, I. H., Schnerr, G. H., and Thalhamer, M. 2007, "*Shock Waves as Driving Mechanism for Cavitation Erosion*," Proceedings ISAIF - International Symposium on Experimental and Computational Aerothermodynamics of Internal Flows, edited by I. Trebinjak, CD-ROM publication, 2007.

[13] Schmidt, S. J., Thalhamer, M., Schnerr, G. H. 2009, "*Density Based CFD Techniques for Simulation of Cavitation Induced Shock Emission*," Proceedings ETC - 8th European Turbomachinery Conference, Graz, Austria, pp. 197-208, 2009.

[14] Sezal, I. H., Schmidt, S. J., Schnerr, G. H., and Thalhamer, M. 2009, "*Shock and Wave Dynamics in Cavitating Compressible Liquid Flows*", Shock Waves, DOI 10.1007/s00193-008-0185-3, 2009.

[15] Reisman, G. E., Wang, Y. -C., and Brennen, C. E. 1998, "*Observations of Shock Waves in Cloud Cavitation*", J. Fluid Mech., Vol. 355, pp. 255-283, 1998.

[16] Huber, R. 2004, "*Geschwindigkeitsmaßstabseffekte bei der Kavitationserosion in der Scherschicht nach prismatischen Kavitatoren*", Report Nr. 102, Lehrstuhl und Versuchsanstalt für Wasserbau und Wasserwirtschaft, TU München, Munich, Germany, 2004.

F. Sixth publication

In the sixth publication [63] the collapse behavior of a random distribution of spherical bubbles is described. 125 spherical vapor bubbles with radii between $0.70\ mm$ and $1.65\ mm$ are located within liquid water above a solid wall. The initial pressure within the bubbles is vapor pressure at room temperature and the pressure far away from the bubble cluster is $40\ bar$. In order to reduce unphysical acoustics, a Laplace law is solved for the derivation of the initial pressure field. A series of 6 computational grids are used with 7^3 to 220^3 finite volumes in the region of the bubble cluster. The influence of the spatial resolution on the collapse duration, the maximum pressure at the wall and on the impulse strength is examined. The study shows that the thermodynamic equilibrium model allows for reliable predictions of collapse phenomena even if the spatial resolution is insufficient to resolve single bubbles. The obtained maximum pressure at the wall, the impulse strength and the collapse duration are nearly independent of the applied spatial resolution. These findings are of substantial importance since they indicate that even under-resolved simulations may allow for reasonable prediction of intense surface loads or erosion endangered areas.

The maximum pressure at the focal point of the main collapse increases proportional to grid refinement. A justification based on the linear decay law of spherical waves is provided [85]. Although viscosity, surface tension, non-condensable gas content and non-equilibrium physics are neglected, typical phenomena such as indentation of bubbles, focusing of the collapse front and rebounds of bubbles are predictable when using a thermodynamic equilibrium model.

The most important finding presented in this publication is the suitability of the proposed thermodynamic model to compute fully resolved, marginally resolved and under-resolved bubble clusters. In the latter case the approach provides an efficient sub-grid scale model for sufficiently dense bubble clusters.

I defined the test-case, developed and implemented the random bubble generator, implemented the Laplace solver for the initial pressure field, proposed the decay law, partially analyzed the results and prepared the manuscript.

F. Sixth publication

WIMRC 3rd International Cavitation Forum 2011
University of Warwick, UK, 4th-6th July 2011

Assessment of the Prediction Capability of a Thermodynamic Cavitation Model for the Collapse Characteristics of a Vapor-Bubble Cloud

Steffen J. Schmidt*, Michael Mihatsch, Matthias Thalhamer and Nikolaus A. Adams

Institute of Aerodynamics and Fluid Mechanics
Technische Universität München
Boltzmannstr. 15, D-85748 Garching, Germany
*steffen.schmidt@aer.mw.tum.de

ABSTRACT

A large number of numerical approaches have been developed for simulating cavitating flows. One model, which is recently applied within the CFD community, is the thermodynamic equilibrium approach. With this approach, the density and the internal energy are the only quantities necessary for specifying the mixture of liquid and vapor in a computational cell. The objective of the present investigation is to demonstrate that with thermodynamic equilibrium approaches even poorly resolved cloud-collapse events (typical for current CFD capabilities applied to complex systems) may provide important information for the prediction of erosion sensitive areas - provided that the temporal resolution of the numerical method is sufficiently high. By performing a sensitivity analysis of the main collapse characteristics with regard to the grid resolution we obtain an uncertainty estimation of the applied methodology.

1. INTRODUCTION

The design of hydraulic machines such as ship propellers, turbines, pumps, injection systems and throttles requires model testing. In particular, the assessment of the probability of cavitation erosion is a severe challenge. However, model tests can be very costly and they may not always provide a perfect representation of the suggested real-scale machinery. A promising way to reduce costs would be reliable CFD simulations. However, the uncertainty of numerical approaches is often too big to provide a secure validation of a suggested design. One reason could be that CFD approaches provide too many degrees of freedom for the user. For example, the proper choice of the grid resolution and the choice of a suitable numerical discretization scheme are sometimes strongly case-dependent. Therefore, "best practice guides" can typically provide only hints instead of sustainable recommendations. In particular, thorough uncertainty quantification is mostly missing. With regard to cavitating flows, the choice of the cavitation model and of case-specific parameters enhances the complexity of modeling and simulation. Of course, expert knowledge is one important key to interpret and to evaluate numerical predictions. Surely, this knowledge will not be replaced by "computer decisions" within the next decade.

Our objective is to develop numerical methods and physically motivated models that reduce uncertainty as much as possible. Additionally, widely applicable numerical methods must be robust with respect to varying operating conditions, and they should require as few predefined parameters as possible. Even if parameter-based models may outperform parameter-free models for selected test-cases, the quality of the prediction is often strongly dependent on a proper choice of the (mainly unknown) parameters. Hence, our developments focus on parameter-free models such as the thermodynamic equilibrium model.

During the last two decades, a wide variety of physical models have been developed for simulating cavitating flows. Typically, these models are incorporated into finite volume methods to obtain approximate solutions of the balance laws of mass, momentum and (sometimes) energy, together with the vapor volume fraction for each computational cell. Thereby, Eulerian-Eulerian approaches are predominant.

We define the following length-scale ratio $\psi:=\Delta_{flow}/\Delta_{CFD}$ where Δ_{flow} is the characteristic length of two-phase structures and Δ_{CFD} corresponds to the characteristic length of a computational cell. In case of $\psi=\Delta_{flow}/\Delta_{CFD}>>1$, two-phase structures are perfectly resolved by the computational cells, while for $\psi=\Delta_{flow}/\Delta_{CFD}<<1$ the structures might be approximated as homogeneous mixture. A particular difficulty arises for $\psi=\Delta_{flow}/\Delta_{CFD}\approx 1$, since two-phase details are neither resolved, nor can they be represented as dispersed mixture. For simulation of cavitating flows, three entirely different Eulerian-Eulerian two-phase approaches will be briefly discussed.

1) Sharp interface models (require $\psi=\Delta_{flow}/\Delta_{CFD}>>1$)

Sharp interface techniques are preferred to investigate the physics of a small number of bubbles in detail. Since the objective of sharp interface methods is to resolve physical phenomena within the bubble as well as along the bubble surface, the required numerical resolution Δ_{CFD} is at least one or two orders of magnitude smaller than the typical diameter of a bubble Δ_{flow}. However, this requirement results in an infeasibility of sharp interface methods to simulate cavitating flow problems with several thousands of bubbles, such as common cloud cavitation. Yet they might be perfectly adequate to simulate pure sheet cavities, as long as the sheets do not disintegrate into clouds.

2) Mixture models assuming a homogeneous dispersion of bubbles (require $\psi=\Delta_{flow}/\Delta_{CFD}<<1$)

Mixture models are typically based on the assumption that the size of a computational cell Δ_{CFD} is sufficiently larger than the diameter of a typical bubble Δ_{flow}. If this assumption is justified, one could model the fluid as dispersed mixture within each computational cell (bubbly flow model). In this case, the temporal evolution of the bubble diameter is often approximated by a modified Rayleigh-Plesset equation (or by simple finite-rate equations). Obviously, the approach is questionable as soon as the size of the bubbles reaches or even exceeds the cell-size of the adopted computational grid. Therefore, these methods are neither designed to simulate clear sheet cavities nor to simulate the collapse of a (resolved) bubble.

3) Thermodynamic equilibrium models (no requirement on ψ)

Thermodynamic equilibrium models are based on the assumption that for each computational cell the density ρ and the internal energy e determine the condition of aggregation, as well as unknown thermodynamic states, such as pressure and temperature. The evaluation of unknown states requires either closed-form equations or tabulated data. Since thermodynamic equilibrium models are free of intrinsic length and time scales, they provide an interesting option for simulating cavitating flows. If a flow detail (for example a single bubble) is resolved by the applied computational grid, then the thermodynamic equilibrium model implicitly captures the interface and performs comparable to a sharp interface technique. If the grid is too coarse to capture the detail, then the model behaves similar to a mixture approach. As a matter of principal, physical effects such as surface tension or finite-rate evaporation cannot be incorporated into thermodynamic equilibrium models.

Our current research focuses on the assessment of the ability of thermodynamic equilibrium approaches to predict the characteristics of cavitating flows, especially the formation of sheet and cloud cavitation as well as collapsing clouds of vapor bubbles and generated shock waves. In this investigation we evaluate the sensitivity of a thermodynamic equilibrium model with respect to the applied computational grid. In particular, we investigate the collapse characteristics of a cloud of vapor bubbles by resolved simulations and by under-resolved numerical simulations.

2. DESCRIPTION OF THE METHODOLOGY

2.1 Cloud Generation

We apply a numerical procedure to generate a random distribution of spherical bubbles. Although experimentally observed clouds certainly show a random character, we assume that the following additional properties are reasonable:

1) The "numerical cloud" consists of 125 spherical vapor bubbles with radii between $R_{min}\approx0.70$ mm and $R_{max}\approx1.65$ mm. The average radius is $R_{av}\approx0.95$ mm. The total vapor volume fraction is 5.8% with respect to the small domain.

2) The bubbles do not intersect; the minimum distance between two bubbles is 0.2 mm.

3) We assume that bubbles are larger and more densely spaced around the center of the cloud than at the outer regions

4) The cloud is located within a liquid-filled cubic domain of 20x20x20 mm³ – see **figure 1**. This domain is embedded into a larger rectangular domain of 4x4x2 m³. The bottom faces of both domains are coplanar and impermeable for representing a solid wall. The other faces of the outer domain correspond to far-field boundaries.

Since we apply a thermodynamic equilibrium approach, we need to simplify the test-case by neglecting surface tension and non-condensable gas content, and we assume the following properties:

1) The initial pressure p_B inside the bubbles is equal to the vapor pressure $p_{sat}=2340$ Pa at T=293 K.

2) The initial pressure within the surrounding liquid satisfies a Laplace law, where the pressure sufficiently far away from the bubbles is p_∞=const.=40 bar, and the pressure at the bubble surfaces is equal to the vapor pressure $p_{sat}=2340$ Pa.

3) The velocity field is initially at rest.

4) The initial temperature is T=293 K.

5) Viscous effects are negligible.

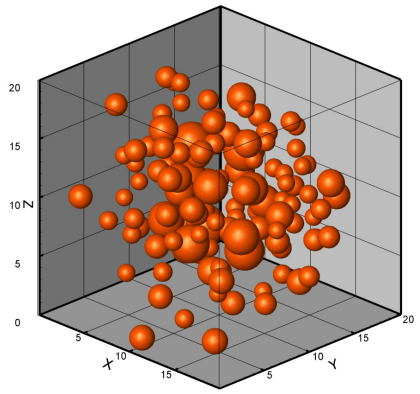

Figure 1: Cloud with 125 spherical non-intersecting vapor bubbles within the small cubic domain of 20³ mm³. The total vapor volume fraction is 5.8% with respect to the volume of the small domain. The lower boundary at z=0 is modeled as solid wall; the other boundaries are connected to a huge outer domain of 4x4x2 m³ (not shown here).

2.2 Discretization of the cloud and applied grids

The simulation of the collapse of the previously described "numerical cloud" requires a discrete representation of the specified properties. We adopt 6 different computational grids to discretize the small domain where the cloud is located. The grids consist of uniform hexahedrons and the resulting numerical resolutions Δ_{CFD} are listed in **table 1**.

	Number of cells	Δ_{CFD}	$\psi := \Delta_{flow}/\Delta_{CFD}$
Grid 1	$220^3 \approx 1.1 \cdot 10^7$	0.09 mm	≈ 16 - 36
Grid 2	$110^3 \approx 1.3 \cdot 10^6$	0.18 mm	≈ 8 - 16
Grid 3	$55^3 \approx 1.7 \cdot 10^5$	0.36 mm	≈ 4 - 8
Grid 4	$28^3 \approx 2.2 \cdot 10^4$	0.71 mm	≈ 2 - 4
Grid 5	$14^3 \approx 2.7 \cdot 10^3$	1.43 mm	≈ 1 - 2
Grid 6	$7^3 \approx 3.4 \cdot 10^2$	2.86 mm	≈ 0.5 - 1

Table 1: Properties of the applied computational grids to discretize the small domain. Δ_{CFD} is the cell length; ψ is the ratio of diameters of the bubbles and the cell length.

On the finest computational grid (Grid 1) each of the smallest bubbles is resolved by at least 2000 cells and each of the largest bubbles is resolved by about 25000 cells.

The analytically defined initial conditions are mapped to the grids by the following approach. First, we detect all computational cells that are either completely inside or completely outside of the bubbles. These cells are marked as "pure state cells". The remaining cells are necessarily "cut cells" that contain liquid and vapor. In case of a "cut cell" we perform an accurate evaluation procedure to obtain the vapor volume fraction α within the cell. Since we assume that the initial temperature field is T=293 K within the whole domain, the thermodynamic properties of a cut cell are obtained by tabulated relations $e=e(\alpha,T)$, $\rho=\rho(\alpha,T)$, $p=p_{sat}(T)$. If a "pure state cell" contains vapor, then the thermodynamic properties of vapor at T=293 K and $p=p_{sat}(T)$ are prescribed. If a pure cell contains water, then the initial temperature T=293 K is assigned. The initial pressure field is determined by solving a Laplace equation within the complete domain (including the large outer region) where the pressure at the far-field is p_∞=40 bar. Only the pure liquid domain is altered since the properties of cut cells or "pure vapor cells" are kept constant. Once the discrete pressure field is available, the thermodynamic properties are specified by evaluating tabulated relations $e=e(p,T)$, $\rho=\rho(p,T)$. The described procedure is employed to provide the initial fields for each computational grid. The resulting discrete representations are shown in **figure 2**. One horizontal cut plane depicts the initial vapor volume fraction by using continuous coloring, and the remaining cut planes show the vapor volume fraction by using cell center coloring. The colored bottom plane indicates the initial pressure field. It can be seen that the bubble shapes are sharply represented by the fine grids 1 and 2, while they are completely under-resolved by the coarse grids 5 and 6. The grids 3 and 4 allow for partial resolution of the bubble shapes.

2.3 Numerical Method

We apply our flow simulation code CATUM (CAvitation Technische Universität München [1, 2]), which is a density based finite volume method employing a Low-Mach-number consistent flux function and an explicit time marching procedure. The spatial reconstruction of the velocity field is a WENO-3 procedure; density and internal energy are reconstructed by monotonic TVD limiters ("minmod"). Time marching is performed through an explicit low storage 4-step Runge-Kutta method with an optimized stability region. The combination of both methods results in a 2nd order numerical approach in space and time for smooth flow while ensuring a sharp representation of discontinuous flow features such as shocks and contact waves. In this investigation we focus on the simulation of inertia-driven effects and wave dynamics wherefore we neglect viscous effects. Hence, the governing equations are the compressible Euler equations.

The working fluids can be characterized by closed-form equations of state, or for complex fluids by look-up tables. In this investigation we use tabulated thermodynamic relations $p=p(\rho,e)$, $T=T(\rho,e)$, $\alpha(\rho,e)$. The tables are obtained from the IAPWS database [3] of equilibrium states of water and water vapor. In order to allow for the simulation of shock formation and wave propagation, the compressibility of the fluids (liquid and vapor) is taken into account. Hence, the numerical time step is necessarily proportional to the ratio of the smallest length scale (minimum grid size) and the fastest signal speed (~ speed of sound of the liquid).

The phase transition model is based on local equilibrium assumptions for pressure, temperature and specific Gibbs functions.

Previous investigations [4, 5] showed that **CATUM** allows for the reliable prediction of erosion-sensitive areas by 3-D unsteady simulations of compressible cavitating flows including collapse-induced shock formation and propagation.

2.4 Simulation of the cloud collapse

The adopted explicit time marching scheme is subject to a numerical constraint on the time-step size (CFL condition). The constraint ensures that even the fastest information (propagating shocks) does not pass more then one computational cell per time step. For the present investigation, the CFL-number is kept constant at CFL=1.4 (4 stage low storage Runge-Kutta). Hence, the time-step sizes are proportional to the size of the cells of the adopted grid. The finest grid (grid 1) requires a time-step size of $1.95 \cdot 10^{-8}$ s, while for the coarsest grid (grid 6) the resulting time-step size is $6.24 \cdot 10^{-7}$ s. The remaining time-step sizes are as follows: $3.90 \cdot 10^{-8}$ s (grid 2), $7.80 \cdot 10^{-8}$ s (grid 3), $1.56 \cdot 10^{-7}$ s (grid 4), $3.12 \cdot 10^{-7}$ s (grid 5).

We adopt two "numerical pressure transducers" located at the center of the bottom wall. The larger transducer records the average static pressure on an area of 1x1 cm² while the smaller one covers an area of 1x1 mm². Both transducers store the static pressure for each instant in time, resulting in a maximum sampling frequency of $5.1 \cdot 10^7$ Hz (grid 1).

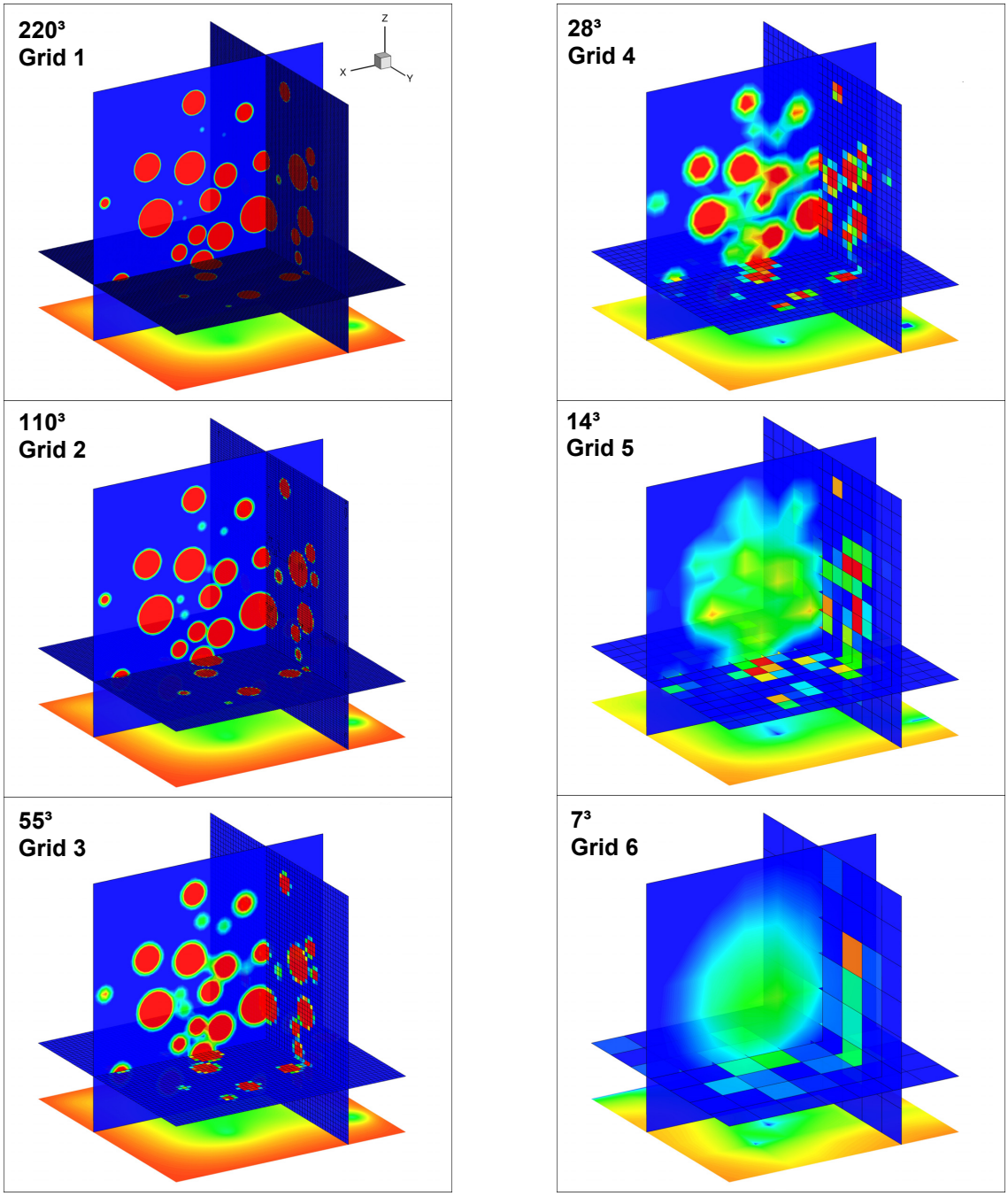

Figure 2: Discretization of the cloud by different computational grids. The forward faced plane depicts the vapor volume fraction α by using continuous coloring (red = pure vapor, blue = pure liquid, other colors represent mixtures). The remaining cut planes are colored by cell value coloring. At the bottom plane, the initial static pressure is depicted.

Aside from the "numerical pressure transducers", the maximum pressure within the complete flow field during each simulation is monitored. Furthermore, we analyze the time history of the total vapor volume within the domain.

The computations are performed on Intel Nehalem-EP based 8-way nodes and consumed 512 CPU-hours on grid 1, 21 CPU-hours on grid 2, 1 CPU-hour on grid 3, and negligible computation times on the coarse grids.

3. ANALYSIS OF THE NUMERICAL RESULTS

The analysis of the simulations focuses on the following characteristics. We evaluate the duration of the collapses by monitoring the total vapor volume. Only the first collapse is taken into account to determine the collapse duration. Since the observed rebounds are relatively weak, this criterion is justified. **Figure 3** depicts the time history of the vapor volume as predicted by the simulations. One observes that the predicted durations agree well for all resolutions. The maximum deviation from the predicted mean collapse duration occurs for grid 3 and is less than ± 6%. **Table 2** provides an overview of the observed collapse durations. Since experimental data are not available for the specific cloud and the specific boundary conditions, we utilize a simplified analytical estimate to evaluate the order of magnitude of the collapse duration. Therefore, we consider the Besant problem (collapse of a single spherical bubble within an infinitely large domain) of an "equivalent bubble". Based on the initial vapor volume of the cloud we obtain the radius R_{equiv}=4.8 mm of a single large bubble with equal vapor volume. This radius is applied to estimate the Rayleigh time (time required for the complete collapse, no gas content, no surface tension, incompressible liquid, spherical collapse). One obtains the analytic expression [6]

$$\tau_{tc} \approx 0.915 \cdot R_0 \cdot \sqrt{\frac{\rho_L}{p_\infty - p_v}}$$

where τ_{tc} is the collapse duration, R_0 the initial bubble radius, ρ_L the constant density of the liquid, p_∞ the constant far-field pressure and p_v the constant vapor pressure within the bubble. Using R_0=R_{equiv}=4.8 mm, p_∞=40 bar, ρ_L=1000 kg/m³ and p_v=0.023 bar one finds a collapse duration of τ_{tc}=6.94·10^{-5} s, which agrees well with the numerically predicted durations.

In the following, the instantaneous maximum pressures within the flow field as well as at the bottom wall of the small domain are analyzed. **Table 2** shows the grid dependence of the maximum pressure within the domain. We observe that the instantaneous maximum pressure within the domain varies by approximately two orders of magnitude. However, the maximum pressure at the wall shows only a weak variation of a factor of about two (see **figure 4**). To examine the numerical predictions we consider the propagation of a linear spherical pressure wave. The amplitude of a linear spherical wave decays inversely proportional to the radius of the wave front [7]. As soon as the wave impinges on the wall, it is reflected and the amplitude after the impingement is about twice the amplitude before the impingement.

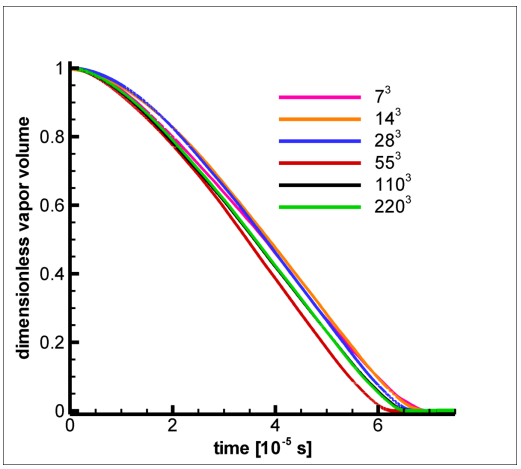

Figure 3: Time history of the dimensionless vapor volume as obtained with 6 different resolutions of the small domain.

	P_{max} (domain)	P_{max} (wall)	Collapse duration
Grid 1	3.14 ·10^9 Pa	4.1 ·10^7 Pa	6.5 ·10^{-5} s
Grid 2	1.17 ·10^9 Pa	3.9 ·10^7 Pa	6.6 ·10^{-5} s
Grid 3	0.63 ·10^9 Pa	3.6 ·10^7 Pa	6.3 ·10^{-5} s
Grid 4	0.34 ·10^9 Pa	3.5 ·10^7 Pa	6.7 ·10^{-5} s
Grid 5	0.12 ·10^9 Pa	2.8 ·10^7 Pa	6.9 ·10^{-5} s
Grid 6	0.07 ·10^9 Pa	1.9 ·10^7 Pa	7.0 ·10^{-5} s

Table 2: Comparison of the maximum pressure within the flow field as well as at the wall (small sensor) and duration of the collapse as observed for different numerical resolutions.

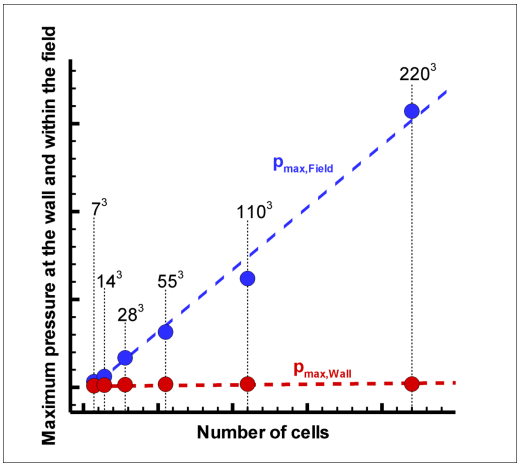

Figure 4: Scaling of the maximum pressures within the flow field (blue) and at the wall (red) with respect to the applied grid resolution.

By combining the linear decay law and the linear wave reflection at solid walls we obtain a (strongly) simplified relation of the maximum wall pressure to the maximum pressure within the flow field. We assume that the maximum wall pressure p_{wall} is the result of a reflected spherical wave at a distance D from its origin. Since the initial radius of the wave front cannot be smaller then half of the cell length Δ_{CFD}, we obtain the relation

$$\frac{p_{max,Field}}{p_{max,Wall}} \approx \frac{D}{\Delta_{CFD}}.$$

Assuming that the collapse is perfectly focused into one fixed point independently of the applied grid, one would expect that D is approximately constant (if nonlinear effects are negligible). By evaluating D we find the following distances of the assumed focus point to the bottom wall: D=7.0 mm (grid 1), D=5.5 mm (grid 2), D=6.4 mm (grid 3), D=6.9 mm (grid 4), D=6.1 mm (grid 5), D=10.6 mm (grid 6). All estimates are in a reliable range. Through this simple analysis we demonstrate that the increase of the observed maximum pressure within the flow field is not a numerical artifact but a physical property that is well captured by the applied methodology.

Figure 5 shows the output of the large pressure sensor (sensor area 1x1 cm², located at the center of the bottom wall). The black line is the signal obtained for grid 1 and the signal obtained with grid 6 is shown in red. The numerical sampling frequencies are 51 MHz (grid 1) and 1.6 MHz (grid 6). One can observe that the peak is more pronounced with the fine grid and the high temporal resolution. In the present case, the duration of the shock-induced peak pressure is only about 5 µs (grid 1). On the coarse grid 6 the amplitude of the peak is reduced and the peak is smeared. In order to compare the transducer signals for all 6 grid resolutions we evaluate the time integral of the pressure. Three evaluations are performed:

$$\text{Impulse Strength 1} := \int_0^{10^{-4}} p\,dt$$

$$\text{Impulse Strength 2} := \int_{5\cdot10^{-5}}^{8.5\cdot10^{-5}} p\,dt$$

$$\text{Impulse Strength 3} := \int_0^{10^{-4}} (p \geq 80\ \text{bar})\,dt$$

The first value corresponds to the impulse strength during 10^{-4} seconds and covers the complete collapse. Impulse strength 2 corresponds approximately to the time interval where the collapse-induced peak pressure is observed. The third value is obtained by integrating the pressure during the time interval where the pressure exceeds 80 bars (twice the far-field value). Although the specific threshold is somewhat arbitrarily chosen, it should allow for comparison of the pressure peaks. The obtained results are listed in **table 3**.

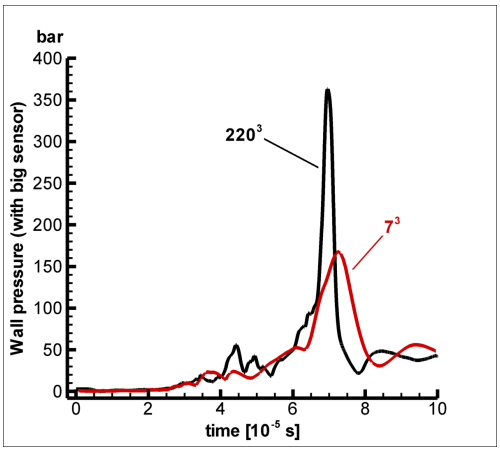

Figure 5: Comparison of the wall pressure as recorded by the numerical pressure sensor (area 1x1 cm²) by applying grid 1 (finest) and grid 6 (coarsest).

	Imp. Strength 1	Imp. Strength 2	Imp. Strength 3
Grid 1	$3.94\cdot10^2$ Pa·s	$2.86\cdot10^2$ Pa·s	$1.82\cdot10^2$ Pa·s
Grid 2	$3.90\cdot10^2$ Pa·s	$2.79\cdot10^2$ Pa·s	$1.77\cdot10^2$ Pa·s
Grid 3	$3.77\cdot10^2$ Pa·s	$2.79\cdot10^2$ Pa·s	$2.12\cdot10^2$ Pa·s
Grid 4	$3.94\cdot10^2$ Pa·s	$2.94\cdot10^2$ Pa·s	$1.99\cdot10^2$ Pa·s
Grid 5	$3.81\cdot10^2$ Pa·s	$2.83\cdot10^2$ Pa·s	$1.84\cdot10^2$ Pa·s
Grid 6	$3.74\cdot10^2$ Pa·s	$2.76\cdot10^2$ Pa·s	$1.84\cdot10^2$ Pa·s

Table 3: Comparison of the impulse strength as obtained with three different evaluation procedures. Criteria are specified above.

Finally, we present a series of snapshots (**figure 6**) of the collapse as predicted by using grid 1. The snapshots do not show equidistant time instants but provide an overview about the observed physical processes. **Pic 1** of **figure 6** shows the initial distribution of the bubbles, together with the static pressure on the wall. In **pic 2** a relatively isolated bubble has collapsed and a spherical shock is indicated by its footprint on the wall. **Pic 3** shows partially deformed bubbles and a slight increase of the pressure on the wall. In **pic 4** some of the bubbles are impinged by liquid jets (thus forming tori). **Picture 5** is the time instant of the final collapse and the occurrence of the maximum pressure within the complete flow field. However, the maximum pressure at the wall is observed slightly afterwards in **pic 6**. Here, already rebounding vapor structures are formed. The rebounding structures reach the maximum vapor volume at **pic 8** and collapse again at **pic 10**. **Picture 11** corresponds to the second rebound and **pic 12** shows the final stage after the third collapse.

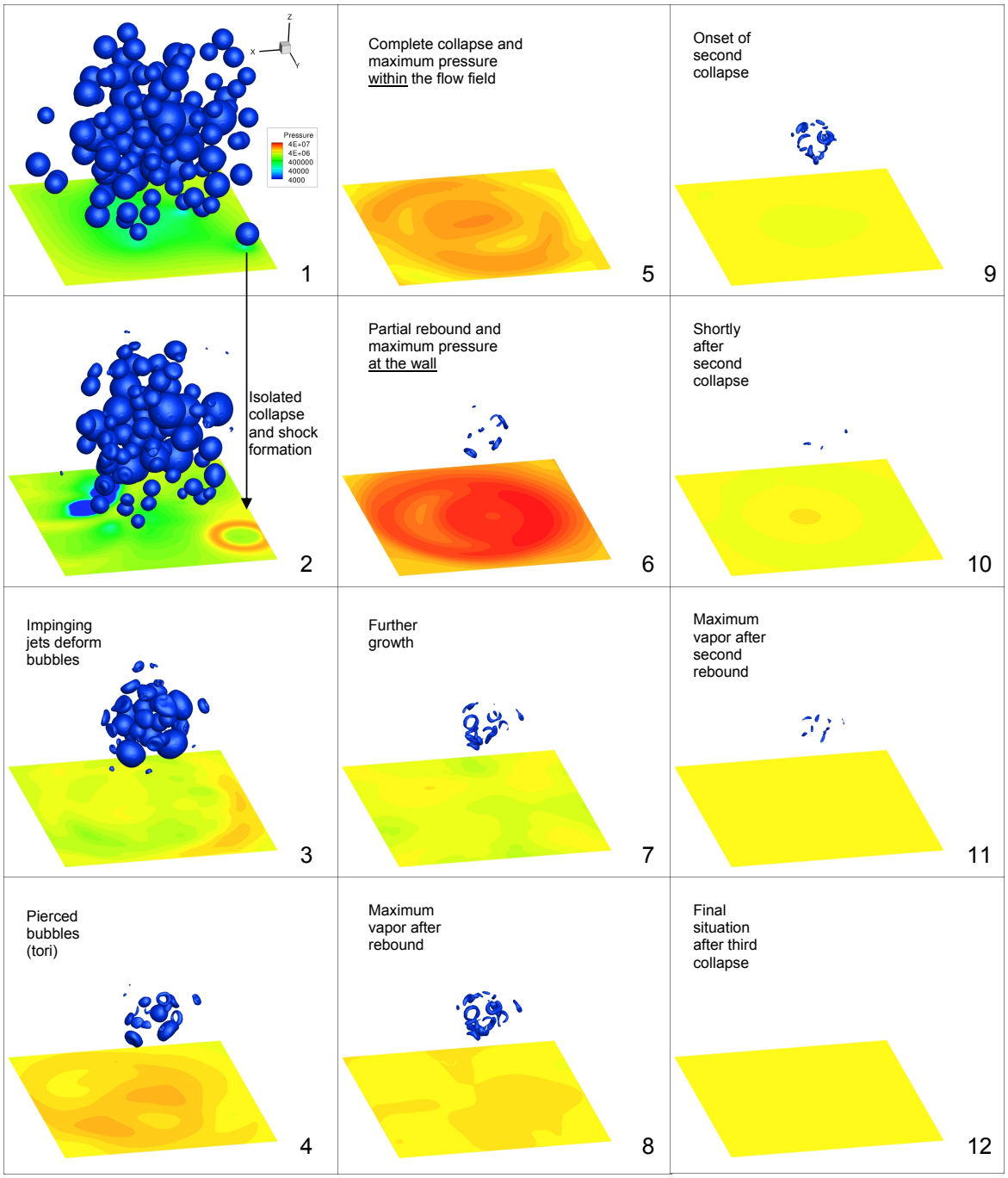

Figure 6: Snapshots of the numerically predicted collapse of the cloud (grid 1 was used).
Time instants: t_1=0 µs, t_2≈28 µs, t_3≈52 µs, t_4≈60 µs, t_5≈64 µs, t_6≈68 µs, t_7≈80 µs, t_8≈84 µs, t_9≈90 µs, t_{10}≈96 µs, t_{11}≈102 µs, t_{12}≈116 µs.

4. DISCUSSION AND FUTURE PROSPECTS

Our numerical investigation of the collapse characteristics of a cloud of bubbles leads to the following conclusions.

1) The combination of a thermodynamic equilibrium model with a density based finite volume method enables the simulation of collapsing vapor bubbles including the subsequent formation of strong shock waves. We conclude that taking compressibility effects into account and providing high temporal resolution are necessary to investigate cloud collapse phenomena.
2) The influence of the spatial resolution on the collapse duration, the maximum pressure at the wall and on the impulse strength is examined. We conclude that the thermodynamic equilibrium model allows for reliable predictions of collapse phenomena even if the spatial resolution is insufficient to resolve single bubbles. The obtained maximum pressure at the wall, the impulse strength and the collapse duration are nearly independent of the applied spatial resolution. This finding is of great importance since it substantiates the methodologies investigated in [4, 5] and [8, 9] to predict erosion-sensitive areas.
3) Although viscosity, surface tension, non-condensable gas content and non-equilibrium physics are neglected, detailed features of cloud collapses are predictable. A comparison of our results with a sharp interface method is planned.

Our current research focuses on the prediction of cavitation erosion by means of numerical simulations. We investigate break-up patterns of unstable sheet cavitation [2] as well as flow features that may be responsible for cavitation erosion. Aside of cavitating water flows [5] we consider cavitation of Diesel-like fluids in high-speed micro channels [8, 9]. Recent results promisingly indicate that the reliable prediction of cavitation erosion could be possible [8, 9]. Additional numerical investigations of the experiments discussed in [10, 11] are currently performed.

Further numerical developments will be the inclusion of viscous effects and of non-condensable gas content.

REFERENCES

[1] Schnerr, G.H., Sezal, I.H., Schmidt, S.J., "*Numerical Investigation of Three-dimensional Cloud Cavitation with Special Emphasis on Collapse Induced Shock Dynamics",* Physics of Fluids, Vol. 20, Issue 4, 040703, 2008.

[2] Schmidt, S.J., Thalhamer, M., Schnerr, G.H., "*Inertia Controlled Instability and Small Scale Structures of Sheet and Cloud Cavitation"* Proc. 7th CAV 2009 - 7th International Symposium on Cavitation, Ann Arbor, Michigan, USA, 16.8.- 21.8.2009, paper 17, CD-ROM publication, 2009.

[3] The International Association for the Properties of Water and Steam, http://www.iapws.org/

[4] Schmidt, S.J., Sezal, I.H., Schnerr, G.H., Thalhamer, M., "*Numerical Analysis of Shock Dynamics for Detection of Erosion Sensitive Areas in Complex 3-D Flows",* Proc. WIMRC Cavitation Forum 2008, pp. 107-120, July 7 - 9, 2008, Warwick, UK, 2008.

[5] Schmidt, S.J., Mihatsch, M., Thalhamer M., Egerer, C., Hickel, S., Adams, N.A., "*Assessment of Erosion Sensitive Areas via Compressible Simulation of Unsteady Cavitating Flows",* International Workshop on ADVANCED EXPERIMENTAL AND NUMERICAL TECHNIQUES FOR CAVITATION EROSION PREDICTION, Grenoble, France, 1.3-2.3.2011, Post-Workshop CD.

[6] Franc, J.-P., Michel, J.-M., "*Fundamentals of Cavitation"*, Kluwer Academic, Dordrecht, 2004

[7] Whitham, G.B., "*Linear and Nonlinear Waves"*, John Wiley and Sons, New York, 1999

[8] Mihatsch, M., Schmidt, S.J., Thalhamer, M., Adams, N.A, Skoda, R., Iben, U., *"Collapse Detection in Compressible 3-D Cavitating Flows and Assessment of Erosion Criteria"*, WIMRC Cavitation Forum 2011, Warwick, UK.

[9] Skoda, R., Iben, U., Morozov, A., Mihatsch, M., Schmidt, S.J., Adams, N.A., *"Numerical simulation of collapse induced shock dynamics for the prediction of the geometry, pressure and temperature impact on the cavitation erosion in micro channels"*, WIMRC Cavitation Forum 2011, Warwick, UK.

[10] Iben, U., Morozov, A., Winklhofer E., Skoda, R., *"Optical investigations of cavitating flow phenomena in micro channels using a nano second resolution"*, WIMRC Cavitation Forum 2011, Warwick, UK.

[11] Franc, J.P., Riondet, M., "*Incubation Time and Cavitation Erosion Rate of Work-Hardening Materials*. CAV2006", Wageningen, The Netherlands, September 2006.

G. Seventh publication

In this publication [66] an optimization of the proposed flux function is presented. Compared to the first formulation [61] the optimized version is significantly faster but equally robust and accurate. A series of validation examples are presented and the inconsistency of classical Riemann solvers in the low Mach number limit is demonstrated by analytical considerations. By computing the steady-state inviscid flow around a 2-D cylinder the accuracy of the method is shown for Mach numbers down to $M = 0.001$. A Riemann problem with initial pressure jump from $2500\ bar$ to $0.025\ bar$ is solved in order to highlight the robustness of the method. Some of the results presented in this investigation have been previously published by the author [65, 67] and corresponding details are discussed in Appendix B and D of this thesis.

I optimized the flux-function, demonstrated the low Mach number problem for classical Riemann solvers, generated the grids for the validation cases, performed simulations and analysis of results for the validation cases and prepared the manuscript.

Riemann Techniques for the Simulation of Compressible Liquid Flows with Phase-transition at all Mach numbers - Shock and Wave Dynamics in Cavitating 3-D Micro and Macro Systems

Steffen J. Schmidt[1], Ismail H. Sezal[2], Günter H. Schnerr[3] and Matthias Talhamer[4]
Technische Universität München, Lehrstuhl für Fluidmechanik - Fachgebiet Gasdynamik, D-85748 Garching, Germany

We investigate numerical flux functions for the inviscid flux components of the 3-D time-dependent balance laws of mass, momentum and energy. Special emphasis is put on the suitability of these fluxes to simulate compressible low speed liquid flows as well as to simulate liquid flows with phase transition. It is demonstrated that the classical approaches based on exact or approximate solutions of the Riemann problem between adjacent cells do not lead to uniformly consistent flux functions with respect to multidimensional low Mach number flow. Therefore, we introduce a uniformly consistent numerical flux function and perform a series of steady and unsteady simulations of pure liquid flow and cavitating liquid flow. We demonstrate the applicability of the proposed CFD-Tool CATUM to resolve wave dynamics and to predict the evolution of cavitation structures inside a 3-D multi-hole injector. Finally, we investigate the 3-D time dependent cavitating flow around a prismatic body. Here, we point out the suitability of our CFD-Tool to predict erosive shock loads of collapsing vapor clouds.

Nomenclature

u, u_i	=	velocity, velocity components	[m·s^{-1}]
c	=	speed of sound	[m·s^{-1}]
M	=	Mach number	
$\vec{q}$	=	vector of conserved quantities	[kg·m^{-3}, kg·m^{-2}·s^{-1} , J·m^{-3}]
$F_i(\vec{q})$	=	flux in coordinate direction x_i	[kg·m^{-2}·s^{-1} , kg·m^{-1}·s^{-2} , J·m^{-2}·s^{-1}]
ρ	=	density, local average density	[kg·m^{-3}]
E	=	mass specific total energy	[J·kg^{-1}]
e	=	mass specific internal energy	[J·kg^{-1}]
p	=	static pressure	[Pa]
T	=	static temperature	[K]
α	=	vapor volume fraction	
ε	=	vapor mass fraction	
σ	=	cavitation parameter	
x_i	=	coordinate direction/ length	[m]
Δt_{CFD}	=	numerical time step	[s]
V_{vap}	=	integrated vapor volume	[% total volume of the computational domain]
i,k	=	indices of computational cells	
f	=	frequency	[Hz]

[1] Ph.D. student, TU München, Lehrstuhl für Fluidmechanik - Fachgebiet Gasdynamik, D-85748 Garching, Germany, AIAA Member.
[2] Ph.D. student, TU München, Lehrstuhl für Fluidmechanik - Fachgebiet Gasdynamik, D-85748 Garching, Germany.
[3] Prof. Dr.-Ing. habil., TU München, Lehrstuhl für Fluidmechanik - Fachgebiet Gasdynamik, D-85748 Garching, Germany.
[4] Undergraduate student, TU München, Lehrstuhl für Fluidmechanik - Fachgebiet Gasdynamik, D-85748 Garching, Germany.

I. Introduction

THE numerical simulation of wave dynamics such as shock formation and propagation in compressible multiphase flows offers the possibility to predict the formation and collapse of cavitation structures as well as to predict collapse induced shocks of cavitating flows. Serious numerical difficulties arise due to the different time-scales defined by the flow velocity *u=O(10) m/s* and the speed of sound *c=O(1000) m/s* of the liquid. As long as no phase transition occurs the Mach number remains very low, typically *0<M<0.1*. However, the thermodynamic properties of two-phase mixtures imply a strong reduction of the speed of sound[1] and hence, the Mach number reaches even supersonic values if the vapor volume content is sufficiently large. The collapse-like condensation of the vapor content results in the formation of shock structures that propagate through the flow[2]. These shocks result in instantaneous loads and are supposed to be a driving mechanism of cavitation erosion. The present investigation focuses on the simulation of 3-D time-dependent cavitating liquid flows including wave dynamics. The resolution of the latter one requires numerical time steps based on the fastest signal speeds of the system, which are of the order of the speed of sound of the liquid. Besides this physical constraint the numerical flux function must resemble the asymptotic behaviour[3] of the continuous equations for $M \rightarrow 0$. It is known that classical Riemann approaches suffer from the low Mach number problem and hence, their application as flux function typically leads to large errors in the calculated flow field[4-6]. Several numerical techniques have been developed to overcome the low Mach number problem. Time derivative preconditioning removes the stiffness of the governing equations and permits accurate steady state solutions in the low Mach number limit[7]. In combination with dual time-stepping approaches these techniques are applicable to simulate unsteady flows as well, but the resolution of wave dynamics is no longer possible[8,9]. Pressure correction methods enable the simulation of low Mach number flow[10], but their application to solve wave propagation problems suffers from the lack of efficiency of these techniques if the physically required time step is very small. If the Mach number is small throughout the flow domain, the discretization of the compressible low Mach number equations[11] is suitable. However, with respect to cavitating flow this condition is not fulfilled. In addition to the numerical difficulties of low Mach number flow the simulation of cavitating flow requires modeling of evaporation/condensation as well as of the resulting two-phase mixtures. The modeling of the phase-change is either achieved by finite rate models[12-14] or by thermodynamic closure relations[15-17]. These models can be applied to single-fluid formulations as well as to two-fluid formulations. The latter ones enforce the solution of two sets of governing equations together with the modeling of mass, momentum and energy transfer between both fluids[18]. A recently developed hybrid model is based on the assumption of locally stratified flow[19]. The advantages of single-fluid formulations together with suitable thermodynamic closure relations are their hyperbolic structure and the existing conservation form of the governing equations[20].

The present investigation is organized as follows: In chapter II we present a mathematical model for time-dependent compressible liquid flows including the effects of evaporation and condensation. Based on the weak form of the conservation laws of mass, momentum and energy we obtain a set of evolution equations. Thermodynamic closure relations are applied to local integral averages of the fluid. Chapter III contains an interpretation of the low Mach number problem as a result of the definition of the pressure flux for classical Riemann approaches. Furthermore, we propose a modified definition of the pressure flux that does not show the low Mach number problem. In chapter IV we perform numerical simulations to validate the modified flux. Finally, our recently developed CFD-Tool CATUM (CAvitation Technische Universität München) is used to simulate 3-D time dependent flow through a multi-hole injector as well as to simulate the cavitating flow around a prismatic body.

II. Mathematical Model

As our major interests contain wave and inertia driven flows we neglect viscous effects. With respect to several experimental investigations it is known that cavitating flow is only weakly dependent on the Reynolds number and thus this approximation is suitable. However, the inclusion of viscous effects within the model is possible.

Let $\vec{q}$ be the vector of conserved quantities defined by the density ρ, the components u_i of the velocities in coordinate direction x_i and the specific total energy E as the sum of the specific internal energy e per unit mass and the specific kinetic energy $0.5 \cdot \sum (u_i)^2$. Let $F_i(\vec{q})$ be the physical flux in coordinate direction x_i, while δ_{ij} and p denote the Kronecker symbol and the pressure respectively

$$\vec{q} = \begin{pmatrix} \rho \\ \rho u_1 \\ \rho u_2 \\ \rho u_3 \\ \rho E \end{pmatrix}, \qquad F_i(\vec{q}) = \rho u_i \cdot \begin{pmatrix} 1 \\ u_1 \\ u_2 \\ u_3 \\ E \end{pmatrix} + p \cdot \begin{pmatrix} 0 \\ \delta_{1i} \\ \delta_{2i} \\ \delta_{3i} \\ u_i \end{pmatrix}. \tag{1}$$

The differential or pointwise form of the Euler equations can be written as

$$\frac{\partial}{\partial t}\vec{q} = -\sum_{i=1}^{3} \frac{\partial}{\partial x_i} F_i(\vec{q}) \,. \tag{2}$$

Instead of enforcing the conservation principles in a pointwise fashion we use the weak form of the Euler equations. Therefore, we partition the flow domain into disjoint fixed control volumes C_k of a corresponding volume V_k, a surface S_k and an outer unit normal vector $\vec{n}_k = (n_{k,1} \quad n_{k,2} \quad n_{k,3})^t$. The weak form of the Euler equations for each control volume C_k follows as

$$\frac{d}{dt}\int_{C_k} \vec{q}\,\mathrm{dV_k} = -\int_{S_k} \sum_{i=1}^{3} n_{k,i} F_i(\vec{q})\mathrm{dS_k} \,. \tag{3}$$

By defining the cell average operator A_k

$$A_k(\vec{q}) := \frac{1}{V_k}\int_{C_k} \vec{q}\,\mathrm{dV_k} \,, \tag{4}$$

we assign to all weak solutions within the cell C_k their common integral average value $\bar{q}_k = A_k(\vec{q})$. It turns out that the weak form of the Euler equations resembles a system of evolution equations of the cell averages of weak solutions

$$\frac{d}{dt}\bar{q}_k = -\int_{S_k} \sum_{i=1}^{3} n_{k,i} F_i(\vec{q})\mathrm{dS_k} \,. \tag{5}$$

Up to now we have not made any additional assumption on the flow field itself, which means that equation (5) is valid for any type of inviscid multicomponent and multiphase flow, even if the species do not share a common pressure, temperature or velocity. Nonetheless, the choice of fixed control volumes C_k introduces local length scales l_k of the order of $l_k = \sqrt[3]{V_k}$ into the physical problem and hence, any process occurring beyond those scales can no longer be resolved. Therefore, the previously defined cell averages can be interpreted as the result of a conservative low pass filtering of the flow field. In the case of cavitating bubbly liquid flow the resolution of two-phase features depends on the fraction $\Psi = R/l_k$ of the bubble radius R and the induced length scale l_k. If $\Psi << 1$ the model resembles the average behavior of a mixture, while it fully resolves single bubbles if $\Psi >> 1$. As the transition from the resolved case to the averaged case and vice versa does not require additional modelling, we denote the evolution of integral averages as a scale adaptive model. Furthermore, the right hand side of equation (5) implies that the evolution of the integral average equations is entirely dependent on the net fluxes of mass, momentum and energy across the surface of each control volume, while explicit knowledge of small scale information within the cell C_k is not required. However, the closure of the defined initial-boundary value problem (5) necessitates constitutive relations for the thermodynamic quantities ρ_k, e_k, p_k as well as consistent initial and boundary conditions. In this section we assume that consistent initial and boundary data are strictly available. Thus, the physical fluxes along the boundary surfaces are known and hence, equation (5) reduces to an initial value problem. At each instant in time the corresponding initial values $\bar{q}_k$ already determine the average density ρ_k,

velocity $\vec{u}_k$ and total energy E_k within the control volume C_k. Therefore, the average specific internal energy e_k is known as well. However, the definition of the average pressure p_k requires additional model assumptions. In this investigation we neglect surface tension and restrict the fluid to consist of two species: water and water vapor. Impurities like solid particles or solute gas are not explicitly modeled, but their effects on the thermodynamic behavior of water are taken into account in a simplified manner. It is known that highly purified water allows for the occurrence of meta-stable states far beyond saturation conditions,[21] whereas tap water does not show this behavior. In the latter case, the large number of impurities immediately results in heterogeneous nucleation[22] and thus in the formation of vapor bubbles. As the specific volume of water vapor is by several orders of magnitude larger than the one of liquid water, the phase transition results in rapid pressure equalization close to the stable saturation state. This allows us to neglect meta-stable states and to consider stable thermodynamic conditions. Consequently, the coexistence of both phases implies that the pressure p_k is determined by the Clausius-Clapeyron relation and the average density ρ_k within cell C_k is a convex combination of the saturation densities $\rho_{l,sat}$, $\rho_{v,sat}$ of liquid and vapor. Furthermore, we define at each instant in time and for each control volume an average temperature T_k in order to relate the saturation density to the internal energy. By defining the vapor volume fraction α_k and the vapor mass fraction ε_k we obtain the unknown quantities T_k, α_k, ε_k and p_k as solutions of the system

$$\rho_k = \alpha_k \cdot \rho_{v,sat}(T_k) + (1-\alpha_k)\cdot \rho_{l,sat}(T_k) \tag{6}$$

$$e_k = \varepsilon_k \cdot e_{v,sat}(T_k) + (1-\varepsilon_k)\cdot e_{l,sat}(T_k) \tag{7}$$

$$\varepsilon_k \cdot \rho_k = \alpha_k \cdot \rho_{v,sat}(T_k) \tag{8}$$

$$p_k = p_{sat}(T_k) \tag{9}$$

$$0 < \alpha, \varepsilon < 1. \tag{10}$$

Thereby, the incorporated temperature dependent functions have to be specified. In the case of water and water vapor we model these with the Oldenbourg polynomials.[23] The required closure relation in the presence of two-phase flow is thus completely defined.

If the average density ρ_k is larger then the saturation density of liquid water, we replace the closure relation with the modified Tait model ($\alpha_k, \varepsilon_k = 0$)

$$\frac{p_k + B}{p_{sat}(T_k) + B} = \left(\frac{\rho_k}{\rho_{l,sat}(T_k)} \right)^N , \tag{11}$$

together with an equation for the internal energy.[24] Even though the temperature variation of the liquid is typically small, the modification of the Tait equation remains necessary in order to ensure a continuous connection of the Tait model to the temperature dependent saturation conditions. For water we use *B=3300 bar* and *N=7.15* independent of the temperature.

If the average density ρ_k is smaller then the saturation density of vapor, the applied constitutive relation models pure vapor *($\alpha_k, \varepsilon_k = 1$)*, treated as calorically perfect gas, where the ratio of the specific heats is given by *κ=1.327* and the specific gas constant is *461.5 J/kg K*.

The comparison of the described thermodynamic closure relations with respect to the IAPWS data[25] demonstrates that the relations accurately model the behaviour of water and water vapor for a large range of thermodynamic subcritical conditions. Moreover, the presented model is neither restricted to the described set of thermodynamic closure relations nor to the assumption of instantaneous pressure equalization. However, the thermodynamic relations must imply a consistent definition of the equilibrium speed of sound *c* to ensure that the model is hyperbolic in time and that the initial-boundary value problem is well posed. Furthermore, the incorporation of small scale information, such as the bubble number density or the bubble size distribution, is possible, but the scale adaptability may then be lost and the model reduces to the dispersed mixture model.

III. Numerical Method

Our CFD-Tool CATUM relies on an approximate solution of the evolution equation (5) for each control volume C_k. As it is stated in chapter 2, the temporal development of Eq. (5) is completely defined by the time dependent fluxes across the surfaces of the control volumes. The hyperbolic character of the compressible formulation of the governing equations motivates a Godunov type approximation of these fluxes. Thereby, the average values $\vec{q}_k$ and $\vec{q}_i$ of two adjacent control volumes C_k, C_i are used to define the Riemann problem *RP* across the shared surface $S_{k,i} = C_k \cap C_i$. The solution $RP(\vec{q}_k, \vec{q}_i)$ of the Riemann problem at the surface $S_{k,i}$ is constant in time within a time interval $\Delta t_{RP} \approx l/(|\vec{u}| + c)$, where l is the length scale of the volume and $|\vec{u}| + c$ represents the fastest signal speed. By replacing the physical fluxes $F(\vec{q}_k)$ in Eq. (5) with the numerical fluxes $F\left(RP(\vec{q}_k, \vec{q}_i)\right)$, we obtain a set of ordinary differential equations, which represent a semi-discrete unsplit finite volume method for hexahedral volumes

$$\frac{d}{dt}\vec{q}_k = -\sum_{i=1}^{6} S_{k,i} \cdot F\left(RP(\vec{q}_k, \vec{q}_i)\right). \tag{12}$$

This framework is well developed for the simulation of steady and unsteady compressible aerodynamics of moderate and high Mach number flows as well as for the investigation of wave propagation phenomena including sharp and accurate shock capturing in unsteady flow. Furthermore, methods based on Eq. (12) are conservative by construction and enable efficient time dependent simulations. Contrary to pressure based approaches, all fluxes are calculated without the need for sub-iterations. However, the application of Godunov type methods to low speed flows requires substantial modification to overcome the low Mach number problem. Otherwise, the accuracy of the Godunov approximation significantly decreases if the Mach number is in the weakly compressible regime, $M \lesssim 0.1$. With respect to the high acoustic impedance $\rho \cdot c$ of liquids, the decrease of accuracy is further intensified. An extensive discussion of the low Mach number problem is beyond the scope of this investigation but can be found in the literature.[26,27] These contributions highlight the inconsistency of the discrete pressure component as part of the numerical momentum fluxes with respect to asymptotic analysis of the governing equations.[27,28]

In order to motivate the subsequent modification of the calculation of the interface pressure p^* we briefly recall the compatibility relations of the 1-D time dependent Euler equations[29]

$$\delta p \pm \rho \cdot c \cdot \delta u = 0 \quad \text{along} \quad \dot{x} = u \pm c\,, \tag{13}$$

$$\delta p - c^2 \cdot \delta \rho = 0 \quad \text{along} \quad \dot{x} = u\,. \tag{14}$$

Assuming smooth state variations across the genuinely nonlinear fields defined in Eq. (13) we obtain an expression of the interface pressure p^* at the shared surface $S_{k,i}$ for subsonic flow[30]

$$p^* = \frac{p_k + p_i}{2} - \frac{\rho_{k,i} \cdot c_{k,i}}{2} \cdot \left(u_i - u_k\right). \tag{15}$$

Thereby, the acoustic impedances at the origins of both characteristics are approximated by an average value of the acoustic impedance denoted by the subscript *k,i*. Although various different approximations are known it should be pointed out that the main feature of all Godunov type methods is the coupling of the interface pressure with the difference of the velocities of both sides of the interface. As it can be seen in Eq. (13) this coupling is weighted by the acoustic impedance, which is close to a constant value if the Mach number remains small within the flow field. Any method based on compatibility relations or on Rankine-Hugoniot relations will lead to an interface pressure p^* that is comparable to the one given by Eq. (15) provided that the Mach number is sufficiently low and that the states on both sides of the interface are sufficiently close to each other.

To demonstrate the failure of Eq. (15) for low Mach number flow we investigate the 2-D potential flow field around a circular cylinder of radius *R* as sketched in Fig. 1. Let M_∞, c_∞, p_∞ and ρ_∞ be the Mach number, the speed of sound, the pressure and the density at the far field of the cylinder. Assume the flow being inviscid, stationary and

adiabatic. Presuming that $M_\infty << 1$ it follows that c as well as ρ will be close to their states c_∞, ρ_∞ at infinity and hence, the approximation of the flow field by the incompressible potential solution is reasonable.

The velocity $u(S)$ as well as the pressure coefficient $c_p(S)$ along a streamline S infinitely close to the cylinder wall can be derived by incompressible potential theory

$$u(S) = 2 \cdot \sin(\varphi) \cdot u_\infty , \qquad c_p(S) = 1 - 4 \cdot \sin^2(\varphi) . \tag{16}$$

It turns out that the average increase of the velocity $u(S)$ from the primary stagnation point at $\varphi=0$ to the thickness maximum at $\varphi=\pi/2$ along S is given by

$$\left.\frac{\partial u(S)}{\partial S}\right|_{average} = \frac{1}{R \cdot \pi / 2}\left(u(\pi/2) - u(0)\right) = \frac{4 \cdot u_\infty}{R \cdot \pi} . \tag{17}$$

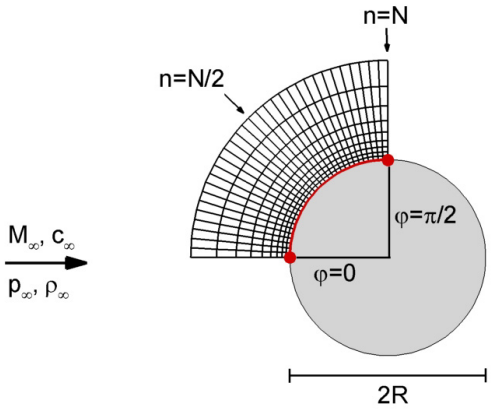

Figure 1: *2-D* plane circular cylinder of radius *R* and sketch of the computational cells in the vicinity of the streamline starting from the primary stagnation point at $\varphi=0$ and passing the point of maximum thickness at $\varphi=\pi/2$. Flow from left to right, $M_\infty << 1$.

Suppose the numerical discretization in circumferential direction of the previously defined *90* degree section of the cylinder is given by N computational cells. The average length ΔS of each cell along S is

$$\Delta S = \frac{R \cdot \pi / 2}{N} . \tag{18}$$

Hence, the average velocity difference Δu between adjacent cells along S is given by

$$\Delta u = \left.\frac{\partial u(S)}{\partial S}\right|_{average} \cdot \Delta S = \frac{2 \cdot u_\infty}{N} . \tag{19}$$

We apply Eq. (15) to approximate the interface pressure p^* for adjacent cells along the *90* degree section of the cylinder wall

$$p^* = \frac{p_k + p_i}{2} - \frac{\rho_{k,i} \cdot c_{k,i} \cdot u_\infty}{N} \approx \frac{p_k + p_i}{2} - \frac{\rho_\infty \cdot c_\infty \cdot u_\infty}{N} . \tag{20}$$

For smooth flow we can approximate the exact value p_{exact} of the pressure at the surface $S_{k,i}$ by Taylor series

$$p_{exact} = \frac{p_k + p_i}{2} + O\left(\Delta S^2\right). \tag{21}$$

Applying Eq. (21) to Eq. (20) we obtain a relation of the numerically predicted pressure coefficient $c_{p,numerical}$

$$c_{p,numerical} = \frac{p^* - p_\infty}{1/2 \cdot \rho_\infty \cdot u_\infty^2} = \frac{p_k + p_l - 2 \cdot p_\infty}{\rho_\infty \cdot u_\infty^2} - \frac{2}{N \cdot M_\infty} \approx c_p - \frac{2}{N \cdot M_\infty}. \tag{22}$$

The first term on the right hand side of Eq. (22) is the exact pressure coefficient c_p, which is of order *1* (see Eq. 16). The second term is of the order of $1/(N \cdot M_\infty)$. Therefore, the numerical error that is introduced by the application of Eq. (15) grows inversely proportional to the Mach number M_∞ as long as the number of cells N is kept constant. This implies that those numerical fluxes $F\left(RP(\vec{q}_k, \vec{q}_i)\right)$ that contain Eq. (20) lead to numerical methods that are not uniformly consistent with respect to the Mach number. We conclude that the low Mach number problem is directly related to the numerical approximation of the interface pressure p^* based on the compatibility relations. As illustrated before, this approximation is not suitable to simulate low Mach number flows as it would require $N \sim M_\infty^{-1}$ along streamlines.

In order to overcome the low Mach number problem we introduce a modified numerical flux $MF(\vec{q}_k, \vec{q}_i)$ for cavitating liquid flow, which is equipped with an asymptotically consistent pressure flux definition. Due to the rotational invariance of the convective fluxes we restrict the presentation of the formulation to one spatial direction x_1. We use the subscripts k,i for the average flow variables corresponding to the control volumes to the left and to the right of the shared surface $S_{k,i}$, which we assume to be part of the x_2, x_3 plane. Provided that the Mach numbers M_k, M_i are low, the velocity u^* at the surface $S_{k,i}$ follows from the locally linearized compatibility conditions[31]

$$u^* = \frac{\rho_k \cdot c_k \cdot u_{k,1} + \rho_i \cdot c_i \cdot u_{i,1} + p_k - p_i}{\rho_k \cdot c_k + \rho_i \cdot c_i}. \tag{23}$$

Contrary to Eq. (15) the pressure p^* at the surface $S_{k,i}$ is computed by

$$p^* = \frac{p_k + p_i}{2}. \tag{24}$$

Equation (24) does not contain additional diffusive components and it leads to a uniformly consistent pressure flux. We achieve an upwind character of the numerical flux by the sign of the velocity u^*. Assuming positive sign we define the following numerical flux $MF(\vec{q}_k, \vec{q}_i)$ in accordance with the physical flux as defined in equation (1)

$$MF(\vec{q}_k, \vec{q}_i) = \rho_k u^* \cdot \begin{pmatrix} 1 \\ u^* \\ u_{k,2} \\ u_{k,3} \\ E_k \end{pmatrix} + p^* \cdot \begin{pmatrix} 0 \\ 1 \\ 0 \\ 0 \\ u^* \end{pmatrix}. \tag{23}$$

For negative mass flow ($u^*<0$) the subscripts k and i are reversed. In the presence of cavitation the local Mach numbers M_k, M_i may reach supersonic values and hence, the numerical flux should resemble pure upwinding of all conserved quantities. In this case, the interface values u^* and p^* are replaced by the corresponding variables on the left or on the right hand side, depending on the flow direction. The final form of the discrete evolution equations reads

$$\frac{d}{dt}\vec{q}_k = -\sum_{i=1}^{6} S_{k,i} \cdot MF(\vec{q}_k, \vec{q}_i) \,. \tag{24}$$

As the density at the interface is defined by a pure one-sided approximation the resulting flux (23) preserves stationary contact discontinuities. In order to increase the spatial accuracy of the method we apply WENO-3 reconstruction procedures[32] to the velocity components and a TVD reconstruction[33] to the density field. As the pressure flux is already second order accurate by definition, no further procedure is required. The spatial discretization is thus second order accurate for smooth solutions and it significantly reduces oscillations in the presence of discontinuities.

We apply an explicit four-stage/low storage Runge-Kutta method with enlarged stability region to advance the system (16) in time. Second order accurate simulations in space and time thereby enforce the numerical time step Δt_{CFD} being determined as the minimum of Δt_{RP} within all control volumes.

IV. Numerical Results

A. 2-D steady state liquid flow at low Mach numbers

In order to demonstrate the potential of the proposed numerical method we investigate several numerical results of low Mach number flows. In accordance to the previous section we discuss the 2-D flow field around a circular cylinder of radius *R*. The boundary conditions at the far field of the computational domain are given by p_∞*=1.5 bar*, T_∞*=300 K* and $M_{\infty,1}=10^{-2}$, $M_{\infty,2}=10^{-3}$ and $M_{\infty,3}=10^{-4}$. All three simulations are performed using the same computational grid consisting of *128 cells* in circumferential direction and *32 cells* in radial direction. The far field of the O-grid is located *65·R* away from the surface of the cylinder. In all cases the fluid is water as given by Eq. (11). For the above stated conditions the speed of sound is given by *c=1500 m/s* and hence, the velocity u_∞ is *15 m/s*, *1.5 m/s* and *0.15 m/s* corresponding to $M_{\infty,1}=10^{-2}$, $M_{\infty,2}=10^{-3}$ and $M_{\infty,3}=10^{-4}$. In order to save computational time we apply local time-stepping with CFL=1.5 in all cases. The reconstruction of the density field is achieved by the Van Leer limiter.

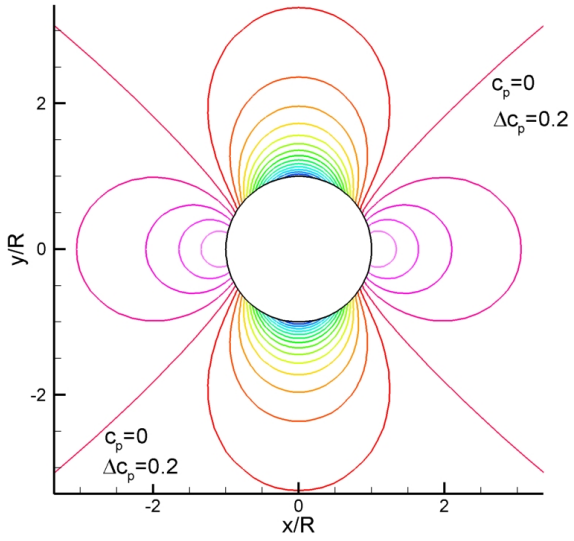

Figure 2: Pressure coefficient c_p (numerical solution - CATUM) of the stationary inviscid 2-D flow around a circular cylinder of radius R at a free-stream Mach number $M_\infty=10^{-4}$. Flow from left to right, liquid water at p_∞=1.5 bar, T_∞=300 K.

Figure 2 depicts isolines of the pressure coefficient c_p as predicted by our numerical method for the free stream Mach number $M_{\infty,3}=10^{-4}$. Although the computational grid is quite coarse the obtained result indicates the quality of the proposed flux function. For the free stream Mach numbers $M_{\infty,1}=10^{-2}$, $M_{\infty,2}=10^{-3}$ we obtain visually identical results.

We compare the numerical results with the solution of the incompressible potential solution along the surface of the cylinder as given in Eq. (16). Figure 3 depicts the dimensionless velocity $u(S)/u_\infty$ and the pressure coefficient c_p for all numerical cases as well as for the analytical solution. Although the numerical method leads to slight under-predictions of $u(S)/u_\infty$ and c_p close to the thickness maximum, the agreement of the numerical result with the analytical solution is good even for the applied coarse computational grid. The calculated drag coefficients are within the range of $c_D=1.4\text{-}1.6\cdot10^{-5}$, which confirms the quality of the numerical solutions. Moreover, the numerical results are nearly indistinguishable with respect to the dimensionless quantities $u(S)/u_\infty$ and c_p for all three Mach numbers. Thus we conclude that the proposed method is uniformly consistent for $M\rightarrow0$.

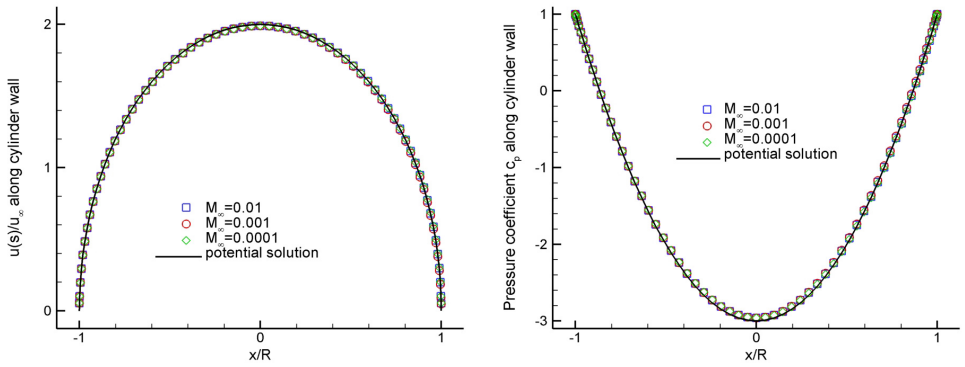

Figure 3: Comparison of the analytically and numerically obtained distributions of the relative velocity $u(S)/u_\infty$ and of the pressure coefficient $c_p(S)$ along the streamline S for the far field Mach numbers $M_{\infty,1}=10^{-2}$, $M_{\infty,2}=10^{-3}$ and $M_{\infty,3}=10^{-4}$. Liquid water at $p_\infty=1.5$ bar, $T_\infty=300$ K.

B. 1-D shock-tube problem

In order to demonstrate the potential of the method to capture and predict wave dynamics we investigate a classical shock-tube problem. We assume a 1-D tube of length $l=1$ m to be filled with water at $T=293$ K. The tube is initially divided into two regions of length $l/2$ by a membrane. On the left hand side, the pressure is given by $p_L=2500$ bar and on the right hand side the pressure is $p_R=0.025$ bar. The flow is initially at rest $(u_L=u_R=0$ m/s) and the densities on both sides are determined by Eq. (11). The numerical domain is divided into 100 computational cells of length 0.01 m. The boundary conditions correspond to solid walls on both ends of the tube. Figure 4 depicts the time evolution of the right traveling shock and the left propagating rarefaction wave. On the left of fig. 4 the pressure ratio p/p_R is plotted for three instants in time. The shock Mach number M_S for the presumed pressure ratio is still rather small, $M_S\approx1.17$. Due to the high acoustic impedance of $O(10^6)$ of the liquid, the convective velocity u reaches hardly 70 m/s, see fig. 4 - right. The shock and the rarefaction wave are captured without the presence of overshoots.

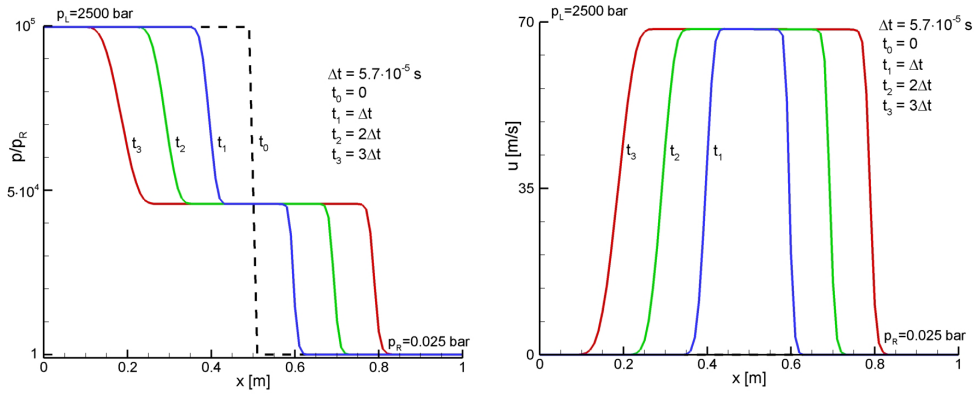

Figure 4: Numerically obtained dimensionless pressure p/p_R and velocity u for 4 equidistant instants in time (t_0=0 s, Δt=5.7·10^{-5} s). Initial conditions within the closed shock-tube: p_L=2500 bar, p_R=0.025 bar, T_L=T_R=293 K, u_L=u_R=0 m/s, initial discontinuity at x=0.5 m, tube length 1 m.

C. 1-D traveling contact wave

Besides the resolution of nonlinear wave dynamics it turns out that the quality of the simulation of cavitating liquid flow strongly depends on the resolution of contact discontinuities. As stated in chapter III, the proposed flux function preserves contacts due to the definition of a common mass flux component and the pure upwinding of the density. However, the averaging that is inherently implied within any finite volume method may lead to inconsistencies if the pressure is not given by a function of the form $p=K_1 \cdot \rho e + K_2$, where $K_{1,2}$ are constants. Here we simulate a traveling contact wave by initializing the previously defined 1-D domain through: $u_L=u_R=500$ m/s, $p_L=p_R=1.0$ bar, $T_L=293$ K and $T_R=323$ K. The densities on both sides are determined by Eq. (11). The boundary conditions for this problem are extrapolated from the interior of the domain. Figure 5 depicts the temperature for three instants in time. The initial discontinuity of the temperature is well preserved although the pressure and the velocity experience the previously stated oscillations due to the form of the Tait model.

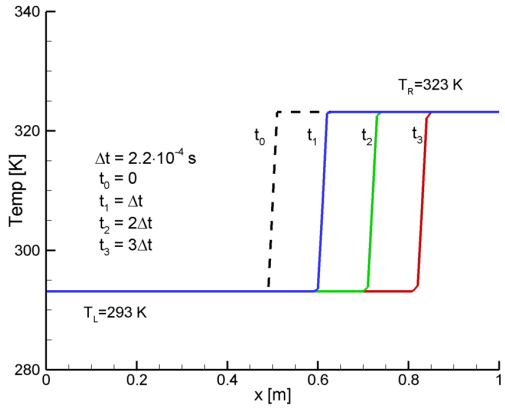

Figure 5: Numerically obtained temperature for 4 equidistant instants in time (t_0=0 s, Δt=2.2·10^{-4} s). Initial conditions within the tube: p_L=p_R=1.0 bar, T_L= 293 K, T_R=323 K, u_L=u_R=500 m/s, initial discontinuity at x=0.5 m, tube length 1 m.

Both numerical tests indicate that nonlinear effects such as the formation of rarefactions and shocks in liquid flow do not lead to numerical instabilities although the pressure flux is significantly less diffusive than the ones derived from Eq. (15). We suggest that the numerical method benefits from the increased stability region (including parts of the imaginary axis) of the low storage Runge-Kutta procedure. The application of the forward Euler time integration method together with the modified flux does not lead to a stable discretization for all investigated test cases while the proposed combination works stable and accurate. Further investigations are required to improve the understanding of the interaction of spatial and temporal discretization procedures.

D. 3-D wave dynamics and cavitation inside a multi-hole injector

The design and improvement of high-speed fuel injection systems of Diesel- and Otto-engines is a challenging field of research. The operating conditions contain exceptional high pressure differences p_{in}-p_{out}=$O(10^3)$ bar, which result in maximum flow velocities up to *500 m/s*. Furthermore, high frequency excitations due to the lift of the needle induce strong wave dynamic flow features. Thereby, the arising pressure drop typically leads to acoustic and hydrodynamic cavitation. The subsequent recondensation of the evaporated liquid enforces the formation of violent shock waves, which often results in cavitation erosion[34,35].

Figure 6 - left - depicts a *180* degree section of a multi-hole fuel injector. The position of the needle is fixed to its maximum lift. Six cylindrical bore holes are connected to the lower part of the sack volume. In order to suppress flow separation, the inlet tips of the bore holes are rounded with a radius of wall curvature of *0.028 mm*. Such a micro-deburr is practically achieved by hydro-erosive grinding and significantly improves the flow characteristics. The inner diameter of the upstream part of the nozzle is *3.9 mm* and the diameter of the needle is *3.26 mm*. The diameters of the spray holes are *0.22 mm* and their length to diameter ratio is *4.54*. On the right hand side of fig. 6 the discretization of the flow domain is depicted. The *6*-fold radial periodicity of the injector allows for the numerical analysis of a *60* degree section. At the outlet of the bore hole an outflow domain is added in order to simulate the arising flow outside of the nozzle as well. This enables the physically consistent treatment of the flow dynamics close to the exit of the bore hole, which cannot be ensured if the domain outside of the nozzle is completely replaced by numerical boundary conditions. To study the mesh dependence of the numerical results, calculations are carried out for three different grids containing 10^5, $2.6 \cdot 10^5$ and $4 \cdot 10^5$ cells. For all cases a high grid quality is achieved by the use of *85* matching O- and H-grids, which consist of low aspect ratio hexahedrons only.

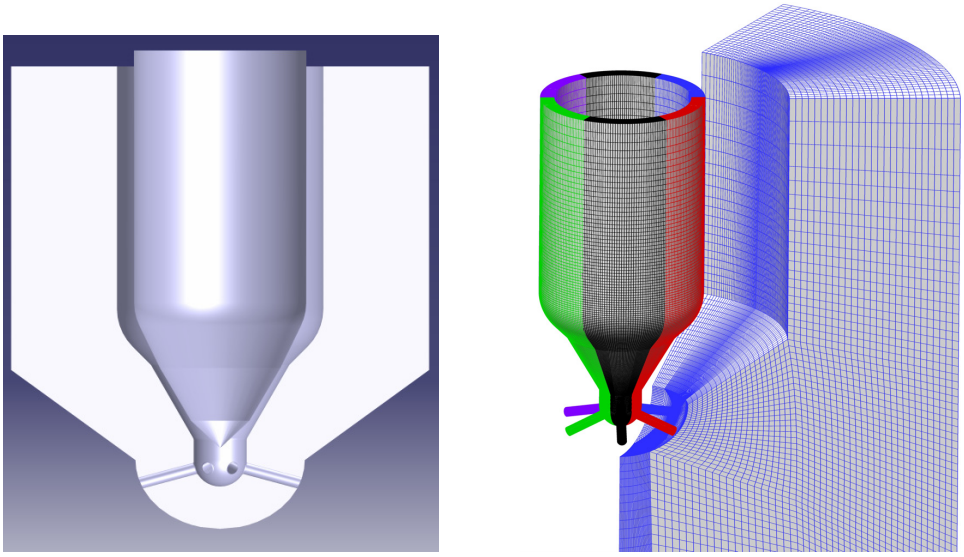

Figure 6: CAD-model and computational grid of the investigated 3-D multi-hole injector. Discretization of the simulated 60 degree section: $4 \cdot 10^5$ cells.

We assume the nozzle and the surrounding domain to be initially filled with pure liquid at rest. The pressure and the temperature are initially set to $p_{init}=p_{out}$ and $T_{init}=333\ K$ throughout the numerical domain. In spite of being a common experimental setup, this assumption may lead to different results than the more practical condition where the nozzle sack and the domain outside of the nozzle are initially filled with gas. However, this will require the implementation of non-condensable gas as a third compressible component into the numerical scheme, which is part of our current research.

All solid walls are treated as adiabatic, inviscid, impermeable and stationary. Hence, the movement of the needle is not modelled. Instead we focus on the maximum lift of the needle as shown in Fig.6.

The numerical boundary treatment along the outer surface of the surrounding domain allows waves passing through (characteristic boundary conditions), but ensures constant prescribed pressure p_{out} asymptotically[36]. Due to the large distances between the bore holes and the boundary surface, the oncoming disturbances are already very weak, which additionally improves the applicability of this boundary treatment. At the inlet area we apply similar boundary conditions, but the prescribed pressure p_{in} now resembles the rail pressure. Although the disturbances at the inlet boundary are partially of the same order as the pre-defined asymptotic conditions, our numerical boundary treatment is able to reproduce the experimentally observed time dependent pressure behaviour.

Due to the six-fold symmetry of the injector geometry we apply symmetry boundary conditions at the lateral section planes. The enforced boundary conditions are thereby identical to those applied to inviscid walls. For this investigation all simulations are performed with water as the test-fluid at an initial temperature $T_{init}=333\ K$.

Figure 7 contains the time history of the mass flow $\dot{m}$ (left) and the corresponding integrated vapor volume V_{vap} (right) for the pressure conditions $p_{in}=600\ bar$ and $p_{out}=26\ bar$. Both graphs are plotted against a logarithmic time axis (large pictures) as well as against a linear time axis (small pictures). The mass flows as well as the integrated vapor volume show a strong transient behaviour and reduce to constant values at time $t\approx10^{-4}\ s$. As it will be presented in the following subsections, the solution turns out to reach a stable steady state at that time. However, the comparison of the final values with their maximum amplitude during the transient flow development demonstrates the necessity of time accurate simulations of injection processes, especially if pilot or multipoint injections are considered. Moreover, the comparison of the mass flow $\dot{m}_{in}$ at the nozzle inlet with the mass flow $\dot{m}_{out}$ at the exit of the spray holes highlights the compressible behaviour of the liquid fluid and the wave dynamics as dominating features. Any incompressible formulation would enforce the velocity field to be strictly divergence free, which implies the equality of $\dot{m}_{in}$ and $\dot{m}_{out}$ throughout the simulation.

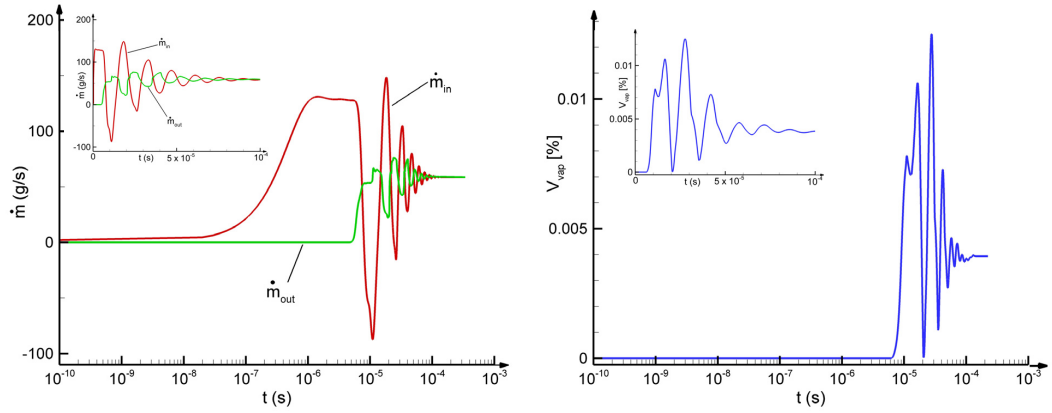

Figure 7: Time history of the mass flow at the inlet $\dot{m}_{in}$ and the outlet $\dot{m}_{out}$ of the injector (left); time history of the integrated vapor volume fraction within the complete computational domain (right).
Fluid: water at $T_{in}=333\ K$, $p_{in}=600\ bar$, $p_{out}=26\ bar$.

Picture 1-12 of Fig. 8 focus on the flow development close to the bore holes. The time interval covers the period $5.48 \cdot 10^{-6}\ s \leq t \leq 8.88 \cdot 10^{-6}\ s$. Picture 1 depicts the multidimensional shock focusing at the lower wall of the sack. The maximum pressure $p_{max}=2163\ bar$ is thereby reached at $t=5.55 \cdot 10^{-6}\ s$ (Pic. 2). In Pic. 3 the shock reaches the exit of the bore hole. There it diffracts to a spherical front and propagates into the outside domain. At this time, the mass flow $\dot{m}_{out}$ at the bore hole exit starts to develop. The shock-strength decreases proportional to the radius of the front and a rarefaction wave propagates inside the throat. This expansion is strong enough to reduce the static pressure to the vapor pressure and thus to enforce cavitation. Two-phase domains are thereby indicated by isolines of the void fraction $\alpha=0.001$. In Pic. 4 and 5 we observe two types of cavitation. Strong expansions around the edges of the spray holes result in vortex cavitation in the surrounding domain of the nozzle. The 3-D toroidal structures of the arising saturation regions outside of the bore holes are indicated by closed isolines. Inside the bore holes acoustic cavitation is visible. Thereby, the whole cross section close to the bore hole exit is affected. However, as typical for wave induced phase transition, the maximum void fraction α is of the order of 10^{-3}. Due to the remaining velocity field the vapor content is compressed and recondenses within $5 \cdot 10^{-7}\ s$ (Pic. 6). In Pic. 8 we observe another acoustic cavitation. Furthermore, a continuous reduction of the pressure inside the sack volume is visible. At the curved bore hole inlet we observe the onset of hydrodynamic cavitation (Pic. 9). The hydrodynamic cavitation pocket forms a torus-shaped structure as well. Only the upper part of the saturated two-phase domain grows along the flow direction, while the lower cavitation region disappears (Pic. 10-12). At this instant in time the integrated vapor volume fraction V_{vap} starts to grow significantly. However, this is due to the growth of the cavity inside the bore holes as well as in the outside domain, where the vortical structures lead to further evaporation.

Figure 9 depicts the formation and collapse of the hydrodynamic cavity. In Pic. 1 the cavitation pocket inside the bore hole already covers two thirds of the length of the bore hole. Further growth of the pocket takes place until the cavity reaches its maximum length at $t=1.67 \cdot 10^{-5}\ s$ (Pic. 2). This instance in time corresponds to the first local maximum of the integrated vapor volume (Fig. 7, right). Both cavities start to recondense, which results in the shrinking of the vapor domains (Pic. 3). At $t=1.95 \cdot 10^{-5}\ s$ the cavitation pocket inside the bore hole fragments slightly behind the bore hole inlet (Pic. 4). Thereby, an increase of the pressure due to inertia forces is visible. The vapor pocket is rapidly compressed along the flow direction until the complete saturated domain disappears. Subsequently, a violent collapse occurs. As this process is accompanied with a significant increase of the velocity behind the collapsing cavity as well as with a requisite decrease of the velocity ahead the cavitation pocket the resulting velocity field directly after the collapse necessarily implies a discontinuity. The resulting "water-hammer" enforces the formation of a shock where the pressure raise is proportional to the velocity difference. Picture 5 depicts the arising shock, which leads to a maximum pressure of $p_{max}=1029\ bar$, which is about twice the inlet pressure $p_{in}=600\ bar$. As it is known from 3-D spherical symmetric explosion theory, the subsequent formation of a rarefaction wave is inevitable. Together with the afresh forming vortex cavitation (Pic. 6) a cavity pocket inside the bore hole starts to grow. At $t=2.77 \cdot 10^{-5}\ s$ the integrated vapor volume again reaches its local maximum value and the periodic behaviour recommences. However, with each repetition of the process the fragmentation of the cavity occurs slightly closer to the outlet of the bore hole. Thus, the collapsing part of the cavity reduces its size and the collapse as well as the combination of shock and rarefaction weakens. Consequently, the vapor volume of the recreated vortex cavitation reduces as well. Finally, the integrated vapor volume reduces its amplitude because the stable part of the cavity increases while the unstable cavitation pockets decrease. This explains the asymptotic behaviour of V_{vap} in Fig. 7 (right).

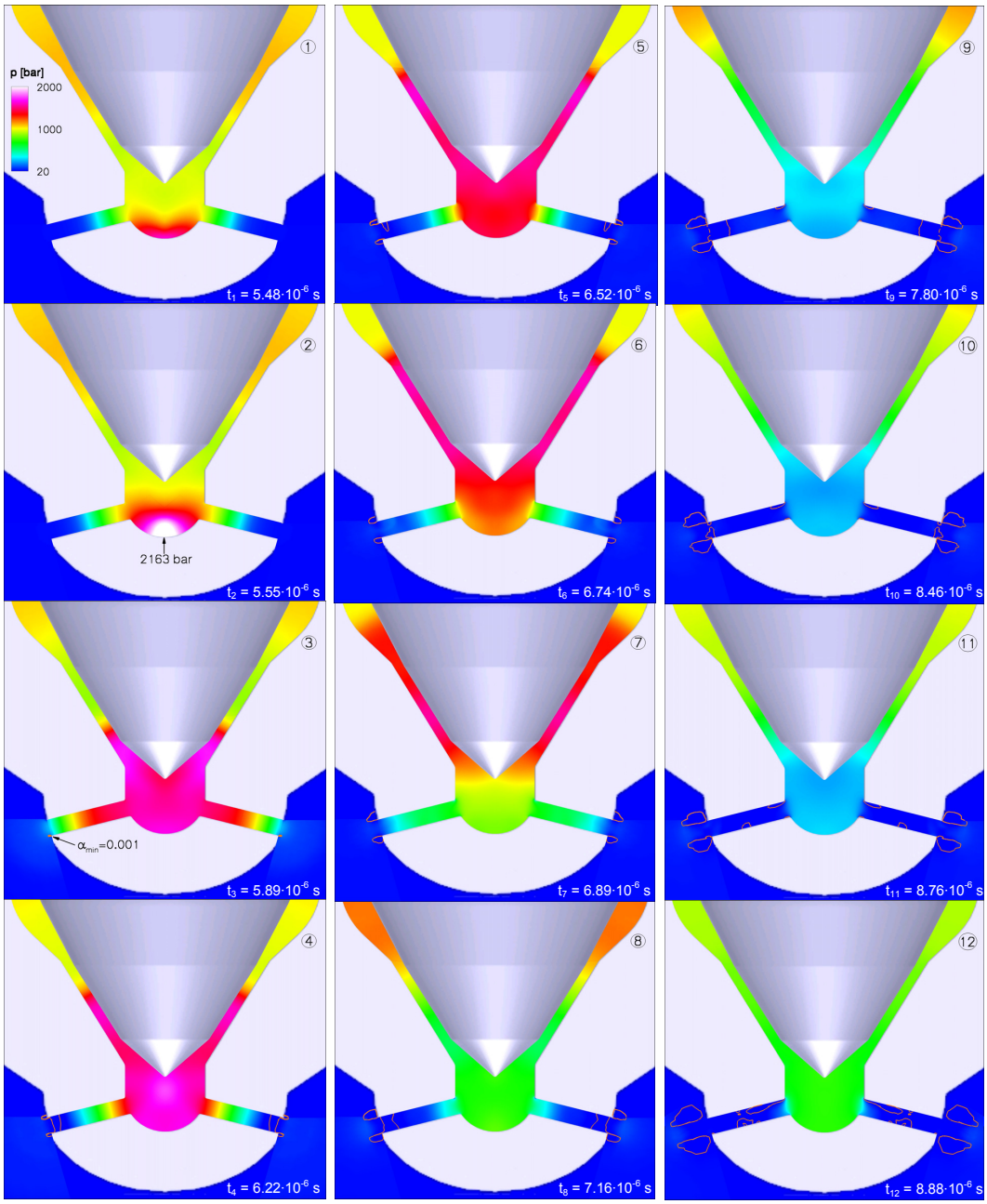

Figure 8: Wave dynamics (visualized by the static pressure) and the development of acoustic and hydrodynamic cavitation (orange isolines with α=0.1%) at the meridional plane of the injector at 12 instants in time. Fluid: water at T_{in}=333 K, p_{in}=600 bar, p_{out}=26 bar.

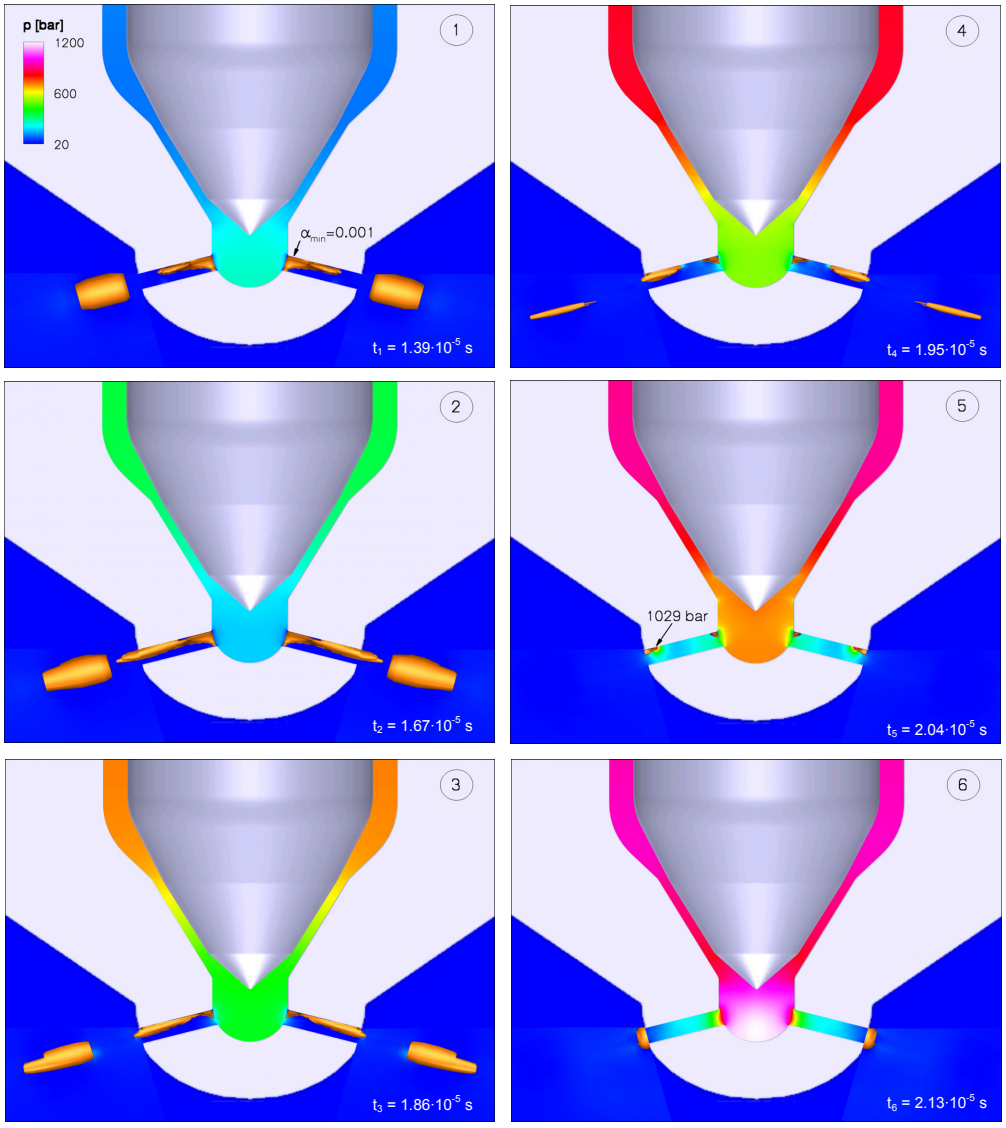

Figure 9: Development, fragmentation and collapse of hydrodynamic cavitation structures (orange iso-surfaces with α=0.1%) within the bore hole of the injector at 6 instants in time. Visualization of the static pressure at the meridional plane. Fluid: water at T_{in}=333 K, p_{in}=600 bar, p_{out}=26 bar.

At time $t=1.1\cdot10^{-4}$ *s* the vortex cavitation is no longer present and the complete hydrodynamic cavity is stationary. The flow field establishes a steady state and thus the vapor volume and the mass flow remain constant. In Fig. 10 (left) the resulting void fraction distribution at the meridional plane of the injector is presented. For the same instant in time we isolate the cavity structure to study their shape in detail (Fig. 10 – right, bottom). At the bore hole inlet the vapor pocket is nearly circular shaped. Slightly downstream of the inlet the structure is confined to the upper part of the spray hole. Although the shape of the cavity varies along the flow direction, the covered area is almost constant for each cross section of the bore hole[37]. Figure 10 depicts a comparison of the experimental results obtained by Busch[38] for the conditions p_{in}=600 bar, p_{out}=1 bar with the results of our numerical simulation. In the visualization of the experimentally obtained cavitation structure the vapor appears as dark area within the bore hole while the visualization of the numerical result depicts an iso-surface of the void fraction of $\alpha=0.1\%$.

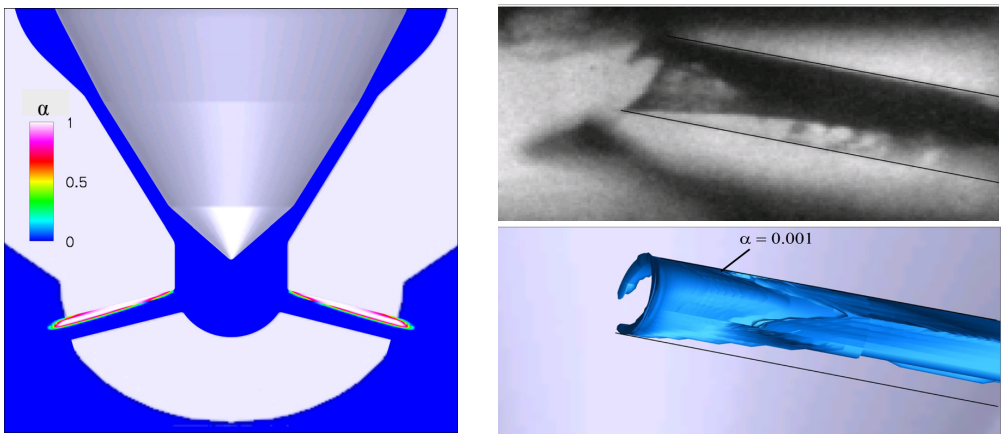

Figure 10: Vapor volume fraction α of the steady state solution at $t=1.1\cdot10^{-4}$ *s* at the meridional plane (left); *3-D* perspective view of the experimentally[38] (right-top) and numerically (right-bottom) obtained cavitation structure within the bore hole. Fluid: water at $T_{in}=333$ *K*, $p_{in}=600$ *bar*, $p_{out}=26$ *bar*.

E. 3-D time dependent cavitating flow around a prismatic body and collapse induced shock formation

The occurrence of cavitation typically leads to a decrease of the efficiency of hydraulic machines. For pumps the NPSH (net positive suction head) significantly reduces as soon as evaporation of the fluid takes place. Furthermore, cavitating flow tends to be inherently time dependent due to the periodic or chaotic fragmentation of vapor sheets and the subsequent formation of vortical cavitation clouds[39,40]. These clouds are convected into areas of increased static pressure where a collapse-like recondensation is initiated. Thereby, shock structures form and propagate through the fluid. If the collapse of a vapor cloud occurs close to a solid surface, e.g. close to a pump or turbine blade, then the shock induced dynamic loads are supposed to be a major part of the mechanism of cavitation erosion[41]. It is further supposed that the interaction of a shock with a simultaneously collapsing single vapor bubble intensifies the erosive behavior. Within a previous investigation[17] we applied the CFD-Tool CATUM to simulate the collapse of a single vapor bubble and found excellent agreement with the theoretical prediction given by the Rayleigh-Plesset equation. However, the resolution of single bubble dynamics is not possible for 3-D cavitating flow as this would require unaffordable high mesh resolution. Here, we investigate the dynamics of large scale structures that can be interpreted as clouds of liquid embedded vapor bubbles. Therefore, we model and discretizise an experimental setup consisting of a rectangular test-section of length *0.85 m*, depth *0.3 m* and height *0.3 m* where a prismatic body of height *0.1 m* is located at the bottom wall. The lateral section of the prismatic body forms an equilateral triangle with side length *0.075 m*. The mesh consists of $3.1\cdot10^{6}$ finite volumes and it is partitioned into *64* bocks (Fig. 11). Liquid water at $T=300$ *K* enters the inlet plane with an average velocity $u_{in}=11$ *m/s*. At the outlet plane of the numerical domain asymptotic non-reflective boundary conditions are applied, which ensure an average pressure $p_{out,mix}=1.12$ *bar*. Based on the inlet velocity, the inlet temperature and the outlet pressure we obtain a

cavitation parameter $\sigma_{ref}=1.8$. The numerical analysis is performed within *240* hours on a *SGI Altix 3700Bx2* using *64* processors.

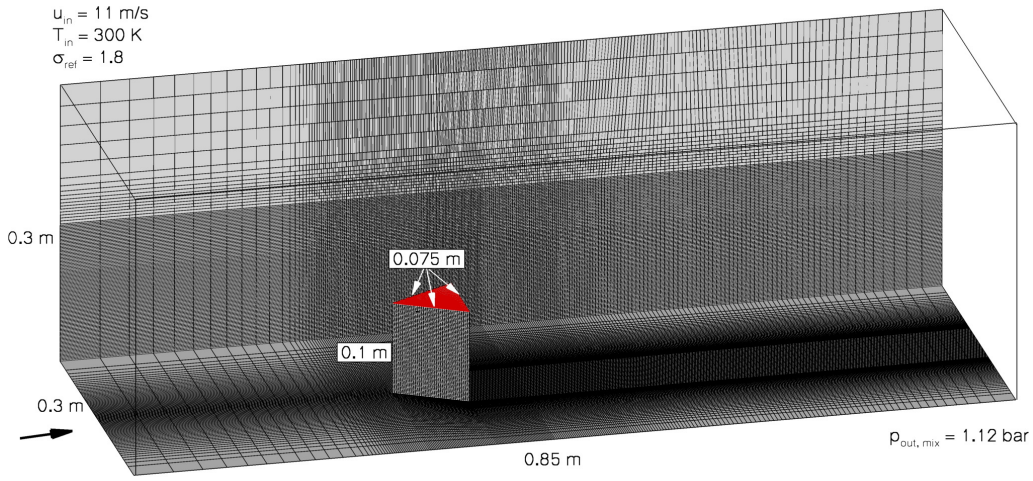

Figure 11: Numerical test-section including the prismatic body and computational discretization of the domain. Fluid: water from left to right, $T_{in}=300$ K, $u_{in}=11$ m/s, $p_{out}=1.12$ bar, $\Delta t_{CFD}=2.9\cdot10^{-7}$ s, $3.1\cdot10^{6}$ finite volumes.

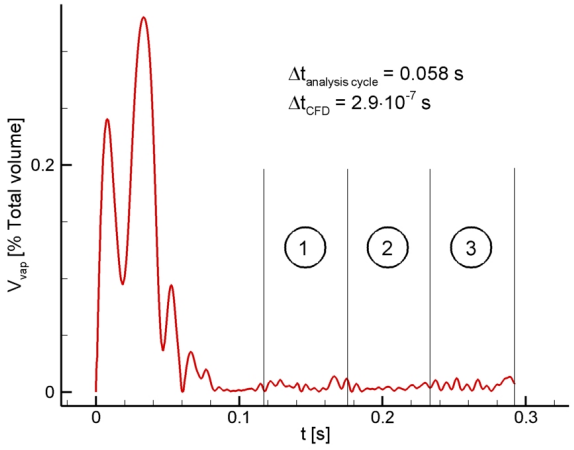

Figure 12: Time history of the integrated vapor volume V_{vap} [% total volume of the computational domain]. Fluid: water, $T_{in}=300$ K, $u_{in}=11$ m/s, $p_{out}=1.12$ bar, $\Delta t_{CFD}=2.9\cdot10^{-7}$ s.

We perform 10^6 time steps with a step size of $\Delta t_{CFD}=2.9\cdot10^{-7}$ *s*, which leads to a physical simulation time of *0.29 s*. The first *0.116 s* of the simulation are not analyzed in detail as during this time the flow dynamics are supposed to be affected by the initialization of the simulation. In Fig. 12 the time history of the integrated vapor volume fraction V_{vap} within the complete numerical domain is shown. Starting from *t=0.116 s* we define three time intervals *1-3* with length $\Delta t_{analysis\ cycle}=0.058$ *s*. Within all three time intervals the graph of the integrated vapor volume fraction V_{vap} contains oscillations of the frequencies $f_1=22.8$ *Hz*, $f_2=62.7$ *Hz* and $f_3=136.8$ *Hz*.

Figure 13 depicts a series of top views of the prismatic body (red) for *10* equidistant instants in time t_1-t_{10} with $\Delta t_{pic}=0.019$ *s*. The flow is from left to right and the arising two-phase structures are visualized by blue iso-surfaces of the void fraction $\alpha=0.1\%$. We observe weakly time dependent cavitating tip vortices at the top of the prismatic body as well as highly unsteady cavitating vortices in the shear layers downstream of the body. Furthermore, we detect a transition of the shape of the cavitation structures from compact clouds in the near wake of the body to elongated structures (tubes) in the far wake (pic. 9 of Fig. 13). One reason therefore is the interaction of the shear layer vortices arising at the vertical edges of the body with the shear layer at the trailing edge at the top of the body.

Figure 14 provides a one-to-one comparison of the visualization of the experimentally observed cavitation pattern[42] with our numerically obtained result for one instant in time. The cavitating vortices at the tip of the body, the dispersed bubbly clouds in the near wake and the tube-like cavitation structures in the far wake are well predicted by the simulation. The agreement of both visualizations confirms our suggestion that the dynamics of cavitating flow are mainly inertia controlled.

Figure 15 depicts three perspective views of the prismatic body as well as of the bottom wall and of one side wall of the numerical test-section. Both walls are colored according to the corresponding static pressure and two-phase structures are visualized by blue iso-surfaces of the void fraction $\alpha=0.1\%$. At $t_1=0.234$ *s* (picture 1 of Fig. 15) we observe a vertical two-phase structure that reaches the bottom wall. In picture 2 at $t_2=t_1+1.17\cdot10^{-4}$ *s* the tube-like structure is fragmented into two parts. The smaller one is located at the bottom wall where it collapses violently. Thereby, the surrounding liquid accelerates towards the center of the cloud and impacts onto the wall at the bottom of the test-section. This impact results in the formation of a spherical shock (picture 3 of Fig. 15, $t_3=t_2+5.85\cdot10^{-5}$ *s*), which propagates through the numerical domain and enforces a strong increase Δp of the static pressure. For the presented collapse the maximum pressure increase reaches $\Delta p=65$ *bar* directly after the impact of the liquid. The pressure increase behind the shock is approximately inverse proportional to the radius of the spherical shock front. Hence, the shock induced load on the walls of the numerical test-section strongly depends on the position of the collapsing cloud. If the distance between the cloud and the wall of the test-section is sufficiently small, then the instantaneous force on the wall might be strong enough to damage the material of the wall. Additionally, it is supposed that the erosive effect of the collapse induced shock is intensified by the interaction of a cloud collapse with a single vapor bubble that is in contact with the wall. Although the mechanism of cavitation erosion is not yet clarified in detail, it is reasonable to consider shock induced loads as a driving mechanism within the complex process of cavitation erosion. Therefore, we investigate the forces acting on the bottom wall of the numerical test-section for the previously defined "analysis cycles" 1-3 as shown in Fig. 12. For each of these time intervals we record the maximum static pressure within those computational cells that are directly located at the bottom wall. The resulting "foot-print" of the maximum pressure is depicted in Fig. 16 for each analysis cycle. Within the experimental investigation[42] the areas of intense erosion at the bottom walls were detected. The centers of these areas are marked by red crosses in Fig. 16 in order to relate the numerical prediction of the maximum forces to the experimentally observed damage at the surface of the bottom wall. Although the numerically predicted maximum loads of *60-100 bar* occur slightly upstream of the experimentally determined areas of most intense erosion, the results demonstrate that the physical model together with the numerical approach is suitable to predict the position of erosion critical areas. Furthermore, it should be pointed out that the experiment runs for about *5400 s* while the numerical simulation covers a small time interval of *0.058 s* for each analysis cycle. Nevertheless, even for the performed short time analysis a statistical behavior is present. We observe 2-5 strong impacts ($\Delta p > 50$ *bar*) per cycle, which leads to an estimated number of impacts of $3\cdot10^5$ for an experimental analysis of *5400 s*. However, as previously stated, the number of erosive events could be 1 or 2 orders of magnitude smaller if it turns out that the coexistence of a cloud collapse together with a single bubble collapse should be the necessary constellation of cavitation erosion. Therefore, further experimental and numerical investigations are required to determine a correlation of erosion rates with the number of cloud collapse events.

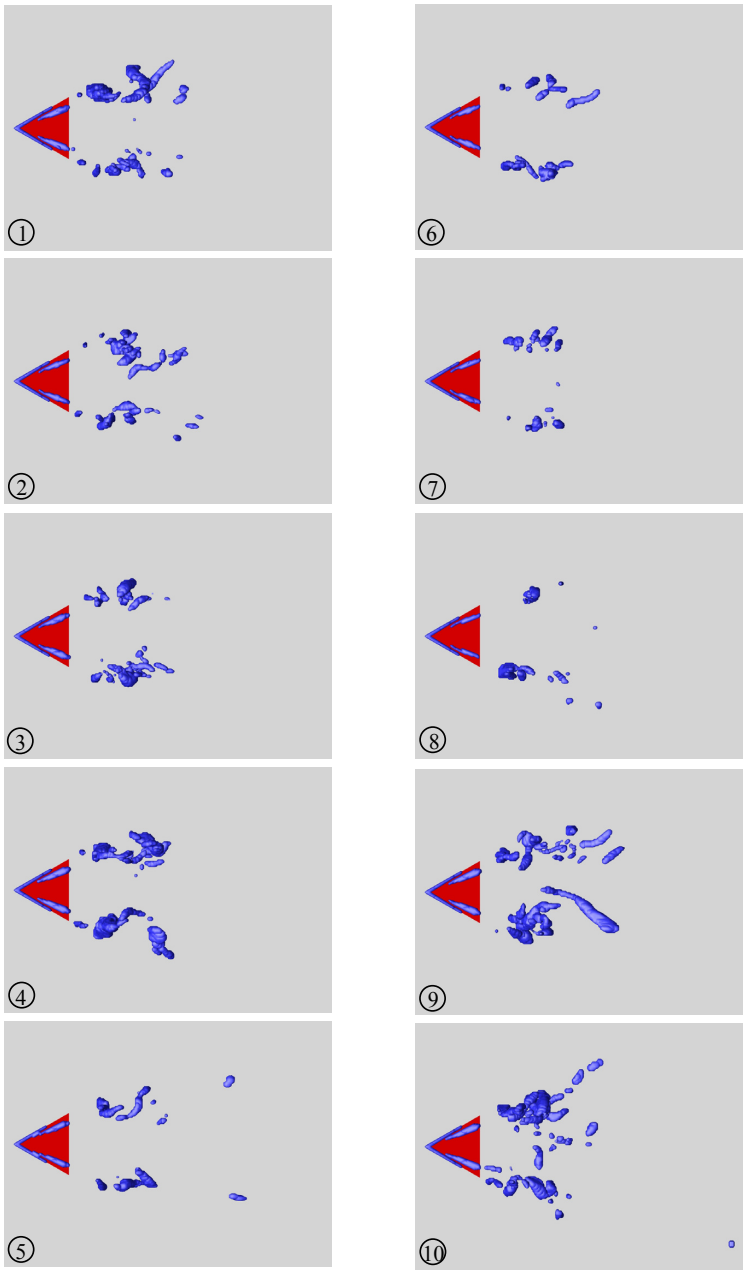

Figure 13: Top view of the prismatic body and arising cavitation structures at 10 equidistant instants in time within the analysis cycles 1-3 of Fig. 12. Blue surfaces indicate two-phase regions with $\alpha \geq 0.1\%$.
Fluid: water from left to right, $T_{in}=300$ K, $u_{in}=11$ m/s, $p_{out}=1.12$ bar, $\Delta t_{CFD}=2.9 \cdot 10^{-7}$ s, $\Delta t_{pic}=0.019$ s.

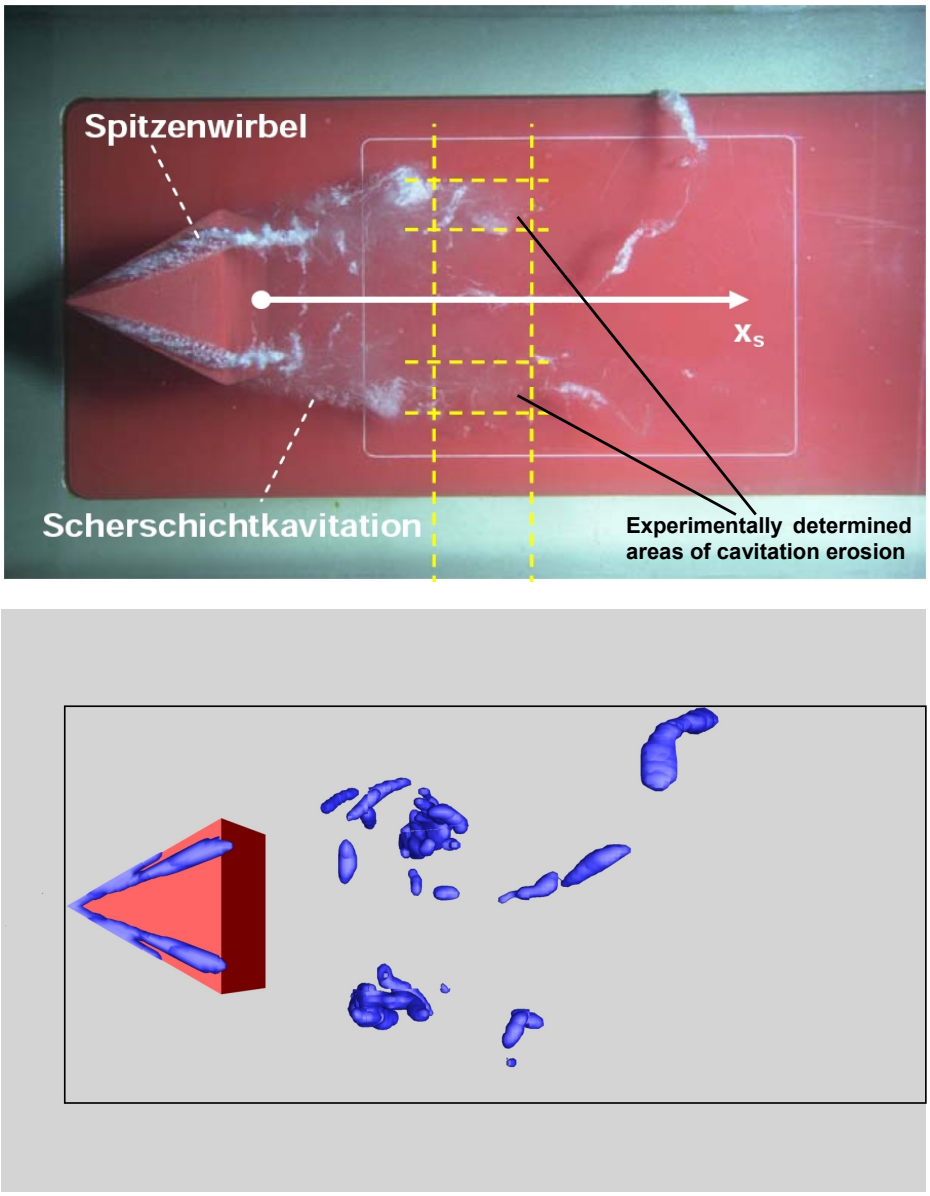

Figure 14: Top view of the prismatic body and arising cavitation structures at one instant in time. Visualization of the experiment[42] (top) and of the numerical result (bottom). Blue surfaces indicate two-phase regions with $\alpha \geq 0.1\%$. Fluid: water from left to right, $T_{in}=300$ K, $u_{in}=11$ m/s, $p_{out}=1.12$ bar, $\Delta t_{CFD}=2.9 \cdot 10^{-7}$ s.

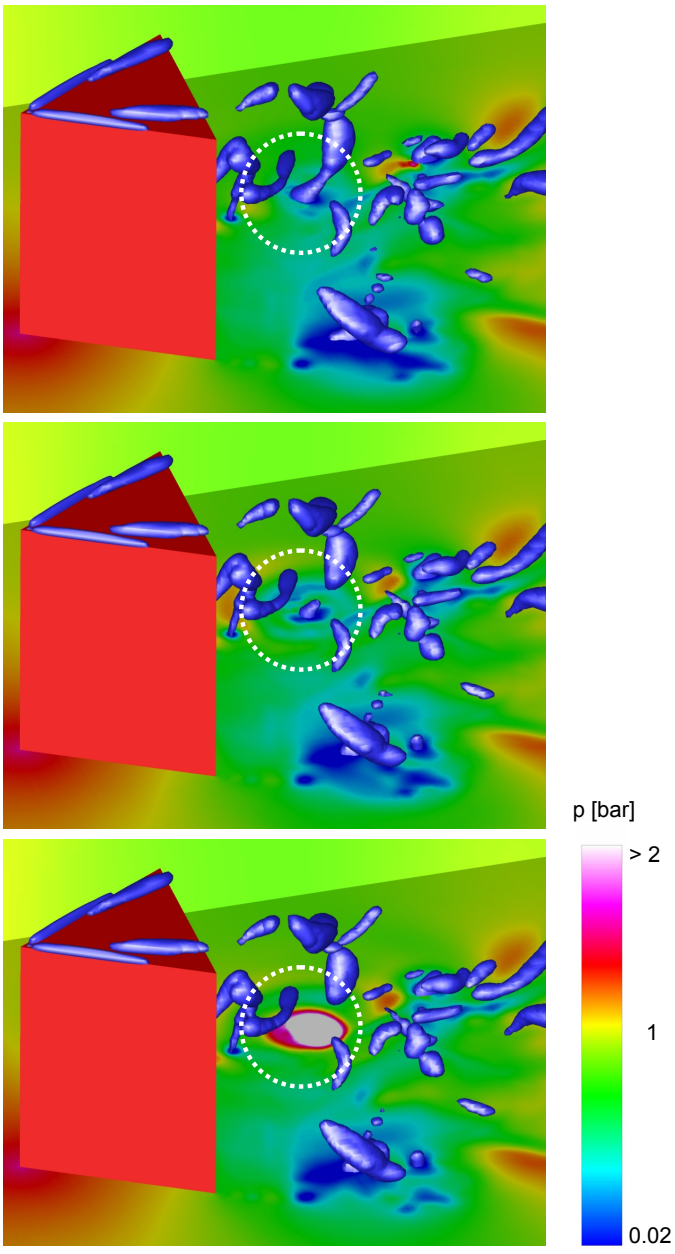

Figure 15: Perspective view of the prismatic body and shock formation due to collapsing cavitation structure at 3 instants in time. The bottom wall and the side wall are colored according to the static pressure. The maximum pressure at the bottom wall reaches 65 bar. Blue surfaces indicate two-phase regions with α≥0.1%.
Fluid: water from left to right, T_{in}=300 K, u_{in}=11 m/s, p_{out}=1.12 bar, Δt_{CFD}=2.9·10^{-7} s.

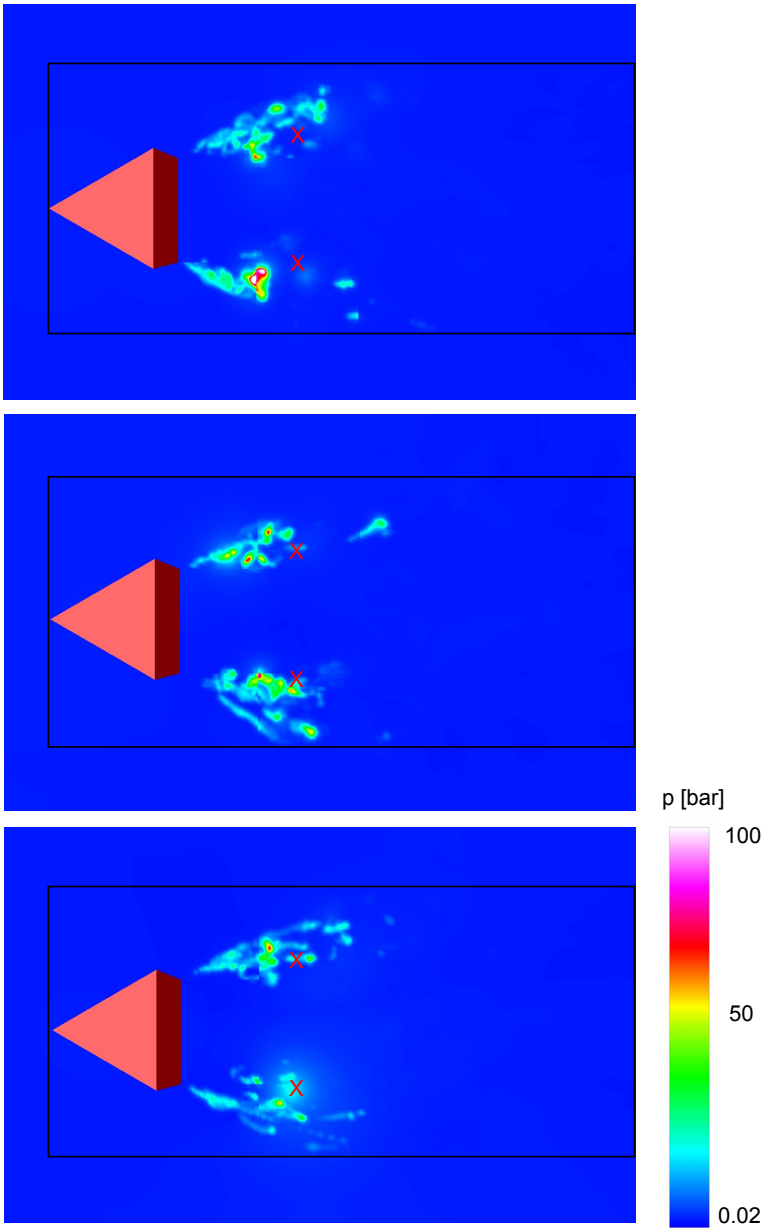

Figure 16: Top view of the prismatic body and the numerically obtained pressure "foot-prints" for the analysis cycles 1-3 as defined in Fig. 12. Red crosses mark the experimentally[42] obtained centers of most intense erosion. In picture 3 the small orange spot to the top left of the red cross corresponds to the collapse depicted in Fig. 15.
Fluid: water from left to right, T_{in}=300 K, u_{in}=11 m/s, p_{out}=1.12 bar, Δt_{CFD}=2.9·10^{-7} s.

V. Conclusion

We apply a conservative thermodynamic model to simulate liquid flows including cavitation/recondensation. In order to resolve wave dynamics in low Mach number flows we introduce a modified numerical flux function that is uniformly consistent for $M \rightarrow 0$ and provides stable time-accurate simulations. The results of our CFD-Tool CATUM are validated with analytical considerations and one-to-one comparisons of numerical and experimental results are presented. We demonstrate the applicability of CATUM to simulate high speed flows in micro-channels including the resolution of wave dynamics during the development of the flow. The obtained two-phase region within the bore-hole of the investigated 6-hole Diesel injector reduces the effective area of the nozzle by 24%, which is in good agreement with the experimental data[43]. The formation of shocks during the last stages of collapsing vapor clouds and its relation to cavitation erosion are discussed in detail for a complex 3-D flow around a prismatic body. Although the numerically predicted critical areas are slightly upstream to the experimentally determined positions we conclude that the results are sufficient to predict erosive effects, which is highly important for the design and the optimization of hydraulic machinery such as pumps, turbines and injection systems.

Further investigations will focus on the effects of non-condensable gas within the liquid. Preliminary numerical tests already indicate that this leads to a reduction of the collapse strength as well as to a reduction of high frequency flow features. Moreover, we are investigating the interaction of collapsing clouds and single bubbles to obtain additional insight into the flow dynamic mechanisms of cavitation erosion.

Acknowledgments

This investigation was partly supported by the Deutsche Forschungsgemeinschaft (DFG) and the "KSB-Stiftung".

References

[1]Brennen, C. E., *Cavitation and Bubble Dynamics*, Oxford Engineering Science Series, Oxford University Press, New York, 1995.

[2]Reisman, G. E., Wang, Y. -C., and Brennen, C. E., "Observations of Shock Waves in Cloud Cavitation," *J. Fluid Mech.*, Vol. 355, 1998, pp. 255-283.

[3]Meister, A., "Asymptotic Single and Multiple Scale Expansions in the Low Mach Number Limit," *SIAM J. Appl. Math.*, Vol. 60, No. 1, 1999, pp. 256-271.

[4]Guillard, H., and Murrone, A., "On the Behavior of Upwind Schemes in the Low Mach Number Limit: II. Godunov Type Schemes," *Computers & Fluids*, Vol. 33, No. 4, 2004, pp. 655-675.

[5]Guillard, H., and Viozat, C., "On the Behavior of Upwind Schemes in the Low Mach Number Limit," *Computers & Fluids*, Vol. 28, No. 1, 1999, pp. 63-86.

[6]Schmidt, S. J., Sezal, I. H., Schnerr, "Compressible Simulation of High Speed Hydrodynamics with Phase Change," In: *ECCOMAS CFD 2006 - European Conference on Computational Fluid Dynamics*, edited by P. Wesseling, E. Onate, J. Périaux, 2006.

[7]Turkel, E., "Preconditioning Techniques in Fluid Dynamics," *Annual Review of Fluid Mechanics*, Vol. 31, 1999, pp. 385-416.

[8]Kunz, R. F, Boger, D. A., Stinebirg, D. R., Chyczewski, T. S., Lindau, J. W., Gibeling, H. J., Venkateswaran, S., and Govindan, T. R., "A Preconditioned Navier-Stokes Method for Two-Phase Flows with Application to Cavitation Prediction," *Computers & Fluids*, Vol. 29, No. 8, 2000, pp. 849-875.

[9]Huang, D. G., "Preconditioned Dual-Time Procedures and its Application to Simulating the Flow with Cavitations," *J. Comput. Phys.*, Vol. 223, No. 2, 2007, pp. 685-689.

[10]Senocak, I., and Shyy, W., "A Pressure Based Method for Turbulent Cavitating Flow Computations," *J. Comput. Phys.*, Vol. 176, No. 2, 2002, pp. 363-383.

[11]Müller, B., "Low Mach Number Asymptotics of the Navier-Stokes Equations and Numerical Implications," von Karman Institute for Fluid Dynamics, Lecture Series 1999-03, 1999.

[12]Sauer, J., "Instationär kavitierende Strömungen - Ein neues Modell, basierend auf Front Capturing (VoF) und Blasendynamik," Ph.D. Dissertation, Universität Karlsruhe, Karlsruhe, Germany, 2000.

[13]Venkateswaran, S., Lindau, J. W., Kunz, R. F., and Merkle, C. L., "Computation of Multiphase Mixture Flows with Compressibility Effects," *J. Comput. Phys.*, Vol. 180, No. 1, 2002, pp. 54-77.

[14]Delale, C. F., Schnerr, G. H., and Sauer, J, "Quasi-One-Dimensional Steady-State Cavitating Nozzle Flows," *J. Fluid Mech.*, Vol. 427, 2001, pp. 167-204.

[15]Berg, A., Iben, U., Meister, A., and Schmidt, J., "Cavitation in Hydraulic Tools Based on Thermodynamic Properties of Liquid and Gas," *Shock Waves*, Vol. 14, 2005, pp. 111-121.

[16]Schnerr, G. H., Schmidt, S. J., Sezal, I. H., and Thalhamer, M., "Shock and Wave Dynamics of Compressible Liquid Flows with Special Emphasis on Unsteady Load on Hydrofoils and on Cavitation in Injection Nozzles," Invited Lecture. In: *Proceedings CAV2006 - Sixth International Symposium on Cavitation*, CD-ROM publication, 2006.

[17]Schnerr, G. H., Sezal, I. H., and Schmidt, S. J., "Numerical Investigation of 3-D Cloud Cavitation with Special Emphasis on Collapse Induced Shock Dynamics," *Phys. Fluids*, (to be published).

[18]Paillère, H, Corre, C., and García Cascales, J. R., "On the Extension of the AUSM+ Scheme to Compressible Two-Fluid Models," *Computers & Fluids*, Vol. 32, No. 6, 2003, pp. 891-916.

[19]Chang, C. -H., and Liou, M. -S., "A robust and accurate approach to computing compressible multiphase flow: Stratified flow model and AUSM+-up scheme," *J. Comput. Phys.*, Vol. 225, No. 1, 2007, pp. 840-873.

[20]Harten, A., Lax, P. D., Lavermore, D., and Morokoff, W. J., "Convex Entropies and Hyperbolicity for General Euler Equations," *SIAM J. Numer. Anal.*, Vol. 35, No. 6, 1998, pp. 2117-2127.

[21]Trevena, D. H., "Cavitation and the Generation of Tension in Liquids," *J. Phys. D: Appl. Phys.*, Vol. 17, 1984, pp. 2139-2164.

[22]Delale, C. F., Okita, K., and Matsumoto, Y., "Steady-State Cavitating Nozzle Flows with Nucleation," *J. Fluids Eng.*, Vol. 127, 2005, pp. 770-777.

[23]Oldenbourg, R., *Properties of Water and Steam in SI-units*, Springer-Verlag, Berlin, 1989.

[24]Saurel, R., Cocchi, J. P., and Butler, P. B., "Numerical Study of Cavitation in the Wake of a Hypervelocity Projectile", *J. Propulsion and Power*, Vol. 15, No. 4, 1999, pp. 513-522.

[25]IAPWS, International Association for the Properties of Water and Steam.

[26]Viozat, C., "Implicit Upwind Schemes for Low Mach Number Compressible Flows," INRIA Report No. 3087, 1997.

[27]Munz, C. -D., Roller, S., Klein, R., and Geratz, K. J., "The Extension of Incompressible Flow Solvers to the Weakly Compressible Regime," *Computers & Fluids*, Vol. 32, No. 2, 2003, pp. 173-196.

[28]Metivier, G., and Schochet, S., "The Incompressible Limit of the Non-Isentropic Euler Equations," *Arch. ration. mech. anal.*, Vol. 158, No. 1, 2001, pp. 61-90.

[29]Hirsch, C., "Numerical Computation of Internal and External Flows", John Wiley & Sons, Chichester, 1988.

[30]Liou, M. -S., "Ten Years in the Making – AUSM-Family," NASA TM-2001-210977, 2001.

[31]Toro, E. H., *Riemann Solvers and Numerical Methods for Fluid Dynamics*, Springer-Verlag, Berlin, 1999.

[32]Shu, C. W., "Essentially Non-Oscillatory and Weighted Essentially Non-Oscillatory Schemes for Hyperbolic Conservation laws," ICASE Report No. 97-65, 1997.

[33]LeVeque, R.J., *Finite Volume Methods for Hyperbolic Problems*, Cambridge University Press, Cambridge, England, UK., 2002.

[34]Schmidt, S. J., Sezal, I. H., Schnerr, G. H., Thalhamer, M., and Förster, M., "Compressible Simulation of Liquid/Vapour Two-phase Flows with Local Phase Transition," In: *ICMF 2007 - International Symposium on Multiphase Flow*, edited by M. Sommerfeld, CD-ROM publication, 2007.

[35]Sezal, I. H., Schmidt, S. J., Schnerr, G. H., Thalhamer, M., and Förster, M., "Shock and Wave Dynamics in Cavitating Compressible Liquid Flows in Injection Nozzles," *Shock Waves*, (submitted).

[36]Rudy, D. H., and Strickwerda, J. D., "A Non-Reflecting Outflow Boundary Condition for Subsonic Navier-Stokes Calculations," *J. Comput. Phys.*, Vol. 36, No. 1, 1980, pp. 55-70

[37]Hiroyasu, H., Arai, M., and Shimizu, M., "Break-up Length of a Liquid Jet and Internal Flow in a Nozzle," ICLASS-91, Gaithersburg, MD, 1991.

[38]Busch, R., "Untersuchung von Kavitationsphänomenen in Dieseleinspritzdüsen," Ph.D. Dissertation, Fachbereich Maschinenbau, Universität Hannover, Hannover, Germany, 2001.

[39]Kjeldsen, M., Arndt, R .E. A., and Effertz, M., "Spectral Characteristics of Sheet/Cloud Cavitation," *J. Fluids Eng.*, Vol. 122, 2000, pp. 481-487.

[40]Foeth, E.J., van Doorne, C.W.H., van Terwisga, T., and Wienke, B., "Time Resolved PIV and Flow Visualization of 3D Sheet Cavitation," *Exp. in Fluids*, Vol. 40, 2006, pp. 503-513.

[41]Schmidt, S. J., Sezal, I. H., Schnerr, G. H., and Thalhamer, M., "Shock Waves as Driving Mechanism for Cavitation Erosion," In: *ISAIF - International Symposium on Experimental and Computational Aerothermodynamics of Internal Flows*, edited by I. Trebinjak, CD-ROM publication, 2007.

[42]Huber, R., "Geschwindigkeitsmaßstabseffekte bei der Kavitationserosion in der Scherschicht nach prismatischen Kavitatoren," Report Nr. 102, Lehrstuhl und Versuchsanstalt für Wasserbau und Wasserwirtschaft, TU München, Munich, Germany, 2004.

[43]Chaves, H., Knapp, M., Kubitzek, A., Obermeier, F., and Schneider, T., "Experimental study of cavitation in the nozzle hole of Diesel injectors using transparent nozzles," SAE Paper 950290, 1995, pp. 645-657.

H. Eight publication

This publication [71] contains a similar analysis as presented in [64] (Appendix C). Again, cavitation phenomena around a twisted hydrofoil are investigated. However, in this publication a NACA0009 hydrofoil at different twist angles is considered. The results compare well with previous observations of the author as well as with experimental findings [23].

An excellent agreement is reported by comparison of the numerically predicted collapse of a spherical bubble with the solution of the Rayleigh-Plesset equation [7]. This indicates the potential of the thermodynamic model for the prediction of bubble collapses as presented in Appendix F [63].

Non-reflecting boundary conditions are implemented in order to reduce artificial wave reflections at the inlet and the outlet of the numerical domain.

I derived the formulation for the boundary conditions, generated all grids, performed most of the simulations, analyzed most of the results and prepared the manuscript.

PHYSICS OF FLUIDS **20**, 040703 (2008)

Numerical investigation of three-dimensional cloud cavitation with special emphasis on collapse induced shock dynamics

Günter H. Schnerr,[a] Ismail H. Sezal, and Steffen J. Schmidt
Technische Universität München, Lehrstuhl für Fluidmechanik-Fachgebiet Gasdynamik, D-85747 Garching, Germany

(Received 30 September 2007; accepted 27 December 2007; published online 30 April 2008)

The aim of the present investigation is to model and analyze compressible three-dimensional (3D) cavitating liquid flows with special emphasis on the detection of shock formation and propagation. We recently developed the conservative finite volume method CATUM (Cavitation Technische Universität München), which enables us to simulate unsteady 3D liquid flows with phase transition at all Mach numbers. The compressible formulation of the governing equations together with the thermodynamic closure relations are solved by a modified Riemann approach by using time steps down to nanoseconds. This high temporal resolution is necessary to resolve the wave dynamics that leads to acoustic cavitation as well as to detect regions of instantaneous high pressure loads. The proposed two-phase model based on the integral average properties of thermodynamic quantities is first validated against the solution of the Rayleigh–Plesset equation for the collapse of a single bubble. The computational fluid dynamics tool CATUM is then applied to the numerical simulation of the highly unsteady two-phase flow around a 3D twisted hydrofoil. This specific hydrofoil allows a detailed study of sheet and cloud cavitation structures related to 3D shock dynamics emerging from collapsing vapor regions. The time dependent development of vapor clouds, their shedding mechanism, and the resulting unsteady variation of lift and drag are discussed in detail. We identify instantaneous local pressure peaks of the order of 100 bar, which are thought to be responsible for the erosive damage of the surface of the hydrofoil. © *2008 American Institute of Physics*.
[DOI: 10.1063/1.2911039]

I. INTRODUCTION

The significance of understanding cavitating flows is undoubtedly related to their occurrence in various technical applications, such as hydraulic machinery and fuel injection systems, as well as in medical procedures. The compressible dynamics of collapsing vapor bubbles or bubbly clouds constitutes a common and important aspect of two-phase flow phenomena within these applications.

Due to the operating conditions of pumps, turbines, and ship propellers, cavitation is hardly avoidable. Caused by the breakup of a sheet cavity, bubbly vapor clouds are convected into regions of increased pressure, where collapselike recondensation leads to the formation of shocks. Thereby, high frequency unsteady load as well as noise production and erosion occur. Cavitating two-phase flow is also experienced in microscale injection systems of internal combustion engines. The corresponding flow characteristics contain high frequency wave dynamics and acoustic cavitation due to the dynamic needle excitation. Furthermore, the extensive acceleration of the flow within the injector leads to hydrodynamic cavitation at the entries to the spray holes. Here, the prediction of cavitation is important to improve the spray characteristics of the fuel and to detect erosion critical areas.

The collapse mechanism of a single isolated bubble has been extensively studied theoretically and experimentally by numerous research groups for different conditions.[1–7] Experimental observations for the collapse of a single bubble as well as a bubble cloud demonstrate that violent shock structures occur. Fujikawa and Akamatsu[8] investigated the behavior of collapsing bubbles and radiated pressure waves. They reported shock intensities at the wall of the order of 100 bar in magnitude when the collapsing bubble is close to the surface. Philipp and Lauterborn[9] observed pressures up to several ten thousand bar acting on the material surface due to the collapse of bubbles, which are in direct contact with the solid wall. Reisman *et al.*[10] experimentally investigated the periodic breakup and collapse of sheet and vortex cavities for different hydrofoils and observed large impulsive surface loads. Moreover, they introduced a classification of local and global shock events according to their flow dynamic origin and suggested that shock dynamics is responsible for the damage and the noise observed in many cavitating flows. Ikeda *et al.*[11] investigated the appliance of collapsing vapor clouds within the technique of shock wave lithotripsy—cavitation controlled lithotripsy.

Besides these experimental investigations, numerical analysis based on various techniques are used to predict cavitating flow characteristics. Dang[12] applied a three-dimensional (3D) panel method based on the incompressible potential theory to predict sheet cavitation as well as the development of the re-entry jet for different hydrofoil geometries. Chen and Heister[13] presented a method developed by Chorin[14] to simulate two-dimensional (2D) cavitating flows where the density of the liquid is assumed to be constant. Methods based on the pressure correction technique are

[a]Electronic mail: schnerr@flm.mw.tu-muenchen.de.

widely applied to simulate the periodic formation of the sheet cavity and its breakup dynamics for 2D and 3D applications. In these approaches, the phase transition is either controlled by bubble dynamic considerations[15] or in accordance to calibrated finite rate models.[16] Typically, both phases are assumed to have constant density. Preconditioning techniques in combination with density based numerical methods enable the incorporation of compressibility effects of both phases. Furthermore, these methods allow for the simulation of low speed unsteady flow by the use of dual time-stepping approach.[17–19] Kunz *et al.*[20] demonstrated the applicability of preconditioning techniques to perform turbulent simulations of unsteady 3D cavitating flows based on a barotropic state law.

Although these methods allow for the prediction of steady and unsteady flow characteristics based on the time scale of the convective velocity, they do not incorporate wave dynamic effects where the time scale is necessarily inverse proportional to the speed of sound c. We therefore propose a numerical approach that is especially developed to predict the formation and propagation of collapse related shocks and rarefaction waves occurring in cavitating flows. In order to model both wave dynamics and hydrodynamics, we present a consistent numerical flux function for low and high speed unsteady flows and propose a phase transition formulation based on stable thermodynamic states of water and water vapor.

II. PHYSICAL MODEL

Cavitating flows involve a large variety of physical phenomena, such as bubble dynamics, nonequilibrium thermodynamics, multiphase turbulence, and multiphase wave dynamics. Each physical aspect incorporates specific spatial and temporal scales, which strongly depend on the considered flow field. Even the use of high performance computers does not presently enable simulations that resolve all scales of the above stated physical phenomena, especially not for 3D unsteady flows arising from typical technical applications. This motivates the development of a scale adaptive physical model based on the conservation principles of mass, momentum, and energy as well as on thermodynamic relations. Particularly, we investigate the potential of modeling the dynamics of cavitating flows by the use of spatially averaged governing equations. Due to the dominance of inertia effects within the considered two-phase flows, we neglect viscous effects and express the conservation principles by the Euler equations. However, the inclusion of dissipative mechanisms into the model is possible without restrictions.

Let $\vec{q}$ be the vector of conserved quantities defined by the density ρ, the components u_i of the velocities in coordinate direction x_i, and the specific total energy E as the sum of the specific internal energy e per unit mass and the specific kinetic energy $\frac{1}{2}\Sigma u_i^2$. Let $F_i(\vec{q})$ be the physical flux in coordinate direction x_i, while δ_{ij} and p denote the Kronecker symbol and the pressure, respectively,

$$\vec{q} = \begin{pmatrix} \rho \\ \rho u_1 \\ \rho u_2 \\ \rho u_3 \\ \rho E \end{pmatrix}, \quad F_i(\vec{q}) = \rho u_i \cdot \begin{pmatrix} 1 \\ u_1 \\ u_2 \\ u_3 \\ E \end{pmatrix} + p \cdot \begin{pmatrix} 0 \\ \delta_{1i} \\ \delta_{2i} \\ \delta_{3i} \\ u_i \end{pmatrix}. \tag{1}$$

The differential or pointwise form of the Euler equations can be written as

$$\frac{\partial}{\partial t}\vec{q} = -\sum_{i=1}^{3} \frac{\partial}{\partial x_i} F_i(\vec{q}). \tag{2}$$

With respect to the classical interpretation, we know that Eq. (2) is valid only if the flow variables are differentiable. However, in order to model wave dynamics of cavitating flows, we have to take discontinuities due to shocks as well as due to phase interfaces into account. Instead of enforcing the conservation principles in a pointwise fashion, we use the weak form of the Euler equations. Therefore, we partition the flow domain into disjoint fixed control volumes C_k of corresponding volume V_k, surface S_k, and outer unit normal vector $\vec{n}_k=(n_{k,1}\ n_{k,2}\ n_{k,3})^t$. The weak form of the Euler equations for each control volume C_k follows as

$$\frac{d}{dt}\int_{C_k} \vec{q} d\mathrm{V}_k = -\int_{S_k} \sum_{i=1}^{3} n_{k,i} F_i(\vec{q}) d\mathrm{S}_k. \tag{3}$$

By defining the cell average operator A_k through

$$A_k(\vec{q}) := \frac{1}{V_k}\int_{C_k} \vec{q} d\mathrm{V}_k, \tag{4}$$

we assign to all weak solutions within the cell C_k their common integral average value $\vec{q}_k=A_k(\vec{q})$. It turns out that the weak form of the Euler equations resembles a system of evolution equations of the cell averages of weak solutions,

$$\frac{d}{dt}\vec{q}_k = -\int_{S_k} \sum_{i=1}^{3} n_{k,i} F_i(\vec{q}) d\mathrm{S}_k. \tag{5}$$

Up to now, we have not made any additional assumption on the flow field itself, which means that Eq. (5) is valid for any type of inviscid multicomponent and multiphase flow, even if the species do not share a common pressure, temperature, or velocity. Nonetheless, the choice of fixed control volumes C_k introduces local length scales l_k of the order of $l_k=\sqrt[3]{V_k}$ into the physical problem and, hence, any process occurring beyond those scales can no longer be resolved. Therefore, the previously defined cell averages can be interpreted as the result of a conservative low pass filtering of the flow field. In the case of cavitating bubbly liquid flow, the resolution of two-phase features depends on the fraction $\Psi=R/l_k$ of the bubble radius R and the induced length scale l_k. If $\Psi \ll 1$, the model resembles the average behavior of a mixture, while it fully resolves single bubbles if $\Psi \gg 1$. As the transition from the resolved case to the averaged case and vice versa does not require additional modeling, we denote the evolution of integral averages as a scale adaptive model. Furthermore, the right hand side of Eq. (5) implies that the evolution of the integral average equations is entirely depen-

dent on the net fluxes of mass, momentum, and energy across the surface of each control volume, while explicit knowledge of small scale information within the cell C_k is not required. However, the closure of the defined initial-boundary value problem (5) necessitates constitutive relations for the cell averaged thermodynamic quantities, ρ_k, e_k, and p_k, as well as consistent initial and boundary conditions. In this section, we assume that consistent initial and boundary data are strictly available. Thus, the physical fluxes along the boundary surfaces are known and, hence, Eq. (5) reduces to an initial value problem. At each instant in time, the corresponding initial values already determine the average density ρ_k, velocity $\vec{u}_k$, and total energy E_k within the control volume C_k. Therefore, the average specific internal energy e_k per unit mass follows from the average total energy E_k by subtracting the specific kinetic energy. However, the definition of the average pressure p_k requires additional model assumptions. In this investigation, we restrict the fluid to consist of water and water vapor. Impurities such as solid particles or solute gas are not explicitly modeled, but their effects on the thermodynamic behavior of water are taken into account in a simplified manner. It is known that highly purified water allows for the occurrence of metastable states far beyond saturation conditions,[21] whereas tap water does not show this behavior. In the latter case, the large number of impurities immediately results in heterogeneous nucleation[22] and, thus, in the formation of vapor bubbles. As the specific volume of water vapor is by several orders of magnitude larger than the one of liquid water, the phase transition results in rapid pressure equalization close to the stable saturation state. This allows us to neglect metastable states and to consider stable thermodynamic conditions. In order to avoid the definition of unknown local parameters such as the average bubble radius or the bubble number density, we have to neglect surface tension and buoyancy effects. Consequently, the coexistence of both phases implies that the pressure p_k is determined by the Clausius–Clapeyron relation and the average density ρ_k within cell C_k is a convex combination of the saturation densities $\rho_{l,\mathrm{sat}}$, $\rho_{v,\mathrm{sat}}$ of liquid and vapor. Furthermore, we define at each instant in time and for each control volume an average temperature T_k in order to relate the saturation density to the internal energy. By defining the vapor volume fraction α_k and the vapor mass fraction ε_k, we obtain the unknown quantities T_k, α_k, ε_k, and p_k as solutions of the system,

$$\rho_k = \alpha_k \rho_{v,\mathrm{sat}}(T_k) + (1-\alpha_k)\rho_{l,\mathrm{sat}}(T_k), \tag{6}$$

$$e_k = \varepsilon_k e_{v,\mathrm{sat}}(T_k) + (1-\varepsilon_k)e_{l,\mathrm{sat}}(T_k), \tag{7}$$

$$\varepsilon_k \rho_k = \alpha_k \rho_{v,\mathrm{sat}}(T_k), \tag{8}$$

$$p_k = p_{\mathrm{sat}}(T_k), \tag{9}$$

$$0 < \alpha, \quad \varepsilon < 1. \tag{10}$$

Thereby, the incorporated temperature dependent functions have to be specified. In the case of water and water vapor, we model these with the Oldenbourg polynomials.[23] The required closure relation in the presence of two-phase flow is thus completely defined.

If the average density ρ_k is larger than the saturation density of liquid water, we replace the closure relation with the modified Tait model $(\alpha_k, \varepsilon_k = 0)$,

$$\frac{p_k + B}{p_{\mathrm{sat}}(T_k) + B} = \left[\frac{\rho_k}{\rho_{l,\mathrm{sat}}(T_k)}\right]^N, \tag{11}$$

together with an equation for the internal energy.[24] Even though the temperature variation of the liquid is typically small, the modification of the Tait equation remains necessary in order to ensure a continuous connection of the Tait model to the temperature dependent saturation conditions. For water, we use $B = 3300$ bar and $N = 7.15$ independent of the temperature.

If the average density ρ_k is smaller than the saturation density of vapor, the applied constitutive relation models pure vapor $(\alpha_k, \varepsilon_k = 1)$, treated as calorically perfect gas, where the ratio of the specific heats is given by $\kappa = 1.327$ and the specific gas constant is 461.5 J/kg K.

The comparison of the described thermodynamic closure relations with respect to the IAPWS data[25] demonstrates that the relations accurately model the behavior of water and water vapor for a large range of thermodynamic subcritical conditions. Moreover, the presented model is neither restricted to the described set of thermodynamic closure relations nor to the assumption of instantaneous pressure equalization. However, the thermodynamic relations must imply a consistent definition of the equilibrium speed of sound c to ensure that the model is hyperbolic in time and that the initial-boundary value problem is well posed. Furthermore, the incorporation of small scale information, such as the bubble number density or the bubble size distribution, is possible, but the scale adaptability may then be lost and the model reduces to the dispersed mixture model.

III. NUMERICAL METHOD AND VALIDATION

Our numerical method CATUM relies on an approximate solution of the evolution equation (5) for each control volume C_k. As stated in Sec. II, the temporal development of Eq. (5) is completely defined by the time dependent fluxes across the surfaces of the control volumes. The hyperbolic character of the compressible formulation of the governing equations motivates a Godunov-type approximation of these fluxes. Thereby, the average values $\vec{q}_k$ and $\vec{q}_i$ of two adjacent control volumes C_k, C_i are used to define the Riemann problem across the shared surface $S_{k,i} = C_k \cap C_i$. The solution $\mathrm{RP}(\vec{q}_k, \vec{q}_i)$ of the Riemann problem at the surface $S_{k,i}$ is constant in time within a time interval $\Delta t_{\mathrm{RP}} \approx l/(|\vec{u}| + c)$, where l is the length scale of the volume and $|\vec{u}| + c$ represents the fastest signal speed. By replacing the physical fluxes $F(\vec{q}_k)$ in Eq. (5) with the numerical fluxes $\mathrm{RP}(\vec{q}_k, \vec{q}_i)$, we obtain a set of ordinary differential equations, which represent a semidiscrete unsplit finite volume method for hexahedral volumes,

$$\frac{d}{dt}\vec{q}_k = -\sum_{i=1}^{6} S_{k,i} \cdot \mathrm{RP}(\vec{q}_k, \vec{q}_i). \tag{12}$$

This framework is well developed for the simulation of steady and unsteady compressible aerodynamics of moderate

and high Mach number flows as well as for the investigation of wave propagation phenomena including sharp and accurate shock capturing in unsteady flow. Furthermore, methods based on Eq. (12) are conservative by construction and enable efficient time dependent simulations. Contrary to pressure based approaches, all fluxes are calculated without the need for subiterations. However, the application of Godunov-type methods to low speed flows requires substantial modification to overcome the low Mach number problem. Otherwise, the accuracy of the Godunov approximation significantly decreases if the Mach number is in the weakly compressible regime, $M \tilde{<} 0.1$, in particular, due to the high acoustic impedance ρc of liquids, the decrease of accuracy is further intensified. An extensive discussion of the low Mach number problem is beyond the scope of this investigation but can be found in the literature.[26,27] These contributions highlight the inconsistency of the discrete pressure component as part of the numerical momentum fluxes with respect to the asymptotic analysis of the governing equations.[27,28]

In order to overcome the low Mach number problem, we introduce a modified numerical flux $\mathrm{MF}(\vec{q}_k, \vec{q}_i)$ for cavitating liquid flow, which is based on the theory of characteristics and equipped with an asymptotically consistent pressure flux definition. Due to the rotational invariance of the convective fluxes, we restrict the presentation of the formulation to one spatial direction x_1. We use the subscripts k, i for the average flow variables corresponding to the control volumes to the left and to the right of the shared surface $S_{k,i}$, which we assume to be part of the x_2, x_3 plane. Provided that the Mach numbers M_k, M_i are low, the velocity u^* at the surface $S_{k,i}$ follows from the locally linearized compatibility conditions,[29]

$$u^* = \frac{\rho_k c_k u_{k,1} + \rho_i c_i u_{i,1} + p_k - p_i}{\rho_k c_k + \rho_i c_i}. \tag{13}$$

The pressure p^* at the surface $S_{k,i}$ is computed by

$$p^* = \frac{p_k + p_i}{2}. \tag{14}$$

Equation (14) does not contain the strong coupling of pressure and velocity as it would be enforced by the compatibility relations. However, this coupling is known to cause the low Mach number problem and, hence, the application of the compatibility conditions to obtain the pressure p^* at the surface $S_{k,i}$ is avoided by the definition of Eq. (14). Although the proposed pressure flux is significantly less dissipative than those of the well known linearized Riemann approaches, we do not observe related numerical instabilities. We conclude that the coupling of pressure and velocity is sufficiently implied within the definition of the velocity u^* (13). Furthermore, we achieve an upwind character of the numerical flux by the sign of the velocity u^*. Assuming positive sign, we define the following numerical flux $\mathrm{MF}(\vec{q}_k, \vec{q}_i)$ in accordance to the physical flux as defined in Eq. (1),

$$\mathrm{MF}(\vec{q}_k, \vec{q}_i) = \rho_k u^* \cdot \begin{pmatrix} 1 \\ u^* \\ u_{k,2} \\ u_{k,3} \\ E_k \end{pmatrix} + p^* \cdot \begin{pmatrix} 0 \\ 1 \\ 0 \\ 0 \\ u^* \end{pmatrix}. \tag{15}$$

For negative mass flow ($u^* < 0$), the subscripts k and i are reversed. In the presence of cavitation, the local Mach numbers M_k, M_i may reach supersonic values and, hence, the numerical flux should resemble pure upwinding of all conserved quantities. In this case, the interface values u^* and p^* are replaced by the corresponding variables on the left or on the right hand side, depending on the flow direction. The final form of the discrete evolution equations reads

$$\frac{d}{dt}\vec{q}_k = -\sum_{i=1}^{6} S_{k,i} \cdot \mathrm{MF}(\vec{q}_k, \vec{q}_i). \tag{16}$$

In order to increase the spatial accuracy of the method, we apply weighted essentially non-oscillatory reconstruction procedures (WENO-3)[30] to the velocity components and a total variation diminishing reconstruction (van Leer)[31] to the density field. As the pressure flux is already second order accurate by definition, no further procedure is required. The spatial discretization is thus second order accurate for smooth solutions and it significantly reduces oscillations in the presence of discontinuities.

We apply an explicit four-stage, second order Runge–Kutta method with enlarged stability region to advance the system (16) in time. Second order accurate simulations in space and time thereby enforce the numerical time step Δt_{CFD} being determined as the minimum of Δt_{RP} within all control volumes.

Up to now, we have presented the numerical treatment of average values corresponding to control volumes inside the computational domain. However, it turns out that the same method is applicable to boundary related cells as well. Therefore, we define additional control volumes—ghost cells—which exist only virtually. The specification of the boundary values is thus equivalent to the definition of the average values within these ghost cells. We discuss the following types of boundary values: inviscid adiabatic walls, inlet and outlet surfaces, and farfield boundaries. Besides the walls, all boundary definitions are approximate in the sense that the physical domain, e.g., a cavitation tunnel, does not provide a determined inlet or outlet. This fact is taken into account by the use of essentially nonreflective conditions. From the theory of characteristics, it follows that at a subsonic inlet surface, four conditions have to be specified, while the fifth one has to be extracted from the interior of the domain. Consequently, only one condition from the outside of the domain is required at a subsonic outlet surface and four conditions follow from the interior. It is known that the specific choice of presumed conditions is not arbitrary but needs to be consistent with the compatibility conditions.[32] We therefore presume temporally mean values of T_∞, $u_{1,\infty}$, $u_{2,\infty}$, and $u_{3,\infty}$ at the inlet and p_∞ at the outlet. For presentation purposes, we assume that $u_{2,\infty}=0$ and $u_{3,\infty}=0$. Let the superscripts $+$, $-$

denote the values of the current and the previous instant in time, let the subscripts g and i denote the average values corresponding to the ghost cell and the adjacent interior cell, and let $\phi = c \cdot \Delta t_{\mathrm{CFD}}/l$ be the dimensionless distance defined by the speed of sound c, the numerical time step Δt_{CFD}, and the cell length l. Within the ghost cells close to the inlet plane, we specify

$$p_g^+ = \frac{p_g^- + 0.5\phi[p_i + p_g^- + \rho_g^- c_g^-(u_{1,\infty} - u_{1,i})]}{1+\phi}, \tag{17}$$

$$u_{1,g}^+ = \frac{u_{1,g}^- + 0.5\phi\left[\frac{(p_g^- - p_i)}{\rho_g^- c_g^-} + u_{1,\infty} + u_i\right]}{1+\phi}, \tag{18}$$

$$\rho_g^+ = \mathrm{Tait}(p_g^+, T_\infty). \tag{19}$$

In analogy, we obtain for the related ghost cells at the outlet,

$$p_g^+ = \frac{p_g^- + 0.5\phi[p_i + p_\infty + \rho_g^- c_g^-(u_{1,i} - u_g^-)]}{1+\phi}, \tag{20}$$

$$u_{1,g}^+ = \frac{u_{1,g}^- + 0.5\phi\left[\frac{(p_i - p_\infty)}{\rho_g^- c_g^-} + u_{1,g}^- + u_i\right]}{1+\phi}, \tag{21}$$

$$\rho_g^+ = \mathrm{Tait}(p_g^+, T_i). \tag{22}$$

We suppose that the numerical inlet and outlet boundaries are located sufficiently far from two-phase domains. This assumption allows us to prescribe the average density by Eq. (19) and Eq. (22) by the modified Tait model for pure liquid water given by Eq. (11). Although we could obtain reasonable results even if this requirement is violated at the outlet of the domain, we recommend ensuring sufficiently large numerical domains.

An exact definition of solid impermeable walls is obtained by enforcing the flow tangency condition at the surfaces. Thereby, the average values assigned to the ghost cells are defined by the asymmetry of the average velocity normal to the boundary and the symmetry of all remaining values.

In order to ensure second order accurate calculations close to the boundary surfaces, the presented procedures are applied to derive average values for an additional set of ghost cells located even more distant to the specific boundary.

Our computational fluid dynamics (CFD) code CATUM is applicable to block structured hexahedron meshes and all numerical approaches operate fully parallelized. In order to validate the proposed model and the numerical method, the simulation of a single vapor bubble collapse is performed. Therefore, we construct a spherical vapor region of radius $R_B = 0.4$ mm located at the center of a cubic 3D liquid domain. The grid resolution of $l_k = 0.02$ mm results in $\Psi = 20$ with respect to R_B and, hence, the initially defined bubble is fully resolved. Based on the requirement stated in Sec. III,

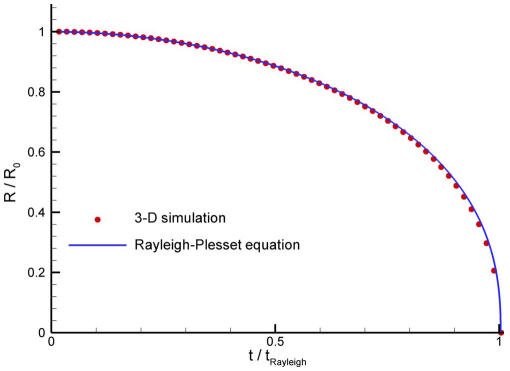

FIG. 1. (Color online) Collapse of a single bubble—comparison of simulation and bubble dynamics. Evolution of dimensionless radius R/R_0 with respect to dimensionless time t/t_{Rayleigh} from 3D CATUM simulation (dots) and solution of the Rayleigh–Plesset equation for collapse of a spherical vapor bubble, $\Delta t_{\mathrm{CFD}} = 6.5 \times 10^{-9}$ s.

we apply numerical time steps of $\Delta t_{\mathrm{CFD}} = 6.5$ ns. The numerical boundaries are located 25 diameters away from the bubble and the corresponding ghost cells model constant pressure $p_\infty = 1.0$ bar and $T_\infty = 293$ K at infinity. Initially, the flow is at rest and the temperature and the pressure within the liquid domain are equal to the farfield values. The pressure inside the bubble is given by the vapor pressure $p_{\mathrm{sat}} = 0.023$ bar at $T = 293$ K. The initially enforced pressure difference leads to the development of a centrally directed flow field, which causes the vapor bubble to collapse. The defined "Besant problem" is well known and its dynamics has been analyzed by various techniques. Although our numerical method includes compressibility effects, we compare our results with the solution of the incompressible Rayleigh–Plesset model. We motivate this comparison regarding the analytical investigation of Gilmore,[33] where it is demonstrated that the incorporation of liquid compressibility results in only a slight increase of the dimensionless collapse time of 0.5% as compared to the incompressible model. In order to achieve similar conditions, we neglect viscosity, surface tension, and noncondensable gas content within the Rayleigh–Plesset model. The first two assumptions are known to have minor influence to the collapse behavior if the initial radius of the vapor bubble is sufficiently large.[34] Figure 1 shows the time dependent evolution of the normalized bubble radius with respect to the time normalized by the Rayleigh time. The solid line corresponds to the solution of the Rayleigh–Plesset equation and the dots represent the results of the 3D compressible simulation. The agreement of both data sets demonstrates the ability of the numerical method to accurately predict inertia controlled effects such as the collapse of a vapor region. Thereby, the applied thermodynamic closure relation allows for the complete recondensation of the vapor. During the collapse, the liquid accelerates toward the center of the bubble and initiates the formation of an outward propagating shock when it impacts at the center of the recondensed bubble. The intensity of the shock is related to the impact

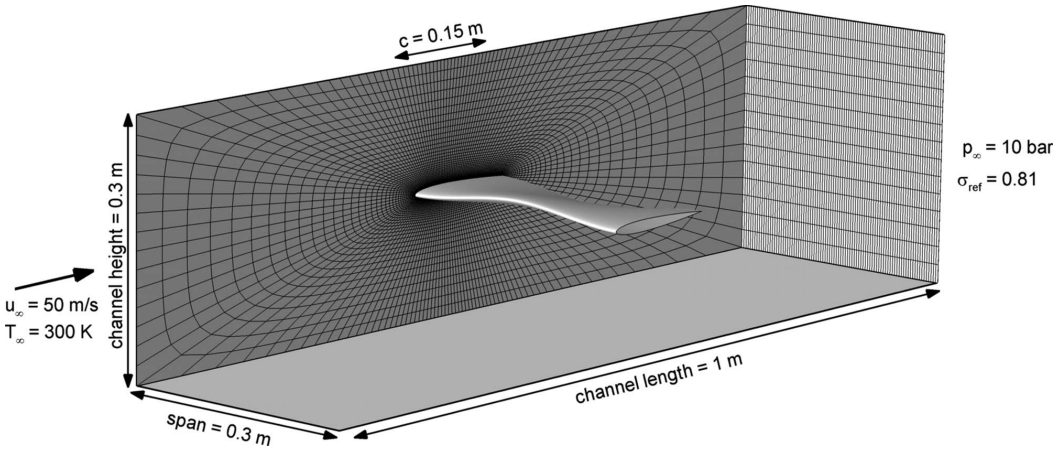

FIG. 2. 3D twisted NACA 0009 hydrofoil—computational domain and boundary conditions. Chord length $c=0.15$ m, span $s=0.3$ m, angles of attack, $-1°$ (walls) and $+10°$ (midspan), channel height of 0.3 m, and channel length of 1 m. Water inflow from left to right, inlet conditions $u_\infty=50$ m/s and $T_\infty=300$ K, outlet condition $p_\infty=10$ bar, and reference cavitation number $\sigma_{\text{ref}}=0.81$ [Eq. (23)]. Grid: 3×10^5 hexahedrons.

velocity of the liquid. For the presumed initial conditions and the defined spatial resolution, we obtain a maximum instantaneous pressure of 1040 bar within the control volume located at the center of the domain. In accordance to the theory, the spherical shock then propagates into the surrounding liquid and attenuates proportional to its distance from the origin. Due to the high acoustic impedance of the liquid, the shock speed is only slightly supersonic.

IV. 3D SHOCK DYNAMICS OF COLLAPSING VAPOR CLOUDS AROUND A CAVITATING TWISTED HYDROFOIL

Our CFD code CATUM is currently applied to simulate wave dynamics in 3D multihole fuel injectors as well as to simulate unsteady shedding mechanisms around 3D hydrofoils. In this investigation, we discuss recently obtained results of shock and cloud dynamics around a twisted hydrofoil.

Figure 2 depicts the numerical test section consisting of a rectangular flow domain of dimensions of $0.3\times0.3\times1.0$ m^3. The hydrofoil is placed at the center of the test section and defined by the NACA 0009 profile with chord length of 0.15 m. The profile is twisted relative to the midspan plane to obtain a varying angle of attack from $-1°$ at the sidewalls to $+10°$ at midspan. Therefore, the interaction of the cavitation pattern with the sidewalls of the test section is avoidable for a certain range of operating conditions.[12] Furthermore, a comparable setup is experimentally investigated by Foeth *et al.*,[35] where it is demonstrated that the described hydrofoil is suitable to study well defined and repeatable shedding structures. The experimentally observed flow field is symmetric with respect to the midspan up to small scale fluctuations. This motivates a symmetric numerical treatment of the test section in order to reduce the computational effort.

We apply an O grid consisting of 300 000 hexahedrons, where we refine the spatial resolution close to the surface of the hydrofoil. Thereby, we obtain cell lengths of 1 mm$\leqslant l_k \leqslant$5 mm of those computational cells, where two-phase flow is supposed to occur. Experimental investigations show that the maximum radius of the vapor bubbles for the considered cloud cavitation pattern is of the order of 1 mm. Therefore, we conclude that the applied spatial resolution covers the interval of $\Psi\ll1$ to $\Psi\approx1$. The resulting requirement on the numerical time step leads to $\Delta t_{\text{CFD}}=45$ ns. At the inlet plane of the numerical domain, we presume pure water with an inlet velocity $u_\infty=50$ m/s and an inlet temperature $T_\infty=300$ K. At the outlet plane, we prescribe $p_\infty=10$ bar. The essentially nonreflective treatment of the boundaries according to Sec. III is applied for both planes. The prescribed temporal mean values allow for the definition of the reference cavitation parameter,

$$\sigma_{\text{ref}}=\frac{p_\infty-p_{\text{sat}}(T_\infty)}{\frac{1}{2}\rho_l(p_\infty,T_\infty)u_\infty^2}=0.81. \tag{23}$$

Previous investigations have demonstrated that the arising long time flow characteristics of this setup are determined by the boundary conditions independent of the initialization of the numerical domain. However, the required computational effort to reach the experimentally observed quasiperiodic shedding behavior is reduced by initializing the two-phase simulation with the steady state solution of a comparable single phase flow.

Figure 3 depicts perspective views of the hydrofoil together with isosurfaces of the void fraction composed of all cells with $\alpha_{\text{min}}=0.05$ at five representative instants in time

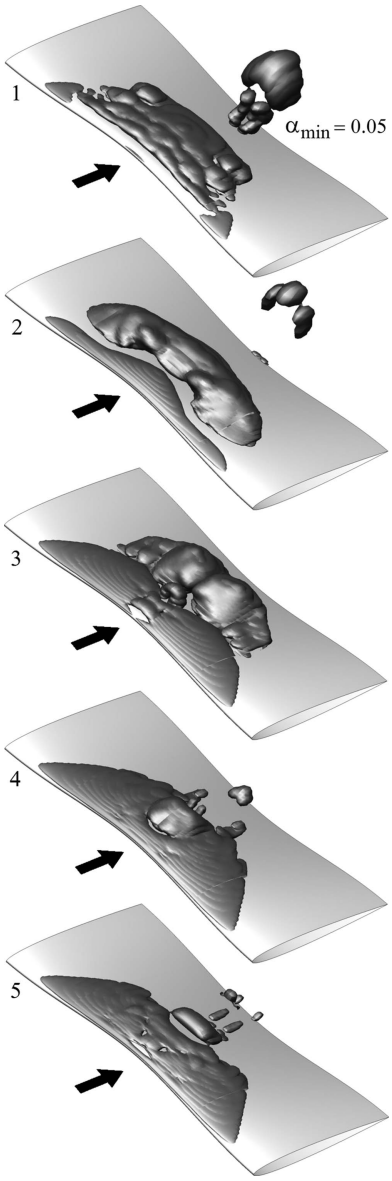

FIG. 3. Unsteady shedding mechanism, cavitation cycle 1 (see Fig. 4), $f \approx 230$ Hz, $\Delta t_{1-5} = 4.1 \times 10^{-3}$ s, and $\Delta t_{CFD} = 4.5 \times 10^{-8}$ s. Isosurfaces of void fraction with $\alpha_{min} = 0.05$ at five instances in time as indicated in Fig. 4, $t_1 = 1.26 \times 10^{-1}$ s, $t_2 = 1.27 \times 10^{-1}$ s, $t_3 = 1.28 \times 10^{-1}$ s, $t_4 = 1.29 \times 10^{-1}$ s, and $t_5 = 1.30 \times 10^{-1}$ s. 3D twisted NACA 0009 hydrofoil, $u_\infty = 50$ m/s, $\sigma_{ref} = 0.81$, $p_\infty = 10$ bar, and water $T_\infty = 300$ K.

within the time interval $\Delta t_{1-5} = 4.1$ ms corresponding to the first investigated shedding cycle—cycle 1 (see Fig. 4). The numerically obtained frequency $f \approx 230$ Hz of the shedding cycles is constant up to 3%. Based on the numerically observed maximum length of the attach sheet cavity (40% of the chord length), we obtain a Strouhal number of $St \approx 0.27$. At the first instant in time, we observe the formation of an attached sheet cavity close to the leading edge of the hydrofoil. Slightly upstream of the trailing edge, a horseshoe shaped detached cloud is visible. The vertical elongation of this cloud is of the order of 50% of the chord length. At the second instant in time, the previously attached sheet separates from the hydrofoil due to the onset of reverse flow between the cavity and the surface of the hydrofoil. Furthermore, the cloud located close to the trailing edge recondenses. At the leading edge of the hydrofoil, the reformation of the attached sheet cavity takes place. In the picture corresponding to the third instant in time, the attached sheet cavity at the leading edge reaches its maximum length and the detached cloud is still connected to the sheet. Here, the re-entry jet below the cloud is no longer formed by pure reverse flow but includes a significant spanwise velocity component, i.e., a side re-entrant jet.[35–37] The collision of the re-entrant flow with the side entrant jets below the vapor cloud causes the cloud to completely separate from the suction side of the hydrofoil. Thereby, the formation of vortices takes place that superimpose onto the main flow and accelerate the cloud downstream. This behavior is observed within various experimental setups and analyzed in detail.[10,35–38] Between time instants 3 and 4, the cloud undergoes a strong compression that is initiated by the surrounding pressure field. Picture 4 of Fig. 3 shows the vapor cloud just before its final collapse occurs. Moreover, two secondary instabilities located at the closure of the triangularly shaped sheet cavity indicate vortex structures due to the side entrant flow. At the last instant in time, a series of small scale vapor structures close to the trailing edge are observed. One of them is located nearly at the same position as the previously collapsed cloud. Indeed, this structure forms due to the postexpansion corresponding to the collapse induced shock.

The dynamic behavior of the shedding mechanism results in strongly time dependent lift and drag variations. Figure 4 depicts the time history of drag force $F_{D,p}$, lift force F_L and integrated vapor volume V_{vap} of cycle 1 and of the subsequent cycle 2. Both forces exhibit significant peaks including highly negative values subsequent to the collapse corresponding to time instant 4 in Figs. 3 and 4. Here, the small vapor cloud located above the trailing edge of the hydrofoil violently collapses and the resulting 3D shock front propagates through the domain. Figure 5 depicts the pressure contours at the midspan plane as well as at the surface of the hydrofoil corresponding to a time instant subsequent to the collapse. The maximum pressure behind the shock reaches 230 bar. This leads to an instantaneous maximum pressure of 105 bar on the surface of the hydrofoil, directly after the shock impinges on the suction side. Thereby, we observe strongly decreasing lift and drag forces for a time interval of 14 ms, corresponding to point 4 in Fig. 4.

Due to the spatial resolution of $\Psi \ll 1$ to $\Psi \approx 1$, the physical model is no longer able to resolve single bubbles but locally predicts an average behavior of liquid and vapor within the computational cells. Nonetheless, the fundamental principles of conservation together with the thermodynamic

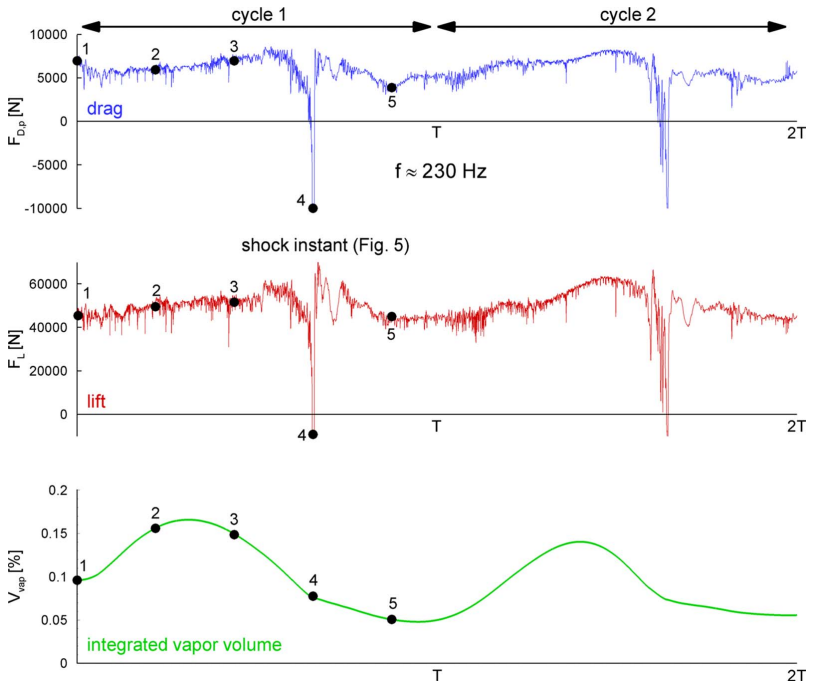

FIG. 4. (Color online) Time history of drag force $F_{D,p}$ (N), lift force F_L (N), and integrated vapor volume V_{vap} of cycles 1 and 2, $f \approx 230$ Hz and $\Delta t_{CFD} = 4.5 \times 10^{-8}$ s. The black dots numbered 1–5 correspond to the five instances in time presented in Fig. 3. 3D twisted NACA 0009, $u_\infty = 50$ m/s, $\sigma_{ref} = 0.81$, $p_\infty = 10$ bar, and water $T_\infty = 300$ K.

closure relations enable the prediction of sheet and cloud cavitation structures, as well as the prediction of shocks due to the collapse of fragmented vapor regions. Furthermore, the agreement of the obtained global flow character with different experimental observations[10,35–38] for comparable experimental setups demonstrates that the dominating flow phenomena for the investigated hydrofoil are essentially inertia controlled.

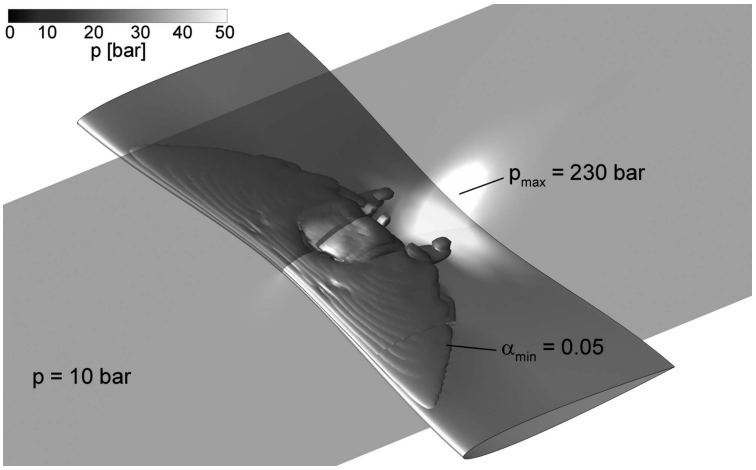

FIG. 5. Instantaneous 3D shock front emerging after cloud collapse at the trailing edge subsequent to time instant 4 of Figs. 3 and 4, $p_{max} = 230$ bar. Isosurfaces of void fraction $\alpha_{min} = 0.05$. 3D twisted NACA 0009 hydrofoil, $u_\infty = 50$ m/s, $\sigma_{ref} = 0.81$, $p_\infty = 10$ bar, and water $T_\infty = 300$ K.

V. CONCLUSIONS

A physical model together with a numerical solution strategy for the simulation of wave dynamics and hydrodynamics in cavitating two-phase flows is presented. A numerical pressure flux function is proposed that enables time accurate simulations of liquid flows including phase transition without the need of any additional preconditioning techniques. Based on the dimensionless quantity $\Psi = R/l_k$, we demonstrate that the thermodynamic model is suitable to predict either the dynamics of a single bubble ($\Psi \gg 1$) or to predict the average behavior of liquid embedded vapor structures ($\Psi \ll 1$). By applying numerical time steps of the order of nanoseconds, we first validate the proposed method against the solution of the Rayleigh–Plesset equation for the Besant problem. Finally, we investigate the highly unsteady 3D cavitating flow over a twisted hydrofoil with special emphasis on the formation and propagation of shocks emitted by collapsing vapor clouds. Thereby, the proposed model predicts complex 3D unsteady shedding cycles including secondary instabilities caused by side-entry flow. Furthermore, we demonstrate that collapse induced shocks generate high impulsive loads on the surface of a hydrofoil. We locate an instantaneous maximum pressure of 105 bar on the surface of the hydrofoil directly after shock impingement. The locations as well as the intensities of these loads are thought to be related to erosion critical areas. Further investigations will include statistical analysis of the observed effects as well as one to one comparison with recently obtained experimental data. Additionally, the effect of noncondensable gas with respect to the formation and collapse of vapor structures will be considered within the thermodynamic closure relation.

ACKNOWLEDGEMENTS

This research project is partly supported by the KSB-Stiftung, Stuttgart, Germany.

[1] M. S. Plesset and A. Prosperetti, "Bubble dynamics and cavitation," Annu. Rev. Fluid Mech. **9**, 145 (1977).
[2] J. R. Blake and D. C. Gibson, "Cavitation bubbles near boundaries," Annu. Rev. Fluid Mech. **19**, 99 (1977).
[3] G. L. Chahine, "Experimental and asymptotic study of non-spherical bubble collapse," Appl. Sci. Res. **38**, 187 (1982).
[4] M. S. Plesset and R. B. Chapman, "Collapse of an initially spherical cavity in the neighborhood of a solid boundary," J. Fluid Mech. **47**, 283 (1971).
[5] R. Hickling and M. S. Plesset, "Collapse and rebound of a spherical bubble in water," Phys. Fluids **7**, 7 (1964).
[6] W. Lauterborn and C.-D. Ohl, "Cavitation bubble dynamics," Ultrason. Sonochem. **4**, 65 (1997).
[7] L. Duchemin, S. Popinet, C. Josserand, and S. Zaleski, "Jet formation in bubbles bursting at a free surface," Phys. Fluids **14**, 3000 (2002).
[8] S. Fujikawa and T. Akamatsu, "Effects of non-equilibrium condensation of vapor on the pressure wave produced by the collapse of a bubble in a liquid," J. Fluid Mech. **97**, 481 (1980).
[9] A. Philipp and W. Lauterborn, "Cavitation erosion by single laser-produced bubbles," J. Fluid Mech. **361**, 78 (1998).
[10] G. E. Reisman, Y.-C. Wang, and C. E. Brennen, "Observations of shock waves in cloud cavitation," J. Fluid Mech. **355**, 255 (1998).
[11] T. Ikeda, S. Yoshizawa, M. Tosaki, J. S. Allen, S. Takagi, N. Ohta, T. Kitamura, and Y. Matsumoto, "Cloud cavitation control for lithotripsy using high intensity focused ultrasound," Ultrasound Med. Biol. **32**, 1383 (2006).
[12] J. Dang, "Numerical simulation of unsteady partial cavity flows," Ph.D. thesis, Technical University of Delft, 2000.
[13] Y. Chen and S. D. Heister, "Two-phase modeling of cavitating flows," Comput. Fluids **24**, 799 (1995).
[14] A. J. Chorin, "The numerical solution of the Navier-Stokes equations for an incompressible fluid," Bull. Am. Math. Soc. **73**, 928 (1967).
[15] J. Sauer, "Instationär kavitierende Strömungen—Ein neues Model, basierend auf Front Capturing (VoF) und Blasendynamik," Ph.D. thesis, Universität Karlsruhe, 2000.
[16] I. Senocak and W. Shyy, "A pressure based method for turbulent cavitating flow computations," J. Comput. Phys. **176**, 363 (2002).
[17] O. Coutier-Delgosha, R. Fortes-Patella, J. L. Reboud, N. Hakimi, and C. Hirsch, "Stability of preconditioned Navier-Stokes equations associated with a cavitation model," Comput. Fluids **34**, 319 (2005).
[18] D. G. Huang, "Preconditioned dual-time procedures and its application to simulating the flow with cavitations," J. Comput. Phys. **223**, 685 (2007).
[19] B. R Shin, S. Yamamoto, and X. Yuan, "Application of preconditioning method to gas-liquid two-phase flow computations," J. Fluids Eng. **126**, 605 (2004).
[20] R. F Kunz, D. A. Boger, D. R. Stinebirg, T. S. Chyczewski, J. W. Lindau, H. J. Gibeling, S. Venkateswaran, and T. R. Govindan, "A preconditioned Navier-Stokes method for two-phase flows with application to cavitation prediction," Comput. Fluids **29**, 849 (2000).
[21] D. H. Trevena, "Cavitation and the generation of tension in liquids," J. Phys. D **17**, 2139 (1984).
[22] C. F. Delale, K. Okita, and Y. Matsumoto, "Steady-state cavitating nozzle flows with nucleation," J. Fluids Eng. **127**, 770 (2005).
[23] R. Oldenbourg, *Properties of Water and Steam in SI-Units* (Springer-Verlag, Berlin, 1989).
[24] R. Saurel, J. P. Cocchi, and P. B. Butler, "Numerical study of cavitation in the wake of a hypervelocity projectile," J. Propul. Power **15**, 513 (1999).
[25] International Association for the Properties of Water and Steam (IAPWS).
[26] H. Guillard and C. Viozat, "On the behavior of upwind schemes in the low Mach number limit," Comput. Fluids **28**, 63 (1999).
[27] C.-D. Munz, S. Roller, R. Klein, and K. J. Geratz, "The extension of incompressible flow solvers to the weakly compressible regime," Comput. Fluids **32**, 173 (2003).
[28] A. Meister, "Asymptotic single and multiple scale expansions in the low Mach number limit," SIAM J. Appl. Math. **60**, 256 (1999).
[29] E. H. Toro, *Riemann Solvers and Numerical Methods for Fluid Dynamics* (Springer-Verlag, Berlin, 1999).
[30] C. W. Shu, "Essentially non-oscillatory and weighted essentially non-oscillatory schemes for hyperbolic conservation laws," ICASE Report No. 97-65, 1997.
[31] R. J. LeVeque, *Finite Volume Methods for Hyperbolic Problems* (Cambridge University Press, Cambridge, 2002).
[32] C. Hirsch, *Numerical Computation of Internal and External Flows* (Wiley, Chichester, 1988).
[33] F. R. Gilmore, "The growth and collapse of a spherical bubble in a viscous compressible liquid," California Institute of Technology Hydrodynamics Laboratory Report No. 26-4, 1952.
[34] J.-P. Franc and J.-M. Michel, *Fundamentals of Cavitation* (Kluwer Academic, Dordrecht, 2004).
[35] E. J. Foeth, C. W. H. van Doorne, T. van Terwisga, and B. Wienke, "Time resolved PIV and flow visualization of 3D sheet cavitation," Exp. Fluids **40**, 503 (2006).
[36] D. F. de Lange and G. J. de Bruin, "Sheet cavitation and cloud cavitation, re-entrant jet and three-dimensionality," Appl. Sci. Res. **58**, 91 (1998).
[37] D. F. de Lange, G. J. de Bruin, and L. van Wijngaarden, "Numerical modeling of unsteady 2D sheet cavitation," Houille Blanche **4/5**, 89 (1997).
[38] Q. Le, J.-P. Franc, and J.-M. Michel, "Partial cavities: Global behavior and mean pressure distribution," J. Fluids Eng. **115**, 243 (1993).

I. Ninth publication

This publication is a review article (chapter 14 in [38]) and contains work from [52,53,63,69]. It summarizes the authors' work on current state-of-the-art in numerical prediction of events in cavitating flows that may lead to erosion.

I prepared the manuscript. [1]

[1] Note that the author's contributions of the work summarized in this review article are already discussed in the original articles in the previous sections.

Chapter 14
Assessment of Erosion Sensitive Areas via Compressible Simulation of Unsteady Cavitating Flows

Steffen J. Schmidt, Michael S. Mihatsch, Matthias Thalhamer and Nikolaus A. Adams

Abstract The objective of this paper is the assessment of the numerical predictability of erosive events arising in cavitating flows. First, a numerical method and an efficient thermodynamic model for the simulation of cavitating flows are briefly described. The prediction of typical flow details is evaluated by simulating the 3-D flow around a quasi 2-D NACA hydrofoil. We find that the maximum length of the attached cavity, the Strouhal number, and the average diameter of detached clouds are essentially grid independent. Scale enrichment and enhanced 3-D flow details are observed on refined grids. Even delicate flow features, such as cavitating vortices and irregular 3-D break-up patterns, are reproduced, provided that the spatial resolution is sufficiently high. The simulation of cloud collapses and resulting instantaneous peak pressures is assessed in a second investigation. Here, we analyze the effect of the computational grid resolution with respect to typical collapse characteristics, such as the collapse duration, and the instantaneous maximum pressure within the flow field and at walls. The proposed methodology is confirmed by a third investigation, where an experimental setup to investigate cavitation erosion is simulated, and regions of experimentally observed cavitation damage are compared with numerical predictions of strong collapses. The excellent agreement of numerically predicted collapse positions and experimentally observed damage justifies the proposed methodology.

14.1 Introduction

The numerical prediction of erosive events arising in cavitating flows is a serious challenge due to the large range of involved spatial and temporal scales. The extent of a partial cavity at the suction side of a propeller blade might be four to

S. J. Schmidt (✉) · M. S. Mihatsch · M. Thalhamer · N. A. Adams
Institute of Aerodynamics and Fluid Mechanics, Technische Universität München, Munich, Germany
e-mail: Steffen.Schmidt@aer.mw.tum.de

K.-H. Kim et al. (eds.), *Advanced Experimental and Numerical Techniques for Cavitation Erosion Prediction*, Fluid Mechanics and Its Applications 106,
DOI: 10.1007/978-94-017-8539-6_14, © Springer Science+Business Media Dordrecht 2014

five orders of magnitude larger than the diameter of a collapsing bubble or of a nucleus [1–5]. Similarly for temporal scales, the duration of a peak pressure due to a shock impinging on a material surface is in the order of a few microseconds, whereas the duration of a typical cloud-shedding process might be several milliseconds [6, 7]. Moreover, the process of cavitation erosion might take place over the lifetime of the propeller. Except for a few academic cases, current computational capabilities do not allow the resolution of all scales arising in typical cavitating flows. Therefore, an accurate prediction of medium and large scale dynamics, such as cloud formation and cloud collapses, is highly desired.

One approach for removing unresolvable small scales is to filter the continuous governing equations using spatial low-pass filters [8]. Filtering not only removes unresolvable small-scale kinematics, it additionally replaces unresolvable two-phase structures with locally homogeneous mixtures. It can be shown that finite-volume methods provide approximate solutions of the top-hat filtered governing equations without explicit filtering [9]. The filter width of a finite volume discretization is related to the computational mesh, which constitutes the lower bound of resolvable spatial scales [10]. In most cases of practical relevance, the computational grid is far too coarse to resolve single bubbles or small-scale kinematics in the range where viscous dissipation is dominant, i.e. the grid is insufficient for direct numerical simulations. However, the investigations summarized within this paper provide a strong indication that a considerable amount of relevant detail for the prediction of cavitation and cavitation erosion are much larger than nuclei or single bubbles.

The time discretization method needs to ensure sufficient resolution of the dynamic processes as well. Here, the predominant physical constraint is the fastest signal speed, which is in the order of the speed of sound in the liquid: e.g., assuming that the spatial resolution is 0.1 mm and the speed of sound is 1,500 m/s, the numerical time step must be on the order of 60–70 ns to resolve collapse-induced peak pressures that are known to be a driving mechanism of cavitation erosion.

14.2 Numerical Method

In the following sections we present investigations of cavitating flows as predicted by our flow simulation code CATUM (CAvitation Technische Universität München [11, 12]), which is a density-based finite volume method employing a low Mach-number consistent flux function and an explicit time marching procedure. Since the objective of this investigation is the prediction of erosive collapses, we focus on inertia-driven dynamics. Thus, the governing equations are the 3-D unsteady Euler equations resulting from mass, momentum and energy balances. We denote that the applied computational grids are far too coarse to resolve boundary layers or kinematics with wave numbers close to the viscous sub-range. Therefore, we neglect viscous effects on purpose and apply a nonlinear

discretization scheme that implicitly provides a sufficient amount of numerical regularization [13].

The spatial reconstruction of the velocity field follows a WENO-3 procedure [14]. Density and internal energy are reconstructed by monotonic TVD limiters ("minmod") [15]. Time marching is performed by adopting an explicit low-storage four-step Runge–Kutta method with optimized stability region [11, 12, 16]. The combination of both methods results in a second-order numerical approach in space and time for smooth flow, and it ensures sharp representation of discontinuous flow features, such as shocks and contact waves.

In order to allow for the simulation of shock formation and wave propagation, the compressibility of the fluids (liquid and vapor) is taken into account. Consequently, the numerical time step is proportional to the ratio of the smallest length scale (minimum grid size) and the fastest signal speed ($\sim$ speed of sound in the liquid). The fluids can be characterized by closed form equations of state, or by look-up tables for complex fluid models, e.g. for fluids where closed form equations are not available or computationally expensive. For this investigation we use closed form equations for the simulation of the flow around a hydrofoil, and more efficient look-up tables for simulation of the cloud collapse and the nozzle-target flow. Both thermodynamic models provide high quality approximations of the IAPWS database [17] of water, vapor, and liquid-vapor equilibrium.

The phase-transition model is based on local equilibrium assumptions for pressure, temperature and specific Gibbs functions [18]. Therefore, two-phase regions are modeled as saturated mixtures (liquid-vapor equilibrium with vapor volume fraction α), where the resulting pressure is the temperature-dependent vapor pressure [19]. For each computational cell, and at each instant in time, the average density, the average momentum, and the average total energy are given by the governing equations. These quantities allow for a cell-wise evaluation of the average internal energy. Using the previously specified local equilibrium assumptions together with suitable fluid-models (closed form equations or look-up tables) all unknown thermodynamic properties can be obtained from density and internal energy. Thereby, the effects of latent heat are fully taken into account and the method is inherently conservative. Moreover, the speed of sound is the equilibrium speed of sound that leads to a well-posed mathematical problem [20].

We consider it advantageous that the equilibrium model does not require user-specified and potentially unknown parameters, such as initial nuclei distributions or evaporation/condensation rates. Surely, equilibrium assumptions might be questionable in case of cavitation inception where meta-stable states (pressures below the vapor pressure or even tension [21, 22]) may occur. However, our observations indicate that equilibrium assumptions may lead to a sufficiently accurate model for developed cavitating flows, such as those investigated within this paper.

14.3 Hydrofoil Cavitation and Predictability of Large and Medium Scale Dynamics

In this section we assess the effect of the chosen computational grid on typical cavitation phenomena around a quasi 2-D hydrofoil. The investigation represents a brief summary of Ref. [23]. We simulate the cavitating flow around a 2-D NACA 0015 hydrofoil (angle of attack 6°, cord length $l_{cord} = 0.13$ m, span width $l_{span} = 0.3$ m), which is placed in the middle of a rectangular test section (height 0.3 m, depth 0.3 m, length 0.9 m). The walls of the test section and the surface of the hydrofoil are modeled as inviscid adiabatic walls, since the grid resolution is insufficient to resolve boundary layers. At the inlet of the numerical domain the velocity $u_{in} = 30$ m/s and the static temperature $T_{in} = 293$ K of the liquid inflow are prescribed. Since the inlet conditions correspond to a pure liquid state, the initial vapor volume fraction is zero. At the outlet the static pressure of $p_{exit} = 4.5$ bar is prescribed. The resulting cavitation number is $\sigma_{ref} = 2(p_{exit}\text{-}p_{sat}(T_{in}))/(\rho_{liquid}\, u_{in}^2) = 1.0$.

The numerical domain is discretized by 2×10^5 cells (coarse grid) and 2.4×10^7 cells (fine grid), respectively. First, a simulation is performed on the coarse grid until the typical periodic shedding of the cavity is statistically developed. This may require 2–5 shedding processes where the maximum length of the sheet might be initially overestimated. To determine the shedding frequency, the integrated vapor volume content V_{vap} [%] within the computational domain is analyzed. The simulated time interval of 0.15 s corresponds to nearly 17 shedding cycles. As depicted in Fig. 14.1—left, the attached cavity is mainly two-dimensional, while spanwise variations of the vapor volume are observed for the detached cloud. The results obtained with the coarse grid are now compared to those obtained by using the refined counterpart with 2.4×10^7 cells, see Fig. 14.1—right. Here, the simulated time interval of 0.11 s corresponds to 12

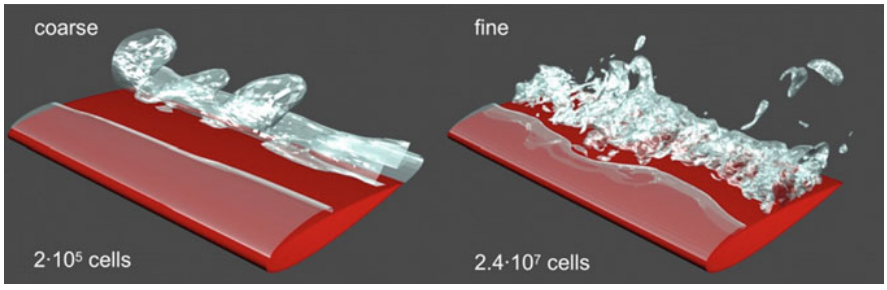

Fig. 14.1 Prediction quality of cavitation phenomena around a hydrofoil. Predicted iso-surfaces of the vapor volume fraction $\alpha = 5$ % using two different computational grids. The maximum length l_{max}/l_{cord} of the sheet cavity is 0.75 (*coarse grid*) and 0.8 (*fine grid*). The shedding frequency is approximately 110 Hz (±5 Hz) on both grids. The typical diameter of the detached cloud close to the trailing edge (as shown in this figure) is approximately $l_{cord}/3$ for both grids

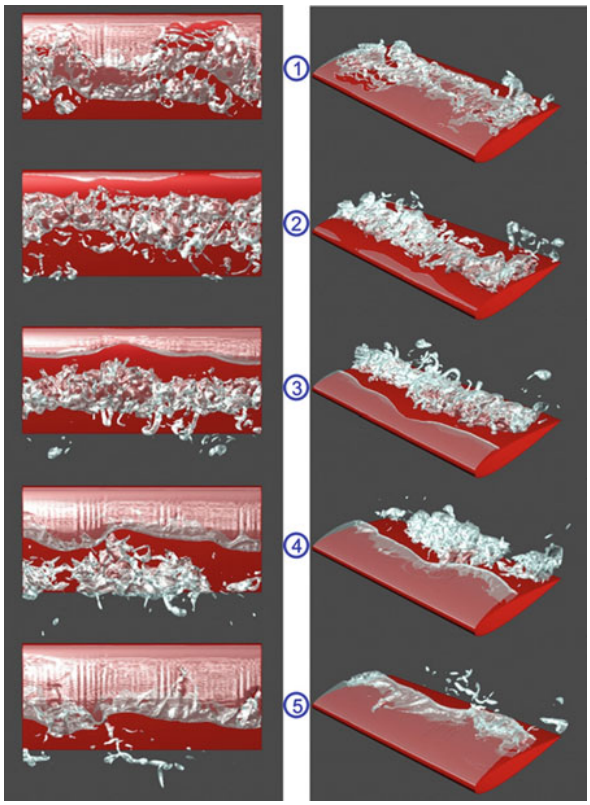

Fig.14.2 A typical shedding cycle with f ≈ 110 Hz using the fine grid. Iso-surfaces of $\alpha = 5$ % at 5 consecutive instants in time showing the break-up of the sheet cavity, the formation of cavitating vortical structures and the disintegration and collapse of two-phase regions. On the *left* the *top* view is presented, while on the *right perspective* views at the same instants in time are shown

shedding cycles. The shedding frequency is approximately 110 Hz on both grids. The numerical time step for the simulation on the fine grid is $\Delta t_{CFD,\,fine} = 8.5 \times 10^{-8}$ s. We observe that the maximum length of the sheet cavity, the typical diameter of the cloud close to the trailing edge, and the shedding frequency compare well for both spatial resolutions. This is a strong indication that large-scale dynamics of cavitating flows can be predicted even if the spatial resolution is relatively coarse. Grid refinement enables the computation of medium-scale phenomena, such as cavitating vortices in the streamwise direction and enhanced cloud fragmentation. All predicted disturbances develop as a result of Rayleigh-Taylor and Kelvin-Helmholtz instabilities initiated by the re-entrant flow. As analyzed in [23], the flow field develops perfectly two-dimensional in case of pure liquid flow ($\sigma_{ref} \gg 1$) where the numerical method predicts a stationary solution. Hence, numerical round-off errors are insignificant, although they might provide initial disturbances. It is thus reasonable to denote the observed instabilities as intrinsic instabilities [3] that seem to be mainly inertia controlled [23].

Figure 14.2 shows a time series of iso-surfaces of the vapor volume fraction $\alpha = 5$ %. On the left the top view is presented, while on the right perspective views at the same instants in time are shown. Due to different illumination on the

left and on the right hand side, slightly different details of the iso-surfaces are highlighted. The position and intensity of the streaks observed on the left side vary from cycle to cycle. Their occurrence seems to be related with the break-up pattern of the previous cycle.

Although the prediction of large-scale dynamics might be sufficient to quantify integral properties such as lift and drag, it is suggested that a sufficient amount of medium-scale dynamics has to be resolved in order to capture at least a certain amount of flow detail that is related to cavitation erosion. In particular, we suggest that it is required to resolve collapsing clouds and collapse-induced peak pressures at the surface of the hydrofoil. These issues are addressed in the following sections.

14.4 Collapse of a Bubble Cluster Versus Collapse of a Vapor Volume Fraction

In the previous section the prediction of medium-scale phenomena, such as cavitating vortices in streamwise direction and enhanced cloud fragmentation was assessed on the example of hydrofoil cavitation. In this section we assess the prediction of the collapse characteristics of a resolved bubble cluster and compare them with the collapse characteristics predicted by under-resolved simulations. This test case is motivated by the observation that our numerical simulations of cavitating flows predict strong shock waves in case of collapsing vapor regions, although the numerical resolution is far too coarse to resolve single bubbles. These shocks result in high instantaneous surface-loads as soon as they impinge onto a material surface. Depending on the flow conditions, the loads last for a few microseconds and can reach several thousand bars. In order to allow for a reliable forecast of erosive collapses, the influence of the numerical resolution on the predicted loads needs to be evaluated.

We generate a random distribution of spherical bubbles with the following properties: The "numerical cloud" consists of 125 spherical vapor bubbles with radii between $R_{min} \approx 0.70$ mm and $R_{max} \approx 1.65$ mm. The average radius is $R_{av} \approx 0.95$ mm and the minimum distance between two bubbles is 0.2 mm. The cloud is located within a liquid-filled cubic domain of $20 \times 20 \times 20$ mm^3, which will be referred to as the "inner domain". This inner domain is embedded into a larger "outer domain" of $4 \times 4 \times 2$ m^3. The inner domain is discretized with uniform cubic cells while stretched cells are applied to discretize the outer domain. The bottom faces of both domains are coplanar and impermeable for representing solid walls. The other faces of the outer domain correspond to far-field boundaries. The total vapor volume fraction is 5.8 % with respect to the inner domain. Since we apply a thermodynamic equilibrium approach, we simplify the test case by neglecting surface tension and non-condensable gas. Furthermore, the following properties are enforced: the initial pressure within the surrounding liquid satisfies a

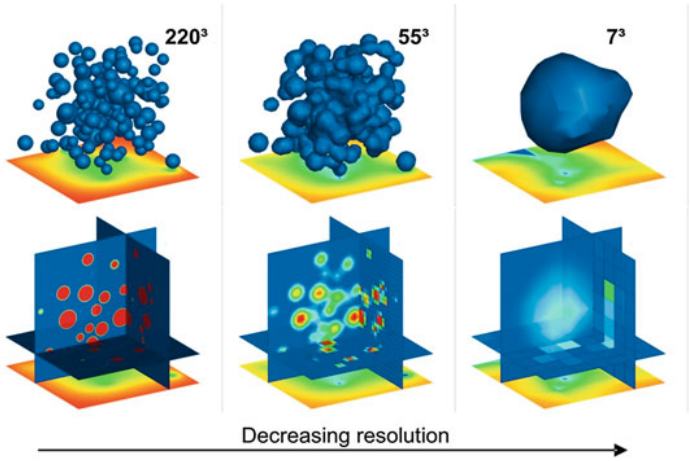

Fig. 14.3 Discrete representation of a bubble cluster using different grids. Bubbles are fully resolved by using 220^3 cells, partial resolution is achieved with 55^3 cells. Bubbles are represented by a locally homogeneous mixture using 7^3 cells

Laplace equation $\Delta p = 0$, where the pressure sufficiently far away from the bubbles is $p_\infty = \text{const.} = 40$ bar, and the pressure inside the bubbles is equal to the vapor pressure $p_v = 2{,}340$ Pa. Thereby we ensure that the initial pressure field does not contain spurious acoustics. It is further assumed that the velocity field is initially at rest and the initial temperature is $T = 293$ K. Viscous effects are neglected.

A series of 6 grids with 7^3, 14^3, 28^3, 55^3, 110^3, and 220^3 cubic cells is used to discretize the inner domain. On the finest computational grid (220^3 cells), the smallest bubbles are resolved by at least 2000 cells each, and each of the largest bubbles is resolved by about 25,000 cells. On the coarsest grid (7^3 cells), the bubbles are no longer resolvable but their vapor volume content contributes to the specified cell-averaged void fraction. Three of the initial fields are shown in Fig. 14.3. One horizontal cut plane shows the initial vapor volume fraction by using continuous coloring and the remaining cut planes show the vapor volume fraction by using cell-center coloring. The colored bottom-plane indicates the initial pressure field. The shapes of the bubbles are sharply represented by the fine grids (220^3, 110^3 not shown), while they are not resolved by the coarse grids (7^3, 14^3 not shown). The medium grids (55^3, 24^3 not shown) allow for partial resolution of the bubble shapes. The finest grid (220^3) requires a time-step size of 1.95×10^{-8} s, while for the coarsest grid (7^3) the resulting time-step size is 6.24×10^{-7} s.

For each computational grid we adopt two "numerical wall pressure transducers" located at the center of the bottom wall. The larger transducer records the average pressure on an area of 1×1 cm^2, while the smaller one covers an area of 1×1 mm^2. Using two sensors with different areas allows for a grid independent

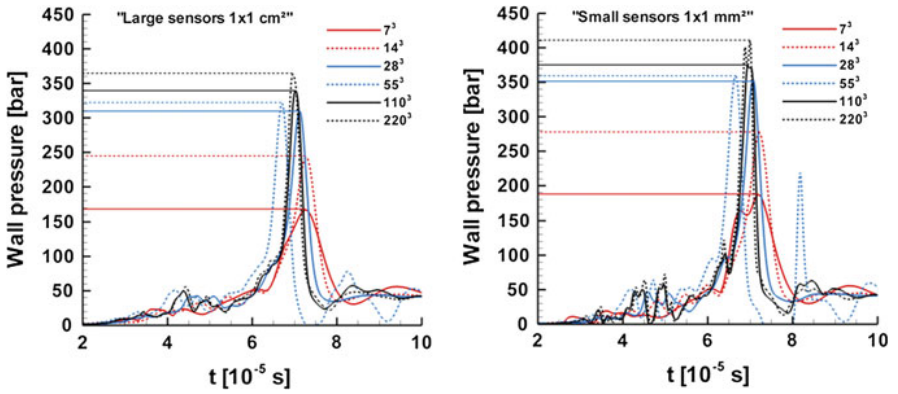

Fig. 14.4 Outputs of two numerical wall pressure transducers. Two numerical wall pressure transducers are adopted to record the pressure at the center of the bottom wall. The large sensor covers an area of 1×1 cm^2 and the small one covers an area of 1×1 mm^2. The figures show the obtained signals for the applied numerical resolutions. It is observed that the signals obtained with the large sensors (*left*) are slightly smeared and the amplitudes are slightly reduced, compared to the signals obtained with the small sensors (*right*)

evaluation of the pressure at the wall. Both transducers store the pressure for each instant in time, resulting in a maximum sampling frequency of 5.1×10^7 Hz (using 220^3 cells). The signals obtained by the large sensor are shown in Fig. 14.4—left, and the corresponding outputs of the small sensor are shown on the right hand side. As expected, the large sensor provides slightly smoother outputs with reduced amplitudes. The numerical sampling frequencies vary from 51 MHz (using 220^3 cells) to 1.6 MHz (using 7^3 cells). The peaks are more pronounced when computing on the fine grid and with high temporal resolution. In the present case, the duration of the shock-induced peak pressure is only about 5 μs for the run using 220^3 cells. On the coarse grid (run using 7^3 cells), the amplitude of the peak is reduced, and the peak is smeared. The small sensor detects a secondary collapse for the simulation using 55^3 cells (dashed blue line). This secondary event is actually the collapse of a small vapor pocket after rebound that occurs in this case close to the surface of the small sensor.

Aside from the "wall pressure transducers", the maximum pressure within the complete flow field is monitored during each simulation. The resulting data are provided in Table 14.1 and visualized in Fig. 14.5—left.

Before we analyze the obtained data, we investigate the following thought experiment: We consider the temporal evolution of a weak spherical shock front with given radius $R(t_2)$ and pressure amplitude $A(t_2)$, where t_2 is a given instant in time and $R(t_2)$ is the distance of the front to its origin. Since the shock is assumed to be weak, we may apply the linear theory [24] and obtain $A(t_2) \times R(t_2) = A(t_1) \times R(t_1)$. If we assume that the pressure amplitude and the radius are known at time $t_2 > t_1$, we can compute the amplitude $A(t_1)$ for any radius $R(t_1) > 0$ as long as the linear theory remains valid. With respect to numerical computations,

Table 14.1 Comparison of recorded maximum pressure within the domain and at the wall (small sensor and large sensor) and comparison of collapse durations with respect to six different numerical resolutions

Grid	p_{max} (domain) (Pa)	p_{max} (wall) small sensor (Pa)	p_{max} (wall) large sensor (Pa)	Collapse duration (s)
220^3	3.14×10^9	4.10×10^7	3.63×10^7	6.5×10^{-5}
110^3	1.17×10^9	3.74×10^7	3.40×10^7	6.6×10^{-5}
55^3	0.63×10^9	3.59×10^7	3.21×10^7	6.3×10^{-5}
28^3	0.34×10^9	3.53×10^7	3.10×10^7	6.7×10^{-5}
14^3	0.12×10^9	2.76×10^7	2.44×10^7	6.9×10^{-5}
7^3	0.07×10^9	1.87×10^7	1.68×10^7	7.0×10^{-5}

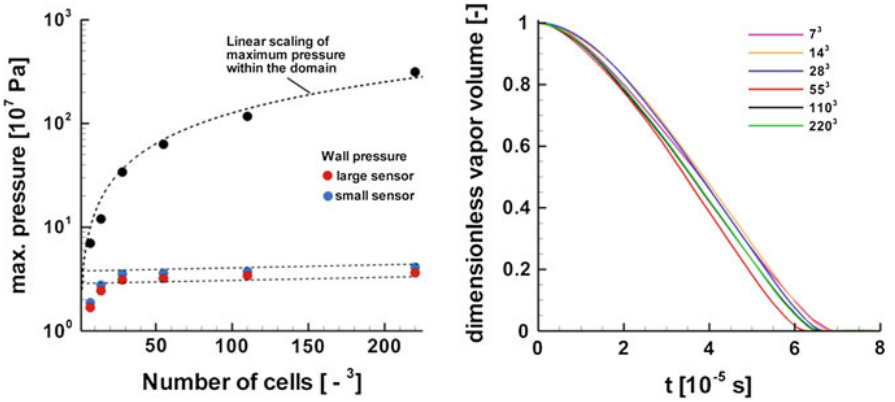

Fig. 14.5 Comparison of maximum pressures within the domain and at the wall (*left*) and collapse durations (*right*) using different numerical resolutions. On the left, the predicted maximum pressures (*logarithmic scale*) within the domain and at the bottom wall are plotted against the applied grid resolution (*number of cells*). One observes an approximately linear increase of the maximum pressure within the domain, and a very weak increase of the maximum pressures at the wall with increased grid resolution. On the right, the temporal evolution of the dimensionless vapor volume as predicted by different grids is shown. It can be concluded that the collapse durations compare well for all numerical resolutions

the smallest resolvable radius of a shock front is limited by the resolution of the applied computational grid. By assuming that the origin of the front is located at the center of a computational cell of size $h \times h \times h$, the smallest resolvable radius R_{min} is approximately $h/2$. Therefore, the maximum resolvable amplitude Amax is directly proportional to the resolution of the applied computational grid. Finally, one obtains $A_{max} = A(t_2) \times R(t_2) / R_{min} \approx 2 \times A(t_2) \times R(t_2) / h$, provided that the origin of the front is located at the center of a computational cell. If the origin of the front is not located at the cell center, the smallest resolvable radius is slightly larger ($h/2 \leq R_{min} \leq h$), and the corresponding maximum amplitude is smaller as well.

Table 14.2 Distance of the focal points to the wall as predicted by six different numerical resolutions

Grid	Wall distance of focal point (mm)	Cell size h (mm)
7^3	10 ± 1.43	2.86
14^3	9.3 ± 0.71	1.43
28^3	8.2 ± 0.36	0.71
55^3	7.8 ± 0.18	0.36
110^3	7.5 ± 0.09	0.18
220^3	7.4 ± 0.05	0.09

The result of this thought experiment allows for an illustrative interpretation of the data provided in Table 14.1 and visualized in Fig. 14.5—left: The collapse of the cloud initiates a shock front at the focal point of the collapse. Due to finite cell sizes, the exact position of the focal point cannot be resolved. Instead, a shock front of radius R_{min} with $h/2 \leq R_{min} \leq h$ is captured. The post-shock pressure of this front constitutes the maximum pressure within the domain. Since the smallest resolvable radius R_{min} is directly proportional to the grid resolution, the maximum amplitude is grid dependent as well. Therefore, the predicted linear increase of the maximum pressure within the domain with respect to the grid resolution (see Table 14.1) is confirmed by theoretical considerations.

On the other hand, if the focal point and the initial amplitude of the shock were grid independent, the amplitude (i.e. the maximum pressure) at the wall would be grid independent since it depends only upon the distance from the focal point to the wall. During our simulations we record the position of the maximum pressure within the domain to estimate the position of the focal points. The distances of the focal points to the wall are summarized in Table 14.2. Note that due to the grid dependent cell size h, an uncertainty of $h/2$ of the position of the focal point is assumed. We notice a slight displacement of the focal point towards the wall with increasing resolution. However, convergence towards the final position is clearly visible. It is supposed that the slight increase of the wall pressure is caused by the displacement of the focal point towards the wall, and by an improved resolution of the shock front. By using at least 28^3 computational cells the predicted wall pressures differ only by about 15 %. Therefore, the investigation demonstrates that the predicted wall pressure is only weakly grid dependent, provided that the position of the focal point is accurately captured.

Furthermore, we analyze the time history of the total vapor volume within the domain. Figure 14.5—right shows the time history of the vapor volume as predicted by the simulations. One observes that the predicted collapse durations agree well for all resolutions. These results confirm that the numerical methodology provides reasonable approximations of collapsing bubble clusters, even if the applied computational grid is far too coarse to resolve individual bubbles. However, this statement might not apply to dilute clusters, where the interaction of the involved bubbles is weak. More details on this investigation are given in Ref. [25].

14.5 Prediction of Erosion-Sensitive Areas in an Axisymmetric Nozzle-Target Flow

We simulate an experimentally investigated nozzle-target flow [26, 27] to evaluate the numerical predictability of erosion-sensitive areas. The experimental setup results in an axisymmetric stagnation flow, as shown in Fig. 14.6—left. At the exit of the nozzle the fluid accelerates along a small radius and forms a toroidal cavitation pocket. Collapse-induced erosion is quantified experimentally within an annulus at the surface of the target disc. The remaining parts are manufactured out of highly cavitation resistant material. Figure 14.6—right shows a cut through the computational domain. In accordance with the experiment, water at approximately room temperature enters the nozzle with an inlet velocity of $u_{in} = 31$ m/s. All observed flow details develop on their own without imposition of additional disturbances, such as random noise. An asymptotic pressure boundary condition $p_e = 10.1$ bar is imposed at the exit of a circular reservoir attached at a radial distance of 100 mm. All solid boundaries are treated as inviscid adiabatic walls, since the applied grid resolution is too coarse to resolve boundary layers. The computational grid consists of 5×10^5 body-fitted hexahedra.

We observe the onset of sheet cavitation at the rounded edge of the nozzle outlet. The fragmentation of the sheet and its transient shedding are strongly non-uniform in circumferential direction. The collapse of the vapor structures is generated by a positive pressure gradient in the radial direction. The part of the simulation analyzed here corresponds to a physical time interval of 7×10^{-2} s, and consists of 2.5×10^6 time steps with a time-step size of $\Delta t \approx 2.8 \times 10^{-8}$ s. Figure 14.7 shows a perspective view of two consecutive time instants with an increment $\Delta t = 2.8 \times 10^{-5}$ s. At the top, vapor structures (marked in red) are observed at a radial position of $\approx 2.6 \times 10^{-2}$ m. At the bottom, most of these vapor structures have already collapsed. At the focal point of the collapse a shock front is initiated that leads to a strong increase of the pressure (Fig. 14.7—bottom).

The duration of the complete collapse is about 2.8×10^{-5} s, which is resolved by approximately 1,000 time steps. Figure 14.8—right shows a photograph (from an angle) of an eroded target disc. The damage exhibits an almost perfect circular shape. Most pits are found at a radial distance between $r = 19$ and $r = 32$ mm measured from the nozzle axis [26]. In [27] the authors present pressure measurements for a series of operating points. They apply a flush-mounted sensor whose sensitive area has a diameter of 3.6 mm and the specified natural frequency is larger than 250 kHz. Pressures up to 400 bar are reported [27] for comparable operating conditions. However, the authors clearly state that the impact pressure can only be estimated if the impacted surface area is known, which is not the case. Figure 14.8—left shows the maximum pressure for each computational cell on the target disc recorded during the analysis interval of 7×10^{-2} s. Only pressures about one order of magnitude higher than the stagnation pressure are shown. The highest recorded value at the wall is 1,560 bar, but values between 250 bar and 700 bar seem to be predominant. The small discrepancy between the

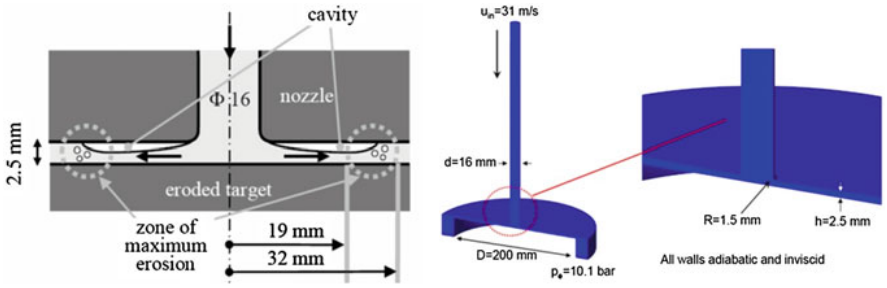

Fig. 14.6 Schematic and numerical model of the experimental setup. Based on [26], reproduced with permission of ASME

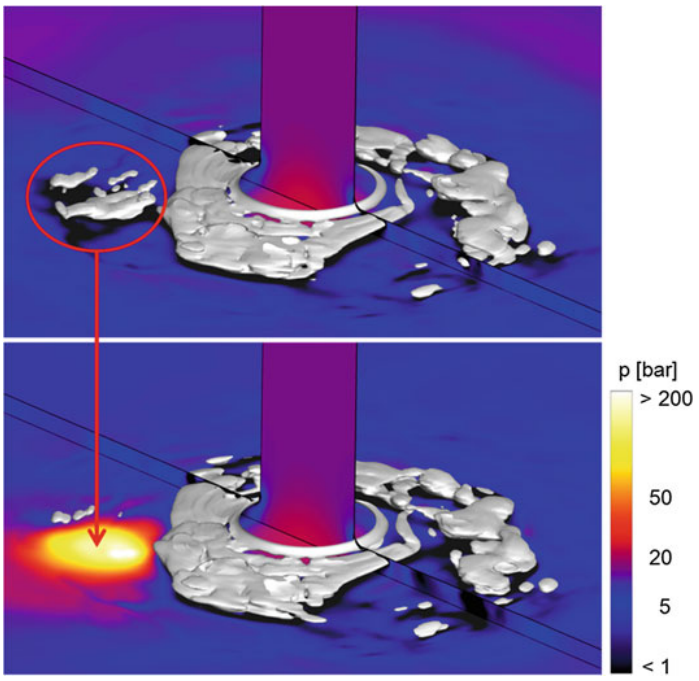

Fig. 14.7 Collapse of vapor structures and resulting shock wave. Iso-surfaces of a vapor volume fraction $\alpha = 10$ % and pressure at the target disc and on a cut-plane at two consecutive instants in time. Top: Fragments of vapor structures are advected into regions of increased pressure. Due to the pressure gradient between the vapor structures and the surrounding liquid an acceleration of liquid towards the center of the vapor pockets is initiated and re-condensation occurs. Bottom: At the final stage of the collapse the inertia of the accelerated liquid results in the formation of a shock ("*water hammer*")

experimentally obtained pressure pulses and our numerical prediction might be related to the different sensitive areas. The sensitive area of the transducer applied in [27] is approximately 10 mm^2, while the areas of the "numerical transducers" are about 0.4–0.6 mm^2. We observe a convincing similarity of the maximum-pressure distribution and the areas of erosion damage as detected experimentally. However, further investigations using much larger analysis intervals are required to improve the statistical relevance of the prediction.

The "foot-print" of maximum pressures on the target disc already provides information about erosion-sensitive areas, but it does not provide information about the frequency of collapses or of the number of collapses above a certain threshold-pressure. To overcome these drawbacks, a numerical "collapse detector" was developed [28]. Cells where the vapor content has condensed entirely during the previous time step are denoted as "collapse candidates". If the surrounding cells of a "collapse candidate" contain only liquid, an isolated collapse is detected. Once a collapse is detected, the maximum pressure is recorded at that instant in time when the divergence of the velocity field changes its sign. The strength of the collapse is characterized by the maximum (negative) divergence of the velocity field and, in particular, by its maximum pressure. The main advantages of the collapse detector as compared to the maximum pressure approach are as follows: The collapse detector automatically distinguishes between collapse-induced maximum pressures and high pressures at stagnation points. Furthermore, the number of collapse events, as well as their position and their strength, provide important information about the stress profile the material is exposed to. This information can be used to estimate erosion rates. A potential drawback of the collapse detector could be the lack of information on the collapse intensity at material surfaces. As proposed in [28], an efficient projection method based on the linear decay law of spherical waves may be used to estimate the surface loads.

Figure 14.9 shows the collapses detected within the gap between the nozzle and the target disc during the analyzed part of the simulation. The collapses are indicated as spheres plotted at the position of collapse occurrence. The diameter of each sphere and its color represent the collapse intensity. On the left side, the collapse pressure is visualized, whereas the collapse pressure projected onto the target wall using the linear decay law of spherical waves is depicted on the right side, respectively. In both cases, most of the collapses are found within the marked area (red circles) where pits were detected experimentally. However, the thickness of the band where the strongest pitting was observed (dark band in Fig. 14.8—right) is narrower than our numerical prediction. Still, both numerical indicators (maximum pressure and detected collapses) might be suitable surrogates for the prediction of cavitation erosion.

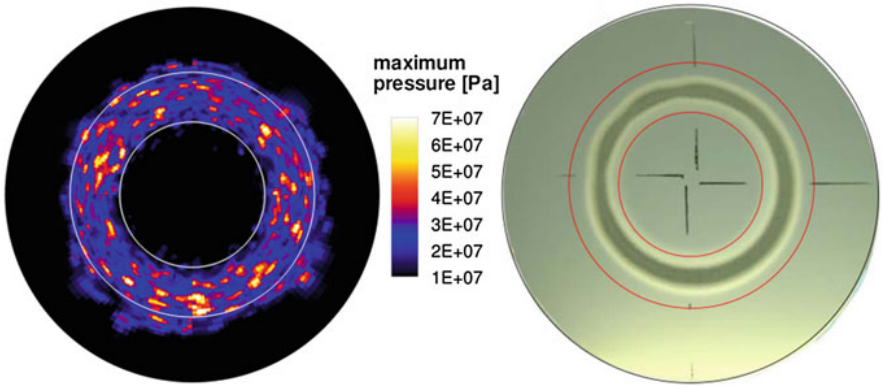

Fig. 14.8 Predicted maximum pressures at the surface of the target disc (*left*) and damaged target (*right*). Regions where the majority of pits occurred are indicated by circles. Based on [26], reproduced with permission of ASME

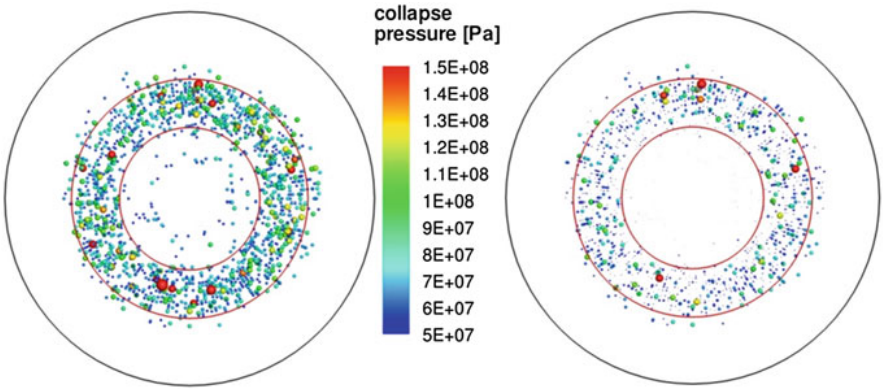

Fig. 14.9 Detected collapses within the gap between the nozzle and the target. Spheres represent detected collapses. Size and color of the spheres indicate the collapse intensity. On the left side, the intensity is the collapse pressure. On the right side, the collapse pressure is weighted by the inverse distance from the collapse location to the target as proposed in [28]. The application of this projection method slightly improves the prediction since the collapses within the inner circle disappear

14.6 Conclusions and Outlook

We assessed the numerical predictability of erosive events, such as collapsing vapor clouds, and resulting shocks. It is demonstrated that at least a certain range of large and medium-scale two-phase structures are represented correctly by our numerical simulations. In particular, typical features of hydrofoil cavitation, such as crescent-shaped regions [29] and irregular break-up patterns are well predicted.

By comparison of the collapse-characteristics of a numerically-resolved bubble cluster with the collapse of a locally homogeneous two-phase mixture it is demonstrated that important information about the collapse intensity and its duration can be obtained even if the numerical resolution is far too coarse to resolve individual bubbles. The ability to predict areas where intense collapse events damage the material is evaluated by the simulation of an experimentally investigated nozzle-target flow. We note a convincing agreement of numerically predicted collapse positions with experimentally observed pitting. Further investigations using state of the art Large Eddy Simulation techniques [10] are planned.

References

1. Knapp RT, Daily JW, Hammitt FG (1970) Cavitation. McGraw-Hill, New York
2. Brennen CE (1995) Cavitation and bubble dynamics. Oxford University Press, Oxford
3. Franc JP, Michel JM (2004) Fundamentals of cavitation. Springer, New York
4. Lecoffre Y (1999) Cavitation Bubble Trackers. Balkema, New York
5. D'Agostino L, Salvetti MV (2007) Fluid dynamics of cavitation and cavitating turbopumps. Springer, New York
6. Lauterborn W (1980) Cavitation and inhomogeneities in underwater acoustics. Springer, Berlin
7. Kendrinskii VK (2005) Hydrodynamics of explosion. Springer, Berlin
8. Gullbrand J, Chow FK (2003) The effect of numerical errors and turbulence models in large-eddy simulations of channel flow, with and without explicit filtering. J Fluid Mech 495:323–341
9. Garnier E, Adams N, Sagaut P (2009) Large eddy simulation for compressible flows. Springer, Berlin
10. Hickel S, Mihatsch M, Schmidt SJ (2011) Implicit large eddy simulation of cavitation in micro channel flows. In: Proceedings of WIMRC cavitation forum 2011, Warwick, UK, e-publication, 4–6 July 2011
11. Schnerr GH, Sezal IH, Schmidt SJ (2008) Numerical investigation of three-dimensional cloud cavitation with special emphasis on collapse induced shock dynamics. Phys Fluids 20(4):040703
12. Schmidt SJ, Sezal IH, Schnerr GH, Thalhamer M (2008) Riemann Techniques for the Simulation of Compressible Liquid Flows with Phase-transition at all Mach numbers—Shock and Wave Dynamics in Cavitating 3-D Micro and Macro Systems. In: 46th AIAA Aerospace Sciences Meeting and Exhibit, 7–10 January 2008, Reno, Nevada, AIAA paper 2008–1238
13. Grinstein FF, Margolin LG, Rider WJ (2007) Implicit large eddy simulation: computing turbulent fluid dynamics. Cambridge University Press, NewYork
14. Jiang GS, Shu CW (1996) Efficient implementation of weighted ENO schemes. J Comput Phys,126:202–228
15. Toro EF (1999) Riemann solvers and numerical methods for fluid dynamics. Springer, Berlin
16. Kennedy CA, Carpenter MH, Lewis RM (2000) Low-storage, explicit Runge-Kutta schemes for the compressible Navier-Stokes equations. Appl Numer Math 35:177–219
17. The International Association for the Properties of Water and Steam. http://www.iapws.org/
18. Hirschfelder JO, Curtiss CF, Bird RB (1954) Molecular theory of gases and liquids. Wiley, New York
19. Moran MJ, Shapiro HN, Boettner DD, Bailey MB (2011) Fundamentals of engineering thermodynamics. Wiley, New Jersey

20. Menikoff R, Plohr BJ (1989) The riemann problem for fluid flow of real materials. Rev Mod Phys 61:75–130
21. Trevena DH (1984) Cavitation and the generation of tension in liquids. J Phys D 17:2139–2164
22. Andersen A, Mørch KA (2011) In situ measurement of the tensile strength of water. In: Proceedings of WIMRC cavitation forum 2011, Warwick, UK, e-publication, 4–6 July 2011
23. Schmidt SJ, Thalhamer M, Schnerr GH (2009) Inertia controlled instability and small scale structures of sheet and cloud cavitation. In: Proceedings of 7th CAV 2009—7th international symposium on cavitation, Ann Arbor, Michigan, USA, 16.8–21.8.2009, paper 17, CD-ROM publication
24. Witham GB (1999) Linear and nonlinear waves. Wiley, New Jersey
25. Schmidt SJ, Mihatsch M, Thalhamer M, Adams NA (2011) Assessment of the prediction capability of a thermodynamic cavitation model for the collapse characteristics of a vapor-bubble cloud. In: Proceedings of WIMRC cavitation forum 2011, Warwick, UK, e-publication, 4–6 July 2011
26. Franc JP, Riondet M (2006) Incubation time and cavitation erosion rate of work-hardening materials. In: Proceedings of CAV2006—6th international symposium on cavitation, Wageningen, The Netherlands, 11–15 September 2006, CD-ROM publication
27. Franc JP, Riondet M, Karimi A, Chahine GL (2011) Impact load measurement in erosive cavitating flow. J Fluids Eng 133:121301–121303
28. Mihatsch M, Schmidt SJ, Thalhamer M, Adams NA (2011) Numerical prediction of erosive collapse events in unsteady compressible cavitating flows. In: Proceedings of marine 2011, International conference on computational methods in marine engineering, Barcelona, 2011
29. Reisman GE, Wang YC, Brennen CE (1998) Observations of shock waves in cloud cavitation. J Fluid Mech 355:255–283

J. Tenth publication

This publication is a review article (chapter 8 in [13]) and contains work from [63, 69] as well as from [43, 45]. Two techniques for simulation of cavitating flows are presented: a sharp interface two-fluid method and the thermodynamic equilibrium single-fluid technique. The first approach is applied to investigate the collapse dynamics of single bubbles in detail. The potential of the second approach is shown on example of cavitation on a hydrofoil [69] and on exapmle of the collapse of a vapor bubble cluster. The bubble cluster is identical to the one discussed in [63] but another simulation with additional grid refinement is analyzed.

I analyzed parts of the results obtained with the single-fluid approach and prepared about 60 % of the manuscript. [1]

[1] Note that the author's contributions of the work summarized in this review article are already discussed in the original articles in the previous sections.

Shocks in Cavitating Flows

Nikolaus A. Adams, Steffen J. Schmidt

Abstract We present two numerical methods for simulation of compressible multiphase flows with phase transition. The first approach is a two-fluid method using sharp interface treatment and non-equilibrium mass transfer terms. This technique is applied to investigate collapsing vapor bubbles and resulting shock patterns. Depending on the bubble–wall configuration, different types of liquid jets are observed during the collapse stages of the bubbles. These results provide detailed insight into collapse processes and resulting peak loads. The second approach is a single-fluid method using local thermodynamic equilibrium assumptions. Its applicability to simulate cavitating flows is assessed on example of hydrofoil cavitation as well as for the collapse of a bubble cluster. Typical features of sheet and cloud cavitation are reproduced and the formation of shocks due to collapsing vapor regions is analyzed. In case of the investigated cluster of vapor bubbles, a collapse front propagating toward the focal point of the collapse is predicted. This process leads to an amplification of the intensity of the final collapse.

1 Modeling and Simulation of Shocks in Compressible Two-Phase Flows

Cavitating flows occur in various technical applications, such as hydraulic machinery, fuel injection systems, reaction and process technology, as well as in medical engineering applications [18], [33]. The quasi-periodic formation of sheet cavities and their subsequent shedding into clouds introduce low frequency time scales that are correlated with the bulk velocity [2]. Subsequent advection of bubbly clouds into

Nikolaus A. Adams
Technische Universität München, Boltzmannstrasse 15, e-mail: nikolaus.adams@tum.de

Steffen J. Schmidt
Technische Universität München, Boltzmannstrasse 15, e-mail: steffen.schmidt@tum.de

regimes of increased pressure results in the collapse-like recondensation of vapor regions [22], [23]. Due to liquid inertia, intense shocks appear at the focal points of collapses [16], [21]. These shocks may lead to material damage (cavitation erosion), noise and vibration [6], [35].

Even at early design stages, reliable forecasts of the expected properties of novel or redesigned hydraulic machinery are nowadays requested [4]. Therefore, an accurate numerical prediction of two-phase flow phenomena, including collapse-induced shock formation and resulting peak loads, is highly desired.

Our primary research objectives are the prediction of sheet and cloud cavitation including formation and propagation of shocks due to collapsing vapor bubbles or clouds. We discuss two numerical approaches: A two-fluid model with sharp interface treatment, and a single-fluid model using thermodynamic equilibrium assumptions. In order to allow for the simulation of shock formation and wave propagation, the compressibility of the fluids (liquid and vapor) is taken into account. Consequently, the numerical time step is proportional to the ratio of the smallest length scale (minimum grid size) and the fastest signal speed ($\approx$ speed of sound in the liquid).

Both methods are based on a well-established numerical technique for simulation of compressible flows, which is the finite volume method. The flow field is partitioned into computational cells for which the integral form of the governing equations is approximated by conservative numerical methods. Therefore, finite volume methods introduce a numerical length scale given by the edge length l_{num} of the finite volumes [9], [7], [8]. On the other hand, two-phase flows include intrinsic length scales l_{phys} given by the characteristic sizes of bubbles, clear cavities, or of vapor cores within vortices. The ratio $\Psi = l_{phys}/l_{num}$ allows for the definition of three different regimes. In case of $\Psi >> 1$, all vapor structures are resolvable and highly accurate methods, such as sharp interface methods, can be used to simulate the flow in detail. If $\Psi << 1$, none of the vapor structures is resolved. In this case, mixture models (e.g. bubbly flow models or single-fluid models based on thermodynamic considerations) might be a sound option for simulation of large scale dynamics, i.e. dynamics that are resolvable with the selected computational grid. However, if $\Psi \approx 1$, the flow is only marginally resolved and sharp interface methods as well as bubbly flow models may run into difficulties. In contrast, single-fluid models based on thermodynamic considerations might remain valid.

The ratio Ψ depends on available computational resources as well as on the complexity of the investigated problem. For example, highly resolved simulations $(\Psi > 100)$ of collapsing single bubbles or of clouds consisting of a small number of bubbles are nowadays performable. Therefore, it seems reasonable to develop highly sophisticated methods that are purpose-made for problems that allow for resolutions with $\Psi >> 1$. These methods might be used to obtain reference solutions using very elaborate physical models. However, for a broad range of engineering applications, such as the cavitating flow around ship propellers, full resolution of all bubbles is unfeasible even if supercomputers are used. Thus, models based on reduced physical complexity are equally desired to predict medium and large scale dynamics even if $\Psi << 1$.

2 Numerical Methods for Compressible Two-Phase Flows

In this investigation we focus on single component fluids at subcritical thermodynamic conditions. The considered fluid is liquid water or water vapor. Other states of matter or additional gas components are not taken into account. We imply that the continuum assumption is valid for each phase, and phase boundaries, if resolvable, are assumed to be sharp. We neglect viscous effects and focus on the prediction of inertia driven dynamics.

Based on previous considerations, two mathematical models for simulation of compressible two-phase flows are now discussed. The first one is a highly sophisticated two-fluid model using a sharp interface approach, and the second one is an efficient single-fluid model using local thermodynamic equilibrium assumptions. Both methods enable simulations including compressibility effects, such as shock formation and propagation. While sharp interface techniques are purpose-made to simulate flows where the resolution of phase boundaries is essential, single-fluid approaches are suggested to be suitable for simulation of medium and large scale dynamics, e.g. sheet and cloud formation, and cloud collapses.

2.1 Two-fluid model with sharp interface treatment

Our two-fluid approach is based on a conservative interface method [12]. Validation and applications of the method can be found in [19], [20]. At each instant in time, the fluid domain $\Omega(t)$ is partitioned into a finite number of subdomains $\Omega_k(t) \subseteq \Omega$ with boundaries $\Gamma(t) := \partial\Omega_k(t)$. For each subscript k, the corresponding subdomain is either filled with pure liquid (li) or with pure vapor (v). A sharp interface $\Gamma(t)$, which is tracked with the level-set approach proposed in [5], separates vapor and liquid within the computational domain. Using two-fluid models with sharp interface treatment, two-phase flows are interpreted as interacting single phase flows. The interaction takes place at the phase boundaries, where transfer terms for mass, momentum and energy, as well as jump conditions (surface tension) can be defined. These models enable investigations which may involve thermal, mechanical and phase non-equilibrium processes, and they are particularly well suited to study bubble dynamics.

We solve the integral form of the Euler equations for both fluids separately on the corresponding subdomains in a conservative way ($m = v, li$).

$$
\begin{aligned}
V\left(\alpha_m^{n+1}\overline{\mathbf{U}}_m^{n+1} - \alpha_m^{n}\overline{\mathbf{U}}_m^{n}\right) = &\int_n^{n+1} dt\ \Delta y\Delta z\left[A_m^{12}\mathbf{F}_m^{12} - A_m^{11}\mathbf{F}_m^{11}\right] \\
&+ \int_n^{n+1} dt\ \Delta x\Delta z\left[A_m^{22}\mathbf{F}_m^{22} - A_m^{21}\mathbf{F}_m^{21}\right] \\
&+ \int_n^{n+1} dt\ \Delta x\Delta y\left[A_m^{32}\mathbf{F}_m^{32} - A_m^{31}\mathbf{F}_m^{31}\right]
\end{aligned}
\tag{1}
$$

$$+ \int_n^{n+1} dt\, \mathbf{X}_m(\Delta\Gamma)\ ,$$

where $\alpha_m\overline{\mathbf{U}}_m$ and $\overline{\mathbf{U}}_m$ are the vector of the conserved quantities in the cut cell and the vector of volume averaged conservative variables respectively. $\mathbf{F}_m^{pq}$ is the average flux across a cell face. The volume fractions α_m and the cell-face apertures A_m^{pq} are reconstructed from the level-set field. The coupling between both fluids is achieved by a conservative interface interaction term $\mathbf{X}_m(\Delta\Gamma)$, where $\Delta\Gamma$ is the interface area within the cut cell.

The interaction term accounts for the contributions of pressure force and phase change, respectively,

$$\mathbf{X}_m(\Delta\Gamma) = \mathbf{X}_m^p + \mathbf{X}_m^t\ . \tag{2}$$

From the solution of the two-material Riemann problem [24] at the interface, the interface pressure p_I and the interface normal velocity $\mathbf{u}_I$ serve to compute the pressure term $\mathbf{X}_m^p$

$$\mathbf{X}_m^p = \begin{pmatrix} 0 \\ p_I\Delta\Gamma\ (\mathbf{n}_m\cdot\hat{i}) \\ p_I\Delta\Gamma\ (\mathbf{n}_m\cdot\hat{j}) \\ p_I\Delta\Gamma\ (\mathbf{n}_m\cdot\hat{k}) \\ p_I\Delta\Gamma\ (\mathbf{n}_m\cdot\mathbf{u}_I) \end{pmatrix}\ . \tag{3}$$

The mass transfer term $\mathbf{X}_m^t$ is given by

$$\mathbf{X}_v^t = -\mathbf{X}_{li}^t = \begin{pmatrix} \dot{m}\,\Delta\Gamma \\ \dot{m}\,\Delta\Gamma\ (\mathbf{v}\cdot\hat{i}) \\ \dot{m}\,\Delta\Gamma\ (\mathbf{v}\cdot\hat{j}) \\ \dot{m}\,\Delta\Gamma\ (\mathbf{v}\cdot\hat{k}) \\ \dot{m}\,\Delta\Gamma\left(e_v + \frac{1}{2}|\mathbf{v}|^2\right) + p_I\,\Delta q^*\,\Delta\Gamma \end{pmatrix}\ , \tag{4}$$

where $\mathbf{v}$ is the velocity of the liquid at the interface in case of evaporation and the velocity of the vapor in case of condensation, respectively. $\Delta q^* = \dot{m}/\rho_{li}$ is the phase-change induced velocity. The phase change $\dot{m}$ at the interface is based on a non-equilibrium assumption proposed by [32]

$$\dot{m} = \frac{\lambda}{\sqrt{2\pi R_v}}\left(\frac{p_s(T_{li})}{\sqrt{T_{li}}} - \frac{p_v}{\sqrt{T_v}}\right)\ . \tag{5}$$

Here, R_v is the specific gas constant in the vapor phase, and λ is the accommodation coefficient for evaporation or condensation (assumed to be constant). T_v and T_{li} are the temperatures of vapor and liquid at the phase interface, respectively. p_v is the actual vapor pressure at the interface, and $p_s(T_{li})$ is the equilibrium (saturation) vapor pressure at temperature T_{li}.

For our computations with the two-fluid method, we use a fifth-order WENO scheme [14] and a third-order TV Runge–Kutta scheme [34] to discretize the Euler equations. Simulations are carried out with the CFL number of 0.6. We model vapor

as ideal gas ($p = R\rho T$ with $\gamma = 1.335$, $R = 461.5\,\mathrm{J/(kg\,K)}$) and use Tait's equation of state for water ($p = B(\rho/\rho_0)^\gamma - B + A$ with $B = 3310\,\mathrm{bar}$, $A = 1\,\mathrm{bar}$, $\rho_0 = 1\,\mathrm{kg/m^3}$ and $\gamma = 7.15$).

2.2 Single-fluid model using local thermodynamic equilibrium assumptions

For single-fluid models, a common set of governing equations is used to describe the kinematics of the flow. The phases are not treated separately but they are characterized by their fractional contributions, i.e. by their mass fractions ε_v, ε_{li} or their volume fractions α_v, α_{li}. Therefore, the governing equations describe the evolution of mixture quantities, such as the mixture density $\widetilde{\rho} := \alpha_v\rho_v + (1-\alpha_v)\rho_{li}$, as well as the momentum and the total energy of the mixture. The phase transition is modeled by an additional equation for the vapor mass

$$\frac{\partial}{\partial t}(\widetilde{\rho}\varepsilon_v) + \nabla\cdot(\widetilde{\rho}\varepsilon_v\mathbf{v}) = \widetilde{\rho}\cdot\frac{D}{Dt}\varepsilon_v = S_{\varepsilon_v}, \tag{6}$$

where $\widetilde{\rho}\varepsilon_v = \alpha_v\rho_v$ and S_{ε_v} is a source term that might depend on pressure, temperature or additional parameters, such as the initial concentration of nuclei or their initial size. One particular intuitive model is derived as

$$\frac{\partial}{\partial t}(\widetilde{\rho}\varepsilon_v) + \nabla\cdot(\widetilde{\rho}\varepsilon_v\mathbf{v}) = -\widetilde{\rho}\cdot\frac{\varepsilon_v - \varepsilon_{v,equi}}{\tau}, \tag{7}$$

where $\varepsilon_{v,equi}$ is a local equilibrium mass fraction of vapor and τ is the relaxation time. The evaluation of the local equilibrium mass fraction ε_{equi} requires further assumptions, such as thermal equilibrium $T_{li} = T_v$, pressure equilibrium $p_{li} = p_v$, and phase equilibrium $\mu_{li} = \mu_v$, where μ denotes the specific Gibbs function of liquid or vapor. With these assumptions one can use thermodynamic databases, such as the *IAPWS* or *NIST* databases [13], to obtain the equilibrium mass fractions directly from the known density $\widetilde{\rho}$ and internal energy $\widetilde{e}$ of the mixture: $\varepsilon_{v,equi} = DATABASE(\widetilde{\rho},\widetilde{e})$. Note that the databases will return $\varepsilon_{v,equi} = 0$ and $\varepsilon_{v,equi} = 1$ if the pure liquid state or the pure vapor state is stable, respectively. In case of $0 < \varepsilon_{v,equi} < 1$, the saturated mixture is the stable thermodynamic state [26].

The derivation of the relaxation time τ is not a straightforward task. However, the limits $\tau \to 0$ and $\tau \to \infty$ are quite intuitive. In case of $\tau \to 0$, the flow is assumed to be in local thermodynamic equilibrium at each point in space and at each instant in time. Therefore, $\varepsilon_v(x,t) = \varepsilon_{v,equi}(x,t)$. On the other hand, if $\tau \to \infty$, the flow is called frozen, which means that the initial state of matter will remain for all time [11].

For our single-fluid model, we assume $\tau \to 0$ and apply our flow simulation code CATUM (CAvitation Technische Universität München [31], [28], [25]), which is a density-based finite volume method employing a low Mach-number consistent

flux function and an explicit time marching procedure. The spatial reconstruction of the velocity field follows a WENO-3 procedure [14]. Density and internal energy are reconstructed by monotonic TVD limiters (”minmod”) [36]. Time marching is performed by adopting an explicit low-storage 4-step Runge-Kutta method with optimized stability region [31], [28], [17].

For this investigation we use closed form equations for the simulation of the flow around a hydrofoil, and more efficient look-up tables for simulation of the cloud collapse. However, both thermodynamic models provide high quality approximations of the IAPWS database [13] of water, vapor, and liquid-vapor equilibria. The phase-transition model is incorporated in the local thermodynamic equilibrium approach. Surely, equilibrium assumptions might be questionable in case of cavitation inception, where meta-stable states (pressures below the vapor pressure or even tension [37], [1]) may occur. However, our observations indicate that equilibrium assumptions may lead to a sufficiently accurate model for developed cavitating flows, such as the investigated flow around the hydrofoil.

2.3 Investigations using the two-fluid model

2.3.1 Collapse of a single vapor-bubble near a solid wall

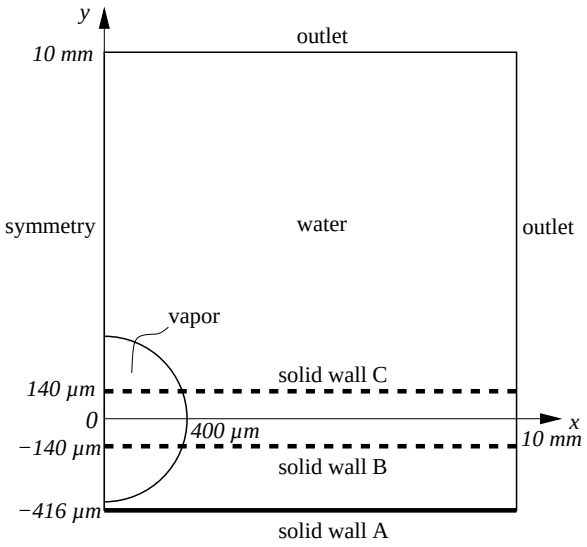

Fig. 1 Sketch of the problem. Three configurations with different wall positions are investigated.

We apply our sharp interface technique to investigate the collapse of a vapor bubble near a solid wall. As shown in Fig. 1, the initial bubble radius is 400 μm and we consider three different wall positions A, B and C. We take advantage of symmetries and compute only one quarter of the bubble. The grid spacing is equidistant in the bubble region with 100 computational cells over the initial bubble radius. Grid stretching is applied in the far-field. Outlet boundary conditions are imposed at $x,y,z = 10$ mm. Data are mirrored on the (X-Y)- and (Y-Z)-plane for visualization. Both fluids have a common initial temperature of 293.0 K which is the saturation temperature corresponding to the initial vapor pressure of 0.0234 bar. Initial liquid pressure is 100 bar and the accommodation coefficient is taken as $\lambda = 0.01$.

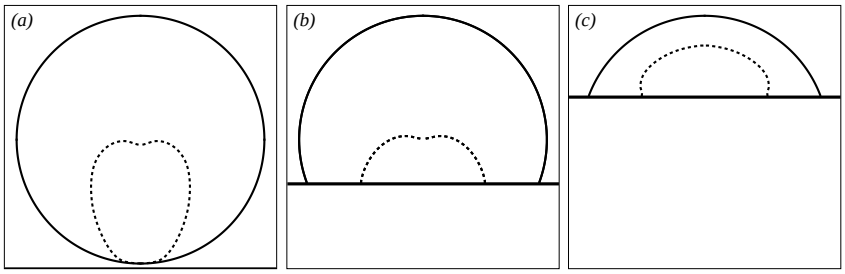

Fig. 2 Initial situation and bubble shape after cavity development for case A, B and C.

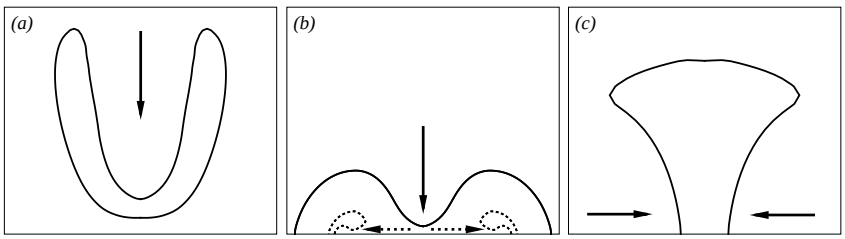

Fig. 3 Liquid jets during vapor bubble collapse near a wall (frame size in μm): a) Wall-normal re-entrant jet for configuration A, b) primary wall-normal re-entrant jet (*solid line*) and secondary wall-parallel outward pointing jet (*dashed line*) for configuration B, and c) wall-parallel inward pointing jet for configuration C. Arrows indicate the jet direction.

For all configurations, the vapor bubble shrinks slowly during the initial period. The rapid stage of the bubble collapse starts with the development of an indentation, followed by the formation of a liquid jet. Two fundamentally different scenarios at the early stages of bubble collapse can be found. For a detached bubble or a bubble cut in the lower hemisphere, the collapse is initiated at the top of the bubble (Fig. 2 a,b). A fast liquid jet develops and penetrates through the bubble in wall-normal direction (Fig. 3 a,b). For an attached bubble cut in the upper hemisphere,

the collapse is initiated between wall and interface (Fig. 2 c) and a liquid jet develops radially toward the bubble center (Fig. 3 c).

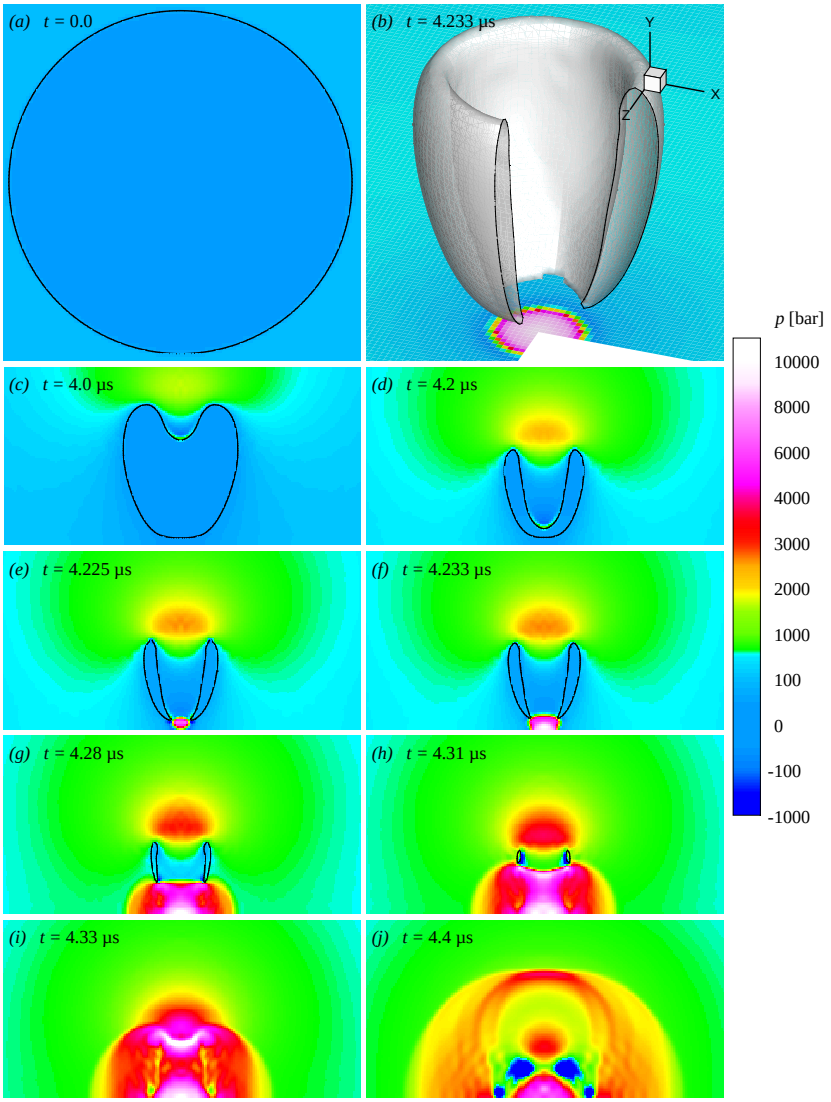

Fig. 4 Collapse of a vapor bubble in configuration A: a) Initial configuration, b) cut through an iso-surface of the zero level-set (interface) at $t = 4.0525\ \mu$s, showing the shape of the bubble and the wall pressure, and c) - j) bubble shape and pressure field at different time instants. All figures except b) have the same magnification scale. The simulation was performed using our two-fluid model with sharp interface technique.

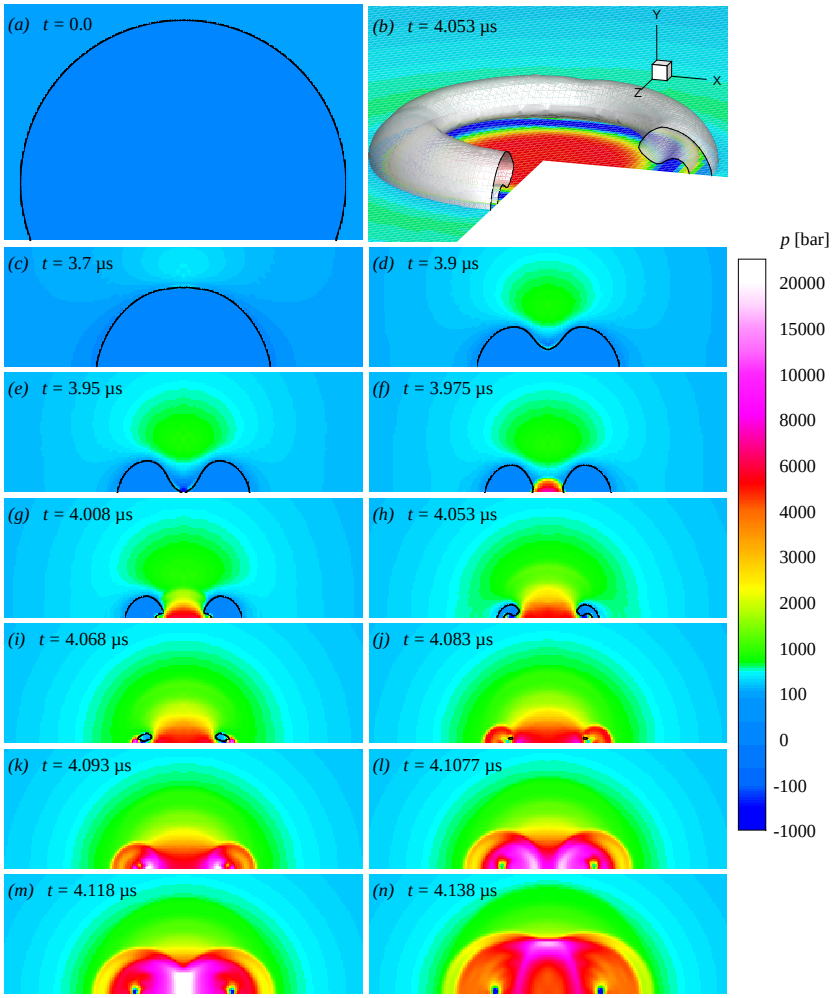

Fig. 5 Collapse of a vapor bubble in configuration B: a) Initial situation, b) cut through an iso-surface of the zero level-set (interface) at $t = 4.053\ \mu$s showing the shape of the bubble and the wall pressure, and c) - n) bubble shape and pressure field at different time instants. All figures except b) have the same magnification scale. The simulation was performed using our two-fluid model with sharp interface technique.

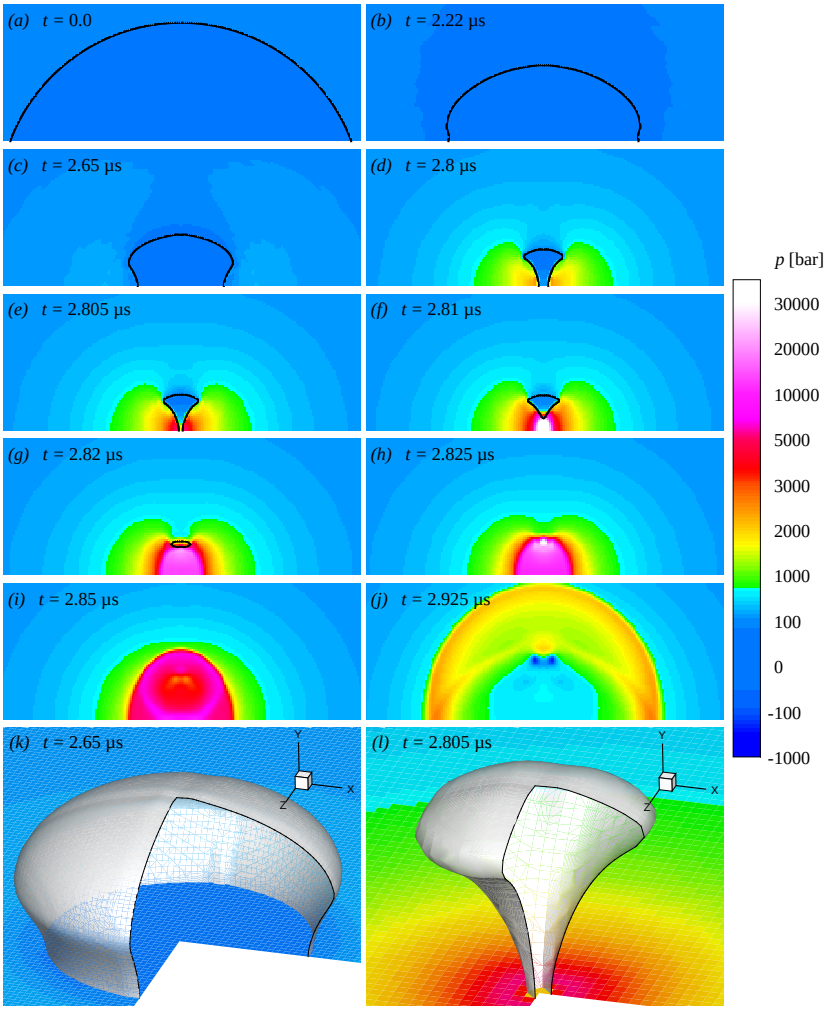

Fig. 6 Collapse of a vapor bubble in configuration C: a) - j) Bubble shape and pressure field at different time instants at same magnification scale, and k) - l) two cuts through an iso-surface of the zero level-set (interface) at $t = 2.65\ \mu$s and $t = 2.805\ \mu$s showing the shape of the bubble and the wall pressure. The simulation was performed using our two-fluid model with sharp interface technique.

The appearance of a secondary jet can be only observed with configuration B since the wall normal jet is deflected at the wall and interacts with the remaining bubble ring (Fig. 3 b, dashed lines). This secondary jet is radially symmetric and develops from the symmetry axis outwards in wall-parallel direction. For configuration A no secondary jet develops as the residual bubble ring is not attached to the

wall. Figures 4 b, 5 b and 6 k-l give a three-dimensional visualization of the bubble shape during the stage of the three different liquid jets.

Figures 4 - 6 visualize the pressure fields during bubble collapse in configuration A, B and C, respectively. The first occurrence of extreme pressure magnitudes coincides with jet breakdown. For cases A and B with a wall-normal re-entrant jet, the observed maximum wall pressures are of comparable magnitude of about 100 times the initial pressure. Slightly larger values for the detached bubble can be attributed to a higher jet velocity. Looking at wall-parallel radial jets, one has to distinguish between the outward-pointing secondary jet of configuration B and the inward pointing primary jet of configuration C. In the latter case, the liquid is gradually compressed while being transported toward the symmetry axis, where maximum pressure occurs. The maximum pressure after inward-pointing, wall-parallel jet breakdown is about six times larger than that for a wall-normal jet. For the outward-running, wall-parallel secondary jet of configuration B, extremely low pressure is observed inside the jet as an expansion of the liquid further decreases the pressure of the high-velocity jet. After the jet breaks down, the liquid pressure increases, but remains significantly smaller than for the inward-pointing jet.

During the final stage of the bubble collapse, two different scenarios occur. For cases A and C, the residual vapor bubble is detached after jet breakdown. Thus, the maximum pressure due to final bubble collapse occurs away from the wall. The emitted shock wave impinges on the wall with reduced magnitude, and the wall pressure does not reach the level observed for jet breakdown, see Figs. 4 and 6. The second scenario can be found for configuration B. After primary and secondary jet breakdown, a residual vapor ring remains at the wall. This ring is surrounded by high pressure which initiates the final collapse radially toward the symmetry axis (Fig. 5). Liquid is compressed toward the center region resulting in large pressure with a maximum at the symmetry axis of about 400 times the initial pressure.

2.4 Investigations using the single-fluid model

The applicability of a local thermodynamic equilibrium approach together with a conservative finite volume method to simulate cavitating flows is assessed in the following sections. First, the cavitating flow around a hydrofoil is simulated and analyzed. As a second investigation, the collapse of a bubble cluster is computed, and local and global collapse characteristics are discussed.

2.4.1 Hydrofoil Cavitation

In this section we assess the predictability of typical cavitation phenomena around a quasi 2-D hydrofoil using our single-fluid model. The investigation represents a sequel to [29]. We apply our single-fluid model to compute the cavitating flow around a 2-D NACA 0015 hydrofoil (angle of attack 6, cord length $l_{cord} = 0.13\ m$,

span width $l_{span} = 0.3\ m$), which is placed in the middle of a rectangular test section (height $h = 0.3\ m$, depth $d = 0.3\ m$, length $l = 0.9\ m$). The walls of the test section and the surface of the hydrofoil are modeled as inviscid adiabatic walls. At the inlet of the numerical domain the velocity $u_{in} = 30\ m/s$ and the static temperature $T_{in} = 293\ K$ of the liquid inflow are imposed. At the outlet the static pressure of $p_{exit} = 4.5\ bar$ is imposed. The resulting cavitation number is $\sigma_{ref} = 2 \cdot (p_{exit} - p_{sat}(T_{in}))/(\rho_{liquid} \cdot u_{in}^2) = 1.0$, where $p_{sat}(T_{in}) = 2340\ Pa$ and $\rho_{liquid} = 998.4\ kg/m$. The numerical domain is discretized by $2.4 \cdot 10^7$ cells. A time step of $8.5 \cdot 10^{-8}\ s$ is applied and a time interval of $0.11\ s$ is simulated. Twelve shedding cycles with an average shedding frequency of $110\ Hz$ are analyzed.

It should be noted that we do not disturb the flow field. All predicted disturbances develop as a result of Rayleigh-Taylor and Kelvin-Helmholtz instabilities initiated by the re-entrant flow. It is thus reasonable to denote the observed cavitation-induced instabilities as intrinsic instabilities [6] that seem to be dominated by inertia [29].

Figure 7 shows a time series of iso-surfaces of the vapor volume fraction $\alpha_v = 5\%$. The time increment between two consecutive instants is $\Delta t \approx 1.14 \cdot 10^{-3}\ s$. One observes the break-up of the sheet (1) including crescent-shaped regions [27]. At time instant (2), the sheet is no longer present but cloudy structures are formed. The time instants (3) and (4) show the re-formation of the sheet and cavitating horseshoe vortices close to the trailing edge. Futher growth of the sheet and the onset of re-entrant flow is detected at time instant (5). Between time instants (6) and (7) the majority of clouds collapse at positions close to the trailing edge. Thereby, strong shockwaves are emitted that will be subsequently discussed. At time instant (8) the maximum length of the sheet is recovered and partial fragmentation due to the re-entrant flow is visible.

The predicted inner structure of the sheet and the clouds is analyzed in Fig. 8. At the top, iso-surfaces of $\alpha_v = 5\%$ are shown, and on the bottom, the vapor volume fraction at the cut-plane $A - A$ is visualized. The sheet cavity essentially consists of vapor ($\alpha_v \approx 1$), while the detached cloud is a mixture of liquid and vapor ($0 < \alpha_v < 1$).

The collapse of vapor clouds close to the trailing edge results in the formation of strong shocks which propagate through the domain. A typical situation is shown in Fig. 9. On the left, a vapor cloud has collapsed and an instantaneous maximum pressure of more than 2400 *bar* at the focal point of the resulting shock $S1$ is recorded. After about 30 μs, the shock front $S1$ is still visible, but its amplitude is reduced to less than 10 *bar* due to spherical decay [38]. However, a second shock $S2$ is observed, where the maximum pressure at the focal point is 1500 *bar*.

Finally, a qualitative comparison of numerically predicted cavitation structures with experimental observations [15] is shown. Although the operating conditions used for the experiment are slightly different, a strong structural similarity is identified. For both investigations, a NACA 0015 hydrofoil is used and the fluid is water at approximately room temperature. The investigations differ since the angle of attack was 8.36 in the experiment and 6 in the simulation. However, the cavitation number applied in the experiment is $\sigma_{exp} = 1.09$, while it is $\sigma_{sim} = 1.0$ for the simulation. Therefore, it is reasonable to assume that the deviations of both set-ups partially

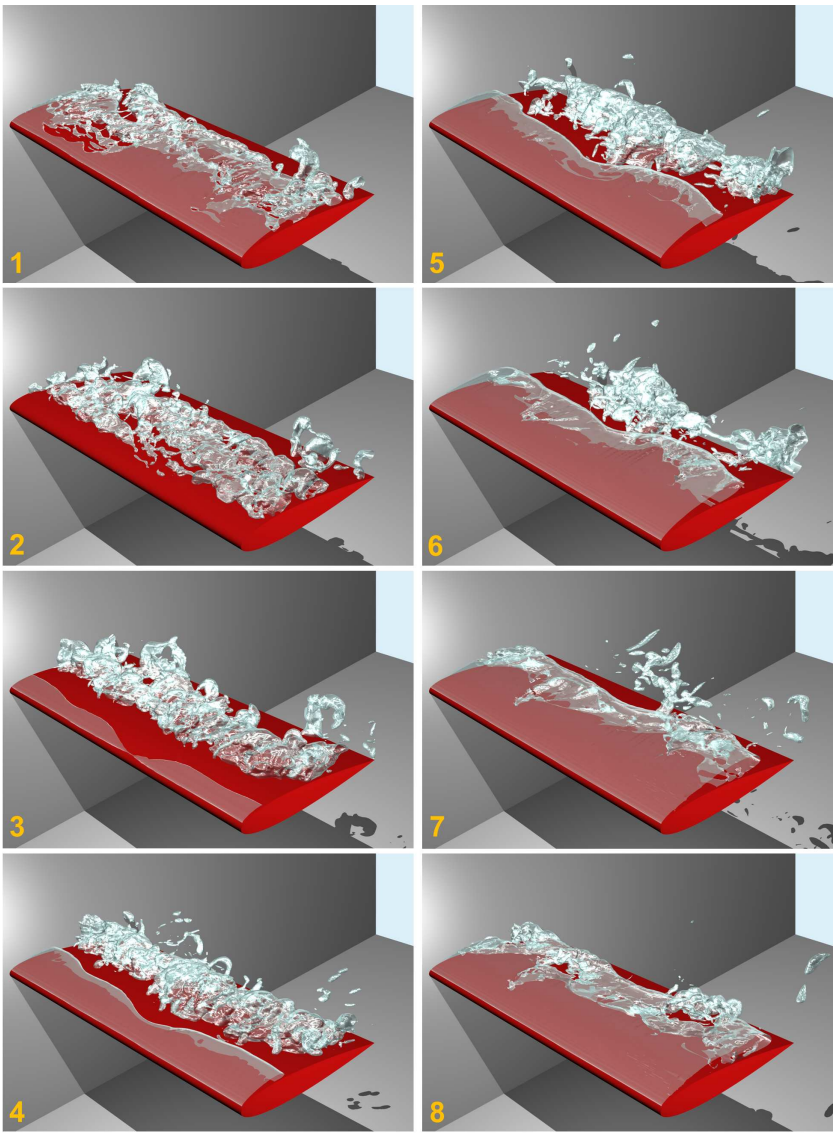

Fig. 7 A typical shedding cycle with shedding frequency $f = 110\ Hz$. Perspective view of NACA 0015 hydrofoil and predicted iso-surfaces of a vapor volume fraction $\alpha_v = 5\%$. The time increment between two consecutive instants is $\Delta t \approx 1.14 \cdot 10^{-3}\ s$. The simulation was performed using our single-fluid model.

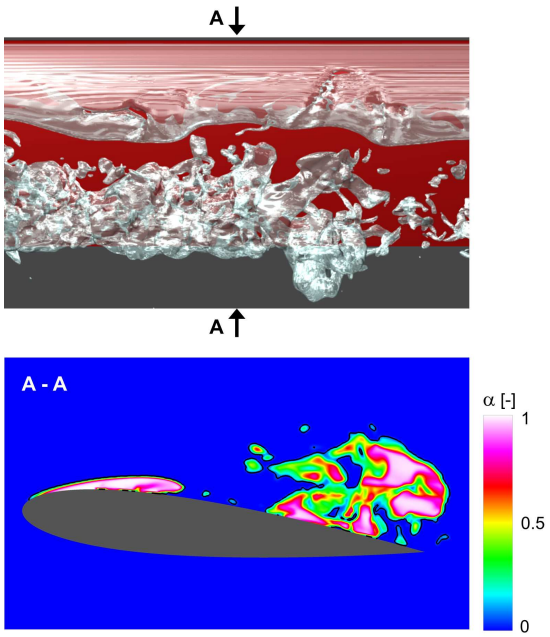

Fig. 8 Iso-surfaces of the vapor volume fraction $\alpha_v = 5\%$ (top) and distribution of the vapor volume fraction at the cut-plane $A-A$. The sheet essentially consists of vapor, i.e. $\alpha_v \approx 1$, while the detached cloud consists of a mixture, i.e. $0 < \alpha_v < 1$. The simulation was performed using our single-fluid model.

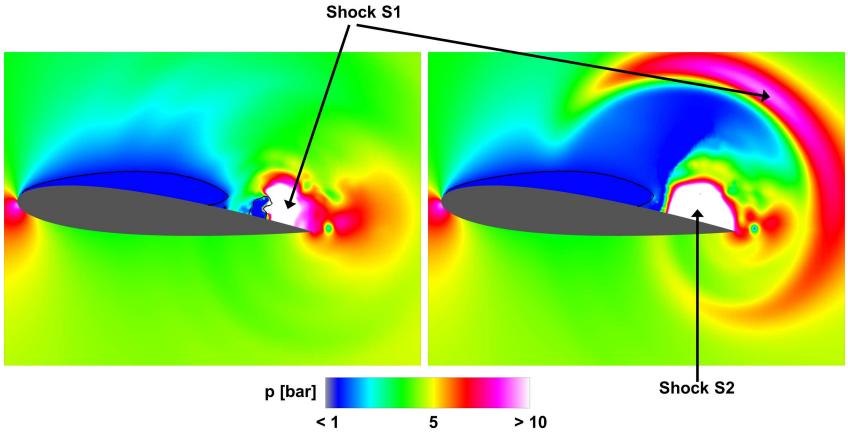

Fig. 9 Shock formation and propagation close to the trailing edge of the hydrofoil. The shock strength are 2400 bar at the focal point of shock *S*1 and 1500 *bar* at the focal point of *S*2. The simulation was performed using our single-fluid model.

cancel each other. In particular, the observed crescent-shaped regions [27] are well represented in the simulation. This is a convincing indication that the applied local thermodynamic equilibrium approach is a suitable technique for the prediction of sheet and cloud cavitation.

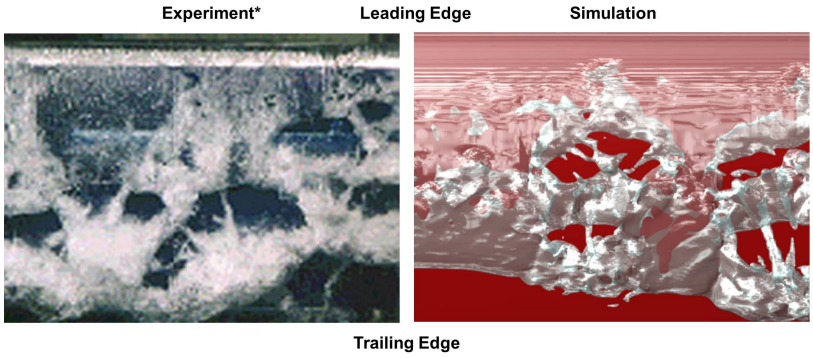

Fig. 10 Comparison of simulated cavitation patterns (iso-surfaces of $\alpha_v = 5\%$) with experimental observation (experiment by [15]). Structures called crescent shaped regions [27] are well reproduced by the simulation. The simulation was performed using our single-fluid model.

2.4.2 Bubble Cloud Collapse

The thermodynamic approach is now applied to investigate the collapse of a bubble cluster [30]. Therefore, we generate a random distribution of bubbles with the following properties: the bubble cluster initially consists of 125 spherical vapor bubbles with radii between $R_{min} = 0.70\ mm$ and $R_{max} = 1.65\ mm$. The average radius is $R_{av} = 0.95\ mm$, and the minimum distance between two bubbles is $0.2\ mm$. The cloud is located within a liquid-filled cubic domain of $20 \cdot 20 \cdot 20\ mm^3$, which will be referred to as the "inner domain". This inner domain is embedded into a larger "outer domain" of $4 \cdot 4 \cdot 2\ m^3$. The inner domain is discretized by using $440^3 = 8.5 \cdot 10^7$ cubic cells with cell-length $h = 45.5\ \mu m$. The large outer domain is discretized by $3.5 \cdot 10^7$ stretched cells. A time-step size of

$$\Delta t = \frac{1.4 \cdot h}{3 \cdot \max(\|\mathbf{v}(t)\| + c(t))}$$

is applied, where $\|\mathbf{v}(t)\|$ and $c(t)$ are the maximum velocity magnitude and the maximum speed of sound at time t, respectively. Since in this case the speed of sound and the maximum velocity undergo significant variations during the stages of the collapse, the resulting dynamic time step is $5.2 \cdot 10^{-9}\ s \leq \Delta t \leq 9.7 \cdot 10^{-9}\ s$.

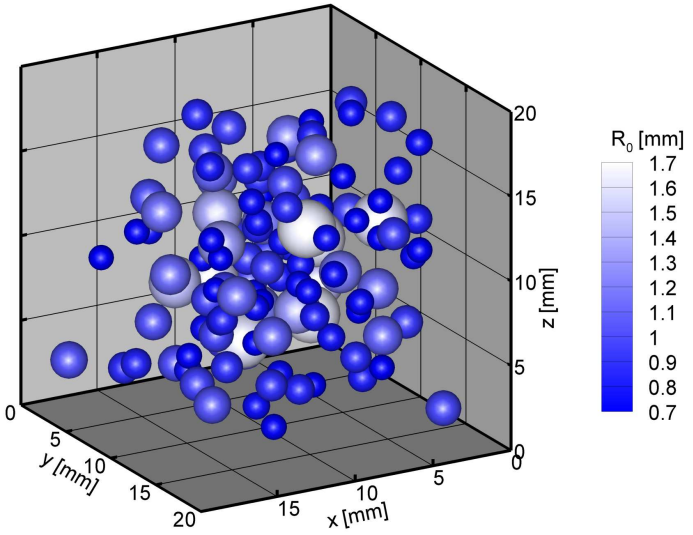

Fig. 11 Initial distribution of bubbles within the small inner domain. Colors represent initial bubble radii R_0.

The bottom faces of both domains are coplanar and impermeable for representing solid walls. The other faces of the outer domain correspond to far-field boundaries. The total initial vapor volume fraction is 5.8% with respect to the inner domain. The initial radius A_0 of the cloud is approximately 10 *mm*. Based on the initial radius A_0, the initial vapor volume fraction $\alpha_{v,0}$ of the cloud is approximately 11%. Hence, the cloud interaction parameter $\beta := \alpha_{v,0} \cdot (A_0/R_{av})^2 \approx 12 >> 1$ indicates strong interaction of the individual bubbles [3]. The following properties are enforced: The initial pressure within the surrounding liquid satisfies a Laplace equation $\Delta p = 0$, where the pressure sufficiently far away from the bubbles is $p_\infty = const. = 40\ bar$, and the pressure inside the bubbles is equal to the vapor pressure $p_{sat} = 2340\ Pa$. Thereby we ensure that the initial pressure field does not contain spurious acoustics. It is further assumed that the velocity field is initially at rest and the initial temperature is $T = 293\ K$. Viscous effects as well as non-condensable gas are neglected.

A series of local and global properties are evaluated to characterize the collapse of the cloud. The time history of the vapor volume $V_{vap}(t)$ of the cloud is used to define an equivalent radius $R_{equiv}(t)$ of a single spherical bubble of equal vapor

volume

$$R_{equiv}(t) := \sqrt[3]{\frac{3}{4\pi} \cdot V_{vap}(t)}.$$

For the investigated case, the initial radius is $R_{equiv}(t_0) \approx 4.78\ mm$. The characteristic collapse time or Rayleigh time τ_{equiv} of the equivalent bubble can be estimated by using a well known relation [6]

$$\tau_{equiv} \approx 0.915 \cdot R_{equiv}(t_0) \cdot \sqrt{\frac{\rho_{liquid}}{p_\infty - p_{sat}}} \approx 6.92 \cdot 10^{-5}\ s. \tag{8}$$

It should be noted that the Rayleigh time as estimated by equation (8) provides an approximation of the collapse duration of a single isolated spherical bubble. Although this estimate might be questionable in case of a collapsing cluster, it can be applied to define the dimensionless time t/τ_{equiv}.

Figure 12 a) shows the evolution of the dimensionless vapor volume $V_{vap}/V_{vap,0}$ and of the dimensionless equivalent radius $R_{equiv}/R_{equiv,0}$ versus the dimensionless time t/τ_{equiv}. The equivalent radius shows its first minimum at $t/\tau_{equiv} = 0.96$ with a value of $R_{equiv}/R_{equiv,0} = 0.04$. Therefore, the duration of the cloud collapse is slightly shorter than the one of an equivalent bubble. We like to point out that the minimum equivalent radius, and hence the minimum vapor volume of the cloud, occurs slightly later than the time instant $t/\tau_{equiv} = 0.95$ where the collapse reaches its maximum intensity (maximum pressure and emission of the strongest shock). Bubbles that have collapsed at an earlier stage lead to an increase of the total vapor volume due to interim rebounds. The rebounds after the main collapse result in a total vapor volume of $R_{equiv}/R_{equiv,0} = 0.18$ at $t/\tau_{equiv} = 1.33$. The dots along the graph of the equivalent radius indicate time instants for which pictures of the cloud are shown in Fig. 13.

Figure 12 b) shows the evolution of the maximum pressure. The highest value ($p_{max} = 9.36\ GPa$) is detected at $t/\tau_{equiv} = 0.95$ and holds for less than 10 *ns*. The total duration of the most intense peak is about 90 *ns*. We found that the durations of all peaks are less than 130*ns*. In total, 120 peaks with maximum pressures higher than 0.45 *GPa* are predicted. Aside of the highest value of $p_{max} = 9.36\ GPa$, two peaks with maximum values above 4.5 *GPa* are recorded.

In Fig. 12 c), the time history of the dimensionless average pressure is presented. The observed maximum value of the average pressure within the small domain is 148 *bar* and it occurs at $t/\tau_{equiv} = 1.01$.

Figure 12 d) presents the time history of the kinetic energy within the small domain. The maximum value is 0.77 *J*. As long as the liquid is accelerated toward the focal point of the collapse, an increase of kinetic energy is predicted. Strong shocks due to collapsing bubbles momentarily decrease the kinetic energy. Once the focal point is reached, the most intense shock is initiated. The outward propagating shock front reduces the kinetic energy by more than 50%.

In order to characterize the instantaneous loads at the wall, we apply a numerical wall pressure transducer. The transducer is located at the center of the wall and the sensitive area is $1 \cdot 1\ mm^2$. Since the numerical time step is adapted dynamically, the

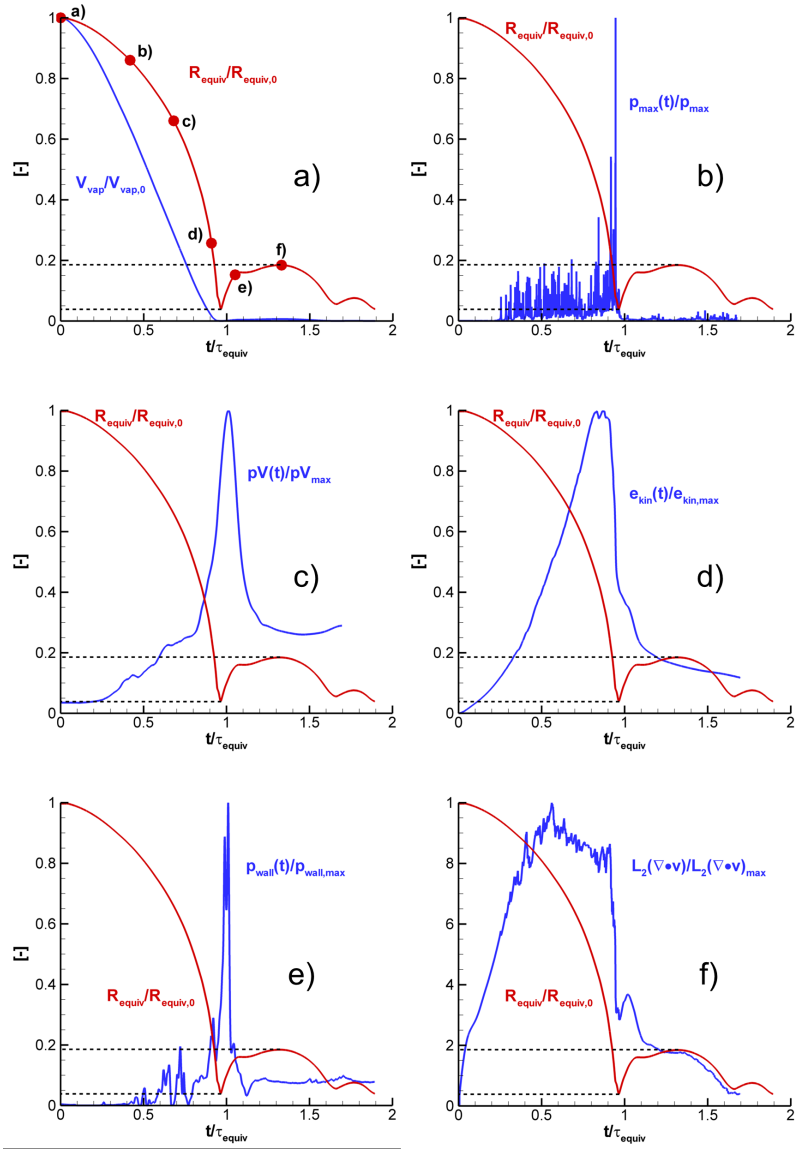

Fig. 12 Analysis of dimensionless collapse characteristics: a) vapor volume $V_{vap}(t)/V_{vap}(t_0)$ and equivalent radius $R_{equiv}(t)/R_{equiv}(t_0)$, b) point-wise maximum pressure within the domain $p_{max}(t)/p_{max,total}$, c) dimensionless average pressure within the small domain, d) kinetic energy within small domain, e) output of the wall pressure transducer, f) L_2-norm of the divergence of the velocity field within the small domain. The simulation was performed using our single-fluid model.

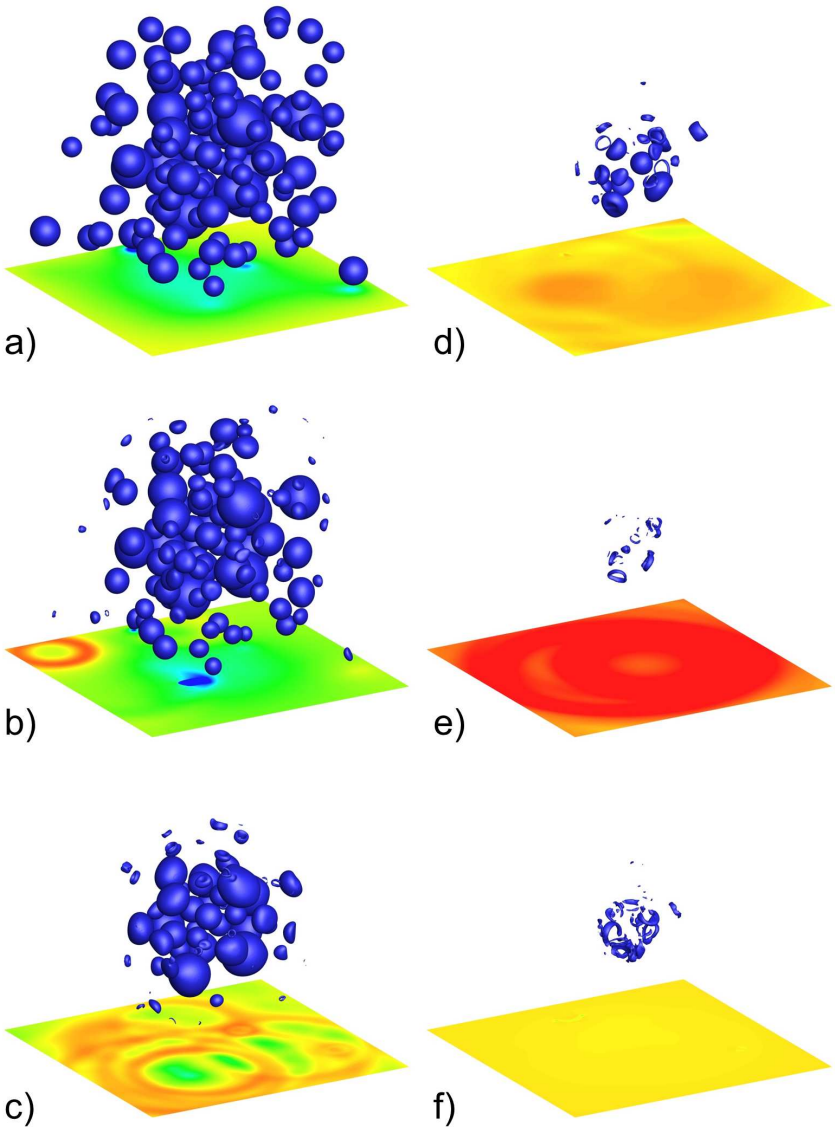

Fig. 13 Visualization of the bubble cluster at six instants in time a) - f). The selected time instants are indicated in picture a) of Fig. 12. The colored bottom plane shows the corresponding pressure field. The simulation was performed using our single-fluid model.

sampling frequency of the transducer is in the range of $0.1-0.2\,GHz$. The output of the transducer is depicted in Fig. 12 e). In accordance with the maximum pressure within the domain (see Fig. 12 b), two close peaks are detected. The duration of each of both peaks is $1.1\cdot 10^{-6}\,s$ and a maximum value of 499 *bar* is predicted at $t/\tau_{equiv}=1.01$. It is interesting to compare the maximum pressure within the domain with the output of the wall pressure transducer, particularly for $0.25\leq t/\tau_{equiv}\leq 0.5$. Although significant peak pressures are predicted within the domain, most of them are not recorded by the wall pressure transducer. We suppose that the surrounding bubbles strongly dampen the intensity of collapse-induced shocks toward the transducer.

In Fig. 12 f), the dimensionless L_2-norm of the divergence of the velocity field is evaluated within the small domain,

$$L_2(\nabla\cdot\mathbf{v}(t)) := \int_{V_{small}} (\nabla\cdot\mathbf{v}(t))^2\,dV.$$

This quantity can be used to characterize the instantaneous amount of expansion and compression within the domain. Again, a significant decrease is predicted once the focal point of the collapse is reached.

Figure 13 shows the progress of the cloud collapse at six instants in time a) - f). The selected time instants are indicated as dots in Fig. 12 a). The bubbles are visualized by iso-surfaces of the vapor volume fraction of $\alpha_v=50\%$, and the static pressure is indicated on the bottom wall. It can bee seen that the outermost bubbles collpase first and emit shock waves. An isolated spherical shock wave is detected in picture b), and a series of shocks are visibles in picture c) of Fig. 13. A collapse front propogates towards the center of the cloud where the final collapse occurs. This process is guided by rebounds of bubbles. Most bubbles show aspherical shapes during their collapse, in particular, one-sided indentation and jet formation are observed. Due to geometric focusing, the collapse front accelerates towards the focal point, and the average pressure increases until the inertia of the impinging liquid enforces the formation of a strong shock at the final stage of the primary collapse. Picture d) of Fig. 13 shows the remaining cloud slightly before the final collapse, and picture e) shows rebounds after the final collapse. Afterwards the peak pressure decays and further growth of the bubbles is observed, compare pictures e) and f).

3 Summary and Future Perspective

We have presented two numerical approaches for simulation of compressible multi-fluid flows with phase-change.

The first one is a sharp interface approach using a two-fluid model. This technique was applied to investigate collapses of single bubbles for three different bubble–wall configurations. For a detached bubble and a bubble cut by the wall in its lower hemisphere, we found the appearance of the well known wall-normal re-entrant jet. For the latter configuration, also a secondary radial and wall-parallel

jet was found. If the bubble is attached, but cut by the wall in its upper hemisphere, the developing jet is wall-parallel and compresses the liquid toward the axis of symmetry. Jet-induced shocks are analyzed and compared in their strength.

The second approach is based on a single-fluid model using local thermodynamic equilibrium assumptions. We assessed the applicability of a local thermodynamic equilibrium approach to simulate sheet and cloud cavitation around a hydrofoil. In particular, typical features of hydrofoil cavitation, such as crescent-shaped regions [27], and irregular break-up patterns [15], are observed. Strong shocks due to collapsing vapor regions close to the trailing edge are predicted. As a second investigation, the local thermodynamic equilibrium approach is used to simulate the collapse of a cluster of resolved vapor bubbles. A collapse front that propagates toward the center of the cluster is predicted. Due to strong focusing of the collapse, an intense peak pressure of more than 9 *GPa* occurs and holds for less than 10 nanoseconds.

Further investigations using state of the art Large Eddy Simulation techniques [10] are planned.

Acknowledgements Computer hardware and computing time were provided by the *Leibniz – Rechenzentrum* (LRZ), which is highly acknowledged. Furthermore, the authors particularly like to thank Eric Lauer, Michael Mihatsch, Matthias Thalhamer, Stefan Hickel and Xiangyu Hu for providing excellent contributions to this work.

References

1. Andersen A., Morch K.A.: In situ Measurement of the Tensile Strength of Water. In: Proc. WIMRC Cavitation Forum 2011, e-publication, July 4 - 6, 2011, Warwick, UK, (2011)
2. Brennen C.E.: Cavitation and Bubble Dynamics. Oxford University Press, (1995)
3. Brennen, C.E.: An Introduction to Cavitation Fundamentals. In: Proc. WIMRC Cavitation Forum 2011, e-publication, July 4 - 6, 2011, Warwick, UK, (2011)
4. D'Agostino L., Salvetti M.V.: Fluid Dynamics of Cavitation and Cavitating Turbopumps. Springer, (2007)
5. Fedkiw R., Aslam T., Merriman B., Osher S.: A non-oscillatory Eulerian approach to interfaces in multimaterial flows (the ghost fluid method). J. Comp. Phys. **152**, 457–492 (1999)
6. Franc J.P., Michel J.M.: Fundamentals of Cavitation. Springer, (2004)
7. Garnier E., Adams N., Sagaut P.: Large Eddy Simulation for Compressible Flows. Springer, (2009)
8. Grinstein F.F., Margolin L.G., Rider W.J.: Implicit Large Eddy Simulation: Computing Turbulent Fluid Dynamics. Cambridge University Press, (2007)
9. Gullbrand J., Chow F.K.: The Effect of Numerical Errors and Turbulence Models in Large-Eddy Simulations of Channel Flow, with and without Explicit Filtering. J. Fluid Mech., Vol. 495, (2003)
10. Hickel S., Mihatsch M., Schmidt S.J.: Implicit Large Eddy Simulation of Cavitation in Micro Channel Flows. In: Proc. WIMRC Cavitation Forum 2011, e-publication, July 4 - 6, 2011, Warwick, UK, (2011)
11. Hirschfelder J.O., Curtiss C.F., Bird R.B.: Molecular Theory of Gases and Liquids. John Wiley and Sons, (1954)
12. Hu X.Y., Khoo B.C., Adams N.A., Huang F.L.: A conservative interface method for compressible flows. J. Comp. Phys. **219**, 553–578 (2006)
13. The International Association for the Properties of Water and Steam, http://www.iapws.org/

14. Jiang G.S., Shu C.W.: Efficient Implementation of Weighted ENO schemes. J. Comp. Phys. **126**, 202–228 (1996)
15. Kawanami J., Kato H., Yamaguchi H.: Three-Dimensional Characteristics of the Cavities Formed on a Two-Dimensional Hydofoil. In: Proc. 3rd CAV 1998 - 3rd International Symposium on Cavitation, Grenoble, France, 7.4.- 10.4.1998, Vol. 1, pp. 191-196, (2009)
16. Kendrinskii V.K.: Hydrodynamics of Explosion. Springer, (2005)
17. Kennedy C.A., Carpenter M.H., Lewis R.M.: Low-storage, Explicit Runge-Kutta Schemes for the Compressible Navier-Stokes Equations. Applied Numerical Mathematics, Vol. 35, (2000)
18. Knapp R.T., Daily J.W., Hammitt F.G.: Cavitation. McGraw-Hill, (1970)
19. Lauer E., Hu X.Y., Hickel A., Adams N.A.: Numerical modelling and investigation of symmetric and asymmetric cavitation bubble dynamics. Phys. Fluids, accepted 2012.
20. Lauer E., Hu X.Y., Hickel A., Adams N.A.: Numerical modelling and investigation of symmetric and asymmetric cavitation bubble dynamics, Comp. Fluids, under revision.
21. Lauterborn W.: Cavitation and Inhomogeneities in Underwater Acoustics. Springer, (1980)
22. Lecoffre Y.: Cavitation Bubble Trackers. Balkema, (1999)
23. Lindau O., Lauterborn W.: Cinematographic observation of the collapse and rebound of a laser-produced cavitation bubble near a wall. J. Fluid Mech. **479**, 327–348 (2003)
24. Menikoff R., Plor B.J.: The Riemann Problem for Fluid Flow of Real Materials. Rev. Modern Physics, Vol. 61, (1989)
25. Mihatsch M., Schmidt S.J, Thalhamer M., Adams N.A.: Numerical Prediction of Ero-sive Collapse Events in Unsteady Compressible Cavitating Flows. In: Proc. Marine 2011, International Conference on Computational Methods in Marine Engineering, Barcelona, (2011)
26. Moran M.J., Shapiro H.N., Boettner D.D., Bailey M.B.: Fundamentals of Engineering Thermodynamics. John Wiley and Sons, (2011)
27. Reisman G.E., Wang Y.-C., Brennen C.E.: Observations of Shock Waves in Cloud Cavitation. Journal of Fluid Mechanics, Vol. 355, (1998)
28. Schmidt S.J., Sezal I.H., Schnerr G.H., Thalhamer M.: Riemann Techniques for the Simulation of Compressible Liquid Flows with Phase-transition at all Mach numbers - Shock and Wave Dynamics in Cavitating 3-D Micro and Macro Systems. In: 46th AIAA Aerospace Sciences Meeting and Exhibit, January 7 - 10, 2008, Reno, Nevada, USA, AIAA paper 2008-1238, (2008)
29. Schmidt S.J., Thalhamer M., Schnerr G.H.: Inertia Controlled Instability and Small Scale Structures of Sheet and Cloud Cavitation. In: Proc. 7th CAV 2009 - 7th International Symposium on Cavitation, Ann Arbor, Michigan, USA, 16.8.- 21.8.2009, paper 17, CD-ROM publication, (2009)
30. Schmidt S.J., Mihatsch M., Thalhamer M., Adams N.A.: Assessment of the Prediction Capability of a Thermodynamic Cavitation Model for the Collapse Characteristics of a Vapor-Bubble Cloud. In: Proc. WIMRC Cavitation Forum 2011, e-publication, July 4 - 6, 2011, Warwick, UK, (2011)
31. Schnerr G.H., Sezal I.H., Schmidt S.J.: Numerical Investigation of Three-dimensional Cloud Cavitation with Special Emphasis on Collapse Induced Shock Dynamics. Physics of Fluids, Vol. 20, Issue 4, (2008)
32. Schrage R.W.: A Theoretical Study of Interphase Mass Transfer. Columbia University Press 1953
33. Shah Y.T., Pandit A.B., Moholkar V.S.: Cavitation Reaction Engineering. Kluwer, (1999)
34. Shu C.W., Osher S.: Efficient implementation of essentially non-oscillatory shock capturing schemes. J. Comp. Phys. **77**, 439–471 (1988)
35. Tomita Y., Shima A.: Mechanisms of impulsive pressure generation and damage pit formation by bubble collapse. J. Fluid Mech. **169**, 535–564 (1986)
36. Toro E.F.: Riemann Solvers and Numerical Methods for Fluid Dynamics. Springer, (1999)
37. Trevena D.H.: Cavitation and the Generation of Tension in Liquids. J. Phys. D: Applied Physics, Vol. 17, (1984)
38. Witham G.B: Linear and Nonlinear Waves. John Wiley and Sons, (1999)

Bibliography

[1] *NIST - National Institute of Standards and Technology*. http://webbook.nist.gov/chemistry/fluid/.

[2] G. Ali. Low mach number flows in time-dependent domains. *SIAM J. APPL. MATH.*, 63, issue 6:2020–2041, 2003.

[3] T. Barberon and P. Helluy. Finite volume simulation of cavitating flows. *Computers and Fluids*, 34:832–858, 2005.

[4] R.E. Bensow and G.Bark. Implicit les predictions of the cavitating flow on a propeller. *Journal of Fluids Engineering*, 132(4):041302, 2010.

[5] A. Berg, U. Iben, A. Meister, and J. Schmidt. Modeling and simulation of cavitation in hydraulic pipelines based on the thermodynamic and caloric properties of liquid and steam. *Shock Waves*, 2005.

[6] P.A. Brandner, G.J. Walker, P.N. Niekamp, and B. Anderson. An experimental investigation of cloud cavitation about a sphere. *Journal of Fluid Mechanics*, 656:147–176, 8 2010.

[7] C.E. Brennen. *Cavitation and Bubble Dynamics*. Oxford University Press, 1995.

[8] Y. Chen and S.D. Heister. Modeling of hydrodynamic nonequilibrium in cavitating flows. *J. Fluids Eng.*, 118:172–178, 1996.

[9] O. Coutier-Delgosha, R. Fortes-Patella, and J.L. Reboud. Evaluation of the turbulence model influence on the numerical simulations of unsteady cavitation. *Journal of Fluids Engineering*, 125(1):38–45, 2003.

[10] O. Coutier-Delgosha, R. Fortes-Patella, J.L. Reboud, N. Hakimi, and C. Hirsch. Numerical simulation of cavitating flow in 2d and 3d inducer geometries. *Int. J. for Numerical Methods in Fluids*, 48:135–167, 2005.

[11] O. Coutier-Delgosha, R. Fortes-Patella, J.L Reboud, N. Hakimi, and C.H. Hirsch. Stability of preconditioned navier–stokes equations associated with a cavitation model. *Computers and fluids*, 34(3):319–349, 2005.

[12] O. Coutier-Delgosha, B. Stutz, A. Vabre, and S. Legoupil. Analysis of cavitating flow structure by experimental and numerical investigations. *J. Fluid Mech.*, 578:171–222, 2007.

[13] C.F. Delale. *Bubble Dynamics and Shock Waves - Series: Shock Wave Science and Technology Reference Library, Vol. 8.* Springer, ISBN: 978-3-642-34297-4, 2013.

[14] C.F. Delale, Z. Baskaya, and S.J. Schmidt. Non-barotropic models of cavitation and their applications. In *In: Proc. ICMF 2010 International Conference on Multiphase Flow, Tampa, Florida, USA, 30.5. -4.6.2010, paper no: DelaleBS-ICMF2010*, 2010.

[15] C.F. Delale, Z. Baskaya, S.J. Schmidt, and G.H. Schnerr. Unsteady bubbly cavitating nozzle flows. In *In: Proc. 7th CAV 2009 - 7th International Symposium on Cavitation, Ann Arbor, Michigan, USA, August 16 - 2, ISBN: 9781617826429*, 2009.

[16] S. Dellacherie. Analysis of godunov type schemes applied to the compressible euler system at low mach number. *J. Comp. Phys.*, 229:978–1016, 2010.

[17] J. Dumond, F. Magagnato, and A. Class. Stochastic-field cavitation model. *Phys. Fluids*, 25:073302, 2013.

[18] J.H. Dynmond and R. Malhotra. The tait equation: 100 years on. *Int. J. Thermophys.*, 9, issue 6:941–951, 1988.

[19] C.P. Egerer, S. Hickel, S.J. Schmidt, and N.A. Adams. Implicit large-eddy simulation of cavitation in a turbulent shear layer. In *Proc. 8th International Symposium on Cavitation (CAV 2012), ISBN: 978-981-07-2826-7*, 2012.

[20] C.P. Egerer, S. Hickel, S.J. Schmidt, and N.A. Adams. Turbulence modulation by phase change in a cavitating shear layer. In *Proc. 9th International ERCOFTAC Symposium on Engineering Turbulence Modelling and Measurements, Greece, 2012*, 2012.

[21] C.P. Egerer, S. Hickel, S.J. Schmidt, and N.A. Adams. *LES of Turbulent Cavitating Shear Layers.* In: Nagel WE, Kröner DH, Resch MM, editors. High Performance Computing in Science and Engineering '13: Springer International Publishing, pp. 349-359, 2013.

[22] C.P. Egerer, S. Hickel, S.J. Schmidt, and N.A. Adams. Large-eddy simulation of turbulent cavitating flow in a micro channel. *Phys. Fluids*, 26:085102, 2014.

[23] E. Foeth. *The Structure of Three-Dimensional Sheet Cavitation.* PhD thesis, TU Delft, 2008.

[24] J.P. Franc. Partial cavity instabilities and re-entrant jet. In *In: Proc. CAV2001 - Fourth International Symposium on Cavitation, Pasadena, USA*, 2001.

[25] J.P. Franc and J.M. Michel. *Fundamentals of Cavitation.* Kluwer Academic Publishers, 2004.

[26] J.P. Franc, M. Riondet, A. Karimi, and G.L. Chahine. Material and velocity effects on cavitation erosion pitting. *Wear*, 274:248–259, 2012.

[27] U. Grigull and E. Schmidt, editors. *Properties of Water and Steam in Si-Units.* Springer, 1981.

[28] H. Guillard and A. Murrone. On the behavior of upwind schemes in the low mach number limit: Ii. godunov type schemes. *Computers and fluids*, 33(4):655–675, 2004.

[29] H. Guillard and C. Viozat. On the behaviour of upwind schemes in the low mach number limit. *Computers and Fluids*, 28:66–86, 1999.

[30] S. Hickel, M. Mihatsch, and S.J. Schmidt. Implicit large eddy simulation of cavitation in micro channel flows. In *In: Proc. WIMRC Cavitation Forum 2011, July 4 - 6, Warwick, UK, ISBN 978-0-9570404-1-0*, 2011.

[31] R. Hirschi, P.H. Dupont, F. Avellan, J.N. Favre, J.F. Guelich, and E. Parkinson. Centrifugal pump performance drop due to leading edge cavitation: numerical predictions compared with model tests. *Journal of fluids engineering*, 120(4):705–711, 1998.

[32] X.Y. Hu, N.A. Adams, and G. Iaccarino. On the hllc riemann solver for interface interaction in compressible multi-fluid flow. *Journal of Computational Physics*, 228(17):6572–6589, 2009.

[33] R. Huber. Geschwindigkeitsmaßstabseffekte bei der kavitationserosion in der scherschicht nach prismatischen kavitatoren. Technical report, Report Nr. 102, Lehrstuhl und Versuchsanstalt für Wasserbau und Wasserwirtschaft, TU München, Germany, 2004.

[34] W. Hundsdorfer and J.G. Verwer. *Numerical Solution of Time-Dependent Advection-Diffusion-Reaction Equations.* Springer, 2003.

[35] A. Jameson, W. Schmidt, and E. Turkel. Numerical solution of the euler equations by finite volume methods using runge-kutta time stepping schemes. *AIAA Paper*, 81:1259, 1981.

[36] A. Karimi and J.L. Martin. Cavitation erosion of materials. *International Metals Reviews*, 31(1):1–26, 1986.

[37] Y. Kawanami, H. Kato, and H. Yamaguchi. Three-dimensional characteristics of the cavities formed on a two-dimensional hydrofoil. In *In: Proc. CAV1998 - Third International Symposium on Cavitation, Grenoble, France, pp. 191-196*, 1998.

[38] K.H. Kim, G. Chahine, J.P. Franc, and A. Karimi. *Advanced Experimental and Numerical Techniques for Cavitation Erosion Prediction.* Springer Netherlands, ISBN: 9789401785389, 2014.

[39] R.T. Knapp, J.W. Daily, and F.G. Hammit. *Cavitation*. McGraw-Hill, 1970.

[40] D. Krefting, R. Mettin, and W. Lauterborn. High-speed observation of acoustic cavitation erosion in multibubble systems. *Ultrasonics sonochemistry*, 11(3):119–123, 2004.

[41] A. Kubota, H. Kato, and H. Yamaguchi. A new modelling of cavitating flows; a numerical study of unsteady cavitation on a hydrofoil section. *J. Fluid Mech.*, 240:59–96, 1992.

[42] R.F. Kunz, D.A. Boger, D.R. Stinebring, T.S. Chyczewski, J.W. Lindau, H.J. Gibeling,

S. Venkateswaran, and T.R. Govindan. A preconditioned navier–stokes method for two-phase flows with application to cavitation prediction. *Computers and Fluids*, 29(8):849 – 875, 2000.

[43] E. Lauer. *Numerical Simulation and Investigation of High-Speed Bubble-Dynamics in Cavitating Flow.* Verl. Dr. Hut, ISBN: 978-3-8439-1358-4, 2013.

[44] E. Lauer, X.Y. Hu, S. Hickel, and N.A. Adams. Numerical investigation of collapsing cavity arrays. *Physics of Fluids*, 24(5):052104, 2012.

[45] E. Lauer, X.Y. Hu, S. Hickel, and N.A. Adams. Numerical modelling and investigation of symmetric and asymmetric cavitation bubble dynamics. *Computers and Fluids*, 69:1–19, 2012.

[46] Y. Lecoffre. *Cavitation Bubble Trackers*. A.A. Balkema, 1999.

[47] E.R. Li, M. Pourquie, and T.J.C. Van Terwisga. A numerical study of steady and unsteady cavitation on a 2d hydrofoil. *Journal of Hydrodynamics, Ser. B*, 22(5):770–777, 2010.

[48] T.G. Liu, B.C. Khoo, and W.F. Xie. Isentropic one-fluid modelling of unsteady cavitating flow. *Journal of Computational Physics*, 201(1):80–108, 2004.

[49] A. Meister. Asymptotic single and multiple scale expansions in the low mach number limit. *SIAM J. Appl. Math.*, 60, issue 1:256–271, 1999.

[50] R. Menikoff and B.J. Plor. The riemann problem for fluid flow of real materials. *Rev. Modern Physics*, 61, issue 1:75–130, 1989.

[51] M. Mihatsch, S.J. Schmidt, M. Thalhamer, N.A. Adams, R. Skoda, and U. Iben. Collapse detection in compressible 3-d cavitating flows and assessment of erosion criteria. In *In: Proc. WIMRC Cavitation Forum 2011, July 4 - 6, Warwick, UK, ISBN 978-0-9570404-1-0*, 2011.

[52] M.S. Mihatsch, S.J. Schmidt, M. Thalhamer, and N.A. Adams. Quantitative prediction of erosion aggressiveness through numerical simulation of 3-d unsteady cavitating flows. In *Proc. 8th International Symposium on Cavitation (CAV 2012), ISBN: 978-981-07-2826-7*, 2012.

[53] M.S. Mihatsch, S.J. Schmidt, M. Thalhamer, and N.A. Adams. Numerical prediction of erosive collapse events in unsteady compressible cavitating flows. In L. Eça, E. Oñate, J. García-Espinosa, T. Kvamsdal, and P. Bergan, editors, *MARINE 2011, IV International Conference on Computational Methods in Marine Engineering, 2013*, volume 29 of *Computational Methods in Applied Sciences*, pages 187–198. Springer Netherlands, ISBN: 978-94-007-6142-1, 2013.

[54] J.C. Padrino, D.D. Joseph, T. Funada, J. Wang, and A. Sirignano. Stress-induced

cavitation for the streaming motion of a viscous liquid past a sphere. *J. Fluid M.*, 578:381–411, 2007.

[55] E. Rapposelli and L. d'Agostino. A barotropic cavitation model with thermodynamic effects. In *Fifth International. Symposium on Cavitation, CAV2003, Osaka, Japan, Nov*, pages 1–4, 2003.

[56] G. E. Reisman, Y.C. Wang, and C.E. Brennen. Observations of shock waves in cloud cavitation. *J. Fluid M.*, 355:255–283, 1998.

[57] D. Rossinelli, B. Hejazialhosseini, P. Hadjidoukas, C. Bekas, A. Curioni, A. Bertsch, S. Futral, S.J. Schmidt, N.A. Adams, and P. Koumoutsakos. 11 pflop/s simulation of cloud cavitation collapse. In *Proc. SC '13 Proceedings of SC13: International Conference for High Performance Computing, Networking, Storage and Analysis, Article No.3, ISBN: 978-1-4503-2378-9*, 2013.

[58] J. Sauer. *Instationär kavitierende Strömungen - Ein neues Modell, basierend auf Front Capturing (VoF) und Blasendynamik.* PhD thesis, Univ. Karlsruhe (TH), 2000.

[59] R. Saurel, J.P. Cocchi, and P.B. Butler. Numerical study of cavitation in the wake of a hypervelocity projectile. *J. Propulsion and Power*, 15, issue 4:513–522, 1999.

[60] R. Saurel, F. Petitpas, and R.A. Berry. Simple and efficient relaxation methods for interfaces separating compressible fluids, cavitating flows and shocks in multiphase mixtures. *Journal of Computational Physics*, 228(5):1678–1712, 2009.

[61] S. Schmidt, I. Sezal, and G.H. Schnerr. Compressible simulation of high-speed hydrodynamics with phase change. In *In: Proc. ECCOMAS CFD 2006 - European Conference on Computational Fluid Dynamics, Egmond aan Zee, The Netherlands, September 5-8, ISBN: 90-9020970-0*, 2006.

[62] S.J. Schmidt. *Ein Verfahren zur präzisen Berechnung dreidimensionaler, reibungsfreier Idealgasströmungen über dem gesamten Kompressibilitätsbereich.* Diplomarbeit an der Fakultät Mathematik der Technischen Universität München, 2005.

[63] S.J. Schmidt, M. Mihatsch, M. Thalhamer, and N.A. Adams. Assessment of the prediction capability of a thermodynamic cavitation model for the collapse characteristics of a vapor-bubble cloud. In *In: Proc. WIMRC Cavitation Forum 2011, July 4 - 6, Warwick, UK, ISBN 978-0-9570404-1-0*, 2011.

[64] S.J. Schmidt, I.H. Sezal, G.H. Schnerr, and M. Thalhamer. Shock waves as driving mechanism for cavitation erosion. In *In: Proc. 8th ISAIF - International Symposium on Experimental and Computational Aerothermodynamics of Internal Flows, Lyon, France, July 2-6, paper ISAIF8-0044, pp. 931-940*, 2007.

[65] S.J. Schmidt, I.H. Sezal, G.H. Schnerr, and M. Thalhamer. Numerical analysis of shock dynamics for detection of erosion sensitive areas in complex 3-d flows. In *In:*

Proc. WIMRC Cavitation Forum 2008, pp. 107-120, July 7 - 9, Warwick, UK, ISBN: 9780902683884, 2008.

[66] S.J. Schmidt, I.H. Sezal, G.H. Schnerr, and M. Thalhamer. Riemann techniques for the simulation of compressible liquid flows with phase-transition at all mach numbers - shock and wave dynamics in cavitating 3-d micro and macro systems. In *In: 46th AIAA Aerospace Sciences Meeting and Exhibit, January 7 - 10, Reno, Nevada, USA, AIAA paper 2008-1238, ISBN: 9781605602011, doi: 10.2514/6.2008-1238*, 2008.

[67] S.J. Schmidt, I.H. Sezal, G.H. Schnerr, M. Thalhamer, and M. Förster. Compressible simulation of liquid/vapor two-phase flows with local phase transition. In *In: Proc. ICMF 2007 - International Conference on Multiphase Flow, Leipzig, Germany, July 9-13, ISBN 3860109138, 9783860109137*, 2007.

[68] S.J. Schmidt, M. Thalhamer, and G.H. Schnerr. Density based cfd-techniques for simulation of cavitation induced shock emission. In *In: Proc. 8th ETC 2009 - 8th European Turbomachinery Conference, Graz, Austria, March 23 - 27, pp. 197-208, ISBN: 9783851250367*, 2009.

[69] S.J. Schmidt, M. Thalhamer, and G.H. Schnerr. Inertia controlled instability and small scale structures of sheet and cloud cavitation. In *In: Proc. 7th CAV 2009 - 7th International Symposium on Cavitation, Ann Arbor, Michigan, USA, August 16 - 21, ISBN: 9781617826429*, 2009.

[70] G.H. Schnerr, S. Schmidt, I. Sezal, and M. Thalhamer. Shock and wave dynamics in compressible liquid flows with emphasis on unsteady load on hydrofoils and on cavitation in injection nozzles. In *In: Proc. CAV2006 - 6th International Symposium on Cavitation, Wageningen, The Netherlands, September 11-15*, 2006.

[71] G.H. Schnerr, I.H. Sezal, and S.J. Schmidt. Numerical investigation of three-dimensional cloud cavitation with special emphasis on collapse induced shock dynamics. *Physics of Fluids*, 20, Issue 4, 2008.

[72] H.R. Schwarz and N. Köckler. *Numerische Mathematik.* Vieweg + Teubner, 2004.

[73] I.H. Sezal, S.J. Schmidt, G.H. Schnerr, M. Thalhamer, and M. Förster. Shock and wave dynamics in cavitating compressible liquid flows in injection nozzles. *Shock Waves*, 19, issue 1:49–58, 2009.

[74] C.W. Shu. Essentially non-oscillatory and weighted essentially non-oscillatory schemes for hyperbolic conservation laws. Technical report, ICASE report No. 97-65.

[75] A.K. Singhal, M.M. Athavale, H. Li, and Y. Jiang. Mathematical basis and validation of the full cavitation model. *J. Fluids Eng.*, 124, issue 3:617–624, 2002.

[76] R. Skoda, U. Iben, A. Morozov, M. Mihatsch, S.J. Schmidt, and N.A. Adams. Numerical simulation of collapse induced shock dynamics for the prediction of the geometry,

pressure and temperature impact on the cavitation erosion in micro channels. In *In: Proc. WIMRC Cavitation Forum 2011, July 4 - 6, Warwick, UK*, 2011.

[77] P.K. Sweby. High resolution schemes using flux-limiters for hyperbolic conservation laws. *SIAM J. Num. Anal.*, 21:995–1011, 1984.

[78] M. Thalhamer, S.J. Schmidt, M. Mihatsch, and N.A. Adams. Numerical simulation of sheet and cloud cavitation and detection of cavitation erosion. In *14th International Symposium on Transport Phenomena and Dynamics of Rotating Machinery, ISROMAC-14, February 27th - March 2nd, Honolulu, HI, USA*, 2012.

[79] A. Theodorakakos, N. Mitroglou, and M. Gavaises. Simulation of heating effects in cavitating flows through diesel fuel injectors caused by extreme fuel pressurisation. *Simulation*, 14:16, 2012.

[80] E.F. Toro. *Riemann Solvers and Numerical Methods for Fluid Dynamics.* Springer, 1999.

[81] D.H. Trevena. Cavitation and the generation of tension in liquids. *J. Phys. D: Appl. Phys.*, 17:2139–2164, 1984.

[82] E. Turkel. Review of preconditioning methods for fluid dynamics. *Applied Numerical Mathematics*, 12(1):257–284, 1993.

[83] C.B. Vreugdenhil and B. Koren. *Numerical Methods for Advection–Diffusion Problems - A robust upwind discretisation method for advection, diffusion and source terms.* Vieweg, 1993.

[84] W. Wallis. *One Dimensional Two-Phase Flow.* McGraw Hill, 1975.

[85] G.B. Whitham. *Linear and Nonlinear Waves.* John Wiley and Sons, 1999.

[86] F. Wrona. *Simulation von kavitierenden Strömungen in Hochdrucksystemen.* PhD thesis, Univ. Stuttgart, 2005.

[87] F.R. Young. *Cavitation.* McGraw-Hill, 1989.

[88] W. Yuan and G. Schnerr. Numerical simulation of two-phase flow in injection nozzles: Interaction of cavitation and external jet formation. *Journal of Fluids Engineering*, 125(6):963–969, 2003.

[89] P.J. Zwart, A.G. Gerber, and T. Belamri. Two-phase flow model for predicting cavitation dynamics. *In Fifth International Conference on Multiphase Flow ICMF2004, Yokohama, Japan*, 2004.